



Technische Universität München

Fakultät für Mathematik
Lehrstuhl M2 - Numerische Mathematik (Prof. Dr. B. Wohlmuth)

Hybrid Finite Element Methods for Non-linear and Non-smooth Problems in Solid Mechanics

Linus Maximilian Wunderlich, M.Sc. (hons)

Vollständiger Abdruck der von der Fakultät für Mathematik der Technischen Universität München zur Erlangung des akademischen Grades eines

Doktors der Naturwissenschaften (Dr. rer. nat.)

genehmigten Dissertation.

Vorsitzender: Prof. Dr. Martin Brokate

Prüfer der Dissertation:

1. Prof. Dr. Barbara Wohlmuth
2. Prof. Dr. Olaf Steinbach, Technische Universität Graz
3. Prof. Alessandro Reali, Ph.D., Università di Pavia

Die Dissertation wurde am 06.07.2017 bei der Technischen Universität München eingereicht und durch die Fakultät für Mathematik am 02.11.2017 angenommen.

“Understanding of mathematics cannot be transmitted by painless entertainment any more than education in music can be brought by the most brilliant journalism to those who never have listened intensively.”

Richard Courant (1888–1972), [58]

Acknowledgements

First and foremost I would like to express my deep gratitude towards my advisor Prof. Dr. Barbara Wohlmuth for her support during the past years. Her mathematical expertise, her passion for scientific work and her advice were essential for the research presented in this thesis. Despite her busy schedule, she always found time for discussion and to share her knowledge. I also thank her for the opportunities for international collaborations and to present my work at several conferences.

I am deeply thankful to my reviewers, Prof. Alessandro Reali, Ph.D. and Prof. Dr. Olaf Steinbach, for their effort in the examination of my thesis. Special thanks also to Prof. Dr. Martin Brokate for taking the chair of the examination committee.

During my time at the chair of numerical mathematics, I profited a lot from the open and friendly atmosphere, leading to many interesting discussions as well as good times spent after work. Therefore, I would like to thank all of my current and former colleagues. Special thanks to Aenne Oelker, Dr. Thomas Horger, Dr. Klaus-Dieter Reinsch and Ettore Vidotto for carefully proofreading parts of my thesis.

Most of the work was prepared in teamwork and I want to thank my collaborators for the pleasant work. Also working with my students, Robert Eder and Markus Muhr, was always a pleasure.

The research collected in this thesis was made possible by financial support, which I gratefully acknowledge. I am thankful for the conceptual and financial support of the TopMath graduate program of the Elite Network of Bavaria. Also the international research training group IGDK 1754 supported main parts of this thesis, especially the cooperation with Prof. Dr. Olaf Steinbach at the TU Graz. My main funding during the last years was provided by the Deutsche Forschungsgemeinschaft within the priority programme SPP 1748, *Reliable Simulation Techniques in Solid Mechanics*, and is gratefully acknowledged.

I am grateful to my mother for her never-ending support and understanding and to my brother for his encouragement. I thank my father for his support and advice during my studies. Finally special thanks to my friends, especially Tobias and Wiebke, for the many welcome distractions and joyful moments.

Abstract

In this thesis, several hybrid finite element methods are studied and applied to non-linear and non-smooth problems in solid mechanics. We consider non-conforming methods based on isogeometric elements and standard polynomial spaces. The potential of isogeometric mortar methods is presented with a vibroacoustical example, which includes material and geometry variations. For non-linear problems of Signorini-type, we provide optimal order a priori estimates for the trace and the flux.

Zusammenfassung

In dieser Arbeit werden verschiedene hybride Finite Element Methoden behandelt und auf nichtlineare sowie nichtglatte Probleme der Festkörpermechanik angewendet. Wir behandeln nichtkonforme Methoden, die auf isogeometrischen Elementen, sowie standard Polynomräumen basieren. Das Potential isogeometrischer Mortar-Methoden wird an einem Beispiel der Vibroakustik, mit Material- und Geometrieänderungen, gezeigt. Für nichtlineare Signorini-Probleme beweisen wir optimale Fehlerabschätzungen für die Randwerte und den Fluss.

Publications by the author

- J. Krämer, C. Wieners, B. Wohlmuth, and L. Wunderlich. A robust weakly conforming hybrid discontinuous Galerkin method for linear elasticity. In preparation, 2017, [136].
- H. R. Bayat, J. Krämer, L. Wunderlich, S. Wulfinghoff, S. Reese, B. Wohlmuth, C. Wieners. Numerical evaluation of discontinuous and nonconforming finite element methods in solid mechanics. Submitted for publication in *Computational Mechanics*, 2017, [19].
- T. Horger, A. Reali, B. Wohlmuth, and L. Wunderlich. Improved approximation of eigenvalues in isogeometric methods for multi-patch geometries and Neumann boundaries. <https://arxiv.org/abs/1701.06353>, 2017, [111].
- T. Horger, B. Wohlmuth, and L. Wunderlich. Reduced basis isogeometric mortar approximations for eigenvalue problems in vibroacoustics. In *Model Reduction of Parametrized Systems*, Springer, 2017, [113].
- J. Krämer, C. Wieners, B. Wohlmuth, and L. Wunderlich. A hybrid weakly nonconforming discretization for linear elasticity. *Proceedings in Applied Mathematics and Mechanics*, 2016, [135].
- O. Steinbach, B. Wohlmuth, and L. Wunderlich. Trace and flux a priori error estimates in finite-element approximations of Signorini-type problems. *IMA Journal of Numerical Analysis*, 2016, [204].
- L. Wunderlich. Contact and mesh-tying using mortar methods. *Mathematisches Forschungsinstitut Oberwolfach*, 2015, [237].
- E. Brivadis, A. Buffa, B. Wohlmuth, and L. Wunderlich. The influence of quadrature errors on isogeometric mortar methods. In *Isogeometric Analysis and Applications 2014*, Springer, 2015, [42].
- E. Brivadis, A. Buffa, B. Wohlmuth, and L. Wunderlich. Isogeometric mortar methods. *Computer Methods in Applied Mechanics and Engineering*, 2015, [43].

Contents

1	Introduction and background	9
1.1	Mathematical background	11
1.1.1	Functional analysis	12
1.1.2	Finite element methods and the Galerkin approach	14
1.2	Solid mechanics	20
1.2.1	Linear elasticity	20
1.2.2	Orthotropic material laws	28
1.2.3	Signorini and contact problems	30
1.2.4	Finite elasticity	31
2	Isogeometric mortar methods	33
2.1	Introduction	34
2.1.1	B-splines and NURBS basics	34
2.1.2	Isogeometric mortar methods	37
2.2	Lagrange multiplier trace spaces	41
2.2.1	Choice of the spaces	41
2.2.2	Numerical results	49
2.3	Biorthogonal basis functions	58
2.3.1	Construction with higher order approximation property	59
2.3.2	Numerical results	63
2.4	Influence of quadrature errors	65
2.4.1	Mortar integrals	66
2.4.2	Numerical results	68
2.5	Isogeometric eigenvalue approximation	75
2.5.1	Influence of the mortar coupling	76
2.5.2	Eigenvalue approximation for a wooden beam	79
3	Efficient vibroacoustical application of isogeometric mortar methods	83
3.1	An isogeometric approximation of a bridge of a violin	84
3.1.1	Problem setting	84
3.1.2	Variations of the violin bridge	86
3.2	Reduced basis methods in vibroacoustics	87
3.2.1	Transforming geometrical to material parameters	88
3.2.2	Reduced basis methods for eigenvalue problems	90

3.2.3	Numerical simulations	92
3.3	Reduced basis methods for complex geometry variations	97
3.3.1	Application of the empirical interpolation method	98
3.3.2	Geometry variations of the violin bridge	100
4	A priori trace and flux estimates for Signorini-type problems	103
4.1	Optimal a priori estimates	103
4.1.1	Primal discretization and main result	104
4.1.2	Equivalent reformulations	105
4.2	Proof of the a priori estimates	108
4.2.1	Application of a Strang lemma	108
4.2.2	A priori estimate of the primal trace	111
4.3	Lagrange multiplier estimates	122
4.4	Numerical results	123
5	Discontinuous and weakly conforming methods	129
5.1	Hybridizable weakly conforming method	130
5.1.1	Problem formulation	130
5.1.2	A priori analysis	132
5.1.3	Hybridization and practical formulations	139
5.2	Numerical evaluation of the non-conforming method	145
5.2.1	Uniform and adaptive refinements	145
5.2.2	Application to contact problems	148
5.2.3	Performance for nearly-incompressible elasticity	151
5.3	Review of interior penalty discontinuous Galerkin methods	153
5.3.1	The discontinuous Galerkin method	154
5.3.2	A low-order hybrid discontinuous Galerkin method	157
5.4	Comparison of the non-conforming and discontinuous methods	158
5.4.1	Comparison of the hybrid approaches	158
5.4.2	Numerical comparison	159
	Conclusion and outlook	167
	Figures	169
	Tables	175
	Bibliography	177

1 Introduction and background

Modern numerical techniques are fundamental for the success of today's engineering. In the mid-20th century numerical methods for structural analysis based on variational discretizations of partial differential equations (PDEs) came up. Among the first approaches are simulations of Boeing for shell-structures in airplanes, presented in [217]. The numerical methods evolved quickly due to the improvement of computers, the gain in experience and a better understanding of the mathematical foundation. Nowadays numerical methods for solid mechanics play a key role in engineering design and construction—from the tiniest piece of a machine up to huge constructions. Their importance extends far beyond the classical fields of mechanical and civil engineering, as many of the used techniques are successfully applied to more general types of PDEs, e.g., in acoustics [125], finance [1], fluid dynamics [67] and medicine [85].

Despite the impressive success, the correct application of numerical methods remains important. An unfortunate example is an accident during the construction of the “Sleipner A” offshore platform in the North sea in 1991, see [14, Section 1.2] and [122]. During a load test, the gravity base structure collapsed. The subsequent investigation showed that the numerical structural analysis underestimated the stress by 47% due to an inappropriate application of the finite element method (FEM).

While a huge research effort resulted in many improvements, several well-known challenges remain. The lacking compatibility of the design and analysis tools used in computer aided engineering (CAE) recently gained attention. The data transfer and meshing of the geometry is estimated to take around 80% of the overall analysis time, see [117, Section 1.1.1]. The aim of isogeometric analysis (IGA) is to make the structural analysis more compatible with computer aided design (CAD) software. Even with increasing computational power, the efficiency of the methods remains crucial, especially for shape optimization and uncertainty quantification, where a series of simulations is necessary. In real-time computations the time-to-solution is crucial as well. Besides improving the discretization methods, model reduction techniques, like reduced basis methods, can help to achieve this goal.

To solve these challenges, numerical analysis and engineering experience often need to go hand in hand. An example are hybrid methods which combine

the use of different techniques in one method, usually with a strong mathematical foundation. Most of the considered methods are non-conforming as they go beyond the original variational framework of the PDE. The gain of more relaxed schemes is diverse: Discontinuous approximations can improve the mesh flexibility, as mesh-conformity is no longer required, while in other cases, constraints on the solution space, e.g., contact conditions, can be more beneficially realized inexactly. Of course, special care is necessary to control the non-conformity as an additional error source is introduced in the approximation.

The problems which are considered in this work can be categorized as follows: We start with linear and non-linear static problems, where the deformation of an elastic body under the influence of given forces is computed in an equilibrium situation. Also the values of the internal stress and possible surface tractions are important. Not only are static problems of interest on their own, but they are also the basis for more complex situations. In structural dynamics, the time-dependent deformation of a body is investigated based on Newton's laws of motion. The basic modes of motion are found by solving an eigenvalue problem.

In both statics and dynamics, the computation of contact boundary conditions remains a challenging task. Here the body may be in contact with another elastic body or a fixed obstacle, but it must not penetrate it. The difficulty lies in the unknown contact area and the contact forces, which influence the solution and make the problem non-linear and non-smooth. As a consequence, the resulting problem must usually be solved based on the minimization of energy and using algorithms of constrained numerical optimization.

This thesis is structured as follows: The remaining sections of Chapter 1 introduce the basic mathematical background and the models of solid mechanics under consideration.

Chapter 2 introduces isogeometric mortar methods and discusses basic properties. The hybrid use of path-wise smoothness with weak continuity at the interface provides the necessary flexibility with the advantages of isogeometric finite elements. The most important part of a mortar method is the Lagrange multiplier space, which can be chosen as a standard trace space as well as using biorthogonal basis functions with higher order approximation properties. Numerical examples include non-linear elasticity and eigenvalue approximations. Special focus lies on the numerical evaluation of surface integrals, as an exact evaluation can be costly. We show that the approximation is sensible with respect to quadrature errors unless a Petrov–Galerkin approach, based on the evaluation of different quadrature rules, is used.

A practical application in vibroacoustics is shown in Chapter 3, where the bridge of a violin is considered. An isogeometric mortar discretization is used

in order to benefit from the good eigenvalue approximation in isogeometric analysis. The bridge is solved as a fully three-dimensional orthotropic model and the discretization is combined with a reduced basis method to shorten the computational time under the influence of material as well as geometry changes.

The mathematical analysis of Signorini-type problems, a model for elastic contact, is shown in Chapter 4, where optimal bounds of the convergence rates for trace errors are proven. The a priori analysis is based on a continuous and a discrete Steklov–Poincaré operator as well as on Aubin–Nitsche-type duality arguments.

Finally, in Chapter 5, non-conforming and discontinuous solution techniques are studied and compared in different benchmark situations of linear and finite elasticity as well as in contact mechanics. In particular, we introduce a hybrid non-conforming method, present local criteria for well-posedness and present a convergence result. We shortly review interior penalty discontinuous Galerkin methods and compare the quality of these methods to standard conforming methods.

1.1 Mathematical background

While the models of solid mechanics considered in this thesis are introduced in Section 1.2, here, we introduce a standard scalar model problem, since most techniques apply to both models. Let $\Omega \subset \mathbb{R}^d$, $d = 2, 3$, be a bounded Lipschitz domain, $\hat{f}, \alpha, \beta: \Omega \rightarrow \mathbb{R}$, $\alpha \geq \alpha_0 > 0$, α_0 constant, and $\beta \geq 0$. Furthermore let the boundary be piecewise smooth and decomposed into two open sets Γ_D, Γ_N with $\Gamma_D \cap \Gamma_N = \emptyset$, $\bar{\Gamma}_D \cup \bar{\Gamma}_N = \partial\Omega$ and $|\Gamma_D| > 0$. On Γ_D Dirichlet boundary data $\hat{u}: \Gamma_D \rightarrow \mathbb{R}$ and on Γ_N Neumann boundary data $\hat{g}_N: \Gamma_N \rightarrow \mathbb{R}$ are given. We consider the following second order elliptic boundary value problem:

$$-\operatorname{div}(\alpha \nabla u) + \beta u = \hat{f} \quad \text{in } \Omega, \tag{1.1a}$$

$$u = \hat{u} \quad \text{on } \Gamma_D, \tag{1.1b}$$

$$\partial_{\mathbf{n}} u = \hat{g}_N \quad \text{on } \Gamma_N, \tag{1.1c}$$

where \mathbf{n} denotes the outer unit-normal on the boundary $\partial\Omega$. For $\alpha = 1$ and $\beta = 0$, (1.1a) is the classical Poisson equation $-\Delta u = \hat{f}$. Existence and uniqueness hold in a weak sense under weak assumptions to the data, as it will be presented in the following, after defining the important function spaces used in this thesis.

1.1.1 Functional analysis

In the following, we recall main functional analysis properties to introduce our abstract framework and then we set the variational problem.

We use standard Lebesgue and Sobolev spaces on a bounded Lipschitz domain $D \subset \mathbb{R}^{d-1}$ or $D \subset \mathbb{R}^d$, see, e.g., [98]. The Lebesgue space of square integrable functions

$$L^2(D) = \left\{ f: D \rightarrow \mathbb{R}: \int_D f(\mathbf{x})^2 \, d\mathbf{x} < \infty \right\}$$

is a Hilbert space with the scalar product $(f, g)_{L^2(D)} = \int_D f(\mathbf{x})g(\mathbf{x}) \, d\mathbf{x}$ and the induced norm $\|f\|_{L^2(D)} = (\int_D f(\mathbf{x})^2 \, d\mathbf{x})^{1/2}$. More precisely, $L^2(D)$ contains equivalence classes of measurable functions, instead of classical functions, see, e.g., [40, Chapter 1.1]. When two functions differ only on a set of zero measure, they are considered to be equal. Wherever the domain under consideration is clear from the context, we also denote $(\cdot, \cdot)_0 = (\cdot, \cdot)_{L^2(D)}$ and $\|\cdot\|_0 = \|\cdot\|_{L^2(D)}$.

A more general definition yields the Banach spaces

$$L^p(D) = \left\{ f: D \rightarrow \mathbb{R}: \int_D |f(\mathbf{x})|^p \, d\mathbf{x} < \infty \right\}, \text{ for } 1 \leq p < \infty,$$

and the special case of essentially bounded functions, which is denoted by $L^\infty(D) = \{f: D \rightarrow \mathbb{R}: \text{ess sup } |f| < \infty\}$.

Due to their definition as equivalence classes, Lebesgue functions do not allow point-evaluations and hence neither classical derivatives. Instead, weak derivatives are defined in a distributional sense, purely based on the property of integration by parts:

$$\int_D \partial_i f(\mathbf{x})g(\mathbf{x}) \, d\mathbf{x} = - \int_D f(\mathbf{x})\partial_i g(\mathbf{x}) \, d\mathbf{x}, \quad g \in C_0^\infty(D),$$

where $C_0^\infty(D)$ denotes the classical space of infinitely differentiable functions, which have a compact support in D . For a multi-index $\boldsymbol{\alpha} = (\alpha_1, \dots, \alpha_d)$ with $|\boldsymbol{\alpha}| = \sum_{i=1}^d \alpha_i$, we denote derivatives as $\partial^\alpha f = \partial_1^{\alpha_1} \cdots \partial_d^{\alpha_d} f$.

For $l \in \mathbb{N}$, $H^l(D)$ denotes the Sobolev space of functions $f \in L^2(D)$ such that their weak derivatives up to the order l are also in $L^2(D)$:

$$H^l(D) = \left\{ f \in L^2(D): \partial^\alpha f \in L^2(D), \quad |\boldsymbol{\alpha}| \leq l \right\},$$

with $\|f\|_l^2 = \|f\|_{H^l(D)}^2 = \sum_{|\boldsymbol{\alpha}| \leq l} \|\partial^\alpha f\|_{L^2(D)}^2$.

The more general case includes the spaces $W^{l,p}(D) = \{f \in L^p(D): \partial^\alpha f \in L^p(D), |\boldsymbol{\alpha}| \leq l\}$. We note that our definition includes the cases $H^0(D) = L^2(D)$

and $W^{0,p}(D) = L^p(D)$.

For vectorial spaces, i.e., $\mathbf{f}, \mathbf{g} \in (H^l(D))^d$, scalar products are evaluated component-based: $(\mathbf{f}, \mathbf{g})_l = \sum_{i=1}^d (f_i, g_i)_l$. As it is clear from the context, we do not distinguish between the vectorial and the scalar version.

For a non-integer index $s > 0$, $H^s(D)$ denotes the fractional Sobolev space, defined by interpolation of Sobolev spaces with integer index, which we introduce using the K-method, see [207]. Let $E_1 \subset E_0$ be two normed spaces with a continuous embedding. For $a \in E_0$ and $t > 0$ one defines

$$K(t; a) = \inf_{a=a_0+a_1, a_1 \in E_1} (\|a_0\|_{E_0} + t\|a_1\|_{E_1}).$$

For $0 < \theta < 1$, $1 \leq q \leq \infty$ (for $\theta = 0, 1$ only with $q = \infty$), we define the normed space

$$(E_0, E_1)_{\theta, q} = \{a \in E_0 : \|a\|_{(E_0, E_1)_{\theta, q}} < \infty\},$$

where for $q < \infty$

$$\|a\|_{(E_0, E_1)_{\theta, q}} = \left(\int_{t=0}^{\infty} \frac{(t^{-\theta} K(t; a))^q}{t} dt \right)^{1/q}$$

and for $q = \infty$

$$\|a\|_{(E_0, E_1)_{\theta, \infty}} = \operatorname{ess\,sup}_{t>0} |t^{-\theta} K(t; a)|.$$

Let $s_1 = \lfloor s \rfloor$, $s_2 = \lceil s \rceil$ and $\theta = s - s_1$, we set $H^s(D) = (H^{s_1}(D), H^{s_2}(D))_{\theta, 2}$. Varying the arguments, we can generate a whole new family of interpolation spaces, the so-called Besov spaces $B_{p,q}^s(D) = (W^{s_1,p}(D), W^{s_2,p}(D))_{\theta, q}$. We note $B_{\theta, q}^s \subset B_{\theta, q'}^s$ for $q' > q$. Besov spaces play an important role in numerical analysis, to keep estimates as strict as possible, whenever standard Sobolev spaces are not sufficient. In this thesis, they are used in Chapter 4.

Sobolev spaces of order one are of particular importance for PDEs of second order. The Sobolev space of order one with vanishing trace is denoted by $H_0^1(D) = \{f \in H^1(D), \operatorname{tr}(f) = 0\}$. We note, that we omit the trace operator, whenever there is no ambiguity. The special case of H^1 functions with homogeneous Dirichlet data on Γ_D is denoted as $H_D^1(D) = \{f \in H^1(D), f|_{\partial D \cap \Gamma_D} = 0\}$.

A special case of fractional Sobolev spaces is $H^{1/2}(\partial D)$, which is the trace space of $H^1(D)$. Working on subsets of the boundary $\gamma \subset \partial D$, special care has to be taken of the value on the boundary of γ . We define by $H_{00}^{1/2}(\gamma) \subset H^{1/2}(\gamma)$ the space of all functions that can be trivially extended on $\partial D \setminus \gamma$ by zero to an element of $H^{1/2}(\partial D)$. The dual space of $H_{00}^{1/2}(\gamma)$ is denoted $H^{-1/2}(\gamma)$. Note

that on closed surfaces, i.e., $\gamma = \partial D$, it holds that $H^{1/2}(\gamma) = H_{00}^{1/2}(\gamma)$.

We consider the following regularity of the data: $\hat{f} \in L^2(\Omega)$, $\alpha, \beta \in L^\infty(\Omega)$ and $\hat{g} \in L^2(\Gamma_N)$. For the ease of the presentation, we consider homogeneous Dirichlet data $\hat{u} = 0$. The standard weak formulation of (1.1) reads as follows: Find $u \in H_D^1(\Omega)$ such that

$$\int_{\Omega} \alpha \nabla u^\top \nabla v + \beta u v \, d\mathbf{x} = \int_{\Omega} \hat{f} v \, d\mathbf{x} + \int_{\Gamma_N} \hat{g}_N v \, d\boldsymbol{\gamma}, \quad v \in H_D^1(\Omega). \quad (1.2)$$

The formulation with inhomogeneous Dirichlet data uses an affine test space which satisfies the Dirichlet condition, see [202, Section 4.1.1] for the details.

We define the bilinear and linear form for the Poisson equation as follows: $a: H_D^1(\Omega) \times H_D^1(\Omega) \rightarrow \mathbb{R}$ and $f: H_D^1(\Omega) \rightarrow \mathbb{R}$, such that

$$a(u, v) = \int_{\Omega} \alpha \nabla u^\top \nabla v + \beta u v \, d\mathbf{x}, \quad f(v) = \int_{\Omega} \hat{f} v \, d\mathbf{x} + \int_{\Gamma_N} \hat{g}_N v \, d\boldsymbol{\gamma}.$$

In the following we see how, under the previously stated assumptions on the data, the variational problem (1.2) is uniquely solvable.

1.1.2 Finite element methods and the Galerkin approach

We first introduce the abstract setting and later specify it in the $H^1(\Omega)$ setting, which is used within this thesis. We refer to standard textbooks, e.g., [34, 40, 179, 202] for a more detailed presentation.

1.1.2.1 Galerkin approach

Let V be a Hilbert space, $a: V \times V \rightarrow \mathbb{R}$ a continuous and coercive bilinear form and $f: V \rightarrow \mathbb{R}$ continuous, i.e., there exist constants $0 < C_1, C_2, C_3 < \infty$, such that

$$\begin{aligned} |a(u, v)| &\leq C_1 \|u\|_V \|v\|_V \quad (\text{continuity}), \\ a(u, u) &\geq C_2 \|u\|_V^2 \quad (\text{coercivity}), \\ |f(u)| &\leq C_3 \|u\|_V \quad (\text{continuity}). \end{aligned}$$

Then the variational problem $u \in V$,

$$a(u, v) = f(v), \quad v \in V,$$

has a unique solution with the stability estimate $\|u\|_V \leq \|f\|_{V^*}/C_2$, where V^* denotes the dual space to V , see [179]. For the weak formulation (1.2),

continuity and coercivity hold under the given assumptions and hence well-posedness is given, see, e.g., [76, Theorem 3.8].

Given a family of discrete subspaces $(V_h)_{h>0}$, such that $V_h \subset V$, $\dim V_h < \infty$ and $\inf_{v_h \in V_h} \|u - v_h\|_V \xrightarrow{h \rightarrow 0} 0$, we define the Galerkin projection as the solution of the following variational problem: Find $u_h \in V_h$, such that

$$a(u_h, v_h) = f(v_h), \quad v_h \in V_h.$$

The discrete problems are uniquely solvable and satisfy the best-approximation property, e.g., [179],

$$\|u - u_h\|_V \leq C_1/C_2 \inf_{v_h \in V_h} \|u - v_h\|_V,$$

hence $u_h \rightarrow u$ in V for $h \rightarrow 0$. We note that the approximation is stable, as it holds $\|u_h\|_V \leq \|f\|_{V^*}/C_2$. A key feature of the Galerkin projection is the Galerkin orthogonality $a(u - u_h, v_h) = 0$ for $v_h \in V_h$.

We refer to [202, Section 11] for the extension of convergence results to the case of inhomogeneous Dirichlet conditions.

1.1.2.2 Finite element methods

With finite element methods, the discrete subspaces are based on piecewise polynomial functions on a triangulation. During refinement of the triangulation, convergence towards the exact solution is guaranteed. The convergence rate is usually given in dependence of the mesh size h .

Let a triangulation \mathcal{T}_h of triangular ($d = 2$) or tetrahedral ($d = 3$) elements τ_h be given, such that $\bar{\Omega} = \bigcup_{\tau_h \in \mathcal{T}_h} \bar{\tau}_h$. The elements shall not overlap and we do not permit hanging nodes. We assume that the elements are able to exactly represent the Dirichlet boundary Γ_D . The elements are assumed to be shape-regular, i.e., there is a global bound on the ratio of the diameter of the element and the radius of the inscribed circle.

Here, we introduce classical finite element spaces, based on piecewise polynomials with continuity across the element boundaries. Splines with a higher global smoothness are considered with isogeometric finite elements, which are considered in large parts of this thesis and are introduced in Section 2.1.

We define the conforming finite element subspace of degree p as

$$V_h = \{v_h \in C^0(\Omega) : v_h|_{\Gamma_D} = 0, v_h|_{\tau_h} \in \mathbb{P}_p, \tau_h \in \mathcal{T}_h\} \subset H_D^1(\Omega),$$

where \mathbb{P}_p denotes the space of polynomials up to the order p . We note that all elements, as well as the local polynomial space, can be obtained by a linear

transformation from one fixed reference element.

Especially engineers often work with quadrilateral ($d = 2$) or hexahedral ($d = 3$) elements. Unlike the previous cases the element do in general not map linearly from the reference element. We define tensor product polynomial spaces on the unit d -cube $(0, 1)^d$ by

$$\mathbb{Q}_p = \text{span}\{q(x_1, \dots, x_d) = x_1^{\alpha_1} x_2^{\alpha_2} \cdots x_d^{\alpha_d}, \quad \alpha_\delta \in \{0, \dots, p\}, \quad 1 \leq \delta \leq d\}.$$

Each element is mapped from the reference element $(0, 1)^d$ by $\mathbf{F}_{\tau_h} \in (\mathbb{Q}_p)^d$ with $\det \mathbf{D}\mathbf{F}_{\tau_h} \geq c_{\tau_h} > 0$, and the global space is defined using this mapping

$$V_h = \{v_h \in C^0(\Omega): v_h|_{\Gamma_D} = 0, \quad v_h \circ \mathbf{F}_{\tau_h}|_{(0,1)^d} \in \mathbb{Q}_p, \quad \tau_h \in \mathcal{T}_h\} \subset H_D^1(\Omega).$$

A variation of quadratic elements on quadrilateral elements are the *serendipity* elements, where the interior bubble function $x_1(1-x_1)x_2(1-x_2)$ is excluded from the space \mathbb{Q}_2 . Extensions to higher orders as well as hexahedral elements are possible, see [10], but not used in this thesis.

We note that for $d = 2$, the restriction of \mathbb{Q}_p to the edge of an element is a polynomial of degree p , which allows the straightforward use of hybrid meshes, containing quadrilaterals and triangles.

For the discretization of vector valued problems, we set $\mathbf{V}_h = (V_h)^d$.

Assuming sufficient regularity, the convergence rate for $H^1(\Omega)$ problems is up to h^p . Let $V = H_D^1(\Omega)$ and assume $u \in H^{s+1}(\Omega)$ for $0 \leq s \leq p$, then it holds, see, [179, Theorem 3.4.1],

$$\|u - u_h\|_{H^1(\Omega)} \leq ch^s \|u\|_{H^{s+1}(\Omega)}.$$

We note that c denotes a generic constant, which will frequently be used throughout this thesis. Its value may be different on each occurrence. It is independent of the mesh size h , but if not noted otherwise it may depend on the polynomial degree and the shape-regularity of the mesh.

Under the stronger assumption of *dual regularity*, the L^2 error can be proven to be of faster convergence, see, e.g., [34]. The dual problem is defined for $g \in L^2(\Omega)$ as $w_g \in V$, such that

$$a(v, w_g) = (g, v)_0, \quad v \in V.$$

We note that the dual problem is equal to the primal problem for symmetric problems. The problem is called dual regular, if it holds $w_g \in H^2(\Omega)$ and $\|w_g\|_{H^2(\Omega)} \leq c \|g\|_{L^2(\Omega)}$ for all $g \in L^2(\Omega)$. Under this assumption it holds

$$\|u - u_h\|_{L^2(\Omega)} \leq ch^{s+1} \|u\|_{H^{s+1}(\Omega)}.$$

The dual techniques used for the proof will be used in a weighted form in Chapter 4, so we work it out in more detail. Let us define $e_h = u - u_h$ and denote by $I_h: H^1(\Omega) \rightarrow V_h$ a quasi-interpolation operator with first order approximation properties (e.g., of Scott–Zhang-type [196]). Then considering the dual solution with the error as the right hand side and using the Galerkin-orthogonality to insert a quasi-interpolation yields

$$\begin{aligned} \|u - u_h\|_{L^2(\Omega)}^2 &= (e_h, u - u_h)_0 = a(u - u_h, w_{e_h}) = a(u - u_h, w_{e_h} - I_h w_{e_h}) \\ &\leq c \|u - u_h\|_{H^1(\Omega)} \|w_{e_h} - I_h w_{e_h}\|_{H^1(\Omega)} \\ &\leq ch^s \|u\|_{H^{s+1}(\Omega)} h \|w_{e_h}\|_{H^2(\Omega)} \\ &\leq ch^{s+1} \|u\|_{H^{s+1}(\Omega)} \|u - u_h\|_{L^2(\Omega)}. \end{aligned}$$

The proof is known as the *Aubin–Nitsche trick*. We note that for model problem (1.1) with $\Gamma_D = \partial\Omega$, the H^2 regularity holds for convex domains and sufficiently smooth coefficients, see, e.g., [34, Chapter 2, Theorem 7.2].

1.1.2.3 Non-conforming approximations and variational crimes

Throughout this thesis several non-conforming methods and related variational crimes by numerical quadrature are discussed, so this section only gives a brief overview. Roughly speaking any method which does not strictly follow the Galerkin approach can be considered a non-conforming method or a variational crime. With non-conforming methods the discrete subspace is no longer conforming, i.e., $V_h \not\subset V$, while for variational crimes the bilinear form is altered, e.g., by the use of a quadrature rule.

The theoretical basis for these non-standard methods are the Lemmata of Strang, which exist in a broad variety of similar forms. A standard formulation is the following, see [34].

For the *first Lemma of Strang*, we assume conformity $V_h \subset V$, but allow inexact bilinear and linear forms (e.g., obtained by numerical quadrature or a modification of the operator):

$$a_h: V_h \times V_h \rightarrow \mathbb{R}, \quad f_h: V_h \rightarrow \mathbb{R}.$$

We assume uniform continuity of a_h and f_h and uniform coercivity of a_h on V_h . Then for $u_h \in V_h$ with

$$a_h(u_h, v_h) = f_h(v_h), \quad v_h \in V_h,$$

it holds for generic constants c , that

$$\begin{aligned} \|u - u_h\|_V &\leq c \inf_{v_h \in V_h} \left(\|u - v_h\|_V + \sup_{w_h \in V_h} \frac{|a(v_h, w_h) - a_h(v_h, w_h)|}{\|w_h\|_V} \right) \\ &\quad + c \sup_{w_h \in V_h} \frac{|f(w_h) - f_h(w_h)|}{\|w_h\|_V}. \end{aligned}$$

The *second Lemma of Strang* involves non-conforming spaces $V_h \not\subset V$. As a consequence, the V norm might not be defined for all discrete spaces. Instead, we use discrete norms $\|\cdot\|_h$, e.g., by a piecewise definition of the norm, leaving apart discontinuities. Assuming uniform ellipticity and continuity in the discrete norms

$$\begin{aligned} a_h(v_h, v_h) &\geq c \|v_h\|_h^2, \quad v_h \in V_h, \\ |a_h(u, v_h)| &\leq c \|u\|_h \|v_h\|_h, \quad u \in V + V_h, v_h \in V_h, \end{aligned}$$

it holds

$$\|u - u_h\|_h \leq c \inf_{v_h \in V_h} \|u - v_h\|_h + c \sup_{w_h \in V_h} \frac{|a_h(u, w_h) - f_h(w_h)|}{\|w_h\|_h},$$

where the first term is called *approximation error* and the second term *consistency error*.

For piecewise discontinuous approximations, the consistency term can usually be transformed into surface integrals over the discontinuity by using integration by parts. Applying suitable coupling conditions, optimal error estimates can be shown, for example as in [40, Chapter 10.3].

1.1.2.4 Saddle point problems

Hybrid methods based on the use of a primal and a dual variable can often be formulated as a saddle point problem. A detailed presentation of the theory of saddle point problems can be found in [32] and also in [34, 40]. In general, saddle point problems arise when the primal problem is posed on a constrained space: $u \in X$,

$$a(u, v) = f(v), \quad v \in X, \quad \text{where } X = \{v \in V : b(v, \mu) = 0, \quad \mu \in M\},$$

where $b: V \times M \rightarrow \mathbb{R}$ is a continuous bilinear form and the Hilbert space M is called the *Lagrange multiplier space*. Including a dual variable $\lambda \in M$, such problems can equivalently be formulated as a saddle point problem $(u, \lambda) \in$

$V \times M$,

$$\begin{aligned} a(u, v) + b(v, \lambda) &= f(v), \quad v \in V, \\ b(u, \mu) &= 0, \quad \mu \in M. \end{aligned}$$

The conditions for well-posedness are more complicated than for standard elliptic problems, since we need to make sure that the condition does not over-constrain the solution. Besides the continuity conditions, we have two conditions. The coercivity of $a(\cdot, \cdot)$ on the constrained space X and an *inf-sup condition* given by

$$\inf_{\mu \in M} \sup_{v \in V} \frac{b(v, \mu)}{\|v\|_V \|\mu\|_M} > 0.$$

Often it is more efficient to consider a discrete pair of subspaces $V_h \subset V$ and $M_h \subset M$, than a conforming subspace $X_h \subset X$. Unlike for conforming approximations, the kernel ellipticity and the inf-sup condition are not automatically fulfilled for $V_h \times M_h$.

If M_h is too small, the bilinear form may not be elliptic on the discrete kernel $X_h = \{v_h \in V_h : b(v_h, \mu_h) = 0, \mu_h \in M\}$. Also choosing M_h too small may reduce the convergence rate, even if V_h allows a better rate. On the other hand, if M_h is too large (or V_h too small), the inf-sup condition may be zero, or h -dependent. A suitable pairing with a uniform inf-sup stability

$$\inf_{\mu_h \in M_h} \sup_{v_h \in V_h} \frac{b(v_h, \mu_h)}{\|v_h\|_V \|\mu_h\|_M} \geq \beta > 0$$

often requires a careful choice of the spaces. Under these assumptions, we have an abstract best approximation property [76, Lemma 2.44]

$$\|u - u_h\|_V + \|\lambda - \lambda_h\|_M \leq c \inf_{v_h \in V_h} \|u - v_h\|_V + c \inf_{\mu_h \in M_h} \|\lambda - \mu_h\|_M.$$

Even for stable spaces, saddle point problems have some disadvantages compared to elliptic problem formulations. In comparison to a purely primal formulation, the number of degrees of freedom is increased. Also the resulting equation system of a saddle point type

$$\begin{pmatrix} A_h & B_h^\top \\ B_h & 0 \end{pmatrix} \begin{pmatrix} u_h \\ \lambda_h \end{pmatrix} = \begin{pmatrix} f_h \\ 0 \end{pmatrix},$$

is indefinite, causing difficulties for linear solvers, see, e.g., [29] for a discussion of this issue and possible algorithms.

An analogue form using inequality constraints is used for Signorini and con-

tact problems, where the inf-sup condition remains a main issue when choosing the approximation spaces, see, e.g., [230].

1.2 Solid mechanics

In this section, the models of solid mechanics, which we use in this thesis, are introduced and some aspects of volume locking are discussed. A detailed presentation can be found in standard textbooks, e.g., [34, 40] for a mathematical introduction and [24, 116] for an engineering introduction.

1.2.1 Linear elasticity

Given a body $\Omega \subset \mathbb{R}^d$ under the influence of specified volume and surface forces, the equations of elasticity model the deformation of the body in an equilibrium state. Key assumption for linear elasticity is an infinitesimally small deformation, which allows us to perform all computations on the undeformed body Ω instead of the (unknown) deformed body. The more general case of finite elasticity is introduced later in Section 1.2.4.

We denote the deformation $\mathbf{u}: \Omega \rightarrow \mathbb{R}^d$ and the transformation $\varphi = \text{id} + \mathbf{u}$, such that $\varphi(\Omega)$ is the deformed body.

Two important measures are the symmetric strain tensor $\boldsymbol{\varepsilon}(\mathbf{u}): \Omega \rightarrow \mathbb{R}_{\text{sym}}^{d \times d}$ and the symmetric stress tensor $\boldsymbol{\sigma}(\mathbf{u}): \Omega \rightarrow \mathbb{R}_{\text{sym}}^{d \times d}$. The strain is a measure for the local change of the shape. While in general, there exist a variety of different strain measures, for the linear theory the infinitesimal strain tensor

$$\boldsymbol{\varepsilon}(\mathbf{u}) = (\nabla \mathbf{u} + \nabla \mathbf{u}^\top) / 2$$

is used. The relation between deformation and strain is often referred to as *kinematic equation* (KE).

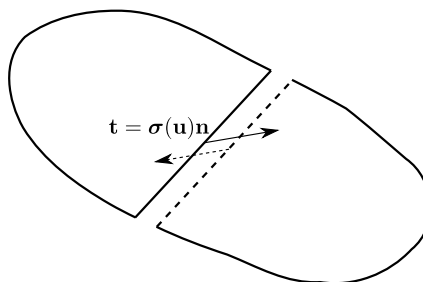


Figure 1.1: Inner forces of a body. Along the imaginary plane cut the traction is $\mathbf{t} = \boldsymbol{\sigma}(\mathbf{u})\mathbf{n}$.

The stress tensor is a measure for the internal forces of the deformed body, such that the traction across any surface with unit normal \mathbf{n} is given by $\boldsymbol{\sigma}(\mathbf{u}) \mathbf{n}$, see Figure 1.1. Based on the angular momentum balance, the stress tensor is symmetric. By Newton's laws of motion, in an equilibrium state all forces acting on an arbitrary volume must sum up to zero. This is the case when

$$-\operatorname{div} \boldsymbol{\sigma}(\mathbf{u}) = \widehat{\mathbf{f}},$$

where $\widehat{\mathbf{f}}: \Omega \rightarrow \mathbb{R}^d$ is the body force acting on Ω , e.g., gravity, see [34, Chapter 6, Equation 2.1]. The relation between body force and stress tensor is referred to as *balance equation* (BE).

The remaining link between the body force and the displacement is the *constitutive equation* (CE), which states the dependency of $\boldsymbol{\sigma}$ and $\boldsymbol{\varepsilon}$. Here we restrict to the three-dimensional space and note that the case $d = 2$, which is divided into plane strain and plane stress, is presented later in this text. We consider the case of hyper-elastic materials, where the stress can be determined by a strain energy function (see also [34, Chapter 6, Definition 2.1])

$$\boldsymbol{\sigma} = \frac{\partial W_{\text{int}}(\boldsymbol{\varepsilon})}{\partial \boldsymbol{\varepsilon}},$$

which is spacially independent for homogeneous materials. We assume a linear dependency according to the generalized Hooke's law, which means that the strain energy function is quadratic. Then we can use the fourth-order tensor

$$\mathbb{C} = \frac{\partial^2 W_{\text{int}}(\boldsymbol{\varepsilon})}{\partial \boldsymbol{\varepsilon}^2} \in \mathbb{R}^{3 \times 3 \times 3 \times 3},$$

and the constitutive equation reads

$$\boldsymbol{\sigma}(\mathbf{u}) = \mathbb{C} \boldsymbol{\varepsilon}(\mathbf{u}).$$

While the elasticity tensor \mathbb{C} has 81 entries, only a part of them are independent, see, e.g. [116, Equations 2.7.3 and 2.7.4]: Due to the symmetry of the stress and strain tensor, the elasticity tensor is symmetric in the sense, that

$$\mathbb{C}_{ijkl} = \mathbb{C}_{jikl} = \mathbb{C}_{ijlk},$$

and as the second derivative of an energy function it also holds

$$\mathbb{C}_{ijkl} = \mathbb{C}_{klij}.$$

Hence 21 independent material parameters remain for the most general an-

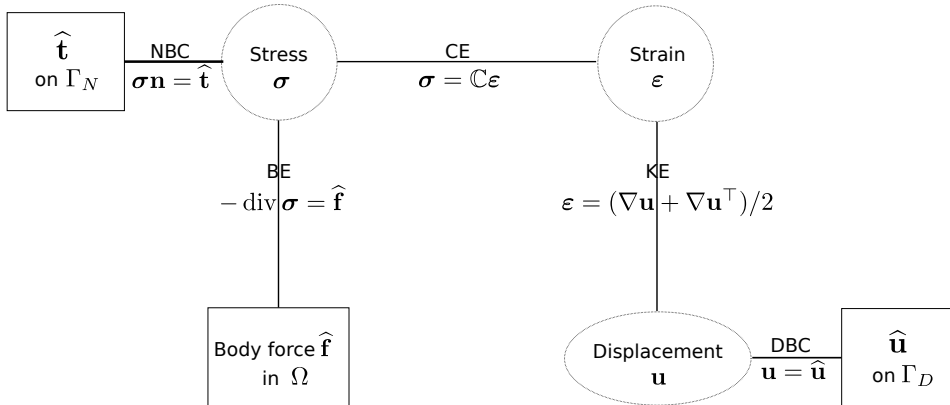


Figure 1.2: Tonti diagram for the equations of linear elasticity.

isotropic case, see also [181, Chapter 2.2]. We note that we consider an orthotropic material law in Section 1.2.2 and assume for now an isotropic material, i.e., the material law holds independently of the chosen coordinate frame.

In the isotropic case two independent material parameters exist. Using the *Lamé parameters* $\mu_{\text{Lamé}}$, $\lambda_{\text{Lamé}}$, the constitutive equation reads

$$\boldsymbol{\sigma}(\mathbf{u}) = 2\mu_{\text{Lamé}} \boldsymbol{\varepsilon}(\mathbf{u}) + \lambda_{\text{Lamé}} \text{tr} \boldsymbol{\varepsilon}(\mathbf{u}) \text{Id}.$$

Instead of the Lamé parameters, a set of parameters with more physical meaning can be used. The elastic modulus (Young’s modulus) E measures the stress-strain relation in the case of uniaxial stress. Poisson’s ratio ν states the expansion of the material in directions perpendicular to the direction of compression.

Both sets of material parameters can be transformed as follows, see [34, Chapter 6, Equation 1.31]:

$$\lambda_{\text{Lamé}} = \frac{\nu E}{(1 + \nu)(1 - 2\nu)}, \quad \mu_{\text{Lamé}} = \frac{E}{2(1 + \nu)} \quad (1.3a)$$

$$E = \frac{\mu_{\text{Lamé}}(3\lambda_{\text{Lamé}} + 2\mu_{\text{Lamé}})}{\lambda_{\text{Lamé}} + \mu_{\text{Lamé}}}, \quad \nu = \frac{\lambda_{\text{Lamé}}}{2(\lambda_{\text{Lamé}} + \mu_{\text{Lamé}})}. \quad (1.3b)$$

An elliptic strain energy is given if $\mu_{\text{Lamé}} > \max\{0, -\frac{3}{2}\lambda_{\text{Lamé}}\}$ (see also [76, Chapter 3.4]), which is equivalent to

$$E > 0, \quad -1 < \nu < 1/2.$$

The balance equation $-\text{div} \boldsymbol{\sigma}(\mathbf{u}) = \hat{\mathbf{f}}$ joint with the constitutive equation $\boldsymbol{\sigma}(\mathbf{u}) = \mathbb{C}\boldsymbol{\varepsilon}(\mathbf{u})$ and the kinematic equation $\boldsymbol{\varepsilon}(\mathbf{u}) = (\nabla\mathbf{u} + \nabla\mathbf{u}^\top)/2$ together

form the Lamé equation, a second order partial differential equation. Natural boundary conditions are fixed deformations (Dirichlet), $\mathbf{u} = \widehat{\mathbf{u}}$ on Γ_D , and a prescribed (possible zero) boundary force (Neumann), $\boldsymbol{\sigma}(\mathbf{u}) \mathbf{n} = \widehat{\mathbf{t}}$. See Figure 1.2 for an overview over the equations. This finalizes the equations of linear elasticity in the strong form [202, Chapter 4.2.3]:

$$\begin{aligned} -\operatorname{div} \boldsymbol{\sigma}(\mathbf{u}) &= \widehat{\mathbf{f}} && \text{in } \Omega, \\ \mathbf{u} &= \widehat{\mathbf{u}} && \text{on } \Gamma_D, \\ \boldsymbol{\sigma}(\mathbf{u}) \mathbf{n} &= \widehat{\mathbf{t}} && \text{on } \Gamma_N. \end{aligned}$$

For simplicity of notation, we consider the homogeneous Dirichlet condition $\widehat{\mathbf{u}} = \mathbf{0}$, which can be interpreted as the geometry being clamped at this part of the boundary. Inhomogeneous Dirichlet conditions can be considered by using an affine trial space as in the scalar elliptic case. The weak form reads $\mathbf{u} \in (H_D^1(\Omega))^d$,

$$\int_{\Omega} \boldsymbol{\sigma}(\mathbf{u}) : \boldsymbol{\varepsilon}(\mathbf{v}) \, d\mathbf{x} = \int_{\Omega} \widehat{\mathbf{f}}^\top \mathbf{v} \, d\mathbf{x} + \int_{\Gamma_N} \widehat{\mathbf{t}}^\top \mathbf{v} \, d\gamma, \quad \mathbf{v} \in (H_D^1(\Omega))^d. \quad (1.4)$$

In the engineering literature, this is often denoted as the *principle of virtual work* or *principle of virtual displacements*, see [206, Chapter 4.2]. Comparing to the Tonti diagram in Figure 1.2, we note that the balance equation and the Neumann boundary conditions are evaluated weakly, the remaining links in a strong form. A variety of multi-field formulations can be derived by including further weak links in the diagram.

Continuity of the bilinear and linear forms can easily be shown. However, it should be noted that the constants depend on the Lamé parameters. The ellipticity of the bilinear form follows by Korn's inequality, see [202, Theorem 4.17]. Since $|\Gamma_D| > 0$, there exists $c > 0$, such that

$$\|\boldsymbol{\varepsilon}(\mathbf{v})\|_{L^2(\Omega)} \geq c \|\mathbf{v}\|_{H^1(\Omega)}, \quad \mathbf{v} \in (H_D^1(\Omega))^d.$$

Variants of Korn's inequality for discontinuous spaces are presented in [39].

While the presented tensor notation yields a simple abstract formulation of the isotropic case, an alternative matrix-vector notation can often be more useful for the implementation as well as for complex material laws. Instead of the symmetric matrices

$$\boldsymbol{\varepsilon} = \begin{pmatrix} \varepsilon_{11} & \varepsilon_{12} & \varepsilon_{13} \\ \varepsilon_{21} & \varepsilon_{22} & \varepsilon_{23} \\ \varepsilon_{31} & \varepsilon_{32} & \varepsilon_{33} \end{pmatrix}, \quad \boldsymbol{\sigma} = \begin{pmatrix} \sigma_{11} & \sigma_{12} & \sigma_{13} \\ \sigma_{21} & \sigma_{22} & \sigma_{23} \\ \sigma_{31} & \sigma_{32} & \sigma_{33} \end{pmatrix},$$

we write the six independent entries in a vector

$$\boldsymbol{\varepsilon} = \begin{pmatrix} \varepsilon_{11} \\ \varepsilon_{22} \\ \varepsilon_{33} \\ \varepsilon_{12} \\ \varepsilon_{13} \\ \varepsilon_{23} \end{pmatrix}, \quad \boldsymbol{\sigma} = \begin{pmatrix} \sigma_{11} \\ \sigma_{22} \\ \sigma_{33} \\ \sigma_{12} \\ \sigma_{13} \\ \sigma_{23} \end{pmatrix},$$

and note that we do not distinguish between both notations as it should not pose any confusion. Then the constitutive tensor for isotropic linear elasticity can be represented as a symmetric 6×6 matrix (see [34, Chapter 6, Equation 3.6]) given by

$$\mathbb{C} = \begin{pmatrix} 2\mu_{\text{Lamé}} + \lambda_{\text{Lamé}} & \lambda_{\text{Lamé}} & \lambda_{\text{Lamé}} & & & \\ \lambda_{\text{Lamé}} & 2\mu_{\text{Lamé}} + \lambda_{\text{Lamé}} & \lambda_{\text{Lamé}} & & & \\ \lambda_{\text{Lamé}} & \lambda_{\text{Lamé}} & 2\mu_{\text{Lamé}} + \lambda_{\text{Lamé}} & & & \\ & & & 2\mu_{\text{Lamé}} & & \\ & & & & 2\mu_{\text{Lamé}} & \\ & & & & & 2\mu_{\text{Lamé}} \end{pmatrix},$$

which can also be expressed in terms of E, ν as:

$$\mathbb{C} = \frac{E}{(1 + \nu)(1 - 2\nu)} \begin{pmatrix} 1 - \nu & \nu & \nu & & & \\ \nu & 1 - \nu & \nu & & & \\ \nu & \nu & 1 - \nu & & & \\ & & & 1 - 2\nu & & \\ & & & & 1 - 2\nu & \\ & & & & & 1 - 2\nu \end{pmatrix}.$$

1.2.1.1 Plane strain and plane stress

Plane strain and plane stress, see [34, Chapter 6, §4], are two kinds of dimensionally reduced material laws. Both of them are two-dimensional models with in-plane loading and different assumptions on the original three-dimensional model. For further dimensionally reduced models, we refer to the literature. Some examples are axisymmetric models [206, Section 3.4.4], as well as plates and shells, where out-of-plane loading is considered [206, Section 9].

The model of plane strain assumes an invariance of the problem with respect to the orthogonal direction of the coordinate frame. More specifically, we assume $\Omega = \Omega_{2D} \times (-\infty, \infty)$ with $\Omega_{2D} \subset \mathbb{R}^2$ and invariance of the data: $\hat{\mathbf{f}}(x_1, x_2, x_3) = \hat{\mathbf{f}}(x_1, x_2)$, $f_3 = 0$ and the analogue for $\hat{\mathbf{u}}$ and $\hat{\mathbf{t}}$. Then we may assume $\varepsilon_{i3} = 0$, $i = 1, 2, 3$, and as a consequence of the three-dimensional constitutive equation

$$\sigma_{33} = \nu(\sigma_{11} + \sigma_{22}).$$

This yields the two-dimensional plane strain constitutive equation

$$\begin{pmatrix} \sigma_{11} \\ \sigma_{22} \\ \sigma_{12} \end{pmatrix} = \frac{E}{(1+\nu)(1-2\nu)} \begin{pmatrix} 1-\nu & \nu & \\ \nu & 1-\nu & \\ & & 1-2\nu \end{pmatrix} \begin{pmatrix} \varepsilon_{11} \\ \varepsilon_{22} \\ \varepsilon_{12} \end{pmatrix},$$

which we can formulate analogously to the three-dimensional equation as

$$\boldsymbol{\sigma}(\mathbf{u}) = 2\mu_{\text{Lamé}} \boldsymbol{\varepsilon}(\mathbf{u}) + \lambda_{\text{Lamé}} \operatorname{tr} \boldsymbol{\varepsilon}(\mathbf{u}) \operatorname{Id}.$$

The plane stress model on the other hand assumes a flat plate with only in-plane loads. For a small thickness parameter $\epsilon > 0$, we assume $\Omega = \Omega_{2D} \times (-\epsilon, \epsilon)$ with $\hat{\mathbf{t}}(x_1, x_2, x_3) = 0$ for $|x_3| = \epsilon$ and the invariance of the data as stated for the plane strain setting. Then we may assume $\sigma_{i3} = 0$, $i = 1, 2, 3$, and have $\varepsilon_{33} = -\frac{\nu}{1-\nu}(\varepsilon_{11} + \varepsilon_{22})$ by the three-dimensional constitutive equation. Then, we may state the two-dimensional plane stress material law as

$$\begin{pmatrix} \sigma_{11} \\ \sigma_{22} \\ \sigma_{12} \end{pmatrix} = \frac{E}{1-\nu^2} \begin{pmatrix} 1 & \nu & \\ \nu & 1 & \\ & & 1-\nu \end{pmatrix} \begin{pmatrix} \varepsilon_{11} \\ \varepsilon_{22} \\ \varepsilon_{12} \end{pmatrix}.$$

1.2.1.2 Locking effects

Locking describes situations, where the convergence of standard finite element methods is severely deteriorated by a known parameter. The most prominent examples are shear locking [9], which occurs during the bending of a long beam, as well as volume locking [15], which occurs for nearly incompressible materials.

A material is incompressible, when its Poisson's ratio ν is close to $1/2$, as very little volume changes are possible under deformation. A prominent and important material of this kind is natural rubber.

In terms of the Lamé parameters, see (1.3), we have $\mu_{\text{Lamé}} \rightarrow E/3$ and $\lambda_{\text{Lamé}} \rightarrow \infty$ for $\nu \rightarrow 1/2$. Thus the term $\lambda_{\text{Lamé}} \operatorname{tr} \boldsymbol{\varepsilon} \operatorname{Id}$ in the constitutive equation must play a key role. As $\operatorname{tr} \boldsymbol{\varepsilon} = \operatorname{div} \mathbf{u}$ measures the local volume change, it becomes obvious that a large value of $\lambda_{\text{Lamé}}$ constrains the compressibility

of the material. The bad behavior of standard numerical methods for nearly incompressible materials is due to the continuity constant, which grows with $\lambda_{\text{Lamé}}$. Therefore, the problem is *ill-conditioned* for large values of $\lambda_{\text{Lamé}}$.

A robust formulation for the incompressible limit can be stated as a mixed problem, defining $p = \lambda_{\text{Lamé}} \operatorname{div} \mathbf{u}$, see [76, Chapter 3.5.3]. This solves the saddle point problem $(\mathbf{u}, p) \in (H_D^1(\Omega))^d \times L^2(\Omega)$,

$$2\mu_{\text{Lamé}} \int_{\Omega} \boldsymbol{\varepsilon}(\mathbf{u}) : \boldsymbol{\varepsilon}(\mathbf{v}) \, d\mathbf{x} + \int_{\Omega} p \operatorname{div} \mathbf{v} \, d\mathbf{x} = \int_{\Gamma_N} \hat{\mathbf{t}}^\top \mathbf{v} \, d\boldsymbol{\gamma}, \quad \mathbf{v} \in (H_D^1(\Omega))^d, \quad (1.5a)$$

$$\int_{\Omega} q \operatorname{div} \mathbf{u} \, d\mathbf{x} - 1/\lambda_{\text{Lamé}} \int_{\Omega} p q \, d\mathbf{x} = 0, \quad q \in L^2(\Omega). \quad (1.5b)$$

For the ease of the presentation, we consider $\hat{\mathbf{f}} = \mathbf{0}$. In the incompressible limit $1/\lambda_{\text{Lamé}} \rightarrow 0$, a well-posed problem similar to the Stokes problem appears. The nearly incompressible case can be considered as a penalty formulation, see [34, Chapter 6, §3] for a detailed analysis of this formulation.

The disadvantage is the saddle point structure and the growing number of unknowns. However, based on this formulation, an easy to implement method, called *reduced integration*, can be derived.

We consider a mixed Q1-P0 formulation, where $(\mathbf{u}, p) \in \mathbb{Q}_1^d \times \mathbb{P}_0$, i.e., the pressure is approximated by piecewise constant functions. Then (1.5b) yields $p_h = \lambda_{\text{Lamé}} \pi_0 \operatorname{div} \mathbf{u}_h$, where π_0 is the L^2 projection onto the piecewise constant functions. Assuming rectangular elements, we note that a one-point quadrature rule (evaluated at the midpoint $\mathbf{x}_{\text{qp}} \in \tau_h$) can exactly evaluate the mean value on the element, i.e., $\operatorname{div} \mathbf{u}_h(\mathbf{x}_{\text{qp}}) = \pi_0 \operatorname{div} \mathbf{u}_h$. Inserting this in (1.5a) yields the purely primal discrete problem $\mathbf{u}_h \in \mathbf{V}_h$,

$$2\mu_{\text{Lamé}} \int_{\Omega} \boldsymbol{\varepsilon}(\mathbf{u}_h) : \boldsymbol{\varepsilon}(\mathbf{v}_h) \, d\mathbf{x} + \lambda_{\text{Lamé}} \sum_{\tau_h \in \mathcal{T}_h} |\tau_h| \operatorname{div} \mathbf{u}_h(\mathbf{x}_{\text{qp}}) \operatorname{div} \mathbf{v}_h(\mathbf{x}_{\text{qp}}) = \int_{\Gamma_N} \hat{\mathbf{t}}^\top \mathbf{v}_h \, d\boldsymbol{\gamma}, \quad \mathbf{v}_h \in \mathbf{V}_h.$$

The implementation is fairly easy, as it suffices to reduce the integration order for the second term of the constitutive equation.

We present illustrative results based on a benchmark problem with an exact solution, see [162, §58]. An infinite plate with a hole of radius 25 is loaded symmetrically. For convenience only one quarter of the plate is considered and symmetry conditions $(\boldsymbol{\sigma}(\mathbf{u}) \mathbf{n})^\top \mathbf{n} = 0$, $\mathbf{u}^\top \mathbf{n} = 0$ are applied on Γ_{symm} . The infinite quarter plane is cut at $x = 100$ and $y = 100$ to obtain a bounded domain and the exact traction is applied. The domain and boundary conditions are displayed in Figure 1.3 (left). The solution is given in the radial and angular

direction, respectively u_r and u_θ ,

$$\mathbf{u} \begin{pmatrix} r \cos(\theta) \\ r \sin(\theta) \end{pmatrix} = \begin{pmatrix} \cos(\theta)u_r(r, \theta) - \sin(\theta)u_\theta(r, \theta) \\ \sin(\theta)u_r(r, \theta) + \cos(\theta)u_\theta(r, \theta) \end{pmatrix}, \quad 0 \leq \theta \leq \pi/2,$$

where

$$\begin{aligned} u_r(r, \theta) &= \\ &= \frac{1}{8\mu_{\text{Lamé}} r} \left((\kappa - 1)r^2 + 2\gamma a^2 + \left(2r^2 - 2(\kappa + 1)a^2/\kappa + 2\frac{a^4}{\kappa r^2} \right) \cos(2\theta) \right), \\ u_\theta(r, \theta) &= -\frac{1}{8\mu_{\text{Lamé}} r} \left(2r^2 - 2(\kappa - 1)a^2/\kappa - 2\frac{a^4}{\kappa r^2} \right) \sin(2\theta), \end{aligned} \quad (1.6)$$

and $a = 25$, $\kappa = 3 - 4\nu$, $\gamma = 2\nu - 1$ depend on Poisson's ratio ν and the Lamé parameter $\mu_{\text{Lamé}}$. See Figure 1.3 (right) for an illustration of the solution.

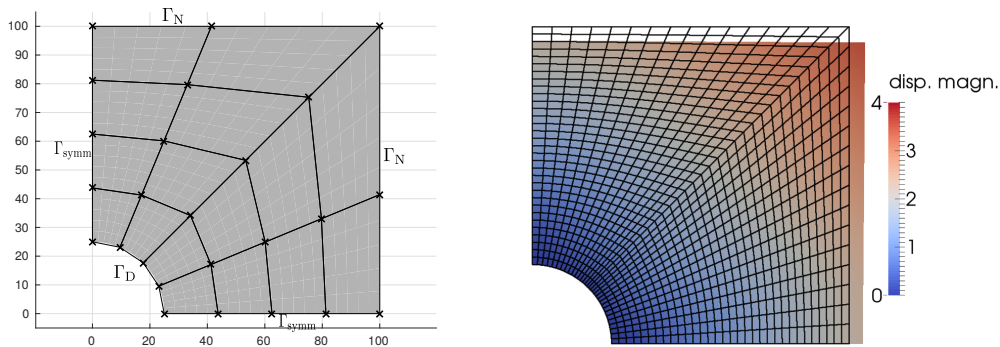


Figure 1.3: Setting of the quarter plate with a hole. Left: Geometry and boundary conditions, with a sample grid on mesh level 1. Right: Undeformed mesh on level 4 with the deformed geometry (amplified).

In Figure 1.4 relative error values are displayed for $\mu_{\text{Lamé}} = 1$, for different values of $\lambda_{\text{Lamé}}$ using full and reduced integration. For the standard bilinear ansatz the severe locking is visible, as the convergence deteriorates with growing $\lambda_{\text{Lamé}}$. Already for $\lambda_{\text{Lamé}} = 10^4$ the relative error remains at 1 on the first three meshes and for $\lambda_{\text{Lamé}} = 10^6$ no improvement can be seen at any of the considered meshes. The case of a bilinear ansatz with a reduced integration shows a huge improvement. For $10^2 \leq \lambda_{\text{Lamé}} \leq 10^6$ the convergence does not worsen at all with a growing incompressibility, as expected due to the equivalent stable saddle point formulation. The biquadratic case shows how a higher order ansatz can improve locking, but only up to a certain point. For $\lambda_{\text{Lamé}} \leq 10^4$ an influence of locking is present, but the convergence is still

practical. For larger values, the situation worsens, but unlike in the bilinear case, an asymptotic behavior can be seen on the finer meshes. Of course a reduced integration can also be applied to the quadratic case to improve locking behavior, but here it serves as an illustrative example.

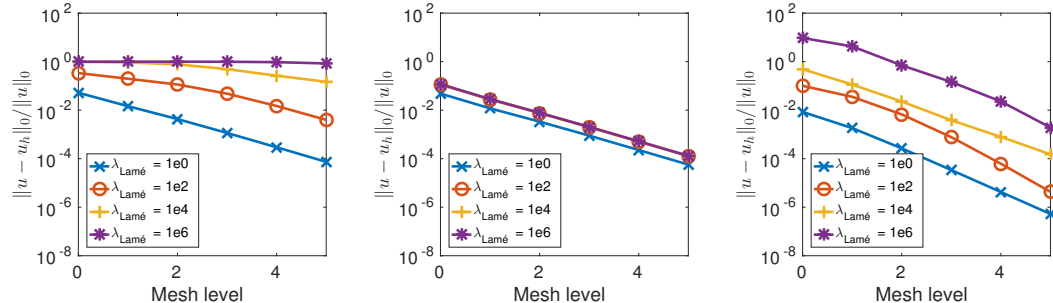


Figure 1.4: Relative $L^2(\Omega)$ error for \mathbb{Q}_1 (left), \mathbb{Q}_1 with reduced integration (middle) and \mathbb{Q}_2 (right). Notation: $1eN = 10^N$.

1.2.2 Orthotropic material laws

Orthotropic materials represent a special case of anisotropic materials. Although the material law is not independent of the coordinate frame, it is invariant with respect to rotations of 180° around three fixed orthogonal axes. While for isotropic materials two independent material parameters exist, there are nine for orthotropic materials.

An example is wood, which consists of three different axes, illustrated in Figure 1.5, namely the fiber direction y , the tangential direction z and the radial direction x . Note that besides the cylindrical structure of a tree trunk, we assume a small size of the domain compared to the diameter of a tree trunk and consider Cartesian coordinates, aligned with the three axes.

By Hooke's law, the stress-strain relation can be stated in the matrix-vector notation as $\boldsymbol{\sigma}(\mathbf{u}) = \mathbb{C}\boldsymbol{\varepsilon}(\mathbf{u})$. Due to the alignment of the coordinate system with the orthotropic structure, the stiffness tensor is given as

$$\mathbb{C} = \begin{pmatrix} A_{11} & A_{12} & A_{13} & 0 & 0 & 0 \\ A_{12} & A_{22} & A_{23} & 0 & 0 & 0 \\ A_{13} & A_{23} & A_{33} & 0 & 0 & 0 \\ 0 & 0 & 0 & G_{yz} & 0 & 0 \\ 0 & 0 & 0 & 0 & G_{xz} & 0 \\ 0 & 0 & 0 & 0 & 0 & G_{xy} \end{pmatrix}, \quad (1.7)$$

with the shear moduli G_{xy}, G_{yz}, G_{xz} and the entries A_{ij} depending on the

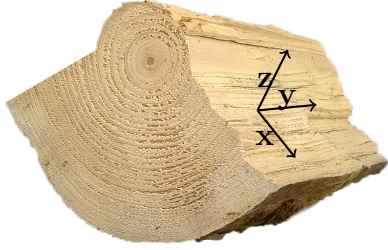


Figure 1.5: Illustration of the orthotropic structure of wood.

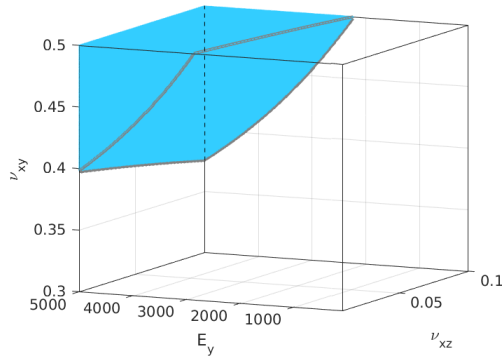


Figure 1.6: Illustration of non-admissible parameter values in a lower-dimensional sub-manifold of the set of all material parameter, varying $\nu_{xz} \in (0.01, 0.1)$, $\nu_{xy} \in (0.3, 0.5)$, $E_y \in (100, 5000)$ and fixing $E_x = 1000$, $E_z = 2000$ and $\nu_{yz} = 0.5$.

elastic moduli E_x, E_y, E_z and the Poisson's ratios $\nu_{xy}, \nu_{yz}, \nu_{xz}$. The formulas for A_{ij} , see, [181, Chapter 2.4], are given by

$$\begin{aligned}
 A_{11} &= \frac{E_x}{D_0} \left(1 - \nu_{yz}^2 \frac{E_z}{E_y}\right), & A_{12} &= \frac{E_y}{D_0} (\nu_{xy} + \nu_{yz} \nu_{xz} \frac{E_z}{E_y}), & A_{13} &= \frac{E_z}{D_0} (\nu_{xy} \nu_{yz} + \nu_{xz}), \\
 A_{22} &= \frac{E_y}{D_0} \left(1 - \nu_{xz}^2 \frac{E_z}{E_x}\right), & A_{23} &= \frac{E_z}{D_0} (\nu_{yz} + \nu_{xy} \nu_{xz} \frac{E_y}{E_x}), & A_{33} &= \frac{E_z}{D_0} \left(1 - \nu_{xy}^2 \frac{E_y}{E_x}\right), \\
 D_0 &= 1 - \nu_{yz}^2 \frac{E_z}{E_y} - \nu_{xy}^2 \frac{E_y}{E_x} - 2 \nu_{xy} \nu_{yz} \nu_{xz} \frac{E_z}{E_x} - \nu_{xz}^2 \frac{E_z}{E_x}.
 \end{aligned}$$

At this point some important differences compared to isotropic material laws are worth pointing out. While in the isotropic case, all Poisson's ratios share the same value, for orthotropic materials they represent three independent material parameters. The only relation between the ratios is $\nu_{ij} E_j = \nu_{ji} E_i$. Also the possible range of the material parameters, i.e., $-1 < \nu < 1/2$ for the isotropic case, is different. A positive definite stiffness tensor and thus a coercive energy functional is only guaranteed if $D_0 > 0$ and $E_x/E_y > \nu_{xy}^2$. Note that Poisson's ratios larger than $1/2$ are permitted, but this does not imply unphysical behavior as in the isotropic case, see, e.g., [183]. The conditions $E_i, G_{ij} > 0$ hold both in the isotropic and orthotropic case. Figure 1.6 depicts a region of non-admissible material data.

1.2.3 Signorini and contact problems

Contact problems are of importance in all kinds of solid mechanical applications. Although their mathematical modeling has a long history, [101], their solution remains challenging and is an active research area. Signorini-type problems can be regarded as a simplified scalar model of elastic contact problems. Signorini and contact problems share a similar formulation including the non-linear boundary condition.

A comprehensive review on contact mechanics can be found in the classical textbooks [142, 234], a mathematical background of variationally consistent discretizations is presented in [230] and a recent overview of different solution schemes is given in [62, 174].

A priori error estimates in the $H^1(\Omega)$ norm for such problems were investigated over many years, see [28, 194] for Signorini and [26, 104, 144] for contact problems. Optimal a priori error estimates for two body contact problems in the $H^1(\Omega)$ norm were established in [115] and more recently reconsidered in [72, 105]. An optimal order a priori analysis for different norms of interest is presented in Chapter 4. First, we introduce elastic contact and then Signorini problems.

1.2.3.1 Elastic contact problems

We consider two bodies Ω^1, Ω^2 with $\Omega^1 \cap \Omega^2 = \emptyset$, where for simplicity we consider Ω^2 to be rigid, i.e., non-deformable, while Ω^1 is deformed as described by the equations of linear elasticity:

$$\begin{aligned} -\operatorname{div} \boldsymbol{\sigma}(\mathbf{u}) &= \hat{\mathbf{f}} & \text{in } \Omega = \Omega^1, \\ \mathbf{u} &= \hat{\mathbf{u}} & \text{on } \Gamma_D = \Gamma_D^1, \\ \boldsymbol{\sigma}(\mathbf{u})\mathbf{n} &= \hat{\mathbf{t}} & \text{on } \Gamma_N = \Gamma_N^1. \end{aligned}$$

Unlike the previous problems, a third part on the boundary Γ_C exists, on which the contact condition is posed. The additional contact condition constrains the displacement, such that it does not penetrate the rigid body Ω_2 . We consider linearized and frictionless contact conditions, defined by the complementarity condition, given by

$$\mathbf{u}^\top \mathbf{n} \leq \hat{g}, \quad (\boldsymbol{\sigma}(\mathbf{u})\mathbf{n})^\top \mathbf{n} \leq 0, \quad (\mathbf{u}^\top \mathbf{n} - \hat{g}) \left((\boldsymbol{\sigma}(\mathbf{u})\mathbf{n})^\top \mathbf{n} \right) = 0, \quad \text{on } \Gamma_C = \Gamma_C^1,$$

where $\hat{g}: \Gamma_C \rightarrow \mathbb{R}$ is the distance between the contact surface and the rigid obstacle, i.e.,

$$\hat{g}(\mathbf{x}) = \inf\{t > 0: \mathbf{x} + t\mathbf{n}(\mathbf{x}) \in \Omega^2\}.$$

The three equations of the complementarity condition can be interpreted as follows: The first equation is the non-penetration condition, as already mentioned. The second condition is a constraint on the sign of the contact force, i.e., the bodies shall not stick together. Finally the complementarity condition guarantees that no contact force can be transmitted as long as there is a positive distance between the bodies.

The case, where both bodies are elastic is formulated similarly. Instead of the condition $\mathbf{u}^\top \mathbf{n} \leq \hat{g}$ a jump operator $[\mathbf{u}^\top \mathbf{n}] \leq \hat{g}$ is used, where, with an appropriate mapping χ from Γ_C^1 to Γ_C^2 , $[\mathbf{u}^\top \mathbf{n}] = (\mathbf{u}^{(1)} - \mathbf{u}^{(2)} \circ \chi)^\top \mathbf{n}^{(1)}$. Additionally, the tangential displacement can be restricted by a friction law, see, e.g., [173, 230], for further reading.

1.2.3.2 Scalar Signorini problems

An analogue inequality constraint for the scalar Poisson equation is given by Signorini-type boundary conditions on Γ_S . For a given initial gap $\hat{g} \in H^{1/2}(\Gamma_S)$, the displacement on the boundary is restricted to $u \leq \hat{g}$. The role of the normal traction in the complementarity condition is taken by the normal derivative and we consider Equations (1.8a) to (1.8d):

$$-\Delta u = \hat{f} \quad \text{in } \Omega, \quad (1.8a)$$

$$u = \hat{u} \quad \text{on } \Gamma_D, \quad (1.8b)$$

$$\partial_{\mathbf{n}} u = \hat{g}_N \quad \text{on } \Gamma_N, \quad (1.8c)$$

$$u \leq \hat{g}, \quad \partial_{\mathbf{n}} u \leq 0, \quad (u - \hat{g}) \partial_{\mathbf{n}} u = 0 \quad \text{on } \Gamma_S. \quad (1.8d)$$

In general, weak solutions of Dirichlet–Neumann problems with smooth data can be represented as a series of singular components and a smooth part. The first singular component has typically a regularity of $H^{3/2-\varepsilon}(\Omega)$. However due to the sign-condition of the Signorini boundary, the regularity is improved. As long as no jump of the outer unit normal is present at the boundary of $\Gamma^{\text{act}} = \{\mathbf{x} \in \Gamma_S : u(\mathbf{x}) = \hat{g}(\mathbf{x})\} \subset \Gamma_S$, the stress intensity factor associated with the first singular component has to be zero. The next singular component typically has a non-zero intensity and is $H^{5/2-\varepsilon}(\Omega)$ regular, see [161].

1.2.4 Finite elasticity

So far, we have considered elasticity under the assumption of infinitesimal small deformations, which allowed us to assume equality of the reference and deformed geometry and to assume a linear constitutive equation. In contrast, the equations for non-linear elasticity are formulated in the deformed formulation. In practice it is often convenient to map them to the initial configuration,

to have a fixed computational domain. We refer to [24, 233] for further reading.

As the stress measure, we consider the 1st Piola–Kirchhoff stress \mathbf{P} , which relates points, surfaces and volumes of the initial domain Ω to the physical forces of the deformed domain. As a consequence it is no longer symmetric, as it transfers between different geometries. Instead of the linearized strain measure $\boldsymbol{\varepsilon}$, we simply consider the deformation gradient $\mathbf{F} = \text{Id} + \text{Grad } \mathbf{u}$. In accordance with most engineering literature, we denote derivatives, vectors and points in the undeformed domain with upper case letters.

Since the 1st Piola–Kirchhoff stress \mathbf{P} measures the true stress, we can easily formulate the strong form on the reference domain:

$$\begin{aligned} -\text{Div } \mathbf{P} &= \hat{\mathbf{f}} && \text{in } \Omega, \\ \mathbf{u} &= \hat{\mathbf{u}} && \text{on } \Gamma_D, \\ \mathbf{P} \mathbf{N} &= \hat{\mathbf{t}} && \text{on } \Gamma_N. \end{aligned}$$

For simplicity, we assume the right hand side and boundary data to be deformation-independent. As already in the linear case, we consider hyper-elastic materials, where the stress is derived by a strain-energy function $\psi(\mathbf{F})$:

$$\mathbf{P}(\mathbf{F}) = \frac{\partial \psi(\mathbf{F})}{\partial \mathbf{F}}.$$

Of course we can now include non-linear constitutive equations. One class of non-linear materials is given by Neo-Hooke material laws, see, e.g., [233, Chapter 3.3.1], where the strain energy is given by

$$\psi(\mathbf{F}) = \frac{\lambda_{\text{Lamé}}}{4}(J^2 - 1 - 2 \ln(J)) + \frac{\mu_{\text{Lamé}}}{2}(\mathbf{F} : \mathbf{F} - d - 2 \ln(J)), \quad (1.9)$$

with $J = \det \mathbf{F}$ and the spacial dimension d .

The standard weak formulation can then be stated analogously to the linear case. We consider the non-linear variational problem $\mathbf{u} \in (H_D^1(\Omega))^d$,

$$\int_{\Omega} \mathbf{P}(\text{Id} + \text{Grad } \mathbf{u}) : \text{Grad } \mathbf{v} \, d\mathbf{x} = \int_{\Omega} \hat{\mathbf{f}}^\top \mathbf{v} \, d\mathbf{x} + \int_{\Gamma_N} \hat{\mathbf{t}}^\top \mathbf{v} \, d\gamma, \quad \mathbf{v} \in (H_D^1(\Omega))^d,$$

where for simplicity $\hat{\mathbf{u}} = \mathbf{0}$. In the interpretation as the principle of virtual displacement, the test function \mathbf{v} is also denoted as $\delta \mathbf{u}$, a virtual displacement and $\text{Grad } \mathbf{v}$ is also referred to as the virtual variation of the deformation gradient $\delta \mathbf{F}$.

2 Isogeometric mortar methods

The term isogeometric analysis (IGA) was introduced in 2005 by Hughes et al. in [117]. Nowadays it includes a family of methods, normally called isogeometric methods, that use B-splines and non-uniform rational B-splines (NURBS) as basis functions to construct numerical approximations of PDEs, [56, 77]. The idea of using spline functions for the approximation of PDEs can even be found in earlier works, see, e.g., [108] and references therein. However, with isogeometric finite elements, the computational domain is represented in the isoparametric way by the same spline functions used for the approximation. The goal is to vastly simplify the mesh generation and refinement processes with respect to standard FEM, possibly bridging the gap between CAD and analysis. IGA is currently a very active research area. It is attractive for a large variety of applications and there exists a fair amount of mathematically sound results, collected in [22]. Besides variational approaches, the global smoothness of splines also allows the use of collocation methods, see [13, 95].

With isogeometric methods, the computational domain is generally split into patches. Within this framework, techniques to couple the numerical solution on different patches are required. Weak coupling techniques are favorable in comparison to strong couplings, to retain the flexibility of the meshes at the interfaces. Mortar methods offer a flexible approach to domain decomposition, originally applied in spectral and finite element methods. In the classical finite element context, mortar methods have been successfully investigated for over two decades, [25, 27, 30, 31, 140], for a mathematical overview see [229]. Further applications of the mortar methods include contact problems, [26, 137, 230, 231, 234], and interface problems, e.g., in multi-physics applications, [215].

In this chapter, we present a mathematical foundation of isogeometric mortar methods with trace spaces of several degrees as well as biorthogonal basis functions. Then, we study aspects of numerical quadrature and eigenvalue approximations in more detail. Results of this section have been published by the author in collaboration with E. Brivadis, A. Buffa and B. Wohlmuth in two articles in the year 2015: in the article “Isogeometric mortar methods” [43] and in a chapter of the book “Isogeometric Analysis and Applications 2014” titled “The influence of quadrature errors on isogeometric mortar methods”, [42]. The results of these papers are also included in the PhD thesis of E. Brivadis [41]. The results of Section 2.1 and 2.2 (excluding the example

of non-linear elasticity in Section 2.2.2.4) are included in the author’s master’s thesis “Modern Discretization Techniques for Partial Differential Equations” [236] of 2014. A summary appeared as an extended abstract in [237].

2.1 Introduction

We start with an introduction to the basics of isogeometric finite element methods, B-splines and NURBS and then also an introduction to isogeometric methods is given, where optimal convergence is stated under certain requirements on the Lagrange multiplier space.

The coupling of multipatch geometries in IGA has been investigated in several articles, i.e., [45, 131, 141, 166, 191], and successful applications of the mortar method are shown in [8, 70, 102]. The use of mortar methods in contact simulations, where isogeometric methods have some advantages over classical finite element methods, was considered in [61, 63, 66, 129, 209, 210]. An approach based on Lagrange multipliers with a more convenient sparsity structure than standard trace spaces was introduced in [69]. Recently dual basis functions were used for contact problems in [197] and a mathematical analysis of isogeometric contact discretizations is presented in [4].

Higher-order couplings recently gained attention. We refer to [127, 128] for Kirchhoff-Love shells. A discussion of strong C^1 couplings in multi-patch settings is given in [33], whereas weak continuity of the normal stress is realized in [53]. Alternative higher-order coupling methods based on least-squares techniques were proposed in [55].

2.1.1 B-splines and NURBS basics

In this section, we give a brief overview on the isogeometric functions and introduce some notations and concepts which are used throughout this chapter. For more details, we refer to the classical literature [21, 56, 172, 195]. Firstly, we introduce B-splines in the one-dimensional case and recall some of their basic properties. Secondly, we extend these definitions to the multi-dimensional case and introduce NURBS and then NURBS parametrizations.

2.1.1.1 Univariate B-splines

We denote by p the degree of the univariate B-splines and an open univariate knot vector by $\Xi = (\xi_1, \dots, \xi_{n+p+1})$, where the first and last entries are repeated $(p + 1)$ -times, i.e.,

$$0 = \xi_1 = \dots = \xi_{p+1} < \xi_{p+2} \leq \dots \leq \xi_n < \xi_{n+1} = \dots = \xi_{n+p+1} = 1.$$

Let us define $Z = (\zeta_1, \zeta_2, \dots, \zeta_E)$ as the knot vector without any repetition, also called breakpoint vector. For each breakpoint ζ_j of Z , the multiplicity m_j is defined as its number of repetitions in Ξ . The elements in Z form a mesh of the parametric interval $(0, 1)$.

We denote by $\widehat{B}_i^p(\zeta)$, $i = 1, \dots, n$, the collection of the univariate B-spline basis functions defined by Ξ and by $S^p(\Xi) = \text{span}\{\widehat{B}_i^p(\zeta): i = 1, \dots, n\}$ the spline space.

Now let us recall few important properties of the univariate B-splines. Each basis function \widehat{B}_i^p is a positive piecewise polynomial of degree p with local support $\text{supp } \widehat{B}_i^p = (\xi_i, \xi_{i+p+1})$, i.e., \widehat{B}_i^p is non-zero on at most $p + 1$ elements. Exactly $p + 1$ basis functions have non-zero values on the element (ζ_j, ζ_{j+1}) . The break point multiplicity $m_j \geq 1$ defines the inter-element continuity, i.e., the basis functions are C^{p-m_j} at each $\zeta_j \in Z$.

Assuming that $S^p(\Xi) \subset C^0(0, 1)$, i.e., $m_j \leq p$, $j = 2, \dots, E - 1$, the derivative operator $\partial_\zeta: S^p(\Xi) \rightarrow S^{p-1}(\Xi')$, with $\Xi' = (\xi_2, \dots, \xi_{n+p})$, is linear and surjective, see [22, 195].

Different refinement strategies are used for splines. Further knots can be inserted with the h -refinement, the degree can be elevated with the p -refinement and a combination of both is done in the k -refinement, see [56, 172] for some algorithmic details on the refinement procedures. In the following, we only consider h -refinement, which is similar to h -refinement of classical finite element methods.

2.1.1.2 Multivariate B-splines and NURBS

A tensor product of univariate B-splines defines multivariate B-splines. For any direction $\delta = 1, \dots, d$, we introduce p_δ the degree of the univariate B-splines, n_δ the number of univariate B-spline functions, Ξ_δ the univariate open knot vector and Z_δ the univariate breakpoint vector. We then define the multivariate knot vector by $\Xi = (\Xi_1 \times \Xi_2 \times \dots \times \Xi_d)$ and the multivariate breakpoint vector by $\mathbf{Z} = (Z_1 \times Z_2 \times \dots \times Z_d)$. We do not define a degree vector for the sake of notation and assume that the degree is the same in all parametric directions, denoted by p .

The break points of \mathbf{Z} form a tensor product mesh of the parametric domain $\widehat{\Omega} = (0, 1)^d$ with the elements collected in $\widehat{\mathcal{M}}$:

$$\widehat{\mathcal{M}} = \{\mathbf{Q}_j = \widehat{\tau}_{1,j_1} \times \dots \times \widehat{\tau}_{d,j_d}: \widehat{\tau}_{\delta,j_\delta} = (\zeta_{\delta,j_\delta}, \zeta_{\delta,j_\delta+1}), 1 \leq j_\delta \leq E_\delta - 1\}.$$

We introduce a set of multi-indices $\mathbf{I} = \{\mathbf{i} = (i_1, \dots, i_d): 1 \leq i_\delta \leq n_\delta\}$ and define multivariate B-spline functions as the tensor product from the univariate

B-splines:

$$\widehat{B}_{\mathbf{i}}^p(\boldsymbol{\zeta}) = \widehat{B}_{i_1}^p(\zeta_1) \dots \widehat{B}_{i_d}^p(\zeta_d), \quad \mathbf{i} \in \mathbf{I}.$$

The multivariate spline space in the parametric domain is then given by

$$S^p(\Xi) = \bigotimes_{\delta=1}^d S^p(\Xi_\delta) = \text{span}\{\widehat{B}_{\mathbf{i}}^p(\boldsymbol{\zeta}), \mathbf{i} \in \mathbf{I}\}.$$

NURBS are rational functions of B-spline functions with a given weight function $\widehat{W}_{\text{weight}}(\boldsymbol{\zeta}) = \sum_{\mathbf{i} \in \mathbf{I}} \omega_{\mathbf{i}} \widehat{B}_{\mathbf{i}}^p(\boldsymbol{\zeta})$ defined by a set of positive weights $\omega_{\mathbf{i}}$, $\mathbf{i} \in \mathbf{I}$. Then the NURBS basis is defined by

$$\widehat{N}_{\mathbf{i}}^p(\boldsymbol{\zeta}) = \frac{\omega_{\mathbf{i}} \widehat{B}_{\mathbf{i}}^p(\boldsymbol{\zeta})}{\widehat{W}_{\text{weight}}(\boldsymbol{\zeta})},$$

which is in general no longer a tensor product of univariate NURBS functions. We consider the NURBS space $N^p(\Xi)$ which is spanned by the functions $\widehat{N}_{\mathbf{i}}^p(\boldsymbol{\zeta})$. The introduction of rational splines enables us to exactly represent conic sections, e.g., circles. Since B-splines can be regarded as NURBS with weights equal to 1 we also refer to them as NURBS, whenever there is no ambiguity.

2.1.1.3 Isogeometric parametrization

In the computer aided geometrical design (CAGD) NURBS are widely used, since they are capable to precisely describe various geometries, including conic sections. With a given set of control points $\mathbf{C}_{\mathbf{i}} \in \mathbb{R}^d$, $\mathbf{i} \in \mathbf{I}$, we can define a parametrization of a NURBS surface ($d = 2$) or solid ($d = 3$) as a linear combination of NURBS and the control points:

$$\mathbf{F}(\boldsymbol{\zeta}) = \sum_{\mathbf{i} \in \mathbf{I}} \mathbf{C}_{\mathbf{i}} \widehat{N}_{\mathbf{i}}^p(\boldsymbol{\zeta}).$$

Then the NURBS geometry is defined as the image of $\widehat{\Omega}$ by the geometric mapping \mathbf{F} , i.e., $\Omega = \mathbf{F}(\widehat{\Omega})$. The physical mesh \mathcal{M} is given as the image of the parametric mesh $\widehat{\mathcal{M}}$ through \mathbf{F} , and its elements are denoted by \mathbf{O} :

$$\mathcal{M} = \{\mathbf{O} \subset \Omega : \mathbf{O} = \mathbf{F}(\mathbf{Q}), \mathbf{Q} \in \widehat{\mathcal{M}}\}.$$

We assume the following regularity of \mathbf{F} , noting that the geometry mapping is mesh-independent.

Assumption 2.1.1. *The parametrization \mathbf{F} is a bi-Lipschitz homeomorphism. Moreover, $\mathbf{F}|_{\overline{\mathbf{Q}}}$ is in $C^\infty(\overline{\mathbf{Q}})$ for all elements of the parametric mesh, and*

$\mathbf{F}^{-1}|_{\bar{\mathbf{O}}}$ is in $C^\infty(\bar{\mathbf{O}})$ for all elements of the physical mesh.

We define the mesh size for any parametric element as $h_{\mathbf{Q}_j} = \text{diam}(\mathbf{Q}_j)$ and for any physical element as $h_{\mathbf{O}_j}$, noting that Assumption 2.1.1 ensures that $h_{\mathbf{Q}_j} \approx h_{\mathbf{O}_j}$. Thus, no distinction is required and we can use the simple notation h_j for the mesh size. The maximal mesh size is defined by $h = \max_j h_j$. The mesh size of the underlying univariate partition Ξ_δ , $\delta = 1, \dots, d$, is denoted by $h_{\delta,j}$, $j = 1, \dots, E_\delta - 1$ and we assume the following mesh regularity.

Assumption 2.1.2. *The partition defined by the breakpoints is globally quasi-uniform, i.e., there exists a constant θ such that the univariate element size ratio is uniformly bounded: $h_{\delta,i}/h_{\delta',j} \leq \theta$, with $\delta, \delta' = 1, \dots, d$ as well as $i = 1, \dots, E_\delta - 1$, $j = 1, \dots, E_{\delta'} - 1$.*

Note that this assumption excludes the case of anisotropic meshes which are used for, e.g., boundary layers, and of graded meshes which are used in case of singularities. However, this assumption is made here only to reduce the technicality of the proofs and a more detailed analysis may show the same results under milder assumptions on the mesh.

2.1.2 Isogeometric mortar methods

In this section, we set the geometry decomposition with the functional framework. Then we discuss the requirements on the approximation spaces in order to have an optimal method.

2.1.2.1 Description of the computational domain

Let a decomposition of the domain Ω into K non-overlapping domains Ω_k be given:

$$\bar{\Omega} = \bigcup_{k=1}^K \bar{\Omega}_k, \text{ and } \Omega_i \cap \Omega_j = \emptyset, i \neq j.$$

For $1 \leq k_1, k_2 \leq K$, $k_1 \neq k_2$, we define the interface as the interior of the intersection of the boundaries, i.e., $\bar{\gamma}_{k_1 k_2} = \partial\Omega_{k_1} \cap \partial\Omega_{k_2}$, where $\gamma_{k_1 k_2}$ is open. Let the non-empty interfaces be enumerated by γ_l , $l = 1, \dots, L$. We define the skeleton $\Gamma = \bigcup_{l=1}^L \gamma_l$ as the union of all interfaces. As with classical mortar methods, for each interface, one of the adjacent subdomains is chosen as the master side and one as the slave side. The slave side is used in the following to define the Lagrange multiplier space that enforces the coupling between the master and the slave side. We denote the index of the former by $m(l)$, the index of the latter one by $s(l)$, and thus $\bar{\gamma}_l = \partial\Omega_{m(l)} \cap \partial\Omega_{s(l)}$. Note that one subdomain can at the same time be classified as a master domain for one

interface and as a slave domain for another interface, see Figure 2.1. On the interface γ_l , we define the outward unit normal \mathbf{n}_l of the master side $\partial\Omega_{m(l)}$ and denote by $\partial u/\partial\mathbf{n}_l$ the normal derivative on γ_l from the master side.

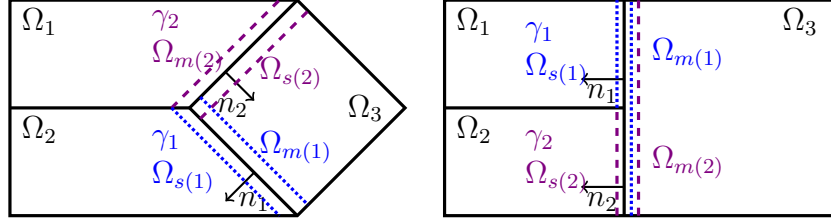


Figure 2.1: Geometrical conforming case (left) and slave conforming case (right).

Each subdomain Ω_k is given as the image of the parametric space $\widehat{\Omega} = (0, 1)^d$ by one single NURBS parametrization $\mathbf{F}_k: \widehat{\Omega} \rightarrow \Omega_k$, see Section 2.1.1.3, which satisfies the Assumption 2.1.1. We assume that the decomposition represents the Dirichlet boundary in the sense, that the pull-back of $\partial\Omega_k \cap \Gamma_D$ is either empty or the union of whole faces of the unit d -cube. The h -refinement procedure, see Sections 2.1.1.2 and 2.1.1.3, yields a family of meshes denoted $\mathcal{M}_{k,h}$, with each mesh being a refinement of the initial one, where we require Assumption 2.1.2. Under these assumptions, the family of meshes is shape regular.

We furthermore assume that for each interface, the pull-back with respect to the slave domain is a whole face of the unit d -cube in the parametric space. Under these assumptions, we are not necessarily in a geometrically conforming situation, but in a *slave conforming* situation, see Figure 2.1 (right). We are in a fully geometrically conforming situation, if we also assume that the pull-back with respect to the master domain is a whole face of the unit d -cube, see Figure 2.1 (left).

2.1.2.2 The variational problem

For each subdomain Ω_k , we consider the space $H_D^1(\Omega_k)$ and globally define the broken Sobolev spaces $V = \prod_{k=1}^K H_D^1(\Omega_k)$, endowed with the broken norm $\|v\|_V^2 = \sum_{k=1}^K \|v\|_{H^1(\Omega_k)}^2$, and $M = \prod_{l=1}^L H^{-1/2}(\gamma_l)$.

For the scalar model problem (1.2), we define the broken bilinear and linear forms $a: V \times V \rightarrow \mathbb{R}$ and $f: V \rightarrow \mathbb{R}$, such that

$$a(u, v) = \sum_{k=1}^K \int_{\Omega_k} \alpha \nabla u^\top \nabla v + \beta u v \, d\mathbf{x}, \quad f(v) = \sum_{k=1}^K \int_{\Omega_k} \widehat{f} v \, d\mathbf{x} + \int_{\partial\Omega_k \cap \Gamma_N} \widehat{g}_N v \, d\gamma.$$

We assume that jumps of α and β are solely located at the skeleton, which is important for a reasonable approximation of the solution by the smooth splines.

2.1.2.3 Isogeometric mortar discretization

In the following, we set our discrete approximation spaces used in the mortar context. We introduce $V_{k,h}$ as the approximation space on Ω_k by

$$V_{k,h} = \{v_k = \widehat{v}_k \circ \mathbf{F}_k^{-1} \in H_D^1(\Omega_k) : \widehat{v}_k \in N^{p_k}(\Xi_k)\},$$

which is defined on the knot vector Ξ_k of degree p_k . We denote by h_k the mesh size of $V_{k,h}$ but note that we use the maximal mesh size $h = \max_k h_k$ as the mesh parameter. In the following lemma, we recall the optimal approximation properties of NURBS spaces, see, e.g., [21, 23, 195].

Lemma 2.1.3. *Given a quasi-uniform mesh and let r, s be such that they satisfy $0 \leq r \leq s \leq p_k + 1$. Then, there exists a constant c depending only on $p_k, \theta_k, \mathbf{F}_k$ and $\widehat{W}_{\text{weight},k}$, such that for any $v \in H^s(\Omega_k)$ there exists an approximation $v_h \in V_{k,h}$, such that*

$$\|v - v_h\|_{H^r(\Omega_k)} \leq ch^{s-r} \|v\|_{H^s(\Omega_k)}.$$

On Ω , we define the product space $V_h = \prod_{k=1}^K V_{k,h} \subset V$, which forms an $H^1(\Omega)$ non-conforming space as it is discontinuous over the interfaces.

The mortar method is based on a weak enforcement of continuity across the interfaces γ_l in broken Sobolev spaces. Let a space of discrete Lagrange multipliers $M_{l,h} \subset L^2(\gamma_l)$ on each interface γ_l be given, which are built on the slave mesh. On the skeleton Γ , we define the discrete product Lagrange multiplier space M_h as $M_h = \prod_{l=1}^L M_{l,h}$. Choices of different spaces are discussed in the next section. Furthermore, we define the discrete trace space with additional zero boundary conditions by $W_{l,h} = \{v|_{\gamma_l} : v \in V_{s(l),h}\} \cap H_0^1(\gamma_l)$.

One possibility for a mortar method is to specify the discrete weak formulation as a saddle point problem: Find $(u_h, \lambda_h) \in V_h \times M_h$, such that

$$a(u_h, v_h) + b(v_h, \lambda_h) = f(v_h), \quad v_h \in V_h, \quad (2.1a)$$

$$b(u_h, \mu_h) = 0, \quad \mu_h \in M_h, \quad (2.1b)$$

where $b(v, \mu) = \sum_{l=1}^L \int_{\gamma_l} \mu [v]_l \, d\gamma$ and $[\cdot]_l$ denotes the jump from the master to the slave side over γ_l .

We note, that the Lagrange multiplier λ_h gives an approximation of the normal flux across the skeleton.

Remark 2.1.4. We note that the formulation for linear elasticity follows the same structure. With $\mathbf{V}_h = (V_h)^d$ and $\mathbf{M}_h = (M_h)^d$, we consider the saddle point problem with the broken bilinear and linear forms of linear elasticity and a vectorial coupling condition:

$$a(\mathbf{u}, \mathbf{v}) = \sum_{k=1}^K \int_{\Omega_k} \boldsymbol{\sigma}(\mathbf{u}) : \boldsymbol{\varepsilon}(\mathbf{v}) \, d\mathbf{x}, \quad f(\mathbf{v}) = \sum_{k=1}^K \int_{\Omega_k} \widehat{\mathbf{f}}^\top \mathbf{v} \, d\mathbf{x} + \int_{\Gamma_N \cap \partial\Omega_k} \widehat{\mathbf{t}}^\top \mathbf{v} \, d\boldsymbol{\gamma},$$

$$b(\mathbf{v}, \boldsymbol{\mu}) = \sum_{l=1}^L \int_{\gamma_l} \boldsymbol{\mu}^\top [\mathbf{v}]_l \, d\boldsymbol{\gamma}.$$

Note that for linear elasticity, the normal stress $\boldsymbol{\sigma}(\mathbf{u}) \mathbf{n}$ is the normal flux, which is approximated by the Lagrange multiplier.

For convenience of notation we present the theoretical results for the scalar case, but note that they directly apply to the case of linear elasticity as well.

It is well-known from the theory of mixed and mortar methods, that the following abstract requirements guarantee the method to be well-posed and of optimal order, see [25, 32]. One is a uniform inf-sup stability of the discrete spaces and the second one an approximation requirement of the Lagrange multiplier. We remark that we denote by $0 < c < \infty$ a generic constant that is independent of the mesh sizes but possibly depends on p_k .

Although the primal variable of the saddle point problem is in a broken H^1 space, the inf-sup stability can be formulated as an L^2 stability over each interface. This implies the $H_{00}^{1/2} - H^{-1/2}$ stability, which can be used in the geometrically conforming situation for $d = 2$ and in weighted L^2 norms, for the other cases, see [35].

Assumption 2.1.5. For $l = 1, \dots, L$ and any $\mu_l \in M_{l,h}$ it holds

$$\sup_{w_l \in W_{l,h}} \frac{\int_{\gamma_l} w_l \mu_l \, d\boldsymbol{\gamma}}{\|w_l\|_{L^2(\gamma_l)}} \geq c \|\mu_l\|_{L^2(\gamma_l)}.$$

The second assumption is the approximation order of the dual space. Since for the dual space weaker norms are used, the approximation order of $M_{l,h}$ with respect to the L^2 norm can be smaller than the one of $W_{l,h}$.

Assumption 2.1.6. For $l = 1, \dots, L$ there exists a fixed $\eta(l)$, such that for any $\lambda \in H^{\eta(l)}(\gamma_l)$ it holds

$$\inf_{\mu_l \in M_{l,h}} \|\lambda - \mu_l\|_{L^2(\gamma_l)} \leq c h^{\eta(l)} \|\lambda\|_{H^{\eta(l)}(\gamma_l)}.$$

The following a priori estimates in the broken V and M norms can be shown by standard techniques, see [27, 30].

Theorem 2.1.7. *Given Assumptions 2.1.5 and 2.1.6, the following convergence is given for the primal solution of (2.1). For $u \in H^{\sigma+1}(\Omega)$, with $1/2 < \sigma \leq \min_{k,l}(p_k, \eta(l) + 1/2)$ it holds*

$$\frac{1}{h^2} \|u - u_h\|_{L^2(\Omega)}^2 + \|u - u_h\|_V^2 \leq c \sum_{k=1}^K h_k^{2\sigma} \|u\|_{H^{\sigma+1}(\Omega_k)}^2.$$

Also an estimate for the dual solution, approximating the normal flux, holds:

$$\sum_{l=1}^L \left\| \alpha \frac{\partial u}{\partial \mathbf{n}_l} - \lambda_h \right\|_{H^{-1/2}(\gamma_l)}^2 \leq c \sum_{k=1}^K h_k^{2\sigma} \|u\|_{H^{\sigma+1}(\Omega_k)}^2.$$

In the geometrically non-conforming case, as well as for $d = 3$, the ratio of the mesh sizes on the master and the slave side enters in the a priori estimate, see [138], which does not play a role here due to Assumption 2.1.2.

Optimality of the mortar method holds, when $\eta(l) = p_{s(l)} - 1/2$ can be chosen. Moreover, the dual estimate could still be improved under additional regularity assumptions, see [158].

2.2 Lagrange multiplier trace spaces

The choice of the Lagrange multiplier space is the most important point of an isogeometric mortar method. From the classical mortar theory, the two abstract requirements previously discussed are given. One is the sufficient approximation order, the other is the requirement of an inf-sup stability. For a primal space of splines of degree p , we investigate three different degrees for the Lagrange multiplier: p , $p - 1$ and $p - 2$. Each choice is from some point of view natural but has quite different characteristic features. An alternative approach to trace spaces are biorthogonal basis functions, which are considered later in Section 2.3.

2.2.1 Choice of the spaces

For a given interface γ_l , we aim at providing multiplier spaces that satisfy the inf-sup stability of Assumption 2.1.5. In our setting, γ_l is a whole face of $\Omega_{s(l)}$, which is defined as $\mathbf{F}_{s(l)}(\widehat{\Omega})$. Without loss of generality we suppose that $\gamma_l = \mathbf{F}_{s(l)}(\widehat{\gamma} \times \{0\})$, $\widehat{\gamma} = (0, 1)^{d-1}$. We consider each interface γ_l separately, so, to shorten the notations, we omit the index l in the following.

Given a Lagrange multiplier space \widehat{M} on the parametric space, we set the Lagrange multiplier space $M = \{\mu = \widehat{\mu} \circ \mathbf{F}_s^{-1}, \widehat{\mu} \in \widehat{M}\}$. By change of variable,

the integral in Assumption 2.1.5 transforms into a weighted integral on the parametric space. Denoting $\widehat{w} = (w \circ \mathbf{F}_s) \cdot \widehat{W}_{\text{weight}} \in S^p(\widehat{\gamma})$ for $w \in W$ and $\widehat{\mu} = \mu \circ \mathbf{F}_s \in \widehat{M}$ for $\mu \in M$, the integral now reads

$$\begin{aligned} \int_{\gamma} w \mu \, d\gamma &= \int_{\widehat{\gamma}} (w \circ \mathbf{F}_s) (\mu \circ \mathbf{F}_s) |\det(\nabla_{\widehat{\gamma}} \mathbf{F}_s)| \, d\mathbf{x} \\ &= \int_{\widehat{\gamma}} \widehat{w} \widehat{\mu} \widehat{W}_{\text{weight}}^{-1} |\det(\nabla_{\widehat{\gamma}} \mathbf{F}_s)| \, d\mathbf{x}, \end{aligned}$$

where $\nabla_{\widehat{\gamma}}$ denotes the surface gradient on $\widehat{\gamma}$. Due to the Assumption 2.1.1 and the uniform positivity of NURBS weights, we can firstly concentrate on the inf-sup condition on the parametric space as follows: Given $\widehat{\gamma} = (0, 1)^{d-1}$, a degree p and knot vectors Ξ_{δ} with $\delta = 1, \dots, d-1$, we denote by $S^p(\widehat{\gamma})$ the corresponding spline space and $S_0^p(\widehat{\gamma}) = S^p(\widehat{\gamma}) \cap H_0^1(\widehat{\gamma})$, and study the following inf-sup stability

$$\sup_{\widehat{w} \in S_0^p(\widehat{\gamma})} \frac{\int_{\widehat{\gamma}} \widehat{w} \widehat{\mu} \, d\mathbf{x}}{\|\widehat{w}\|_{L^2(\widehat{\gamma})}} \geq c \|\widehat{\mu}\|_{L^2(\widehat{\gamma})}. \quad (2.2)$$

for any $\widehat{\mu} \in \widehat{M}$, for three choices of Lagrange multiplier spaces \widehat{M} . Then, in the case (2.2) is satisfied, we show that the desired inf-sup stability, i.e., Assumption 2.1.5, is satisfied.

In the following, we give details of this inf-sup study and sort out the useful dual degrees for isogeometric mortar methods.

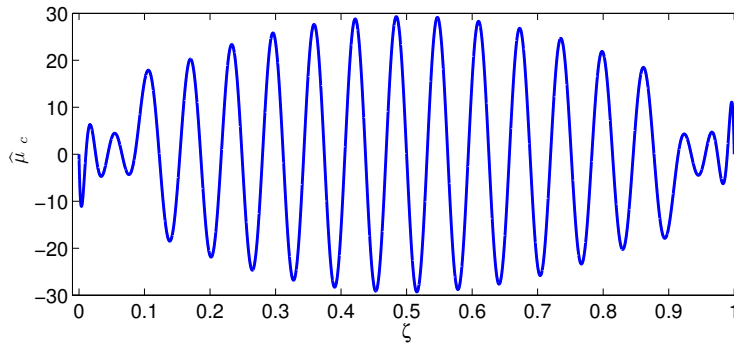
2.2.1.1 Choice 1: unstable pairing $p/p - 1$

Theorem 2.1.7 states that an order $p = \min_k p_k$ a priori bound can only be obtained if $\eta(l)$ can be set less than or equal to $p - 1/2$. This observation motivates the choice of a spline space of order $p - 1$ as dual space. Then in Assumption 2.1.6 $\eta(l)$ can be set to p and, provided that the uniform inf-sup stability of Assumption 2.1.5 holds, a convergence rate equal to p would be reached.

Denote by $\widehat{M}^1 = \text{span}_{i=1, \dots, n^{(1)}} \{\widehat{B}_i^{p-1}\}$ the spline space of order $p - 1$ built on the knot vector(s) Ξ'_{δ} with $\delta = 1, \dots, d - 1$ obtained from the restriction of Ξ to the corresponding direction(s) removing in the underlying univariate knot vector the first and the last knots. The superscript 1 refers to the degree difference between the primal and the dual space.

Unfortunately, as we will see, this choice lacks the uniform inf-sup condition (2.2) and thus also Assumption 2.1.5. Indeed, a checkerboard mode which yields an h -dependent inf-sup constant can be constructed.

The easiest test case considers B-splines on a uniform knot vector for $h = 2^{-j}$, where j is the number of uniform refinements: $\Xi = (0, \dots, 0, h, 2h, \dots,$


 Figure 2.2: Checkerboard mode for $d = 2$ and $p = 6$.

1, \dots , 1). We construct a multiplier $\hat{\mu}_c \in \widehat{M}^1$ which yields an h -dependent inf-sup constant as

$$\hat{\mu}_c = \sum_{i=1}^{n^{(1)}} \hat{\mu}_i \widehat{B}_i^{p-1}, \quad \hat{\mu}_i = (-1)^i (i-1)(n^{(1)} - i),$$

which is shown in Figure 2.2. For the bivariate case, a tensor product using $\hat{\mu}_c$ in each direction is chosen. The numerical stability constants were computed by a direct evaluation of the supremum

$$\sup_{\widehat{w} \in S^p(\widehat{\gamma})} \frac{\int_{\widehat{\gamma}} \widehat{w} \hat{\mu}_c \, d\mathbf{x}}{\|\widehat{w}\|_{L^2(\widehat{\gamma})}},$$

and dividing the result by $\|\hat{\mu}_c\|_{L^2(\widehat{\gamma})}$. The results are shown in Figure 2.3 for $d = 2$ and $d = 3$, where an h -dependency of order h^{d-1} can be observed. Note that on the same mesh, the stability constant is larger for higher degrees, but the asymptotic rate of the h -dependency is the same.

Remark 2.2.1. *Numerical experiments show, that the inf-sup constant can be recovered by the use of a staggered grid, which is similar to the behavior known from the finite element method. Another possibility is to use a coarse dual mesh for the Lagrange multipliers.*

2.2.1.2 Choice 2: stable pairing $p/p - 2$

An unstable pairing appears roughly speaking when the Lagrange multiplier space is too large. An easy way to overcome this is by using a smaller space, which motivates our second choice. If the spline space $S^p(\widehat{\gamma})$ is globally C^1 , then it is also possible to construct a spline space of degree $p - 2$

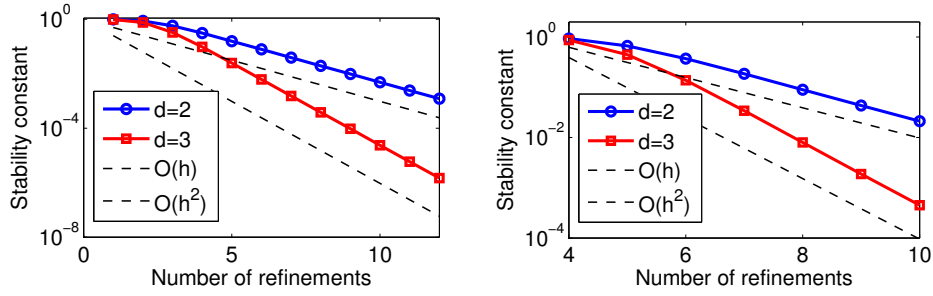


Figure 2.3: h -dependency of the L^2 inf-sup constant for dimension $d = 2$ and $d = 3$. Left: $p = 2$. Right: $p = 10$.

on the knot vector(s) Ξ''_δ with $\delta = 1, \dots, d - 1$ obtained from the restriction of Ξ to the corresponding direction(s) removing in the underlying univariate knot vector the first and the last two knots. We denote this space by $\widehat{M}^2 = \text{span}_{i=1, \dots, n^{(2)}} \{\widehat{B}_i^{p-2}\}$, which however will not provide a guaranteed order p convergence rate based on Theorem 2.1.7. The best approximation property of the Lagrange multiplier space only allows a $p - 1/2$ order convergence in the broken V and M norms, provided that the pairing is uniformly stable. In what follows, we prove that \widehat{M}^2 verifies the inf-sup stability (2.2).

The proof is based on an identification of the primal trace space and the dual space using derivatives and integrals as well as on an auxiliary stability result for the degree $p - 1$. We sketch the main steps and refer to [43] for more details. Let us first introduce some preliminary notation.

First, we define three spline spaces and a bijective derivative operator, that maps between them. To shorten our notation, we denote by S^q with $q = p - 2, p - 1$, and p the spline spaces of degree q , which are constructed on Ξ'', Ξ' and Ξ , respectively. Furthermore let us define the spline space with zero mean value for $d = 2$: $S_{\text{zmv}}^{p-1} = \{\widehat{s}(x) \in S^{p-1} : \int_0^1 \widehat{s} dx = 0\}$, as well as the bijective derivative operator $D = \partial_x$.

For $d = 3$ the tensor product structure must be taken into account and we define

$$S_{\text{zmv}}^{p-1} = \left\{ \widehat{s} \in S^{p-1} : \int_0^1 \widehat{s}(x, \bar{y}) dx = 0 = \int_0^1 \widehat{s}(\bar{x}, y) dy, \quad \bar{x}, \bar{y} \in [0, 1] \right\}.$$

We consider the mixed derivative $D = \partial_{xy}$ and the associated tensor product Sobolev space

$$H^{1,1}(\widehat{\gamma}) = H^1(0, 1) \otimes H^1(0, 1) = \left\{ \widehat{v} \in L^2(\widehat{\gamma}) : \partial_x^i \partial_y^j \widehat{v} \in L^2(\widehat{\gamma}), \quad i, j \in \{0, 1\} \right\},$$

endowed with the norm $\|\widehat{v}\|_{H^{1,1}(\widehat{\gamma})}^2 = \|\widehat{v}\|_{H^1(\widehat{\gamma})}^2 + \|\partial_{xy}\widehat{v}\|_{L^2(\widehat{\gamma})}^2$.

To simplify the notation, we will denote in the following $Z = H^1(\widehat{\gamma})$ for $d = 2$ and $Z = H^{1,1}(\widehat{\gamma})$ for $d = 3$. The bijectivity of D from S_0^p to S_{zmv}^{p-1} as well as from S_{zmv}^{p-1} into S^{p-2} was shown in [43, Lemma 10], together with the coercivity $\|v\|_{L^2(\widehat{\gamma})} \leq c \|Dv\|_{Z'}$. The bijectivity is shown by an explicit construction of the inverse as an integral. To apply the bijectivity of the derivative in the proof of the inf-sup condition, we can no longer work with the L^2 norm, but need to consider the Z' and Z norms. Let us remark that $S^{p-1} \subset Z$ holds due to the assumption $S^p \subset C^1$.

The following lemma states an auxiliary stability result in these norms.

Lemma 2.2.2. *For any $\widehat{g}^{p-1} \in S_{zmv}^{p-1}$, it holds*

$$\sup_{\widehat{f}^{p-1} \in S_{zmv}^{p-1}} \frac{\int_{\widehat{\gamma}} \widehat{g}^{p-1} \widehat{f}^{p-1} \, d\mathbf{x}}{\|\widehat{f}^{p-1}\|_{Z'}} \geq c \|\widehat{g}^{p-1}\|_Z.$$

Proof. In the case $d = 2$ standard techniques, e.g., [138, Lemma 1.8], show that the $Z - Z'$ inf-sup condition holds on S^{p-1} , i.e., for $\widehat{g}^{p-1} \in S^{p-1}$ it holds,

$$\sup_{\widehat{f}^{p-1} \in S^{p-1}} \frac{\int_{\widehat{\gamma}} \widehat{f}^{p-1} \widehat{g}^{p-1} \, d\mathbf{x}}{\|\widehat{f}^{p-1}\|_Z} \geq c \|\widehat{g}^{p-1}\|_{Z'}.$$

To show that the restriction to S_{zmv}^{p-1} retains this stability, we trivially restrict \widehat{f}^{p-1} to S_{zmv}^{p-1} and replace \widehat{g}^{p-1} by its (Z -stable) L^2 projection onto S_{zmv}^{p-1} . Now using [32, Proposition 3.4.3], we interchange the spaces of the infimum and the supremum which yields the result.

The case $d = 3$ requires a bit more care, since $Z = H^{1,1}(\widehat{\gamma})$ is no longer a standard Sobolev space and thus the Z stability of the Fortin operator cannot be shown as in the case $d = 2$. Instead, we make use of a tensor product of the univariate Fortin operators. See [23] for another application of a tensor product of projection operators.

We construct the Fortin operator as the tensor product of univariate L^2 projections and then we show its Z stability. We define $\overline{\Pi}_i: L^2(0,1) \rightarrow S^{p-1}(\Xi_i)$ as the L^2 projection into the univariate spline spaces and their extensions onto $\widehat{\gamma}$ by $\Pi_1: L^2(\widehat{\gamma}) \rightarrow L^2(\widehat{\gamma})$ and $\Pi_2: L^2(\widehat{\gamma}) \rightarrow L^2(\widehat{\gamma})$, such that

$$[\Pi_1 \widehat{f}](\xi, \eta) = [\overline{\Pi}_1 \bar{f}_\eta](\xi), \quad [\Pi_2 \widehat{f}](\xi, \eta) = [\overline{\Pi}_2 \bar{f}_\xi](\eta).$$

Here \bar{f}_η and \bar{f}_ξ are parametrized univariate functions which are defined such that $\widehat{f}(\xi, \eta) = \bar{f}_\xi(\eta) = \bar{f}_\eta(\xi)$. Now the tensor product of the projections can be defined as $\Pi = \overline{\Pi}_1 \otimes \overline{\Pi}_2: L^2(\widehat{\gamma}) \rightarrow S^{p-1}$ by $\overline{\Pi}_1 \otimes \overline{\Pi}_2 = \Pi_1 \circ \Pi_2 = \Pi_2 \circ \Pi_1$.

Using the tensor product structure of S^{p-1} and the univariate projection property of $\bar{\Pi}_i$, a direct calculation shows that Π is the L^2 projection into S^{p-1} , i.e., the Fortin operator.

To show the Z stability, we apply the univariate stability properties on ‘slices’ of the domain, over which we then integrate using the Fubini–Tonelli formula. For a fixed $\bar{x}, \bar{y} \in (0, 1)$, we denote $I_{\bar{y}} = \{(x, \bar{y}) \in (0, 1)^2\}$ and $I_{\bar{x}} = \{(\bar{x}, y) \in (0, 1)^2\}$. First, for any $\bar{y} \in (0, 1)$, we have by the stability of the univariate projection:

$$\|\partial_{xy}\Pi_1\hat{w}\|_{L^2(I_{\bar{y}})} = \|\partial_x\Pi_1(\partial_y\hat{w})\|_{L^2(I_{\bar{y}})} \leq c\|\partial_y\hat{w}\|_{L^2(I_{\bar{y}})} + c\|\partial_{xy}\hat{w}\|_{L^2(I_{\bar{y}})},$$

where we will use $\hat{w} = \Pi_2\hat{v}$. Since the analogue result for Π_2 and any $\bar{x} \in (0, 1)$ also holds, and $\|f\|_{L^2(\hat{\gamma})}^2 = \int_0^1 \|f_y\|_{L^2(I_y)}^2 dy = \int_0^1 \|f_x\|_{L^2(I_x)}^2 dx$, we have

$$\|\partial_{xy}\Pi\hat{v}\|_{L^2(\hat{\gamma})}^2 \leq \int_{y \in I^2} \|\partial_y\Pi_2\hat{v}\|_{L^2(I_y)}^2 dy + \int_{y \in I^2} \|\partial_{xy}\Pi_2\hat{v}\|_{L^2(I_y)}^2 dy \leq c\|\hat{v}\|_Z^2,$$

i.e., the operator is Z stable.

The $Z - Z'$ stability of S_{zmv}^{p-1} can be concluded like in the univariate case, but with a tensor product-like projection onto S_{zmv}^{p-1} and the proof ends the same way as the case $d = 2$ using [32, Proposition 3.4.3]. \square

It remains to combine these preliminary results to prove the main theorem of this section. We use the bijectivity between the spline spaces of different degrees and integration by parts to estimate the inf-sup term by the equal order $p - 1$ stability which was estimated in Lemma 2.2.2.

Theorem 2.2.3. *Let $p \geq 2$ and the knot vectors Ξ_δ , $\delta = 1, \dots, d - 1$, be such that $S^p(\hat{\gamma}) \subset C^1(\hat{\gamma})$. The dual space \widehat{M}^2 satisfies*

$$\sup_{\hat{w} \in S_0^p} \frac{\int_{\hat{\gamma}} \hat{\mu} \hat{w} \, d\mathbf{x}}{\|\hat{w}\|_{L^2(\hat{\gamma})}} \geq c\|\hat{\mu}\|_{L^2(\hat{\gamma})}, \quad \hat{\mu} \in \widehat{M}^2,$$

with a constant c independent of the mesh size, but possibly dependent on p .

Proof. Given any $\hat{\mu}^{p-2} \in S^{p-2}$, we may introduce $\hat{g}^{p-1} \in S_{\text{zmv}}^{p-1}$, such that $D\hat{g}^{p-1} = \hat{\mu}^{p-2}$ and integration by parts yields

$$\sup_{\hat{w}^p \in S_0^p} \frac{\int_{\hat{\gamma}} \hat{w}^p \hat{\mu}^{p-2} \, d\mathbf{x}}{\|\hat{w}^p\|_{L^2(\hat{\gamma})}} = \sup_{\hat{w}^p \in S_0^p} \frac{\int_{\hat{\gamma}} \hat{w}^p D\hat{g}^{p-1} \, d\mathbf{x}}{\|\hat{w}^p\|_{L^2(\hat{\gamma})}} = \sup_{\hat{w}^p \in S_0^p} \frac{\int_{\hat{\gamma}} \hat{g}^{p-1} D\hat{w}^p \, d\mathbf{x}}{\|\hat{w}^p\|_{L^2(\hat{\gamma})}}.$$

We note that for $d = 3$ integration by parts must be performed for each direction. In both cases the boundary terms vanish due to the homogeneous boundary values of the space S_0^p .

Now, let us denote $\widehat{f}^{p-1} = \mathbf{D} \widehat{w}^p \in S_{\text{zmv}}^{p-1}$ and use the coercivity of the derivative:

$$\begin{aligned} \sup_{\widehat{w}^p \in S_0^p} \frac{\int_{\widehat{\gamma}} \widehat{g}^{p-1} \mathbf{D} \widehat{w}^p \, \mathbf{d}\mathbf{x}}{\|\widehat{w}^p\|_{L^2(\widehat{\gamma})}} &\geq \sup_{\widehat{w}^p \in S_0^p} c \frac{\int_{\widehat{\gamma}} \widehat{g}^{p-1} \mathbf{D} \widehat{w}^p \, \mathbf{d}\mathbf{x}}{\|\mathbf{D} \widehat{w}^p\|_{Z'}} \\ &= \sup_{\widehat{f}^{p-1} \in S_{\text{zmv}}^{p-1}} c \frac{\int_{\widehat{\gamma}} \widehat{f}^{p-1} \widehat{g}^{p-1} \, \mathbf{d}\mathbf{x}}{\|\widehat{f}^{p-1}\|_{Z'}}. \end{aligned}$$

Now, we make use of the $Z' - Z$ stability on the equal order pairing, as stated in Lemma 2.2.2. Since $\mathbf{D} \widehat{g}^{p-1} = \widehat{\mu}^{p-2}$, we have

$$\sup_{\widehat{f}^{p-1} \in S_{\text{zmv}}^{p-1}} c \frac{\int_{\widehat{\gamma}} \widehat{f}^{p-1} \widehat{g}^{p-1} \, \mathbf{d}\mathbf{x}}{\|\widehat{f}^{p-1}\|_{Z'}} \geq c \|\widehat{g}^{p-1}\|_Z \geq c \|\widehat{\mu}^{p-2}\|_{L^2(\widehat{\gamma})},$$

which yields the stated inf-sup condition. Note, that this proof is not restricted to the uni- and bivariate case, but can be applied to tensor products of arbitrary dimensions. \square

While we considered an inf-sup condition in the parametric space (2.2), the inf-sup condition of Assumption 2.1.5 needs to be fulfilled in the physical domain. From Theorem 2.2.3, the inf-sup stability in the physical space can be shown:

Theorem 2.2.4. *Let (2.2) holds and let $M_h^2 = \{\mu = \widehat{\mu} \circ \mathbf{F}_s^{-1}, \widehat{\mu} \in S^{p-2}(\widehat{\gamma})\}$, and $W_h = \{w = ((\widehat{w}/\widehat{W}_{\text{weight}}) \circ \mathbf{F}_s^{-1}), \widehat{w} \in S_0^p(\widehat{\gamma})\}$ be respectively the Lagrange multiplier space and the primal trace space given in the physical domain. Then, for sufficiently small h , the pairing $W_h - M_h^2$ fulfills a uniform inf-sup condition, i.e., for each $\mu \in M_h^2$, it holds*

$$\sup_{w \in W_h} \frac{\int_{\gamma} \mu w \, \mathbf{d}\gamma}{\|w\|_{L^2(\gamma)}} \geq c \|\mu\|_{L^2(\gamma)}.$$

The proof shown in [43, Theorem 13] makes use of a superconvergence argument to eliminate the (piecewise smooth) integration weight introduced by mapping from the geometry to the parametric space. A similar argument is made in [4] to show the inf-sup condition in a contact setting with a curved boundary, where the Lagrange multiplier is defined only in the normal direction.

Remark 2.2.5. *An analogue proof shows the stability of a pairing of order p and $p - 2k \geq 0$ for $k \in \mathbb{N}$. However, for $k > 1$ the dual approximation order in the L^2 norm ($p - 2k$) is very low and will reduce the convergence order*

drastically, i.e., to $(p - 2k + 3/2)$. Since for Signorini and contact problems, the regularity of the solution is usually bounded by $H^{5/2-\varepsilon}(\Omega)$, see, e.g., [161], low dual degrees might be reasonably used in these cases.

2.2.1.3 Choice 3: stable p/p pairing with boundary modification

The previous choices were motivated by Assumptions 2.1.5 and 2.1.6. While the first choice does not yield uniform stability, the second choice does not guarantee optimal order p convergence. Finally, we consider the natural equal order pairing in more detail. In the classical finite element context, it is well-known that the simple choice of taking the Lagrange multiplier space as the space of traces from the slave side leads to troubles at cross points for $d = 2$ and wirebaskets for $d = 3$, i.e., $(\cup_{l \neq j} \partial\gamma_l \cap \partial\gamma_j) \cup (\cup_l \partial\gamma_l \cap \partial\Omega_D)$. As a remedy, in the finite element method a modification is performed, see [27, 229], which we adapt to isogeometric analysis. This local modification ensures at the same time accuracy, see Assumption 2.1.6, and stability, see Assumption 2.1.5. The modification considered here results in a reduction of dimension of the dual space by reducing the degree in the neighborhood of the cross point (wirebasket).

We present the construction for the univariate case ($d = 2$), since the construction for the bivariate case ($d = 3$) can be done as a tensor product. For an open knot vector and the corresponding B-spline functions \hat{B}_i^p , we define the modified basis \tilde{B}_i^p , $i = 2, \dots, n - 1$ as follows

$$\tilde{B}_i^p(\zeta) = \begin{cases} \hat{B}_i^p(\zeta) + \alpha_i \hat{B}_1^p(\zeta), & i \in \{2, \dots, p + 1\}, \\ \hat{B}_i^p(\zeta), & i \in \{p + 2, \dots, n - p - 1\}, \\ \hat{B}_i^p(\zeta) + \beta_i \hat{B}_n^p(\zeta), & i \in \{n - p, n - 1\}. \end{cases}$$

The coefficients α_i and β_i are chosen such that the basis function is a piecewise polynomial of degree $p - 1$ on the corresponding element while retaining the inter-element continuity on $\hat{\gamma}$, i.e., as

$$\alpha_i = - \left(\hat{B}_i^p \right)^{(p)}(\zeta) / \left(\hat{B}_1^p \right)^{(p)}(\zeta), \quad \zeta \in (0, \zeta_2),$$

$$\beta_i = - \left(\hat{B}_i^p \right)^{(p)}(\zeta) / \left(\hat{B}_n^p \right)^{(p)}(\zeta), \quad \zeta \in (\zeta_{E-1}, 1).$$

Note that the coefficients are well-defined since \hat{B}_i^p is a polynomial of degree p on one single element. Figure 2.4 shows an example for degree $p = 3$. We see that the basis functions may lose the positivity on the boundary element, but the construction guarantees that the resulting basis forms a partition of unity.

A recursive algorithms for the evaluation exists, since derivatives of B-spline functions are a combination of lower order B-spline functions, see [56, Section 2.1.2.2]. With this recursive formula it can easily be seen that the coefficients are uniformly bounded under the assumption of quasi-uniform meshes. Then, we define the space of equal order Lagrange multipliers as $\widehat{M}^0 = \text{span}_{2, \dots, n-1} \{\widetilde{B}_i^p\}$.

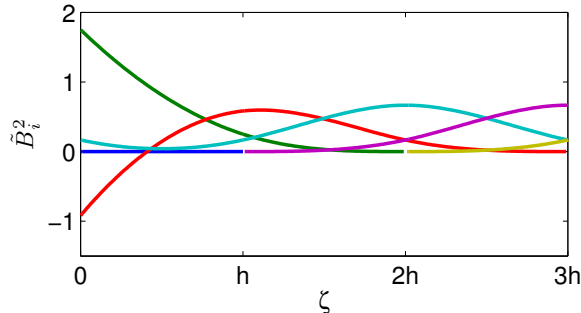


Figure 2.4: Boundary modification of a spline of degree 3 for $d = 2$, left modification.

Theorem 2.2.6. *Assumption 2.1.6 holds for the dual space \widehat{M}^0 .*

Proof. Since the space of global polynomials of degree $p - 1$ is contained in the dual space \widehat{M}^0 , we can directly argue as in [21, Section 3]. \square

2.2.2 Numerical results

In this section, we apply isogeometric mortar methods to four examples, in order to validate its optimality and enlighten some additional practical aspects. All our numerical results were obtained on a Matlab code, which is based on the isogeometric toolbox GeoPDEs, [60, 219]. In the following we denote the pairing with primal degree p and dual degree q by P p -P q . The first example is a multi-patch NURBS geometry with a curved interface, solving the equations of linear elasticity. The computed primal and dual error rates are optimal for different considered pairings. Although NURBS are capable of exactly representing many geometries, it is not always possible to have a matching interface between subdomains. For this reason in the second example, we introduce an additional variational crime by a geometry approximation. It can be seen, that the proposed method is robust with respect to a non-matching interface. In the third example, the effect on the Lagrange multiplier of an unstable pairing is considered. The last example shows the behavior in case of non-linear elasticity, where a common benchmark is adapted to a bimaterial compression test.

2.2.2.1 A linear elasticity problem

As the first example, we apply the presented method to an example of plane strain linear elasticity, see Remark 2.1.4. We consider the problem of an infinite elastic plate with a circular hole subjected to tension loading in $x = -\infty$ and $x = +\infty$, similar to the one considered in Section 1.2.1.2. Based on the symmetric setting, only a quarter of the plate is considered. This setting, which has an analytical solution, [212], is a typical benchmark in isogeometric analysis since NURBS offer the possibility to exactly represent the geometry. However, it cannot be parametrized smoothly as a single patch, so it is convenient to consider it in a multi-patch.

The domain $\Omega = \{(x, y) \in (0, 2)^2 : x^2 + y^2 > 0.04\}$ is shown in Figure 2.5 and we apply the exact traction on $\Gamma_N = \{2\} \times (0, 2) \cup (0, 2) \times \{2\}$, symmetry conditions on $\Gamma_{\text{symm}} = \{0\} \times (0, 2) \cup (0, 2) \times \{0\}$ and homogeneous Dirichlet conditions on $\Gamma_D = \{(x, y) \in (0, 2)^2 : x^2 + y^2 = 0.04\}$.

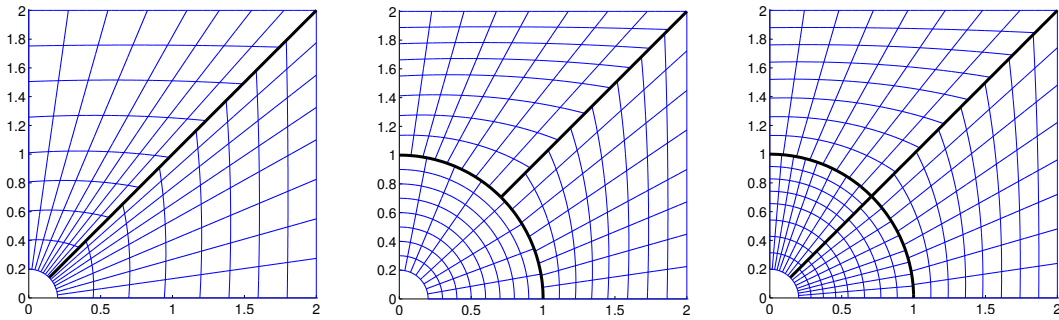


Figure 2.5: Different parametrizations of the infinite plate with a hole. From left to right: 2, 3 and 4 subdomains.

Let us consider three different parametrizations of this test, see Figure 2.5. Two geometrically conforming cases have 2 and 4 patches. In the four patch situation, the four interfaces intersect in a cross-point and the boundary modification of the dual space is required. In addition, we consider a slave conforming case consisting of 3 patches for which the boundary modification is necessary for the same degree pairing. In each case, the results are compared to the analytical solution. A numerical convergence study is presented in Figure 2.6 for a primal degree $p = 4$ and the corresponding stable reduced degrees.

In the left column of Figure 2.6 we see that the broken V error of the primal variable remains optimal for the pairings introduced in Section 2.2.1, i.e., for P4-P4 and P4-P2. A severely slower convergence is observed for P4-P0, as it is expected by the theory since the dual approximation order of Assumption 2.1.6 is too low.

We note that in two cases we observe a better convergence than expected

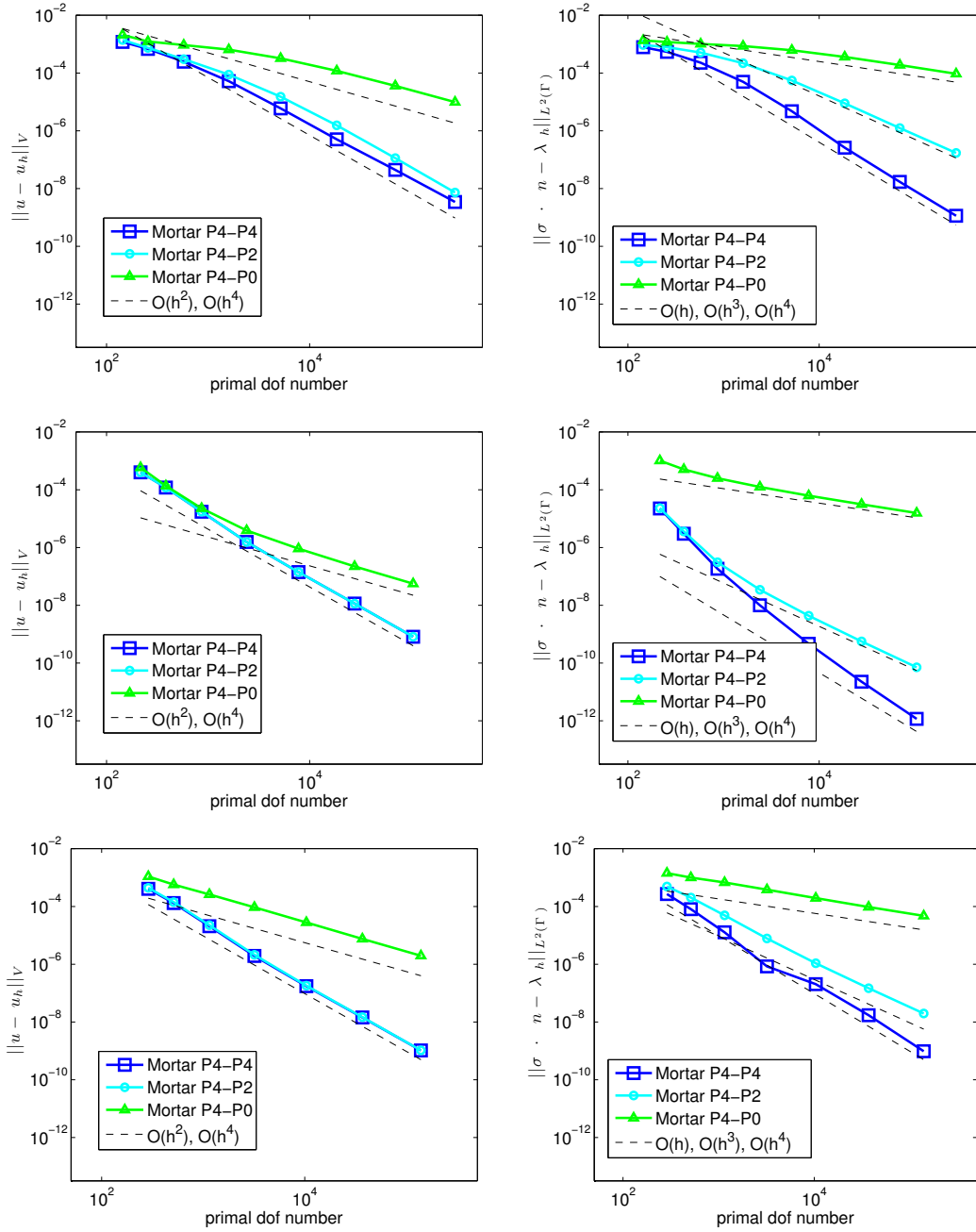


Figure 2.6: Left: Broken V primal error curves. Right: L^2 dual error curves. Respectively from the top to the bottom, for the 2, 3 and 4 patch parametrizations, for several pairings.

from Theorem 2.1.7: for the primal variable with the P4-P2 pairing and for the Lagrange multiplier with the P4-P4 pairing. From the theory we were expecting a reduced order for the primal variable in the broken V norm with the pairing P4-P2. However, numerically we obtain a better order. This observation was also made in several examples of [43]. Theorem 2.1.7 indicates that for this case a \sqrt{h} is lost in the convergence order, which is not observed in our situation. Closer investigations reveal, that the loss of a \sqrt{h} can typically be observed in situations where the slave mesh is considerably coarser than the master mesh. See also [197, Section 5.1] for similar observations with a primal degree 2 and biorthogonal basis functions of the approximation order 0.

Under sufficient regularity in Theorem 2.1.7 a gap remains between the convergence order of the Lagrange multiplier and its approximation order in the equal order case. As noted earlier the gap could be closed for standard finite elements in [158]. Here we obtain the best approximation rates for the L^2 error of the dual variable for all pairings.

2.2.2.2 A scalar problem on a two patch domain with a non-matching interface

Let us consider the standard Poisson equation solved on the unit square $\Omega = (0, 1)^2$, which is decomposed into two patches presented in Figure 2.7. As the subdomains cannot exactly be represented by the chosen spline spaces for the geometry approximation, the subdomains do not match at the interface, see Figure 2.7. This geometry approximation introduces an additional variational crime to the weak formulation.

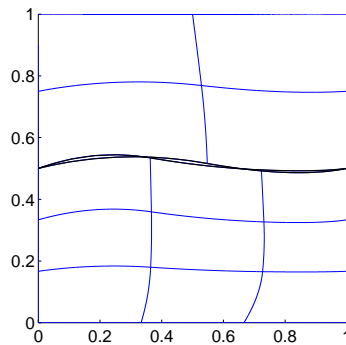


Figure 2.7: Non-conforming mesh with a non-matching interface.

The internal load and the boundary conditions have been manufactured to have the analytical solution $u(x, y) = \sin(5y) \sin(6x)$. Firstly, to measure

the influence of the geometrical approximation on the accuracy of the mortar method, we consider the same degree pairing in a setting, which requires no boundary modification. This is granted by setting homogeneous Neumann conditions on $\Gamma_N = \{0, 1\} \times (0, 1)$ and Dirichlet conditions on the remaining part $\Gamma_D = \partial\Omega \setminus \Gamma_N$. Figure 2.8, shows the numerically obtained error decay in the L^2 norm. For an equal order p pairing, we observe an optimal convergence order of $p + 1$ for the L^2 error in the primal variable. These optimal L^2 rates are in accordance with the theory of finite element methods, see [145]. We also compare the primal error of a matching and non-matching geometry. As Figure 2.8 shows, no significant quantitative difference can be observed in the asymptotic convergence order. Moreover, as in the previous example, we observe a higher rate than expected from Theorem 2.1.7.

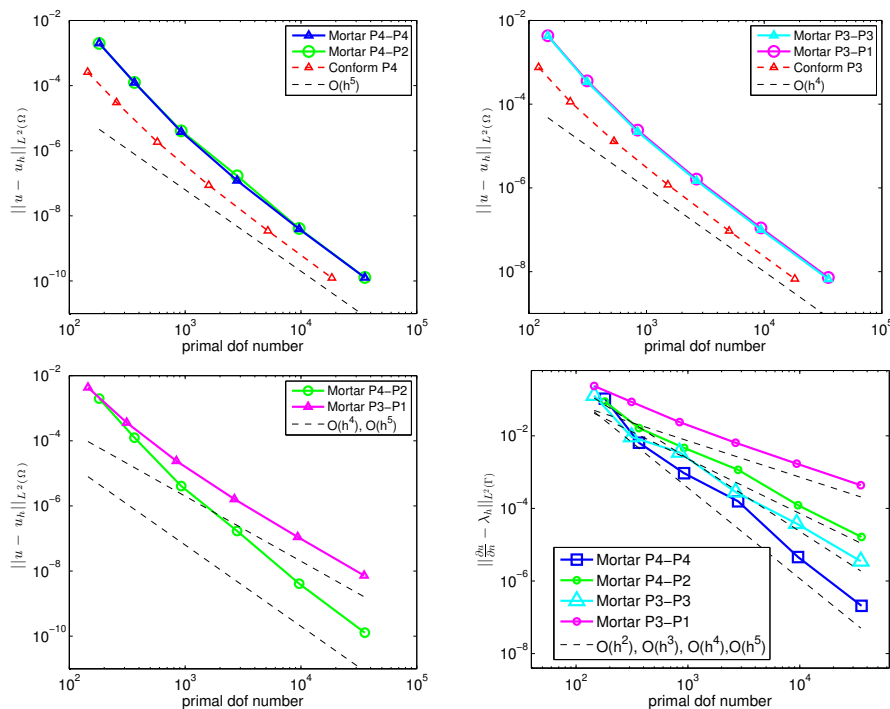


Figure 2.8: Several L^2 error curves. Top left: Primal error for stable pairings of primal degree $p = 4$. Top right: Primal error for stable pairings of primal degree $p = 3$. Bottom left: Direct comparison of the primal error for pairings P4-P2 and P3-P1. Bottom right: Dual error for stable pairings of primal degree $p = 3$ and $p = 4$.

To conclude, this example shows that the influence of the additional geometry error in the mortar method context is quite small. We note that recently, the coupling of non-matching interfaces with even larger gaps gained attention, e.g., in [106, 107].

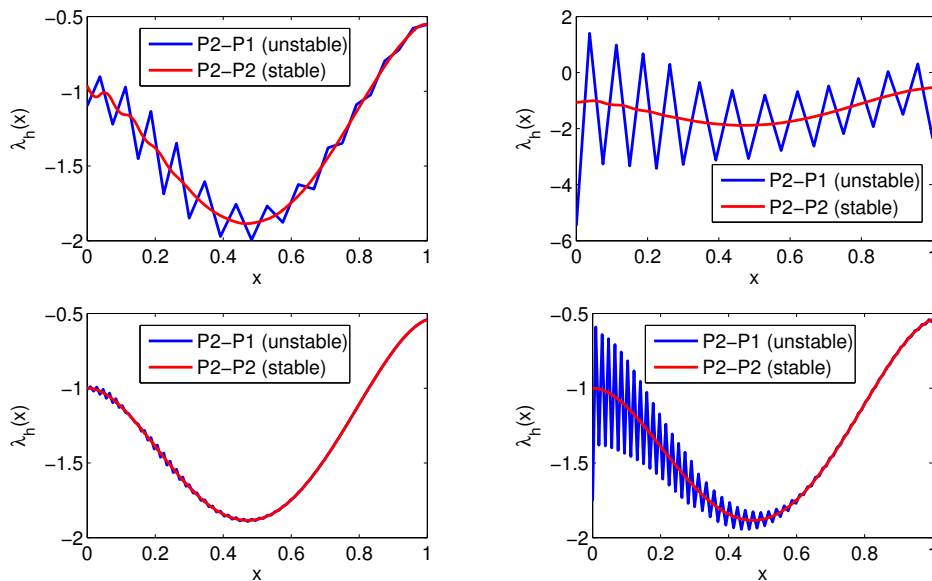


Figure 2.9: Discrete Lagrange multiplier. Left: Dirichlet-Neumann problem. Right: Pure Dirichlet problem. Top: Mesh level 3 ($h = 1/16$). Bottom: Mesh level 5 ($h = 1/64$).

2.2.2.3 The influence of the unstable $p/p - 1$ pairing

Let us now consider the $p/p - 1$ pairing on a simple setting to illustrate the effects of the instability. We solve the Poisson equation on the unit square, decomposed into two patches by the interface $(0, 1) \times \{1/2\}$. The internal load and the boundary conditions are applied such that the analytical solution is $u(x, y) = (\cos(x) + 16x^2(1 - x)^2) \exp(y - 1/2)$. On the boundary parallel to the interface, we apply Dirichlet conditions. On the remaining part, we compare two different cases: firstly Neumann conditions and secondly Dirichlet conditions, i.e., then the problem is a pure Dirichlet problem.

Starting from a coarse initial mesh, we refine uniformly and focus on the Lagrange multiplier. In Figure 2.9, we show numerical results for the pairing P2-P2 and P2-P1. We note that the latter one was observed to be unstable in Section 2.2.1.1, with an inf-sup constant of order $\mathcal{O}(h)$. Spurious oscillations induced by the lack of a uniform inf-sup stability are clearly observed in the P2-P1 case. The oscillations are remarkably stronger for the pure Dirichlet problem than for the Dirichlet-Neumann problem. We point out that the primal space in case of the pure Dirichlet problem is smaller than in the other case, while for the P2-P1 case the dual space is the same in both cases. This additionally reduces the inf-sup constant and yields larger spurious oscillations visible in the right pictures of Figure 2.9. In contrast, for the P2-P2 pairing

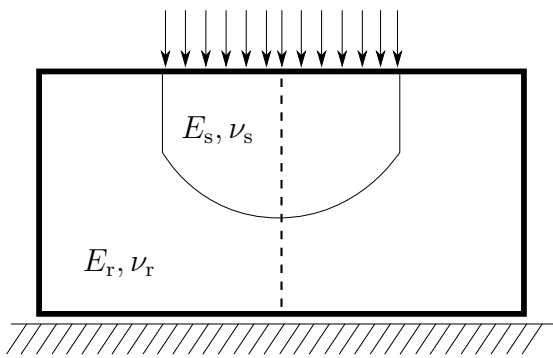


Figure 2.10: Setting and symmetry of the compressed bimaterial block.

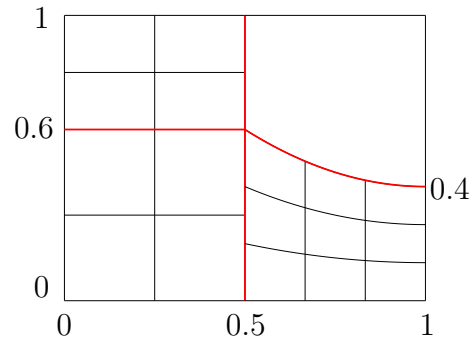


Figure 2.11: Isogeometric initial grid of the left half of the block with four patches and four interfaces marked in red.

a cross point modification as introduced in Section 2.2.1.3 is applied, which preserves the uniform stability.

2.2.2.4 Non-linear compression test of a bimaterial

After some examples with linear equations, we now evaluate the performance for finite elasticity. We adapt a frequently used benchmark problem and consider an nearly incompressible block, which is compressed by a steel punch, which is pushed into the block $\Omega = (0, 20) \times (0, 10)$ (all dimensions in mm with a virtual thickness of 1 mm) by a pressure $\hat{p} = 300$ MPa. The horizontal degrees of freedom on the top of the block as well as the vertical degrees of freedom on the bottom of the block are restricted to zero. The remaining boundary degrees of freedom are not restricted, i.e., homogeneous Neumann boundaries. The punch has a parabola shaped bottom and is described by

$$\Omega_s = \left\{ (x, y) \in \mathbb{R}^2 : 5 < x < 15, \quad \frac{2}{25}(x_1 - 10)^2 + 4 < y < 10 \right\}.$$

The material data are $E_r = 240.565$ MPa, $\nu_r = 0.49$ for $\Omega \setminus \overline{\Omega}_s$ and $E_s = 200\,000$ MPa, $\nu_s = 0.285$ on Ω_s . See Figure 2.10 for an illustration of the setting.

For the computation, we exploit the symmetry and consider the computational domain $\Omega = (0, 10)^2$ with symmetry boundary conditions on the boundary $x_1 = 10$, i.e., $\mathbf{u}^\top \mathbf{N} = 0$, $\mathbf{P}(\text{Id} + \text{Grad } \mathbf{u})\mathbf{N}^\top \mathbf{N} = 0$.

We consider a bimaterial of two Neo-Hooke materials, see (1.9). Based on

the introduction in Section 1.2.4, we define the broken non-linear form of finite elasticity

$$a(\mathbf{u}, \mathbf{v}) = \sum_{k=1}^K \int_{\Omega_k} \mathbf{P}(\text{Id} + \text{Grad } \mathbf{u}) : \text{Grad } \mathbf{v} \, dx.$$

With this form, which is linear in the second argument, we solve the analogue saddle-point problem to (2.1):

$$\begin{aligned} a(\mathbf{u}_h, \mathbf{v}_h) + b(\mathbf{v}_h, \boldsymbol{\lambda}_h) &= f(\mathbf{v}_h), \quad \mathbf{v}_h \in \mathbf{V}_h, \\ b(\mathbf{u}_h, \boldsymbol{\mu}_h) &= 0, \quad \boldsymbol{\mu}_h \in \mathbf{M}_h. \end{aligned}$$

The non-linear equation is solved in several load-steps and with a Newton-iteration. We note that during the Newton-iteration for the saddle-point system only the block related to the non-linear form $a(\cdot, \cdot)$ needs to be recomputed. The coupling parts, related to the bilinear form $b(\cdot, \cdot)$, are kept constant within the Newton iteration, as we evaluate the coupling on the reference domain and not on the deformed domain.

We consider a sequence of uniformly refined meshes consisting of the four spline patches shown in Figure 2.11 that are weakly coupled over four interfaces. The initial mesh takes into account the curved interface precisely and the local mesh size is adapted to the different materials as well as the expected deformation, see Figure 2.11. The deformed body with the stress distribution is shown in Figure 2.12. We note a stress singularity at the corner of the steel inclusion, see also [192].

We evaluate the convergence of equal order isogeometric mortar methods with $p = 2, 3, 4$ by evaluating the vertical displacement on the midpoint of the initial configuration $\mathbf{A} = (10, 10)$. As the reference value, we extrapolate the result of quartic splines on the finest grid: $u_2^{\text{ex}}(\mathbf{A}) \approx -1.82878$. The convergence of the vertical displacement can be seen in Figure 2.13. In addition, the vertical displacement and the relative error on the first four meshes are tabulated in Table 2.1. Extra to the isogeometric computations, as a reference, a computation using linear and quadratic finite elements was performed using the parallel finite element software M++ [223]. The finite element computation is based on a conforming mesh with a piecewise linear approximation of the curved interface. We see a significant advantage of the isogeometric mortar formulation compared to the standard finite element method. While the higher isogeometric degrees yield a slightly better error per degree of freedom, the convergence rate is not improved due to the reduced regularity of the bimaterial problem.

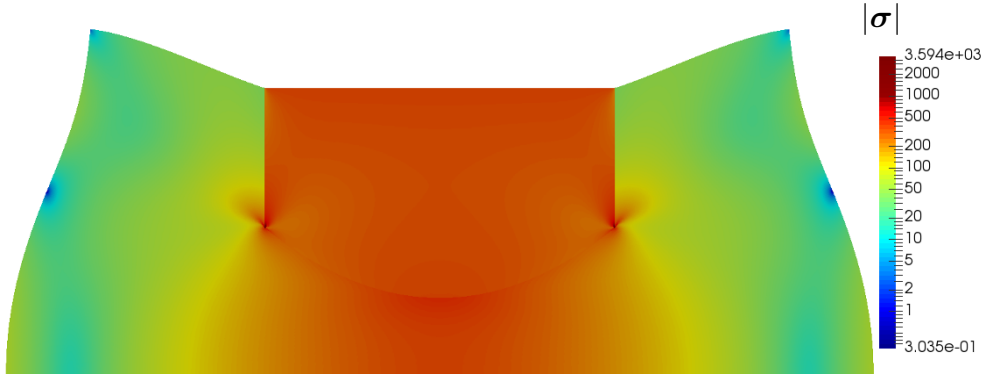
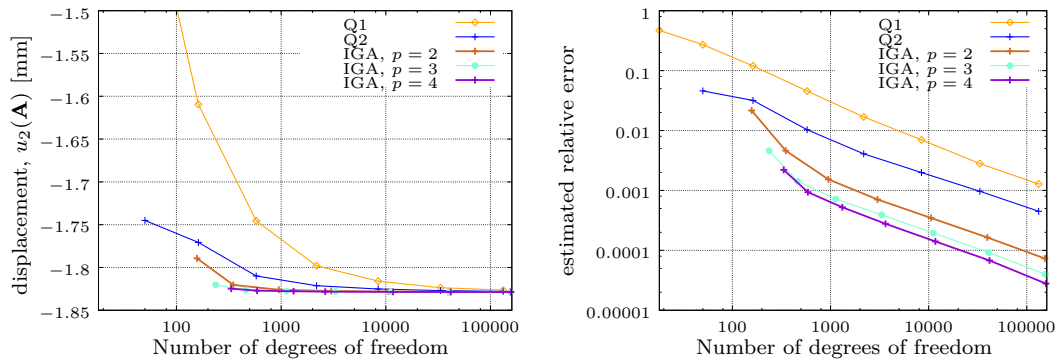

 Figure 2.12: Compressed bimaterial block with stress distribution $|\sigma|$.

 Figure 2.13: Vertical displacement at the control point \mathbf{A} and the estimated relative error $|u_2(\mathbf{A}) - u_2^{\text{ex}}(\mathbf{A})|/|u_2^{\text{ex}}(\mathbf{A})|$ with $u_2^{\text{ex}}(\mathbf{A}) \approx -1.82878$.

Table 2.1: Vertical displacement evaluated on the first four grid levels and the estimated relative error.

		initial mesh	mesh lvl 1	mesh lvl 2	mesh lvl 3
$p = 2$	ndof	157	349	949	3013
	$u_2(\mathbf{A})$	-1.789343	-1.820342	-1.825976	-1.827490
	rel. error	2.156e-2	4.614e-3	1.533e-3	7.057e-4
$p = 3$	ndof	237	461	1125	3317
	$u_2(\mathbf{A})$	-1.820397	-1.826188	-1.827464	-1.828065
	rel. error	4.584e-3	1.417e-3	7.195e-4	3.910e-4
$p = 4$	ndof	333	589	1317	3637
	$u_2(\mathbf{A})$	-1.824751	-1.827070	-1.827821	-1.828272
	rel. error	2.203e-3	9.351e-4	5.244e-4	2.778e-4

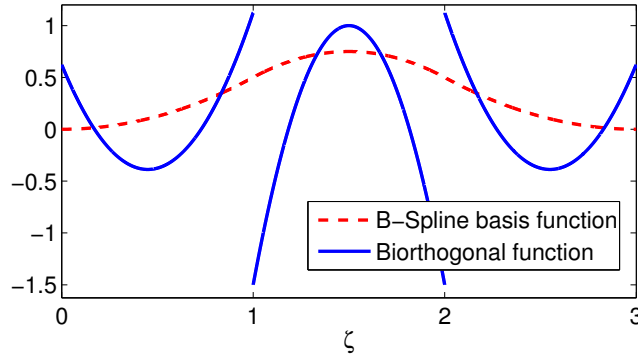


Figure 2.14: A quadratic basis function and its corresponding (rescaled) biorthogonal basis function with the same support.

2.3 Biorthogonal basis functions

An alternative concept to the previously considered trace spaces are biorthogonal basis functions. The potential of the use of biorthogonal basis functions was already identified and briefly discussed in [43], but no details were worked out. A Lagrange multiplier basis $(\psi_i)_i$ is called biorthonormal, if it fulfills

$$\int_{\gamma} N_i^p(\mathbf{x}) \psi_j(\mathbf{x}) \, d\gamma = \delta_{ij} \int_{\gamma} N_i^p(\mathbf{x}) \, d\gamma.$$

Of special interest, are biorthogonal basis functions which span on each element the same space as the primal basis and have a local support. The inf-sup condition stated in Assumption 2.1.5 is fulfilled, see [138, Remark 2.11]. A straightforward construction of such a biorthogonal basis with $\text{supp } N_i^p = \text{supp } \psi_i$ is easily possible by an inversion of a mass matrix on each element, see Figure 2.14 for a primal quadratic basis function and its corresponding biorthogonal basis function. These basis functions proved to be advantageous for contact problems, which have a reduced regularity, but not for domain decomposition purposes, see [197]. The reason is that the standard dual basis does only have reproduction properties of order zero, i.e., it cannot reproduce any polynomials besides constant ones. As a consequence the approximation property stated in Assumption 2.1.6 is not given and the convergence order in Theorem 2.1.7 will be drastically reduced.

In the following, we present a more involved construction, which allows us to control the polynomial reproduction by enlarging the support of the basis function. The foundation of the construction is a collection of discontinuous functions, which are orthogonal to the whole primal basis. A specific combina-

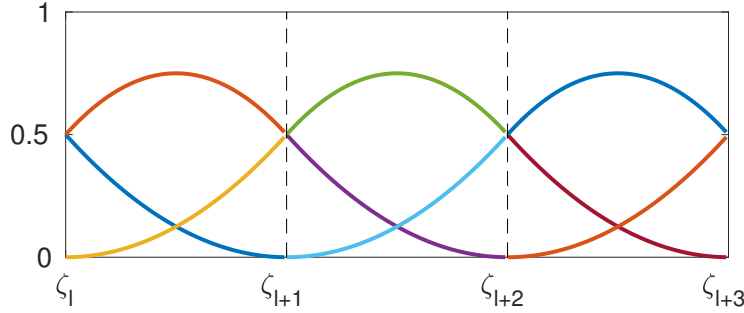


Figure 2.15: Construction of the broken space W_h^{-1} from the primal space W_h for $p = 2$.

tion of these orthogonal functions allows us to gain polynomial reproduction, while keeping the support local.

2.3.1 Construction with higher order approximation property

We restrict ourselves to the one-dimensional construction, since multivariate biorthogonal basis functions can be constructed by a tensor product structure. However it should be noted that the biorthogonality of tensor product splines only holds on the parametric domain and with respect to the standard L^2 scalar product. To use the biorthogonal basis for three-dimensional problems, we can formulate the mortar coupling with respect to the parametric space, instead of the exact geometry as before.

Without loss of generality, we consider the unit interval $\gamma = (0, 1)$. Let W_h be a B-spline space of degree p on γ with the break points $0 = \zeta_1 < \zeta_2 < \dots < \zeta_E = 1$ and the basis $(\hat{B}_i^p)_{i=1, \dots, n}$, where $n = \dim W_h$. NURBS and the weight of a geometry transformation can be included in the considered L^2 scalar product.

We use the construction described in [169], which only slightly needs to be adapted to splines. Instead of the purely algebraic construction introduced there, we consider an equivalent functional setting.

In addition to W_h , we consider a broken polynomial space:

$$W_h^{-1} = \{v \in L^2(0, 1) : v|_{(\zeta_i, \zeta_{i+1})} \in \mathbb{P}_p\}$$

of dimension $N = \dim W_h^{-1} = (E - 1)(p + 1)$. We note that, besides possible Dirichlet boundary conditions, the broken space W_h^{-1} is obtained by breaking apart the spline space W_h . See Figure 2.15 for an illustration of the broken space.

We seek dual basis functions $\psi_j \in W_h^{-1}$ satisfying biorthogonality:

$$\int_{\gamma} \widehat{B}_i^p \psi_j \, dx = \delta_{ij},$$

as well as polynomial reconstruction of degree q . Polynomial reproduction holds exactly if the quasi-interpolation

$$Qf = \sum_{i=1}^n (f, \widehat{B}_i^p)_0 \psi_i \quad (2.3)$$

is invariant for polynomials $p \in \mathbb{P}_q$, i.e., $Qp = p$.

Since $W_h \subset W_h^{-1}$, we can extend the B-spline basis $(\widehat{B}_i^p)_{i=1,\dots,n}$ of W_h to a basis $(\varphi_i)_{i=1,\dots,N}$ of W_h^{-1} , such that $\varphi_i = \widehat{B}_i^p$ for $i \leq n$. To retain a local support, we suggest the following construction:

The basis is build using an auxiliary decomposition of W_h^{-1} into n subspaces, related to the primal basis functions. Each basis function \widehat{B}_i^p is supported on $n_i \leq p+1$ elements. Restricting \widehat{B}_i^p to each of these elements yields the n_i parts $\widehat{B}_{i,j}^p \in W_h^{-1}$ (each supported on a single element), such that $\widehat{B}_i^p = \sum_{j=1}^{n_i} \widehat{B}_{i,j}^p$. We collect the local contributions $W_{h,i}^{-1} = \text{span}\{\widehat{B}_{i,j}^p: j = 1, \dots, n_i\}$ and note that $W_h^{-1} = \bigoplus_{i=1}^n W_{h,i}^{-1}$. The collection of $\widehat{B}_{i,j}^p$ forms a basis of W_h^{-1} , but the basis does not include the original B-splines as desired. Therefore we construct another basis as follows.

For $i = 1, \dots, n$, we extend \widehat{B}_i^p by $n_i - 1$ basis functions $\phi_{i,j}$ to a basis of $W_{h,i}^{-1}$, which guarantees $\text{supp } \phi_{i,j} \subset \text{supp } \widehat{B}_i^p$. We note that we do not require the basis to be orthogonal but a good condition number of the basis is advantageous for the numerical computations. Combining these local basis functions yields the desired basis of W_h^{-1} :

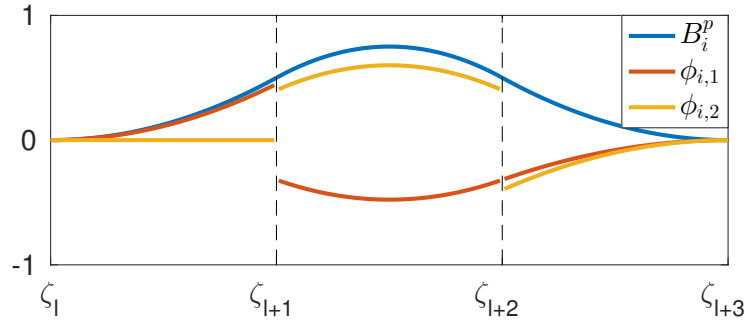
$$(\varphi_i)_{i=1,\dots,N} = (\widehat{B}_1^p, \dots, \widehat{B}_n^p, (\phi_{1,j})_{j=1,\dots,n_1-1}, \dots, (\phi_{n,j})_{j=1,\dots,n_n-1}).$$

See Figure 2.16 for an illustration of a possible realization of the local basis $(\widehat{B}_i^p, (\phi_{i,j})_{j=1,\dots,n_i-1})$ for a fixed $i \in \{1, \dots, n\}$. In the case of Dirichlet conditions on the space W_h , the corresponding basis functions must additionally be reincluded in the basis of W_h^{-1} .

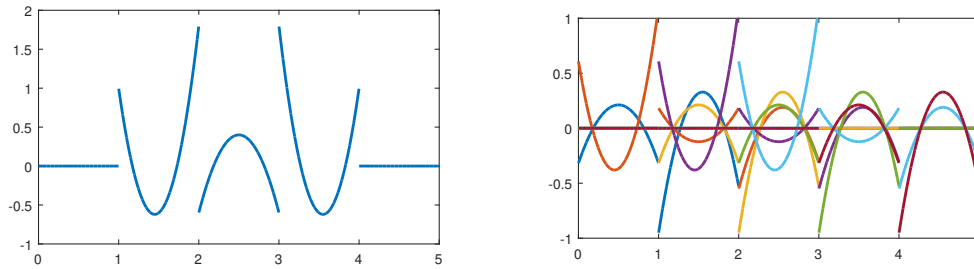
By a local inversion of the mass matrix, we can construct a dual basis $\tilde{\psi}_i$ on W_h^{-1} , biorthogonal to the recently constructed primal basis $(\varphi_i)_{i=1,\dots,N}$:

$$\int_{\gamma} \tilde{\psi}_i \varphi_j \, dx = \delta_{ij}.$$

See Figure 2.17 for an illustration of $\tilde{\psi}_i$ for $i = 1, \dots, n$, which is biorthogonal


 Figure 2.16: Local basis contribution based on the B-spline \widehat{B}_i^p for $p = 2$.

to \widehat{B}_i^p and $\widetilde{\psi}_j$ for $j > n$, which is orthogonal to all \widehat{B}_i^p .


 Figure 2.17: Orthogonal basis function with same support (left) and basis functions orthogonal to all N_i (right) for $p = 2$.

Clearly for any choice of $(z_{ki})_{k,i}$,

$$\psi_i = \widetilde{\psi}_i + \sum_{k=n+1}^N z_{ki} \widetilde{\psi}_k, \quad \text{for } i = 1, \dots, n, \quad (2.4)$$

is a biorthogonal basis to $(\widehat{B}_i^p)_{i=1, \dots, n}$.

We can choose z_{ki} for $k = n+1, \dots, N$ and $i = 1, \dots, n$ such that polynomial reconstruction holds and a local support is preserved.

Polynomial reconstruction of degree q holds if the quasi-interpolation (2.3) is invariant for polynomials $p \in \mathbb{P}_q$, i.e.,

$$(p, \varphi_j)_0 = \sum_{i=1}^n (p, \widehat{B}_i^p)_0 (\psi_i, \varphi_j)_0, \quad \text{for any } j = 1, \dots, N, \quad p \in \mathbb{P}_q.$$

For $j = 1, \dots, n$ it holds $\varphi_j = \widehat{B}_j^p$ and we may use the biorthogonality of ψ_i

and φ_j :

$$\sum_{i=1}^n (p, \widehat{B}_i^p)_0 (\psi_i, \varphi_j)_0 = \sum_{i=1}^n (p, \widehat{B}_i^p)_0 \delta_{ij} = (p, \varphi_j)_0.$$

For $j = n + 1, \dots, N$, biorthogonality cannot be directly used due to the modification of the basis ψ :

$$\sum_{i=1}^n (p, \widehat{B}_i^p)_0 (\psi_i, \varphi_j)_0 = \sum_{i=1}^n (p, \widehat{B}_i^p)_0 \left(\tilde{\psi}_i + \sum_{k=n+1}^N z_{ki} \tilde{\psi}_k, \varphi_j \right)_0 = \sum_{i=1}^n (p, \widehat{B}_i^p)_0 z_{ji}.$$

To sum up, it remains to solve

$$\sum_{i=1}^n (p, \widehat{B}_i^p)_0 z_{ji} = (p, \varphi_j)_0, \quad \text{for } z_{ji}, \quad i = 1, \dots, n, \quad j = n + 1, \dots, N.$$

As for each $j = n + 1, \dots, N$ these are $q + 1$ conditions to solve for n values of z (with $n \gg q + 1$ on a sufficiently fine mesh), we have some flexibility in the choice of the unknown z . This flexibility allows us to choose z sparsely, such that the resulting basis functions have a local support.

For a fixed $\hat{j} = n + 1, \dots, N$, let us choose an index set $\mathcal{I}(\hat{j})$ with $|\mathcal{I}(\hat{j})| = q + 1$, and set $z_{\hat{j}i} = 0$ for $i \notin \mathcal{I}(\hat{j})$. Then it remains to solve the square linear equation system

$$\sum_{i \in \mathcal{I}(\hat{j})} (p, \widehat{B}_i^p)_0 z_{\hat{j}i} = (p, \varphi_{\hat{j}})_0, \quad p \in \mathbb{P}_q. \quad (2.5)$$

Although the equation system is split into parts, we do not solve for one dual basis function with each system. Instead, we can choose which dual basis functions shall be influenced by $\tilde{\psi}_{\hat{j}}$. We note this already by looking at the dimensions. We solve $N - n$ equation systems of dimension $(q + 1) \times (q + 1)$, each one defining n values of z .

Leaving apart the special case, where $z_{\hat{j}i} = 0$ appears in the solution of (2.5), we can see the support of ψ_i by the choice of the index sets. With (2.4), any j with $i \in \mathcal{I}(j)$ yields $\text{supp } \tilde{\psi}_j \subset \text{supp } \psi_i$ and we can estimate the support of ψ_i indirectly.

As an example, let us consider the reproduction order $q = p$ and for simplicity no repeated knots. For any $\psi_{\hat{j}}$, we consider the mid-element of its support. If the function is supported on an even number of elements, we arbitrarily choose the mid-element closer to the boundary. The indices of all $p + 1$ basis functions \widehat{B}_i^p that are non-zero on this element are considered in $\mathcal{I}(\hat{j})$. This way the support of each biorthogonal basis functions contains maximal $2p + 1$ elements, compared to $p + 1$ elements of the primal function. Assumption 2.1.6 is fulfilled by construction, yielding optimal convergence rates by

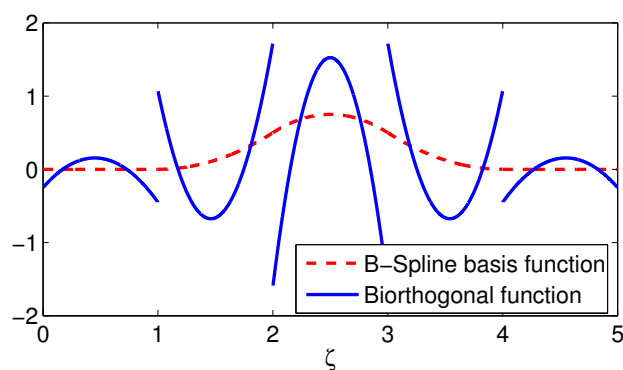


Figure 2.18: A quadratic basis function and its corresponding (rescaled) biorthogonal basis function with a local support and optimal approximation properties.

Theorem 2.1.7. See Figure 2.18 for an example with $p = 2$ and compare with the straightforward construction of Figure 2.14.

2.3.2 Numerical results

We test the newly constructed biorthogonal basis in a systematical convergence test. We consider two geometries, a square domain and a curved annulus, each one being divided into two subdomains. Two analytically known solutions are defined, one solving the Poisson problem, the other one the equation of linear elasticity and we consider spline spaces of degree 2, 3 and 4. Additionally, the ratio of the master and slave mesh sizes is investigated by considering three cases. In two cases the ratio between the mesh sizes on the two subdomains is $3 : 2$, in case (a) the slave mesh is finer, in case (b) the master mesh. In the third case, (c), the mesh size ratio is approximately one. See Figure 2.19 for the initial mesh of all cases.

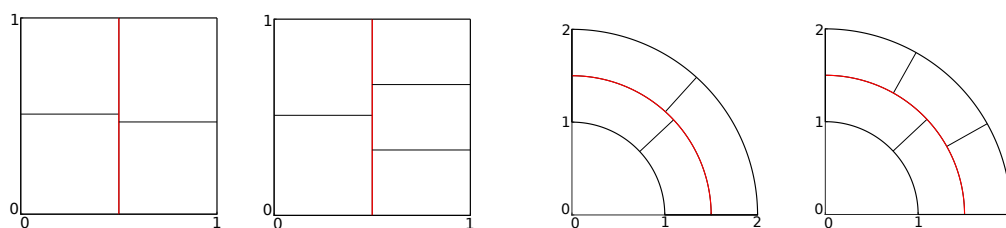


Figure 2.19: Initial meshes. Left: Square with mesh size ratio $\approx 1 : 1$ (c) and $2 : 3$ (a,b). Right: Annulus with mesh size ratio $\approx 1 : 1$ (c) and $2 : 3$ (a,b).

The manufactured solution for the Poisson problem is

$$u(x, y) = \sin(2\pi(x - 0.33)) \cos(2\pi y),$$

with $f = -\Delta u$ and the exact trace as Dirichlet boundary conditions.

The solution for elasticity is manufactured, based on the solution for the infinite plate with hole. To avoid a radial symmetric solution, we slightly shift the function. With $r^2 = (x + 0.5)^2 + y^2$ and $\theta = \arctan(y/(x + 0.5))$:

$$\mathbf{u} \begin{pmatrix} r \cos(\theta) \\ r \sin(\theta) \end{pmatrix} = \begin{pmatrix} \cos(\theta)u_r(r, \theta) - \sin(\theta)u_\theta(r, \theta) \\ \sin(\theta)u_r(r, \theta) + \cos(\theta)u_\theta(r, \theta) \end{pmatrix},$$

with u_r, u_θ as in (1.6). See Figure 2.20 for the stress distribution of the solution on the annulus domain.

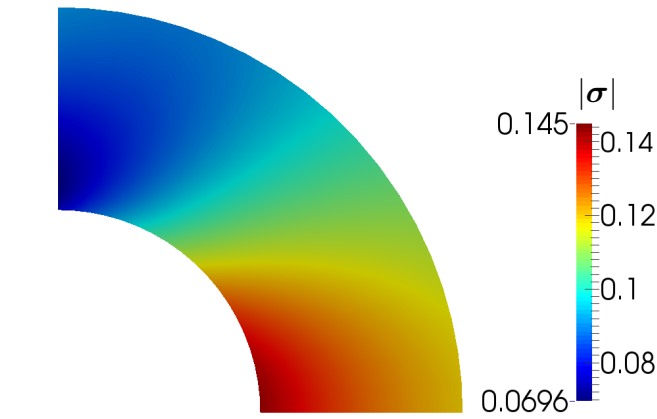


Figure 2.20: Stress magnitude of the elasticity equation on the annulus.

In all cases, the result of a biorthogonal dual basis is compared to a standard equal order pairing as a reference computation. We consider convergence in the $H^1(\Omega)$ error, but note that the $L^2(\Omega)$ errors behave similar in all considered cases. For the square geometry, the convergence rates are shown in Figure 2.21. We see optimal convergence rates in all considered cases. However, for the biorthogonal basis, we observe a slightly larger error in the pre-asymptotics of the Poisson equation, in the case where the slave mesh is coarse in comparison to the master mesh. The effect gets larger with increasing polynomial degree, but the difference between the error curves vanishes with more mesh refinements. For the example of elasticity, no difference in the six shown curves can be noticed.

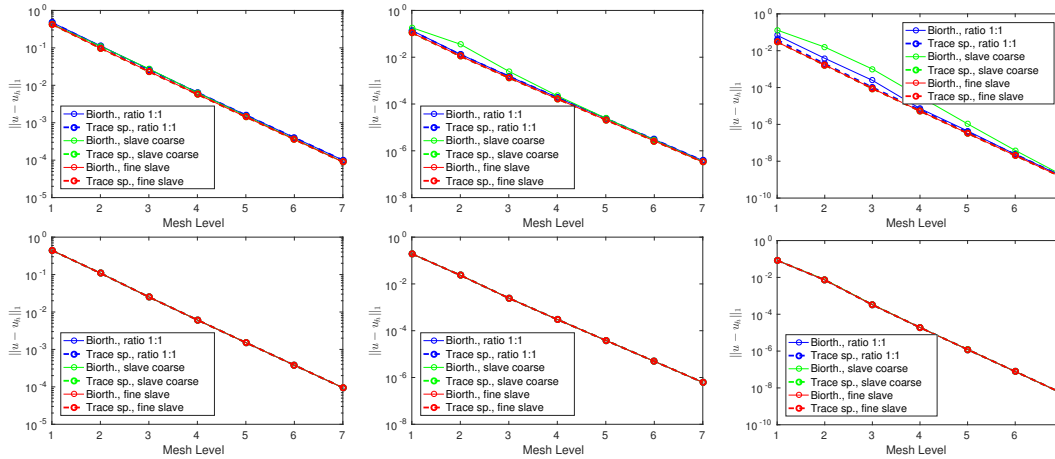


Figure 2.21: H^1 error for the square geometry. From left to right: $p = 2, 3, 4$. Top: Poisson equation. Bottom: Elasticity equation.

The results on the annulus, shown in Figure 2.22, show a similar effect. However, compared to the square domain, the pre-asymptotics is seen more intense, now including the case of linear elasticity. As on the square mesh, the difference in the error vanishes with more mesh refinements. In contrast to the previous example also a difference for the equal order can be seen. The error on the mesh with a size ratio 2 : 3 is smaller compared to the mesh size ratio 1 : 1, independent of the master-slave choice, which could be due to the local refinement of the outer ring. The difference is about the same magnitude as the error increase due to the pre-asymptotics of the biorthogonal basis. For the example of elasticity, this effect cannot be seen.

This indicates how small issues can increase the error by a similar value as the observed pre-asymptotics and again shows the promising behavior of the novel biorthogonal basis.

2.4 Influence of quadrature errors

In order to evaluate the bilinear form $b(\lambda, v)$ (and $b(\mu, u)$), on each interface γ we need to compute the mortar integrals $\int_{\gamma} \lambda v^+ d\gamma$ and $\int_{\gamma} \lambda v^- d\gamma$, with v^+ the trace of v from the master domain Ω_m , and v^- the trace of v from the slave domain Ω_s . In this section, we comment on the difficulty of the numerical integration for the mortar integral as well as on its importance. Different strategies to evaluate the mortar integral, involving variational crimes, are compared numerically with the precise evaluation.

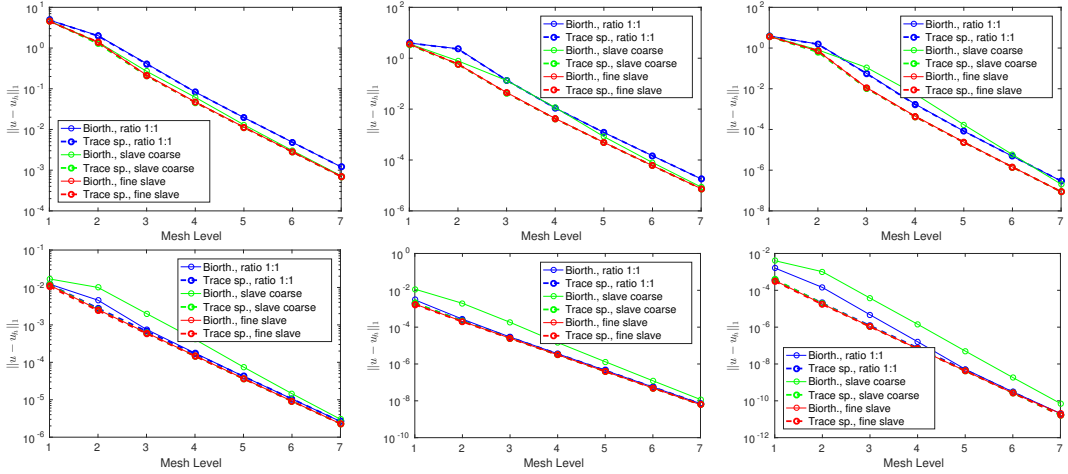


Figure 2.22: H^1 error for the annulus geometry. From left to right: $p = 2, 3, 4$. Top: Poisson equation. Bottom: Elasticity equation.

2.4.1 Mortar integrals

The evaluation of the first interface integral of a mortar formulation, the master-slave mortar integral, is particularly challenging due to the product λv^+ of functions which are defined on different meshes. Quadrature rules based on the slave mesh do not respect the knots of the master mesh and vice versa for a quadrature based on the master mesh.

Of course, the use of a suitable quadrature rule based on a merged mesh, which respects the mesh lines of both the master and the slave domain, leads to an accurate evaluation of the integral. However, the segmentation process to construct such an auxiliary mesh is challenging, see, e.g., [66, 102, 155, 175, 176, 227]. In an isogeometric context, the merged mesh is constructed in the physical space and then pulled back to the parametric space for each subdomain. The complexity of constructing such a mesh becomes even more severe in the case of two-body contact problems, where the relative position of the meshes might change in every time or load step.

This computational complexity, made it seem very appealing to use a higher order quadrature rule either based on the slave mesh or on the master mesh to approximate the master-slave mortar integral, see [61, 81, 216] for some applications in the classical finite element and the isogeometric context. However in the finite element case, early results in [47, 151] show that this strategy does not necessarily yield optimal methods. More precisely, in the case when only the master mesh is chosen, the best approximation error is affected, while for the case when only the slave mesh is chosen it is the consistency error. Numerical results confirm the lack of optimality with the master integration

approach, while with the slave integration approach reasonable results are obtained. However these results are not optimal in terms of the Lagrange multiplier norm.

Based on the global smoothness of splines, one could expect the sensitivity with respect to the quadrature rules for isogeometric methods to be less than for classical finite element methods. This motivates us to study the slave-integration rule and the non-symmetric integration for splines of maximal regularity.

We denote the quadrature rule based on the boundary mesh of the slave domain as \sum_- , i.e., $\int_\gamma \lambda v^+ d\gamma \approx \sum_- \lambda v^+$. In the examples a Gaussian quadrature rule is used, and we vary the number of Gauss nodes. In all cases, we choose sufficiently many nodes, such that the integration of B-splines on a merged mesh would have been exact. The mortar method with pure slave integration is obtained by evaluating all interface integrals in (2.1) using this quadrature rule: Find $(\tilde{u}_h, \tilde{\lambda}_h) \in V_h \times M_h$, such that

$$\begin{aligned} a(\tilde{u}_h, v_h) + \sum_- (v_h^+ - v_h^-) \tilde{\lambda}_h &= f(v_h), \quad v_h \in V_h, \\ \sum_- (\tilde{u}_h^+ - \tilde{u}_h^-) \mu_h &= 0, \quad \mu_h \in M_h. \end{aligned}$$

The notation $\tilde{\cdot}$ is used to stress the difference to the discrete solution with exact integration.

In the next section, we present numerical examples which show severe deviations even in the isogeometric case. Even though the global smoothness of the integrated function is increased in comparison to the standard finite element case, a non-matching integration approach drastically reduces the convergence order.

In addition, we consider an alternative approach which was proposed in [47, 151] which uses both integration rules. We denote by \sum_+ a quadrature rule based on the boundary mesh of the master domain Ω_m . The approach results in the following non-symmetric saddle point problem: Find $(\tilde{u}_h, \tilde{\lambda}_h) \in V_h \times M_h$, such that

$$\begin{aligned} a(\tilde{u}_h, v_h) + \sum_+ v_h^+ \tilde{\lambda}_h - \sum_- v_h^- \tilde{\lambda}_h &= f(v_h), \quad v_h \in V_h, \\ \sum_- (\tilde{u}_h^+ - \tilde{u}_h^-) \mu_h &= 0, \quad \mu_h \in M_h. \end{aligned}$$

The non-symmetric saddle point problem corresponds to a Petrov–Galerkin approach in the purely primal formulation. The formulation was motivated by different requirements for the integration of the primal and dual test functions. Numerical examples show error values very close to the case of exact integration, but we note that from the theoretical side even the well-posedness of the

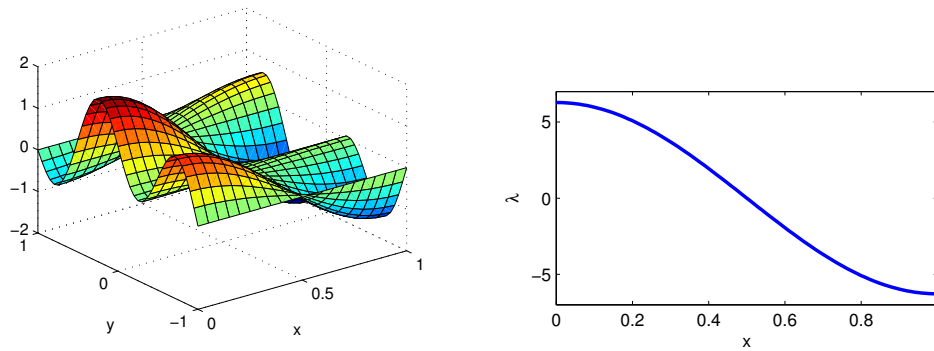


Figure 2.23: Left: Primal solution on Ω . Right: Lagrange multiplier along the interface.

non-symmetric saddle point problem remains open. The numerical examples in the next section show that the results are generally close to those from the exact integration case also in an isogeometric context.

2.4.2 Numerical results

In this section, we numerically study the effects of the presented inexact quadrature rules, on the optimality of the mortar method, based on two-dimensional and three-dimensional settings.

2.4.2.1 Two-dimensional example

In the two-dimensional example, we consider the Poisson problem $-\Delta u = f$ on the rectangular domain $\Omega = (0, 1) \times (-1, 1)$ which is decomposed into two patches by the straight interface $\gamma = (0, 1) \times \{0\}$. The upper domain is chosen as the slave domain. The internal load and the boundary conditions are set to have the exact solution

$$u(x, y) = \cos(\pi x) \left(\cos\left(\frac{\pi}{2}y\right) + \sin(2\pi y) \right).$$

The normal derivative on the interface is given by $2\pi \cos(\pi x)$, see Figure 2.23. Neumann conditions are applied on the left and right boundary parts, such that no cross point modification is necessary, see Section 2.2.1.3.

We consider three different mesh cases, presented in Figure 2.24. In the first two cases, the initial master mesh is a refinement of the initial slave mesh. The initial slave mesh consists of just one element. In the case M1, one uniform refinement step is applied to build the master mesh, in the case M2 two uniform refinement steps. Both cases serve as the most simple situation to investigate

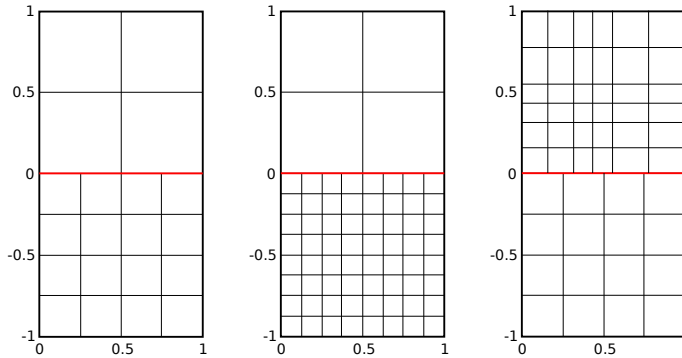


Figure 2.24: Different meshes with one uniform mesh refinement (i.e., level 1). From the left to the right: M1 to M3.

the influence of the quadrature error. Case M3 was chosen such that at no refinement level parts of the slave and master boundary meshes do coincide. The initial interior knots of the slave domain were chosen as $\{\pi/10, 1 - \pi/7\}$ in both parametric directions, which yields nine elements. The initial master mesh consists of four uniform elements.

We present different numerical error studies, during uniform refinement of the slave and the master domains. While the inter-element smoothness of the dual functions can influence the accuracy of the quadrature based on the master mesh, it does not influence the one based on the slave mesh. Hence for the slave integration approach, we consider the equal order pairing with maximal smoothness, $M_h = M_h^0 \subset C^{p-1}(\gamma)$, while for the non-symmetric approach we vary the dual degree.

Slave integration approach As the first test, we consider mesh case M3, to study the impact of the integration error in a general situation. The numerical error for a different number of additional Gauss points and different spline degrees is shown in Figure 2.25. For a spline of degree p , we start with a quadrature rule of $p+1$ Gauss points and investigate the effect of using a higher number of Gauss nodes. The primal and dual solutions are both affected by the inexact quadrature, which shows the non-optimality of the method. The same characteristic behavior can be seen in all considered cases: Up to a certain refinement level, the results with inexact quadrature rules coincide with the ones with an exact quadrature. At some refinement level, the convergence order is reduced and the error is significantly larger than the exact integration one. This level, where the reduced convergence starts depends on the considered error norm, the order p and the considered number of Gauss nodes. Higher order splines are seen to be more sensitive to the numerical quadrature than

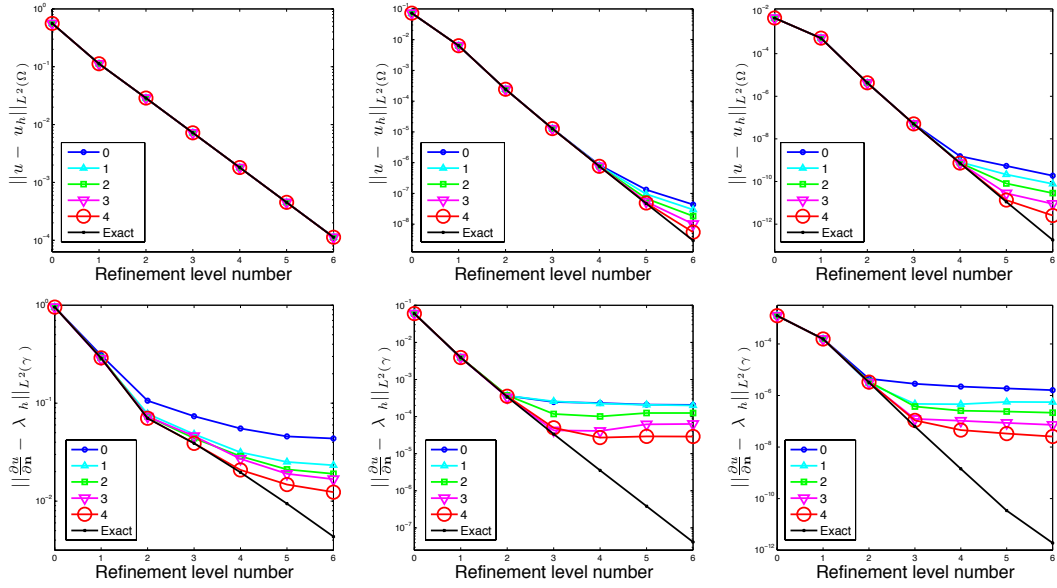


Figure 2.25: L^2 primal (top) and dual (bottom) error curves for the case M3. Equal order pairings with $p = 1, 3, 5$ (from left to right) for the slave integration approach and a different number of additional quadrature points.

the lower order splines.

Almost all cases of Figure 2.25 show poor approximation and a reduced convergence order independent of the spline degree. In particular, the $L^2(\gamma)$ error of the Lagrange multiplier is very low and in some cases even no convergence at all can be observed.

Table 2.2: Last estimated order of convergence of the primal and dual L^2 errors for the cases M1 and M2. Pairing P5-P5 for the slave integration approach and a different number of additional quadrature points.

add. q.p.	primal error		dual error	
	case M1	case M2	case M1	case M2
0	1.63	1.74	0.50	0.50
2	1.63	1.55	0.50	0.50
4	1.63	1.56	0.50	0.50

The second test studies a simpler situation and shows that even there the impact of the slave integration is severe. We consider the cases M1 and M2, for which the master mesh is a refinement of the slave mesh. In Figure 2.26 the results of the cases M1 and M2 for a spline degree $p = 3$ are displayed.

Also in this simpler context, we observe the low convergence orders of the primal and dual (not shown) variable, as in the case M3. As expected, for a fixed number of slave elements, the error is increasing with the number of master elements. This is due to the fact, that there are more points of reduced smoothness which are not taken into account by the quadrature rule. Now, we study the final numerical convergence rate more detailed. Table 2.2 gives the estimated convergence orders for a spline degree $p = 5$. The dual $L^2(\gamma)$ rate breaks down to an order of $1/2$, and the primal $L^2(\Omega)$ rate is about $3/2$.

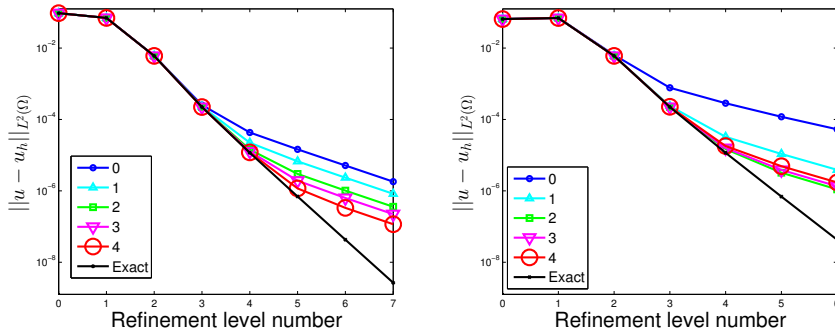


Figure 2.26: L^2 primal error curves for the cases M1 (left) and M2 (right). Pairing P3-P3 for the slave integration approach and a different number of additional quadrature points.

As the last test concerning the slave-integration in 2D, we compare the case M3 with a similar situation in which the master and slave domains are reverted. The results show, that the integration error is increasing with more master elements. This shows that, as often performed in practice, it is favorable to choose the domain with the smaller mesh size as the slave domain.

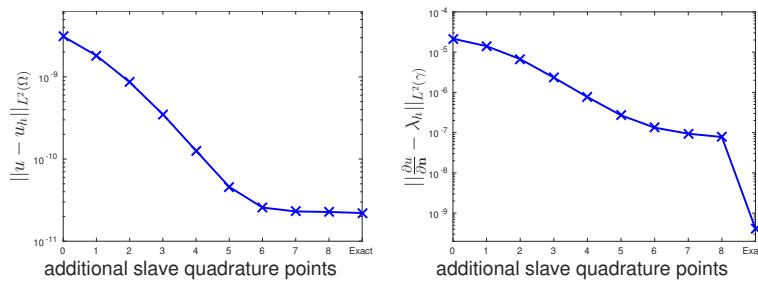


Figure 2.27: L^2 primal (left) and dual (right) error at refinement level number 6 as a function of the number of additional quadrature points for the case M3. Pairing P3-P3 for the slave integration approach.

In all examples it could be seen, that using the slave integration method

on coarse meshes it is possible to recover the accuracy of the optimal mortar method by simply using sufficiently many Gauss points, see Figure 2.27. However, the necessary number of Gauss points grows drastically with the refinement level and soon gets impracticably large, as see the right picture of Figure 2.27. In several cases we saw that the deviation to the mortar method was more extreme for a higher spline degree.

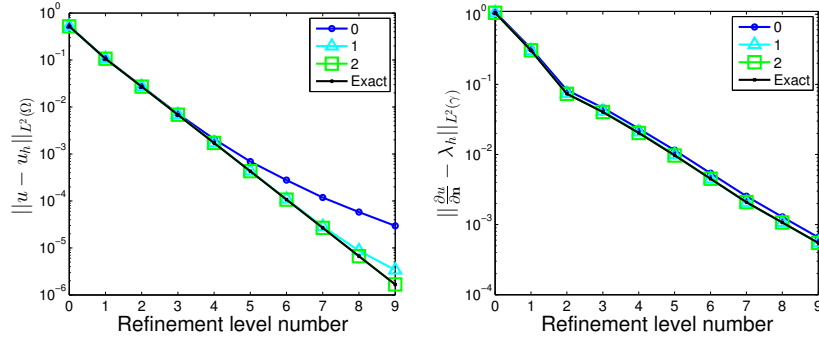


Figure 2.28: L^2 primal (left) and dual (right) error curves for the case M3. Equal order pairing $p = 1$ for the non-symmetric approach and a different number of additional quadrature points.

Non-symmetric approach In Section 2.4.1, a non-symmetric saddle point problem based on the two different quadrature rules was presented to overcome the non-optimality of the pure slave integration approach. It was originally introduced for classical finite element methods, but, due to the sub-optimal results seen in the previous section, it is also interesting to consider it in an isogeometric context.

At first, we consider equal order pairings. Almost all tested cases show comparable results with the non-symmetric approach as with an exact integration. Only in a few cases differences could be seen. For example, in the case M3 with $p = 1$, non-optimal rates are seen in Figure 2.28. For all cases, where the non-symmetric approach shows no disturbance in comparison to the exact integration, no results are shown here. As an example for degree $p = 5$, convergence almost up to machine precision can be seen without any remarkable difference compared to the case of an exact integration.

As a second case, dual spaces with a lower degree than the primal one are studied. In Section 2.2 we have shown stability for these pairings if the primal and the dual degree have the same parity. As with the previously considered equal order case, the dual error does not show a notable deviation when using the non-symmetric approach. Primal error curves for all stable different degree

pairings up to a primal degree $p = 4$ are presented in Figure 2.29. From the theory, sub-optimal primal error rates are expected even with an exact integration, although, as in several cases, improved convergence rates are observed here. For a dual degree $p - 2k$, $k \in \mathbb{N}_{>0}$, we theoretically expect a convergence of order $\mathcal{O}(h^{p-2k+5/2})$ in the $L^2(\Omega)$ norm, which is marked as dashed lines in Figure 2.29. We observe small differences compared to the exact integration

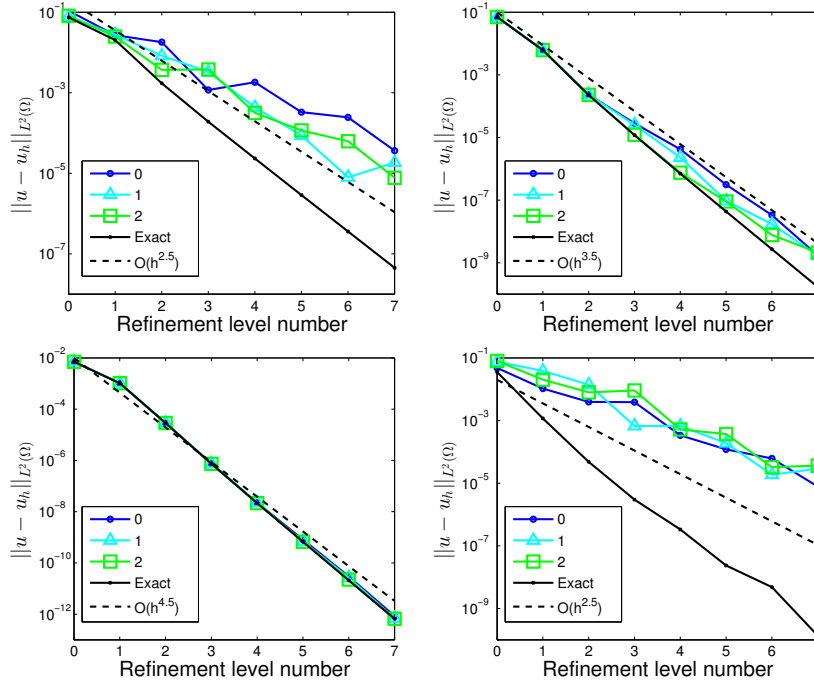


Figure 2.29: L^2 primal error curves for the case M3. Different order pairings for the non-symmetric approach and a different number of additional quadrature points. Top left: P2-P0. Top right: P3-P1. Bottom left: P4-P2. Bottom right: P4-P0.

results for the P4-P2 and P3-P1 pairings, but note that the convergence rate is not significantly different than the theoretical expectation. For the P4-P0 and P2-P0 pairings the situation is different, as the rate is disturbed more severely and lies even below the theoretical expectation. This might be due to the discontinuity of the dual basis functions. For discontinuous functions, the numerical quadrature, which does not respect these discontinuities, introduces large errors.

2.4.2.2 Three-dimensional example

As a second example, we consider a three-dimensional problem with a curved interface. We consider the Poisson problem $-\Delta u = f$ on a unit-cube $\Omega =$

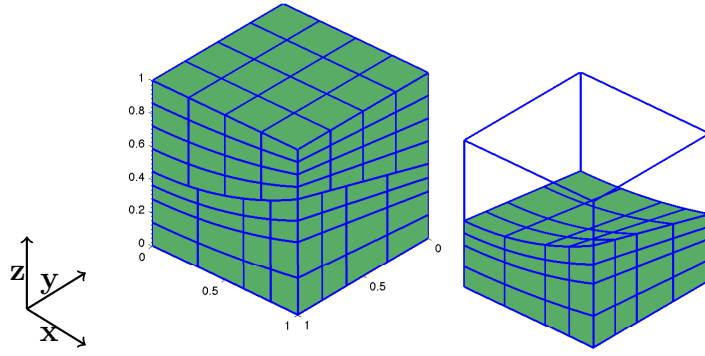


Figure 2.30: Meshes at refinement level 1 (left) and the slave domain (right) illustrating the curved interface.

$(0, 1)^3$, divided into two patches by the interface $\gamma = \{(x, y, \rho(x, y)), (x, y) \in (0, 1)^2\}$, with $\rho(x, y) = 1/8(1+x)(1+y^2) + 1/5$, see Figure 2.30. The bottom domain is set as the slave domain. The internal load and the boundary conditions are set such that the solution is

$$u(x, y, z) = \cos(2\pi x) \cos(2\pi y) \sin(2\pi z).$$

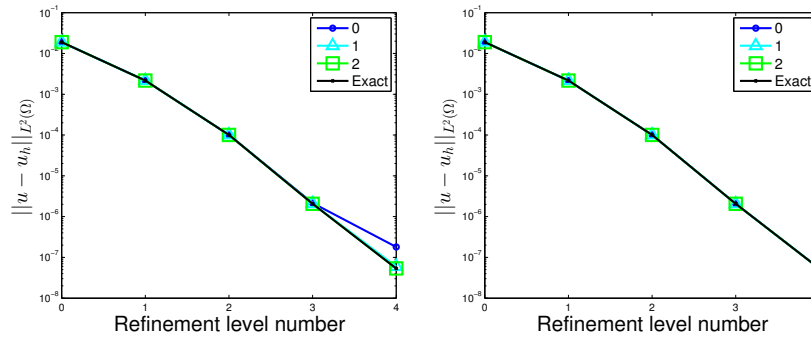


Figure 2.31: L^2 primal error curves for the pairing P4-P4, for the three-dimensional example with the slave integration approach (left) and the non-symmetric approach (right). Each of the curves being obtained with a different number of additional quadrature points.

Note that, due to the curved interface, the normal derivative has a complicated form, but is still explicitly computable. Dirichlet conditions are applied on the top and the bottom side (where $z \in \{0, 1\}$) and Neumann conditions are applied to the four remaining sides of the cube, such that no cross point

modification is necessary. The initial master mesh has 8 uniform elements, while the initial slave mesh has 8 elements given by the breakpoint vector $(0, \pi/5, 1)$ in each direction. During refinement no mesh lines in the interior of the slave domain will match with the master mesh. In the following, we provide some numerical error studies for the slave integration and the non-symmetric approach.

The results for both approaches are similar to the 2D results. The deviation for the slave integration approach is shown in Figure 2.31 for the P4-P4 pairing. We note that the results for the P2-P2 and P3-P3 pairing as well as the dual error curves have a similar behavior, although they are not shown here. The non-symmetric approach does not lead to reduced rates using equal

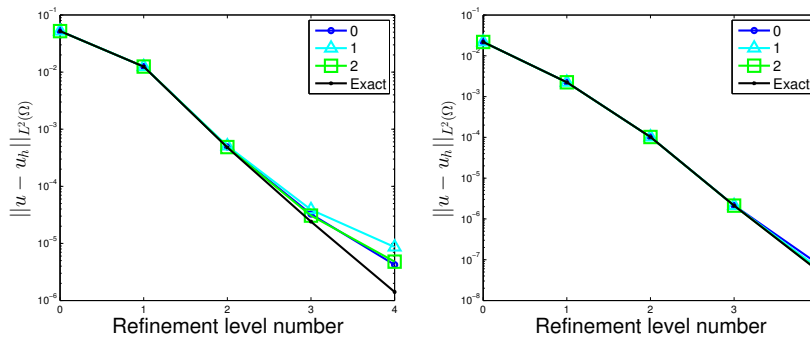


Figure 2.32: L^2 primal error curves for the three-dimensional example with the pairings P3-P1 (left) and P4-P2 (right), for the non-symmetric approach and a different number of additional quadrature points.

order pairings on the considered meshes (up to refinement level 4). As in the two-dimensional case, with a lower order dual space, a difference to the exact integration case can be seen. The disturbance in the primal variable of the P3-P1 and P4-P2 pairings can be seen in Figure 2.32.

2.5 Isogeometric eigenvalue approximation

After studying isogeometric mortar methods on several linear and non-linear right hand side problems, we now consider the approximation of eigenvalue problems. The approximation of eigenvalues is of importance, especially in vibroacoustics, which is considered in the following chapter. It was noticed early that isogeometric methods possess superior approximation of eigenvalues in comparison to classical finite element methods, see [56, 57, 89, 118, 119]. In this section, we investigate numerically the influence of the mortar coupling and then show a three-dimensional example.

Some results of this section have been included in the article “Improved approximation of eigenvalues in isogeometric methods for multi-patch geometries and Neumann boundaries” published 2017 on arxiv.org, joint with T. Horger, A. Reali and B. Wohlmuth, [111].

We solve the generalized eigenvalue problem for the Poisson problem: Find $(u_h, \lambda_h) \in V_h \times M_h$, $\lambda_h^{\text{ev}} \in \mathbb{R}$, such that

$$a(u_h, v_h) + b(\lambda_h, v_h) = \lambda_h^{\text{ev}} m(u_h, v_h), \quad v_h \in V_h, \quad (2.6a)$$

$$b(\mu_h, u_h) = 0, \quad \mu_h \in M_h, \quad (2.6b)$$

with the additional bilinear form $m(u, v) = \sum_{k=1}^K \int_{\Omega_k} uv \, d\mathbf{x}$. We note that the saddle point formulation introduces $2 \dim M_h$ spurious eigenvalues to the spectrum, which are infinite. We restrict ourselves to the physical relevant eigenpairs $(\lambda_h^{\text{ev}}, u_h)$. These are characterized by the fact that they are also eigenpairs of the constrained mortar formulation, i.e., they satisfy $u_h \in X_h$ and

$$a(u_h, v_h) = \lambda_h^{\text{ev}} m(u_h, v_h), \quad v_h \in X_h = \{v_h \in V_h : b(\mu_h, v_h) = 0, \mu_h \in M_h\}.$$

2.5.1 Influence of the mortar coupling on eigenvalue approximations

In this numerical study, we compare the eigenvalue approximation of isogeometric mortar methods to single-patch mortar methods as well as finite element methods. First, we consider a one-dimensional model and then a unit-square with a non-matching mesh.

The following results show the normalized discrete eigenvalue $\lambda_h^{\text{ev}}/\lambda^{\text{ev}}$, which directly relates to the relative error in the eigenvalue since $(\lambda_h^{\text{ev}} - \lambda^{\text{ev}})/\lambda^{\text{ev}} = \lambda_h^{\text{ev}}/\lambda^{\text{ev}} - 1$. In some cases, especially in dynamics, the overall approximation of the spectrum is important, see [118]. Here we simply concentrate on vibroacoustical applications, where we are interested in a good rate of error per degree of freedom for a specific amount of eigenvalues. As such, we consider the eigenvalues relative to the number of degrees of freedom. We note that due to the saddle point formulation, in the mortar case the amount of eigenvalues is less than the number of degrees of freedom.

2.5.1.1 One-dimensional example

We start our study with the one-dimensional case, as here the behavior of classical finite elements and single-patch isogeometric methods is very well-known, e.g., [119]. Pure Dirichlet conditions are applied on the unit-interval $\Omega = (0, 1)$,

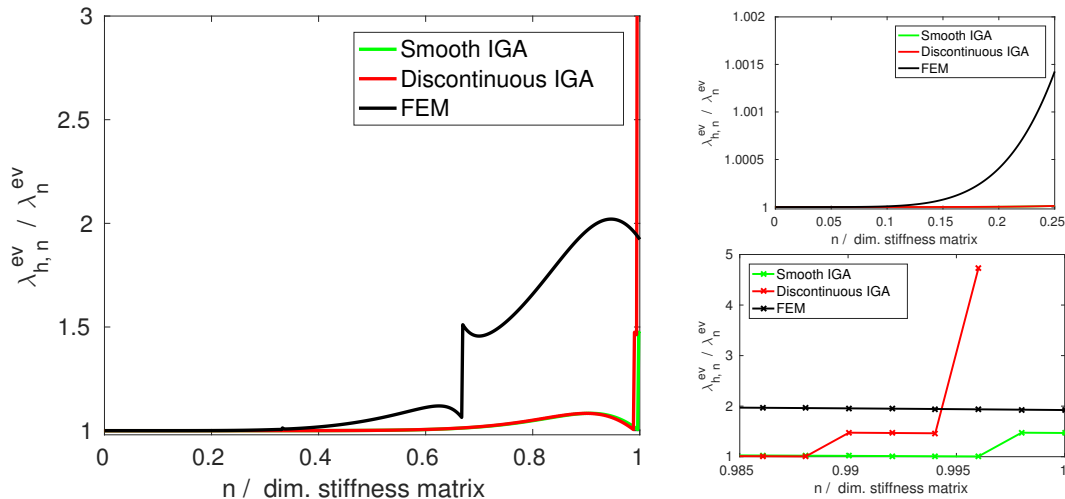


Figure 2.33: Comparison of the eigenvalue approximation of standard FEM and IGA with a smooth and a discontinuous ansatz on a one-dimensional domain with $p = 3$. Left: Whole spectrum. Right: Zoom onto the first (top) and last (bottom) eigenvalues.

where the eigenvectors of the Poisson equation are $u_n(x) = \sqrt{2} \sin(n\pi x)$ with the corresponding eigenvalue $\lambda_n^{ev} = n^2\pi^2$, $n = 1, 2, \dots$, see [118].

As the model for the mortar method, we consider a broken space, where the continuity condition, $[u] = 0$ at the point of discontinuity $x = 0.5$, is realized by a Lagrange multiplier. The eigenvalue approximation using this coupled discontinuous space are compared to the ones using a classical finite element space and an isogeometric space of maximal regularity. The results shown in Figure 2.33 compare the approximation of the eigenvalues for $p = 3$ with respect to the dimension of the stiffness matrix. In all three cases the dimension of the stiffness matrix is the same, namely 503, which yields 501 eigenvalues for the case of the coupled space, due to the saddle point structure.

In the classical finite element case, we clearly see the well-known branching, where a fixed part of the spectrum is severely worse approximated than the rest. With the isogeometric methods this branching is not present and we see an overall similar behavior of the coupled space and the one-patch space. The exception are the last few eigenvalues, which are more prominent with the discontinuous space, see the bottom right of Figure 2.33. Further studies and a technique to remove these ‘outlier’ can be found in [111]. Besides these ‘outliers’, the approximation using the coupled space shows the same good behavior as a one-patch space, making it very well suited for the use in vibroacoustics. The zoom onto the first 25% of the spectrum in Figure 2.33 shows the clear advantage of isogeometric methods, also in the multi-patch case, compared to classical finite element methods.

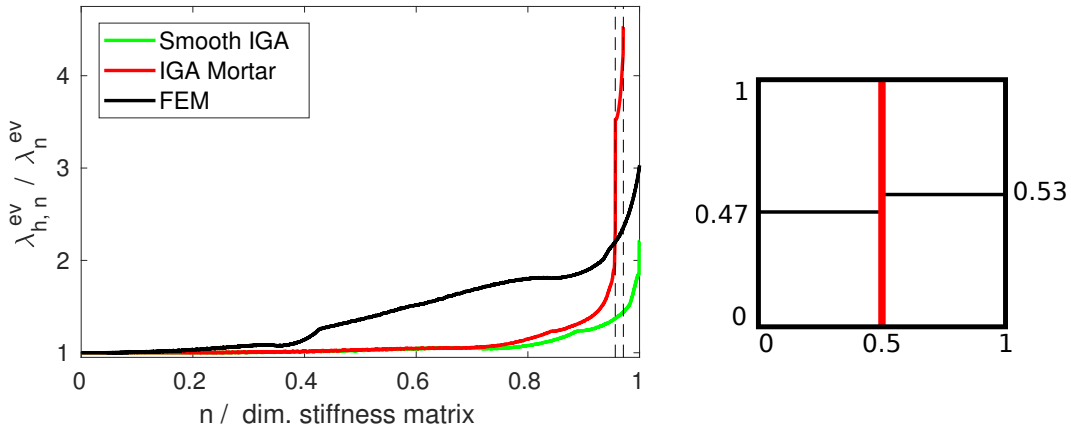


Figure 2.34: Comparison of the eigenvalue approximation of standard FEM and IGA with a smooth and a discontinuous ansatz on a unit square with $p = 3$. Left: Whole spectrum with dashed lines at $n = \dim X_h - \dim M_h$ and $n = \dim X_h$. Right: Non-conforming initial mesh on the unit square.

2.5.1.2 Non-conforming two-dimensional example

The one-dimensional results were very promising, but are incomplete in the sense that non-matching meshes at the interface cannot be considered. This short extension on a two-dimensional domain shows that the results can be transferred also to real mortar situations.

We consider the unit square with pure Dirichlet conditions. For the conforming methods a uniform mesh is considered, while a non-matching mesh is used for the mortar methods, see Figure 2.34 (right).

We choose the dimension as similar as possible, but note that we restrict ourselves to uniform refinements of the initial mesh. The number of degrees of freedom is 4 225 for the single-patch isogeometric method, 4 485 for the isogeometric mortar method and 9 025 for the finite element method.

The resulting approximation of the spectrum is shown in Figure 2.34 (left). Again, we see a good approximation of the first 75% of the spectrum, which are the important modes for a vibroacoustical study. However, compared to the one-dimensional case, the number of outliers is significantly increased as the number of degrees of freedom at the interface is increased, which we can roughly estimate by $\dim M_h$.

We note that besides the interface also the boundary conditions cause outliers for the single patch approximations, getting larger with higher degree.

In conclusion, we see that isogeometric mortar methods are well suited for vibroacoustics. We show a three-dimensional example and in the next chapter a parameter-dependent application.

2.5.2 Eigenvalue approximation for a wooden beam

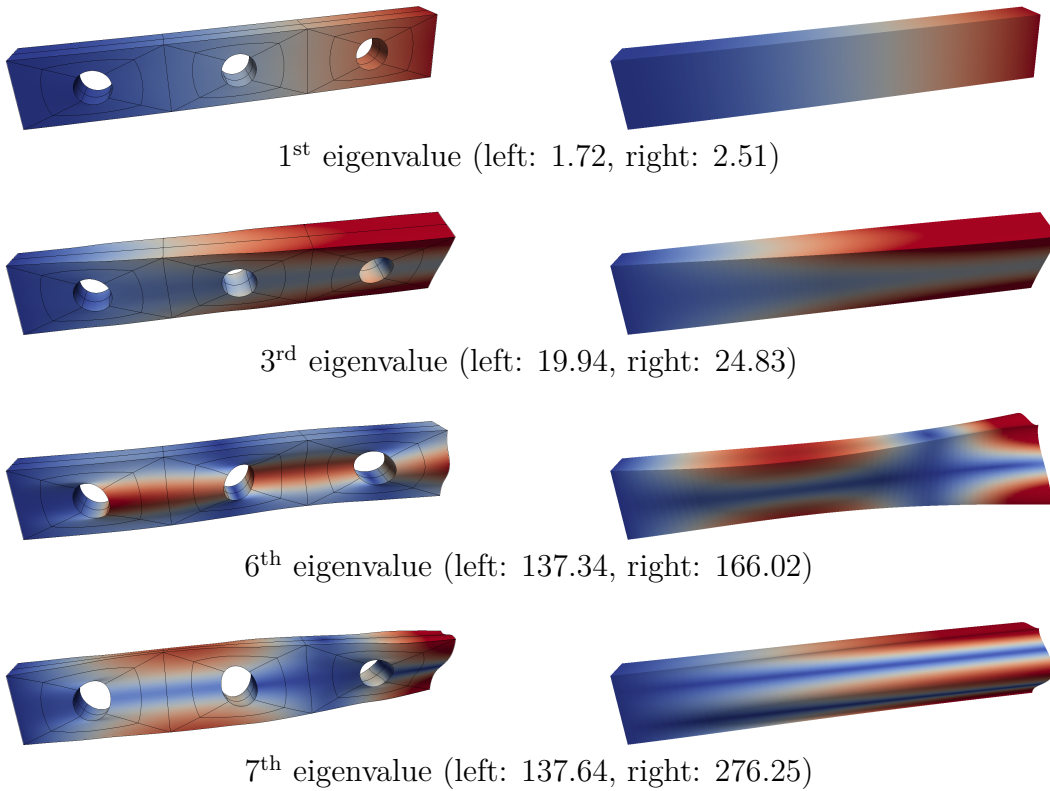


Figure 2.35: Comparison of some eigenvalues and eigenfunctions of the beam with holes with the ones of a standard beam.

We consider a three-dimensional orthotropic beam $(0, 6) \times (-0.5, 0.5) \times (0, 0.5)$ (all dimensions given in cm) with three cylindrical cut-outs. For an isogeometric discretization, we partition the domain into 12 subdomains with 14 interfaces, see Figure 2.36. The beam is fixed on the left side, i.e., $\Gamma_D = \{0\} \times (-0.5, 0.5) \times (0, 0.5)$.

We solve the version of the generalized eigenvalue problem (2.6) for linear elasticity: $(\mathbf{u}_h, \boldsymbol{\lambda}_h) \in \mathbf{V}_h \times \mathbf{M}_h$, $\lambda_h^{\text{ev}} \in \mathbb{R}$:

$$\begin{aligned} a(\mathbf{u}_h, \mathbf{v}_h) + b(\mathbf{v}_h, \boldsymbol{\lambda}_h) &= \lambda_h^{\text{ev}} m(\mathbf{u}_h, \mathbf{v}_h), & \mathbf{v}_h \in \mathbf{V}_h, \\ b(\mathbf{u}_h, \boldsymbol{\mu}_h) &= 0, & \boldsymbol{\mu}_h \in \mathbf{M}_h, \end{aligned}$$

with the additional bilinear form

$$m(\mathbf{u}_h, \mathbf{v}_h) = \int_{\Omega} \rho \mathbf{u}_h^{\top} \mathbf{v}_h \, d\mathbf{x}.$$

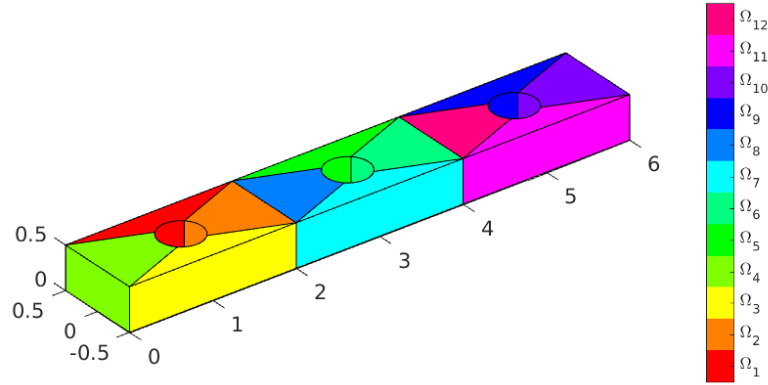


Figure 2.36: Geometry of the beam with three holes and its decomposition into 12 patches.

for the mass with a constant positive density ρ . We use the stable P4-P4 pairing as the isogeometric discretization.

The orthotropic material data are

$$\begin{aligned} E_x &= 287.23 \text{ MPa}, & E_y &= 883.00 \text{ MPa}, & E_z &= 939.38 \text{ MPa}, \\ \nu_{yz} &= 0.023, & \nu_{xz} &= 0.03, & \nu_{xy} &= 0.038, \\ G_{yz} &= 787.65 \text{ MPa}, & G_{xz} &= 487.66 \text{ MPa}, & G_{xy} &= 299.25 \text{ MPa}, \end{aligned}$$

and $\rho = 1 \text{ g/cm}^3$.

Some of the first eigenfunctions are displayed and compared to a standard beam of the same size in Figure 2.35. We investigate the approximation of the first 100 eigenvalues in Figure 2.37.

Table 2.3: Number of degrees of freedom for the beam with holes on different mesh levels

mesh level	0	1	2	3
nr. primal dof	4 425	7 668	18 240	61 776
nr. dual dof	915	1 350	2 472	5 724
total nr. dof	5 340	9 018	20 712	67 500
$\max_{n=1,\dots,100} \lambda_n^{\text{ev}} - \lambda_{h,n}^{\text{ev}} / \lambda_n^{\text{ev}}$	65.7%	36.9%	17.3%	—
$\max_{n=1,\dots,1000} \lambda_n^{\text{ev}} - \lambda_{h,n}^{\text{ev}} / \lambda_n^{\text{ev}}$	276.5%	135.8%	49.4%	—

Since no eigenvalues are known analytically, we consider the values on mesh level 3 as reference values. For the low eigenvalues the approximation is very close to the reference value. The first 37 eigenvalues on level 2 show a relative error of less than 10% and the maximal relative error of the first 100 eigenvalues

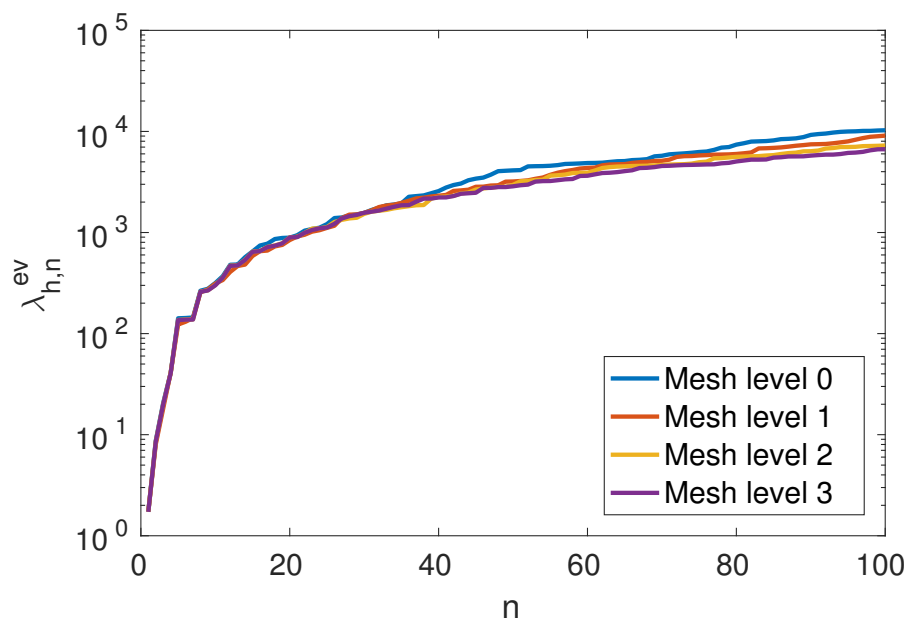


Figure 2.37: The first 100 eigenvalues on the initial mesh and after up to three refinement steps.

is 17.28%. More details on the approximation on the different levels are shown in Table 2.3. While for conforming approximation it strictly holds that $\lambda_{h,n}^{ev} \geq \lambda_n^{ev}$, non-conforming approximation may show some eigenvalues violating this condition.

The promising quality of eigenvalue approximations motivates a practical application in vibroacoustics that is presented in the following chapter.

3 Efficient vibroacoustical application of isogeometric mortar methods

In this chapter, we show how isogeometric mortar methods can efficiently be applied to complex parameter-dependent problems. We give a motivation for the considered problem and then present results of several model order reductions.

Eigenvalue problems appearing in the context of vibroacoustics often depend on several parameters. In this chapter, we consider a geometry- and material-dependent violin bridge. The eigenvalues of a violin bridge play a crucial role in transmitting the vibration of the strings to the violin body and hence influence the sound of the instrument, see [82, 232]. The geometric setup includes geometry parameters, in the first part of this chapter this is a thickness parameter and later it includes more complex variations. The geometry is mapped onto a reference domain and the thickness parameter is transformed to a material parameter. Due to the easy geometry handling of the complicated curved domain and the improved eigenvalue approximations compared to classical finite element methods, see Section 2.5, we consider an isogeometric discretization. Flexibility for the tensor product spline space is gained by a mortar domain decomposition of the non-convex domain as introduced in Section 2.

For practical computations often a series of simulations is necessary. Examples are shape or parameter optimization, parameter-identification or uncertainty quantification. Then model order reduction can be crucial to obtain results of the desired quality in a reasonable amount of time and with the present hardware. For a fast and reliable evaluation in the real-time and multi-query context, we use reduced basis methods, which have proven to be a powerful tool, see [75, 153, 171] for some applications.

The efficiency of reduced basis methods is based on an affine parameter-dependency of the problem. This allows a decomposition of the computation into a one-time complex offline and a fast online phase. With complex geometry variations, the parameter dependency is no longer affine and no efficient offline-online decomposition is possible. We apply the empirical interpolation

method (EIM) [17] to obtain a decomposable approximation.

Parts of the results of Section 3.1 and 3.2 have been published by the author in collaboration with T. Horger and B. Wohlmuth in the article “Reduced basis isogeometric mortar approximations for eigenvalue problems in vibroacoustics” in 2017, [113], and they are included in the PhD thesis of T. Horger [109].

3.1 An isogeometric approximation of a bridge of a violin

The numerical simulation of vibroacoustic applications quite often involves complex domains. Typical examples are large structures, such as, e.g., bridges, technical devices such as, e.g., loudspeakers but also parts of string instruments such as, e.g., violin bridges, see Figure 3.1. Within the abstract framework of modal analysis, the fully bi-directional mechanical-acoustic coupled system can be reduced to a generalized eigenvalue problem.



Figure 3.1: Example of a violin bridge.

3.1.1 Problem setting

The vibroacoustical properties of the violin bridge has already gained some scientific attention. Besides investigations based on measurements, e.g., in [123, 186], also finite element discretizations were considered, see, e.g., [185, 238]. In comparison to classical finite element discretizations, an isogeometric discretization poses two main advantages. A convenient and precise handling of the curved geometry and an improved approximation of the eigenvalues. Also the higher order approach prevents negative locking effects of the thin structure.

For the three-dimensional geometry of a violin bridge, we consider the eigenvalue problem of elasticity

$$-\operatorname{div} \boldsymbol{\sigma}(\mathbf{u}) = \lambda^{\text{ev}} \rho \mathbf{u},$$

where $\rho > 0$ is the constant mass density, and $\boldsymbol{\sigma}(\mathbf{u})$ is based on the linear orthotropic material law, see Section 1.2.2. We recall that the three axes are given by the fiber direction y , the in plane orthogonal direction z and the radial direction x , see Figure 3.1.

The curved domain of the violin bridge can be very precisely described by a spline volume. Since it is not suitable for a single-patch description, we decompose it into 16 three-dimensional spline patches shown in Figure 3.2. While the description of the geometry could also be done with fewer patches, the number of 16 patches Ω_l gives us regular geometry mappings and a reasonable flexibility of the individual meshes.

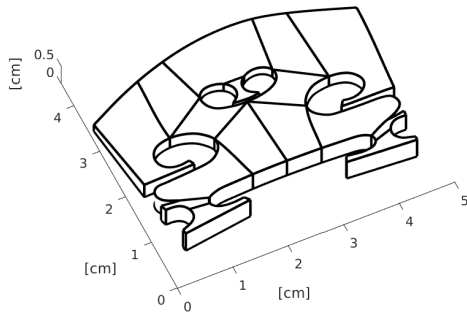


Figure 3.2: Decomposition of the three-dimensional geometry into 16 patches Ω_k and 16 interfaces γ_l .

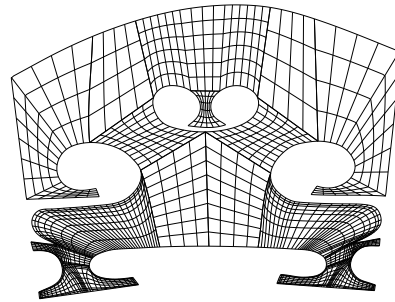


Figure 3.3: Non-matching isogeometric mesh of the violin bridge.

The eigenvalue problem on the multi-patch geometry is solved using an equal order isogeometric mortar method as described in Section 2.2. The detailed eigenvalue problem then solves $(\mathbf{u}_h, \boldsymbol{\lambda}_h) \in \mathbf{V}_h \times \mathbf{M}_h$, $\lambda_h^{\text{ev}} \in \mathbb{R}$, such that

$$\begin{aligned} a(\mathbf{u}_h, \mathbf{v}_h) + b(\mathbf{v}_h, \boldsymbol{\lambda}_h) &= \lambda_h^{\text{ev}} m(\mathbf{u}_h, \mathbf{v}_h), \quad \mathbf{v}_h \in \mathbf{V}_h, \\ b(\mathbf{u}_h, \boldsymbol{\mu}_h) &= 0, \quad \boldsymbol{\mu}_h \in \mathbf{M}_h. \end{aligned}$$

We use an anisotropic equal-order mortar discretization that is convenient for the thin structure of the bridge. In plane, we use splines of degree $p = 3$ on the non-matching mesh that is shown in Figure 3.3. The mesh is locally adapted to possible corner singularities of the solution. In the z -direction a single element of degree $p = 4$ is used to avoid shear locking. The resulting equation system has 45 960 degrees of freedom for the displacement whereas the surface traction

on the interfaces is approximated by 2025 degrees of freedom.

3.1.2 Variations of the violin bridge

Considering violin bridges, it is of importance to take some variations of the setting into account. Especially the fact that the bridge is typically drafted individually for each violin and made of a natural material makes the possible variations important in a numerical simulation. Here, we focus on the changes of the geometry and the material data.

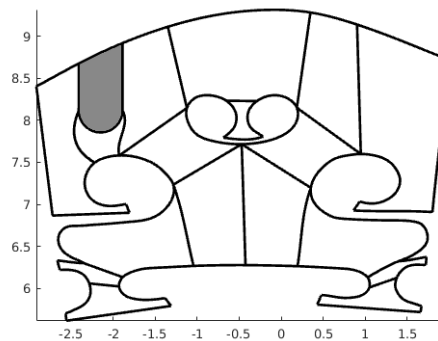


Figure 3.4: Decomposition of the bimaterial bridge into 18 patches, coupled at 20 interfaces. Ebony inlay marked in gray.

Geometry changes can be of interest for the experimental use of new bridge designs, see [44, Chapter 11.2.5], but also for the individual fit to the instrument, which is our main motivation. A violin maker starts with a blank bridge, which is cut and individually adapted to the violin, see, e.g., [185]. With this process the influence of small geometry variations is of importance, which is considered in Section 3.3.2.

The variation of material parameters can also be considered in various situations. The uncertainty of the precise material data, but also the comparison of different wood-types is the motivation for the parameters chosen in Section 3.2. In addition a more radical change in the bridge design can introduce different materials. An example are bridges that include a U-shaped inlay of ebony, which supports the position of the highest string (E string). Also a bi-material inclusion is easily handled by the isogeometric mortar discretization, see Figure 3.4 for the 18 patches and the interfaces.

As an illustration, we compare the eigenvalues and eigenfunctions of the standard violin bridge with the one including an ebony inlay in Figure 3.5.

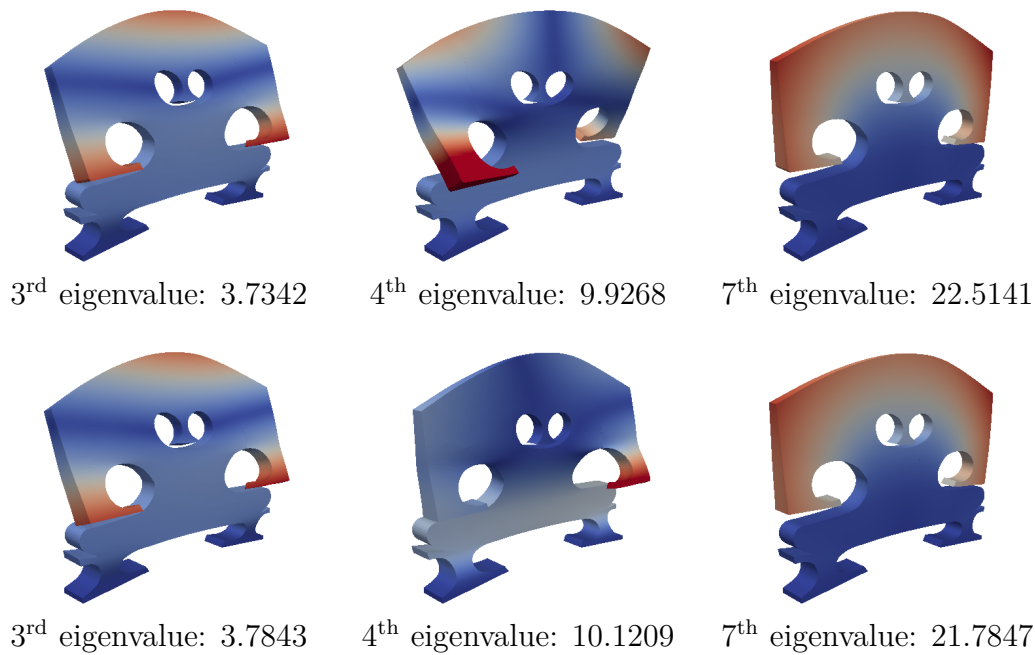


Figure 3.5: Comparison of some eigenvalues and eigenfunctions with and without inlay. Top: No inlay. Bottom: Bimaterial bridge.

We consider a bridge made of red maple with the orthotropic material data given as in [83, Chapter 5]. The material data for ebony were chosen isotropic as $E = 15\,000$ MPa with $\nu = 0.33$. We note that the fourth eigenfunction is influenced strongly by the inlay. The isogeometric discretization is robust and shows no spurious oscillations around the curved interfaces and the material jump.

3.2 Reduced basis methods in vibroacoustics

The reduced basis method is a model order reduction technique for parameter-dependent PDEs. It is based on a Galerkin projection onto a *reduced space*, which is created by snapshots of the PDE, computed based on a sampling of the parameter range. For a comprehensive review on reduced basis methods, see, e.g., [103, 178, 189] or [177, Chapter 19] and the references therein. The methodology has been applied successfully to many different problem classes, among others Stokes problems [120, 148, 188, 190], variational inequalities [92, 99] and linear elasticity [160]. Recently, reduced basis methods for parameterized elliptic eigenvalue problems (μ EVPs) have gained attention,

With this transformation, the eigenvalue problem in the continuous H^1 -setting reads, since $\det \mathbf{DF}(\widehat{\mathbf{x}}; \boldsymbol{\mu}) = \mu_{10}^{-1}$ is constant, as

$$\int_{\widehat{\Omega}} \widehat{\boldsymbol{\varepsilon}}(\widehat{\mathbf{u}}_h) \widehat{\mathbf{C}}(\mu_{10}) \widehat{\boldsymbol{\varepsilon}}(\widehat{\mathbf{v}}_h) \, d\widehat{\mathbf{x}} = \lambda_h^{\text{ev}} \int_{\widehat{\Omega}} \rho \widehat{\mathbf{u}}_h^\top \begin{pmatrix} 1 & & \\ & 1 & \\ & & \mu_{10}^{-2} \end{pmatrix} \widehat{\mathbf{v}}_h \, d\widehat{\mathbf{x}}.$$

For the mortar formulation, the coupling conditions at the interfaces needs to be transformed as well. Here we assume that the meshes on the physical domain are obtained by mapping the meshes on the reference domain by \mathbf{F} .

$$\begin{aligned} \int_{\gamma(\boldsymbol{\mu})} [\mathbf{u}_h(\mathbf{x})] \boldsymbol{\mu}_h(\mathbf{x}) \, d\gamma(\mathbf{x}) &= \int_{\widehat{\gamma}} [\mathbf{DF}(\widehat{\mathbf{x}}; \boldsymbol{\mu})^{-\top} \widehat{\mathbf{u}}_h(\widehat{\mathbf{x}})] \boldsymbol{\mu}_h(\mathbf{F}(\widehat{\mathbf{x}}; \boldsymbol{\mu})) \mu_{10} \, d\gamma(\widehat{\mathbf{x}}) \\ &= \mu_{10} \int_{\widehat{\gamma}} [\widehat{\mathbf{u}}_h(\widehat{\mathbf{x}})] \begin{pmatrix} 1 & & \\ & 1 & \\ & & \mu_{10}^{-1} \end{pmatrix} \boldsymbol{\mu}_h(\mathbf{F}(\widehat{\mathbf{x}}; \boldsymbol{\mu})) \, d\gamma(\widehat{\mathbf{x}}). \end{aligned}$$

Here $\widehat{\boldsymbol{\mu}}_h = \boldsymbol{\mu}_h \circ \mathbf{F}$ is in the parameter-independent Lagrange multiplier space of the reference domain if $\boldsymbol{\mu}_h$ is in the parameter-dependent one of the physical domain. The remaining parameter dependency is a simple scaling of the Lagrange multiplier and does not influence the constrained primal space. This shows us how the parameter-dependent standard mortar coupling can be transformed to a parameter-independent one.

While these lines use the special structure of the geometry variation \mathbf{F} , the coupling can still be transformed to a parameter-independent one even in more general situations, by considering a suitable weighted L^2 space.

The remaining material parameter, the constant mass density ρ , does not influence the eigenvectors. Only the eigenvalues are rescaled, which is a trivial parameter dependence. For this reason, the density is kept constant in the reduced basis computations and can be varied in a post-process by rescaling the eigenvalues.

The ten described parameters yield an affine parameter dependence of the mass and the stiffness, with $Q_a = 10$, $Q_m = 2$:

$$a(\cdot, \cdot; \boldsymbol{\mu}) = \sum_{q=1}^{Q_a} \theta_a^q(\boldsymbol{\mu}) a^q(\cdot, \cdot), \quad m(\cdot, \cdot; \boldsymbol{\mu}) = \sum_{q=1}^{Q_m} \theta_m^q(\boldsymbol{\mu}) m^q(\cdot, \cdot), \quad (3.1)$$

where $\theta_m^1(\boldsymbol{\mu}) = 1$ can be chosen parameter-independent. We note that by another transformation, also m could be chosen parameter-independent. However, as we do not encounter any problems with its parameter dependency, we do not consider this in the following.

3.2.2 Reduced basis methods for eigenvalue problems

In this section, we discuss the application of the reduced basis methods presented in [112] for the approximation of the parameter-dependent eigenvalue problem on the reference domain. With abuse of notation, the spaces and bilinear forms after the transformation to the reference domain are denoted as before. In general, reduced basis techniques where the detailed problem is in saddle point form also require the construction of a reduced basis for the dual space, as for variational inequalities or when the coupling is parameter-dependent, see [90, 93, 99, 164]. To ensure the inf-sup stability of the discrete saddle point problem, supremizers can be added to the primal space, which additionally increases the size of the reduced system, see [188, 190]. In our case, it is sufficient to define a reduced basis for the primal space, as shown in the following.

By the transformation described above, we obtained the parameter-independence of $b(\cdot, \cdot)$ and the dual space. Therefore we can reformulate the detailed saddle point problem (2.1) in a purely primal form posed on the constrained space

$$\mathbf{X}_h = \{\mathbf{v}_h \in \mathbf{V}_h, b(\mathbf{v}_h, \boldsymbol{\mu}_h) = 0, \boldsymbol{\mu}_h \in \mathbf{M}_h\}.$$

We recall that this formulation is not suitable for solving the detailed problem, since, in general, it is costly to explicitly construct a basis of \mathbf{X}_h and furthermore this severely disturbs the sparsity of the detailed matrices.

The construction of the reduced basis is done by the following two steps, see [112] for more details. Firstly, an initial basis is constructed by a small-sized proper orthogonal decomposition (POD) based on detailed solutions, see, e.g. [178, Chapter 6]. With a POD, an optimal basis for the approximation of a given snapshot sampling is constructed. The computation effort grows largely with the number of samples as a singular value decomposition of the inner-product matrix of all snapshots is computed. In our case the POD basis is used as an initial basis and a small number of snapshots is sufficient. This basis is then enhanced by a greedy algorithm based on an asymptotically reliable error estimator, see [178, Chapter 7]. There, the space is built hierarchically as in each step a snapshot with the largest estimated error is added to the space. Due to the use of an offline-online decomposable error estimator, the computational effort of each greedy step is reasonable small.

All detailed solutions satisfy the weak coupling property, hence the reduced basis functions do as well. As a result, the saddle-point problem is reduced to the following positive definite problem, posed on the reduced space $\mathbf{X}_N = \text{span}\{\boldsymbol{\zeta}_n \in \mathbf{X}_h, n = 1, \dots, N\}$: For $i = 1, \dots, K$ (where $N \geq K$) find the

eigenvalues $\lambda_{\text{red},i}^{\text{ev}}(\boldsymbol{\mu}) \in \mathbb{R}$ and the eigenfunctions $\mathbf{u}_{\text{red},i}(\boldsymbol{\mu}) \in \mathbf{X}_N$, such that

$$a(\mathbf{u}_{\text{red},i}(\boldsymbol{\mu}), \mathbf{v}_h; \boldsymbol{\mu}) = \lambda_{\text{red},i}^{\text{ev}}(\boldsymbol{\mu}) m(\mathbf{u}_{\text{red},i}(\boldsymbol{\mu}), \mathbf{v}_h; \boldsymbol{\mu}), \quad \mathbf{v}_h \in \mathbf{X}_N. \quad (3.2)$$

3.2.2.1 Offline-online decomposition

The efficiency of reduced basis methods is based on the acceleration of the reduced model in terms of the computing time. Under the assumption of an affine parameter dependence, see (3.1), this can be guaranteed by an offline-online decomposition of the reduced computation. There the assembly of the reduced system (3.2) is decomposed into a one-time computational effort and an efficient parameter-dependent part.

The main effort of a naive implementation is typically given by the assembly of the parameter-dependent stiffness and mass matrix. However, based on an affine parameter dependency, we can precompute parameter-independent parts of the stiffness matrix in the offline-phase, as

$$a(\boldsymbol{\zeta}_n, \boldsymbol{\zeta}_m; \boldsymbol{\mu}) = \sum_{q=1}^{Q_a} \theta_a^q(\boldsymbol{\mu}) a^q(\boldsymbol{\zeta}_n, \boldsymbol{\zeta}_m)$$

and analogously also for the mass matrix. In a one-time computation, we can compute $a^q(\boldsymbol{\zeta}_n, \boldsymbol{\zeta}_m)$ and $m^q(\boldsymbol{\zeta}_n, \boldsymbol{\zeta}_m)$, which is computationally expensive, as they involve the detailed system. In particular this involves all necessary numerical integration.

In the online phase, which is computed for each parameter of interest, it remains to compute $\theta_a^q(\boldsymbol{\mu})$ and $\theta_m^q(\boldsymbol{\mu})$ and to combine the matrices of the reduced dimension. The coefficients are usually fast to compute and, due to the small dimension of the reduced system, also computing the parameter-dependent reduced matrices is computationally inexpensive. In particular, no more computations involving the detailed system are necessary at this stage.

3.2.2.2 Adaptation of the error estimator

We use the error estimator presented in [112, Corollary 3.3], which can directly be used in our setting, only the offline-online decomposition needs to be modified slightly. In contrast to the original setting, where the mass matrix was assumed to be parameter-independent, we need to include the affine decomposition of the mass matrix.

The estimator is based on the residual

$$r_i(\cdot; \boldsymbol{\mu}) = a(\mathbf{u}_{\text{red},i}(\boldsymbol{\mu}), \cdot; \boldsymbol{\mu}) - \lambda_{\text{red},i}^{\text{ev}}(\boldsymbol{\mu}) m(\mathbf{u}_{\text{red},i}(\boldsymbol{\mu}), \cdot; \boldsymbol{\mu})$$

measured in the dual norm $\|\cdot\|_{\hat{\boldsymbol{\mu}}; \mathbf{X}'_h}$. The dual norm is defined for a reference parameter $\hat{\boldsymbol{\mu}} \in \mathcal{P}$, by $\|g\|_{\hat{\boldsymbol{\mu}}; \mathbf{X}'_h} = \sup_{\mathbf{v}_h \in \mathbf{X}_h} g(\mathbf{v}_h) / \hat{a}(\mathbf{v}_h, \mathbf{v}_h)^{1/2}$ for $g \in \mathbf{X}'_h$, where $\hat{a}(\mathbf{u}, \mathbf{v}) = a(\mathbf{u}, \mathbf{v}; \hat{\boldsymbol{\mu}})$. An error representation $\hat{\mathbf{e}}_i(\boldsymbol{\mu}) \in \mathbf{X}_h$ is then defined by

$$\hat{a}(\hat{\mathbf{e}}_i(\boldsymbol{\mu}), \mathbf{v}_h) = \mathbf{r}_i(\mathbf{v}_h; \boldsymbol{\mu}), \quad \mathbf{v}_h \in \mathbf{X}_h.$$

We follow [112, 149] to adapt the offline-online decomposition by adding terms corresponding to the mass components $m^q(\cdot, \cdot)$. We can relate the decomposition of the mass to the already known decomposition of the stiffness matrix, by formally defining a bilinear form $a(\mathbf{u}, \mathbf{v}; \boldsymbol{\mu}) - \lambda_{\text{red}, i}^{\text{ev}}(\boldsymbol{\mu}) m(\mathbf{u}, \mathbf{v}; \boldsymbol{\mu})$. For convenience of the reader we recall the main steps. Let $(\boldsymbol{\zeta}_n)_{1 \leq n \leq N}$ be an orthonormal basis (w.r.t. $m(\cdot, \cdot; \hat{\boldsymbol{\mu}})$) of \mathbf{X}_N and let us define $\boldsymbol{\xi}_n^q \in \mathbf{X}_N$ and $\boldsymbol{\xi}_n^{\text{m}, q} \in \mathbf{X}_N$ by

$$\begin{aligned} \hat{a}(\boldsymbol{\xi}_n^q, \mathbf{v}_h) &= a^q(\boldsymbol{\zeta}_n, \mathbf{v}_h), \quad \mathbf{v}_h \in \mathbf{X}_h, \quad 1 \leq n \leq N, \quad 1 \leq q \leq Q_a, \\ \hat{a}(\boldsymbol{\xi}_n^{\text{m}, q}, \mathbf{v}_h) &= m^q(\boldsymbol{\zeta}_n, \mathbf{v}_h), \quad \mathbf{v}_h \in \mathbf{X}_h, \quad 1 \leq n \leq N, \quad 1 \leq q \leq Q_m. \end{aligned}$$

We identify the function $\mathbf{u}_{\text{red}, i}(\boldsymbol{\mu}) \in V_N$ and its vector representation with respect to the basis $(\boldsymbol{\zeta}_n)_{1 \leq n \leq N}$ such that $(\mathbf{u}_{\text{red}, i}(\boldsymbol{\mu}))_n$ denotes the n -th coefficient. Then, given a reduced eigenpair $(\mathbf{u}_{\text{red}, i}(\boldsymbol{\mu}), \lambda_{\text{red}, i}^{\text{ev}}(\boldsymbol{\mu}))$, we have the error representation

$$\begin{aligned} \hat{\mathbf{e}}_i(\boldsymbol{\mu}) &= \sum_{n=1}^N \sum_{q=1}^{Q_a} \theta_a^q(\boldsymbol{\mu}) (\mathbf{u}_{\text{red}, i}(\boldsymbol{\mu}))_n \boldsymbol{\xi}_n^q \\ &\quad - \lambda_{\text{red}, i}^{\text{ev}}(\boldsymbol{\mu}) \sum_{n=1}^N \sum_{q=1}^{Q_m} \theta_m^q(\boldsymbol{\mu}) (\mathbf{u}_{\text{red}, i}(\boldsymbol{\mu}))_n \boldsymbol{\xi}_n^{\text{m}, q}. \end{aligned}$$

As a consequence, with $\|\mathbf{r}_i(\cdot; \boldsymbol{\mu})\|_{\hat{\boldsymbol{\mu}}; \mathbf{X}'_h}^2 = \hat{a}(\hat{\mathbf{e}}_i(\boldsymbol{\mu}), \hat{\mathbf{e}}_i(\boldsymbol{\mu}))$, the computational costly part of the error estimator can be performed in the offline phase, see [112, Section 3.3] for further details.

3.2.3 Numerical simulations

In this section, we illustrate the performance of the proposed algorithm by numerical examples. The detailed computations were performed using the isogeometric mortar code presented in the previous chapter, the reduced computations are based on RBmatlab [71, 112].

The ten parameters $\boldsymbol{\mu} = (\mu_1, \dots, \mu_{10})$, as described in Section 3.2.1, are used: the elastic moduli $\mu_1 = E_x$, $\mu_2 = E_y$, $\mu_3 = E_z$, the shear moduli $\mu_4 = G_{yz}$, $\mu_5 = G_{xz}$, $\mu_6 = G_{xy}$, Poisson's ratios $\mu_7 = \nu_{yz}$, $\mu_8 = \nu_{xz}$, $\mu_9 = \nu_{xy}$ and the scaling of the thickness μ_{10} .

Table 3.1: Reference parameter and considered parameter ranges.

	$\hat{\boldsymbol{\mu}}$	\mathcal{P}_1	\mathcal{P}_2
E_x [MPa]	14 000	13 000 – 15 000	1 000 – 20 000
E_y [MPa]	2 280	1 500 – 3 000	100 – 5 000
E_z [MPa]	1 160	750 – 1 500	100 – 2 000
G_{yz} [MPa]	465	100 – 1 000	10 – 5 000
G_{xz} [MPa]	1 080	500 – 1 500	100 – 2 500
G_{xy} [MPa]	1 640	1 000 – 2 000	100 – 5 000
ν_{yz}	0.36	0.3 – 0.4	0.1 – 0.5
ν_{xz}	0.0429	0.03 – 0.06	0.01 – 0.1
ν_{xy}	0.448	0.4 – 0.5	0.3 – 0.5

We choose the parameter values according to real parameter data given in [183, Table 7-1]. Two different scenarios are considered. In the first setting, the wood type is fixed and natural variations of the material data are taken into account, see [183, Section 7.10]. To capture the sensitivity of the violin bridge with respect to the uncertainty in the material parameter we choose a rather small parameter range around the reference parameter. The reference data of *fagus sylvatica*, the common beech, as given in Table 3.1, are chosen. The parameter range \mathcal{P}_1 is also given in Table 3.1. The thickness parameter μ_{10} varies between 1/2 and 2 with reference value 1, and the mass density is fixed in all cases as 0.720 g/cm³.

In the second test setting, also different wood types are considered, while the range of the thickness remains as before. Here we have to consider a larger parameter set, which includes the parameters for several types of wood and results the parameter set \mathcal{P}_2 , see Table 3.1. Not all parameters in this large range are admissible for the orthotropic elasticity as they do not fulfill the conditions for the positive definiteness of the elastic tensor, stated in Section 1.2.2. Consequently, we constrain the tensorial parameter space by

$$1 - (\nu_{yz}^2 E_z / E_y + \nu_{xy}^2 E_y / E_x + 2\nu_{xy}\nu_{yz}\nu_{xz} E_z / E_x + \nu_{xz}^2 E_z / E_x) \geq c_0,$$

as well as $E_x / E_y - \nu_{xy}^2 \geq c_1$ where the tolerances $c_0 = c_1 = 0.01$ are chosen, such that the wood types given in [183, Section 7.10] satisfy these conditions. We refer to Figure 1.6 for a lower-dimensional sub-manifold of \mathcal{P}_2 which includes non-admissible parameter values.

Table 3.2: The 10 smallest eigenvalues for different thickness parameters, with the other parameters fixed to the reference value.

EV	$\mu_{10} = 0.5$	$\mu_{10} = 1.0$	$\mu_{10} = 2.0$	ratio 0.5/1.0	ratio 1.0/2.0
1	0.4057	1.3238	3.6954	0.3065	0.3582
2	1.1613	3.8870	10.8071	0.2988	0.3597
3	4.4096	12.9562	26.5621	0.3403	0.4878
4	6.1371	19.3254	30.0050	0.3176	0.6441
5	13.5564	27.3642	53.2657	0.4954	0.5137
6	19.2229	46.2521	93.9939	0.4156	0.4921
7	27.6118	65.0940	111.6075	0.4242	0.5832
8	39.3674	96.8069	129.3406	0.4067	0.7485
9	57.8266	107.6749	189.6090	0.5370	0.5679
10	68.0131	130.8876	241.7695	0.5196	0.5414

First, the effect of the varying thickness parameter on the solution of our model problem is studied. In Table 3.2 the first eigenvalues for different values of the thickness are listed and we observe a remarkable and non-linear parameter dependency. A selection of corresponding eigenfunctions is shown in Figure 3.6, where the strong influence becomes even more evident, since in some cases even the shape of the eigenmode changes when varying the thickness.

In all of the following reduced basis tests, the relative error values are computed as the mean value over a large amount of random parameters. The L^2 error of the normed eigenfunctions is evaluated as the residual of the L^2 projection onto the corresponding detailed eigenspace. This takes into account possible multiple eigenvalues and the invariance of eigenfunctions with respect to a scaling by (-1) .

The first test is the simultaneous approximation of the first five eigenpairs on both parameter sets \mathcal{P}_1 and \mathcal{P}_2 . An initial basis of size 25 computed by a POD is used and then enriched by the greedy algorithm up to a basis size of 250. Figure 3.7 shows the error decay for the different eigenvalues and eigenfunctions. Very good convergence is observed, with a similar rate in all cases. As expected the magnitude of the error grows with the dimension and range of the parameter set.

Let us shortly note on the effectivities of the error estimator and the resulting speed-up. As an example, for the parameter range \mathcal{P}_1 with the thickness varying as well, the effectivities are around 4–16. With the largest reduced space, of dimension 250, the computational speed-up of the eigenvalue solver in Matlab is of a factor of 552.

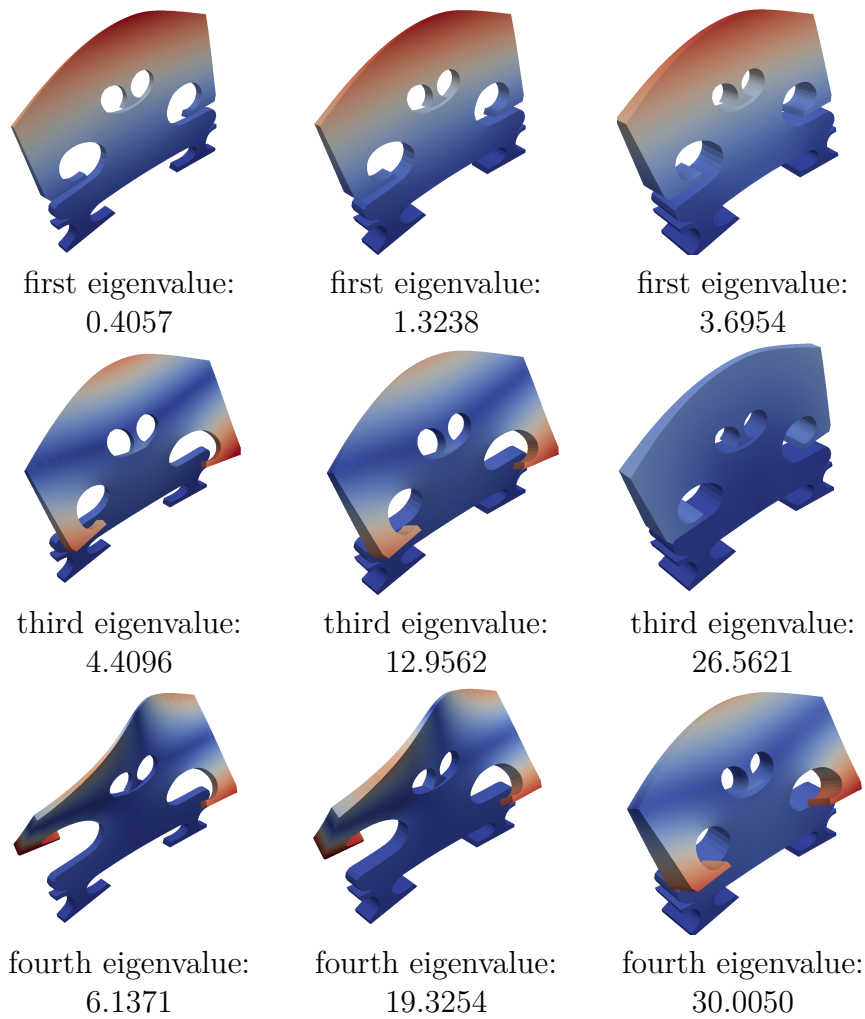


Figure 3.6: Influence of the thickness of the bridge on several eigenfunctions.

An approximation of a larger number of eigenpairs does not pose any unexpected difficulties. The error values for an approximation of the first 15 eigenpairs in the parameter set \mathcal{P}_1 are shown in Figure 3.8, where we see a good convergence behavior. The basis size which is necessary for a given accuracy increases in comparison to the previous cases of 5 eigenpairs, due to the larger number of eigenfunctions for a fixed parameter, which are orthogonal to each other.

For the relative errors for the eigenvalues, shown in Figure 3.7 and Figure 3.8, we see that for a fixed basis size, the higher eigenvalues have a better relative approximation than the lower ones. In contrast, considering the eigenfunc-

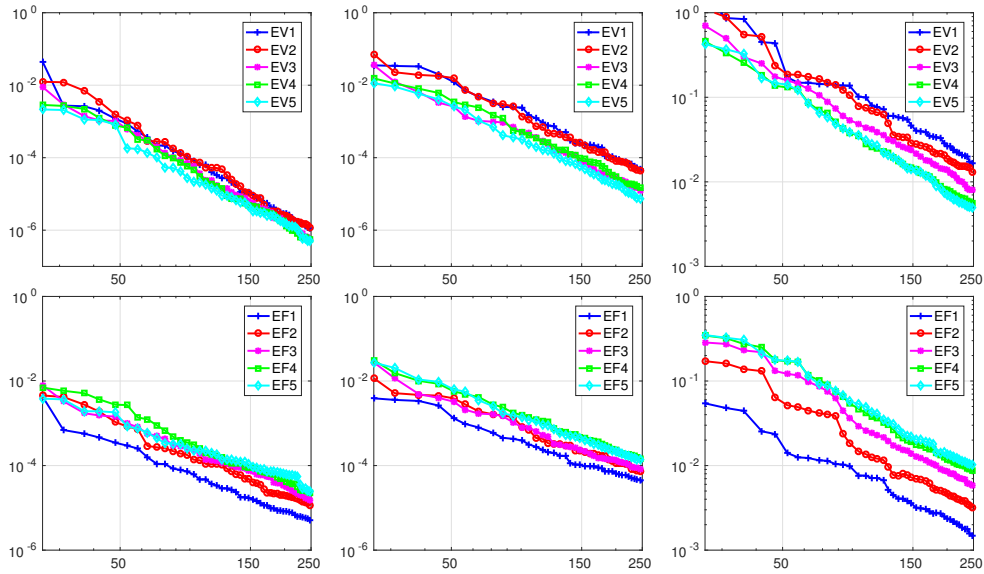


Figure 3.7: Convergence of the relative error of the eigenvalues (top) and eigenfunctions (bottom). Parameter range \mathcal{P}_1 with a fixed thickness $\mu_{10} = 1$ (left), with varying thickness $\mu_{10} \in [1/2, 2]$ (middle) and parameter range \mathcal{P}_2 with varying thickness $\mu_{10} \in [1/2, 2]$ (right).

tions, the errors of the ones associated with the lower eigenvalues are smaller compared to the ones associated with the higher eigenvalues. This observation also holds true for the absolute error in the eigenvalues. This is related to the fact that the eigenvalues depend sensitively on the parameters. In Figure 3.9, we illustrate the possible values of the first and 15th eigenvalue.

In summary, we have successfully applied a reduced basis method to an isogeometric mortar discretization approximating the vibrations of parameter-dependent violin bridges. In all of the considered test scenarios, we obtained highly accurate approximations for both eigenvalues and eigenmodes. At the

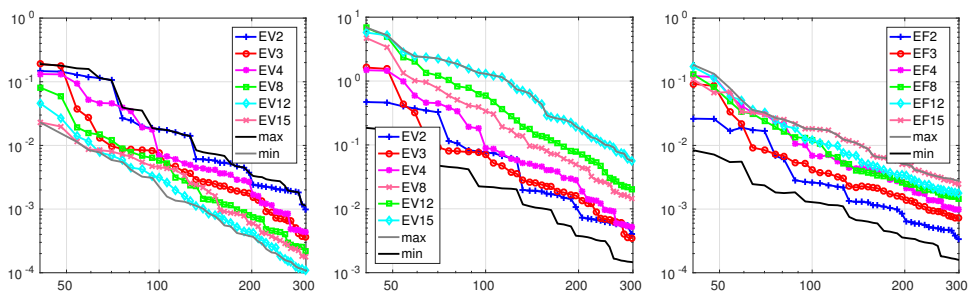


Figure 3.8: Convergence of the relative (left), absolute (middle) error of the eigenvalues and eigenfunctions (right). Parameter range \mathcal{P}_1 with varying thickness $\mu_{10} \in [1/2, 2]$, simultaneous approximating 15 eigenpairs.

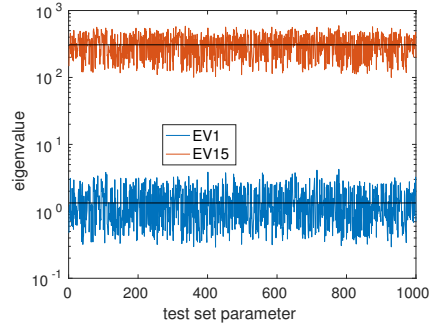


Figure 3.9: Sampling of the first and 15th eigenvalue within the parameter set \mathcal{P}_1 with varying thickness $\mu_{10} \in [1/2, 2]$ as used in the test set. Extremal values: $\min \lambda_1 = 0.29$, $\max \lambda_1 = 4.24$, $\min \lambda_{15} = 100.19$, $\max \lambda_{15} = 593.65$.

same time, we have significantly reduced the complexity and thus the run-time. Instead of a detailed saddle point system with 47 985 degrees of freedom, we solve eigenvalue problems on positive-definite systems with less than 300 degrees of freedom, a huge gain in efficiency. Of special interest is not only the variation in the material parameter, but also to take into account possible changes in the geometry. Here we have considered a variable thickness of the violin bridge, which can after a transformation be interpreted as an additional material parameter and then the indefinite saddle point problem can be avoided.

3.3 Reduced basis methods for complex geometry variations

We have seen a simple geometry parameter and its approximation using reduced basis methods. Here we extend the previous model to include also more complex geometry variations. On a reference domain $\widehat{\Omega} \subset \mathbb{R}^d$, we define m geometry variations $\varphi_i: \widehat{\Omega} \rightarrow \mathbb{R}^d$, which influence the parameter-dependent domain. The m -dimensional parameter $\boldsymbol{\mu} = (\mu_1, \dots, \mu_m)$ defines $\Omega(\boldsymbol{\mu})$ mapped from $\widehat{\Omega}$ by $\mathbf{F}(\cdot; \boldsymbol{\mu}) = \text{id} + \mu_1 \varphi_1 + \dots + \mu_m \varphi_m$, i.e., $\Omega(\boldsymbol{\mu}) = \mathbf{F}(\widehat{\Omega}; \boldsymbol{\mu})$.

Remark 3.3.1. *In the considered case, the domain is described by isogeometric patches. The structure of the spline geometry allows an easy representation and manipulation of the boundary. However, this does not trivially extend to a useful variation in the interior of the domain. This requires a careful choice of the discretization in the interior, e.g., by harmonic extensions, based on Coon's patch or even by a manual correction, see also [88, Section 4.5].*

We aim to solve the parametrized eigenvalue problem of elasticity. The

stiffness and mass integral on the domain $\Omega(\boldsymbol{\mu})$ are transformed to the reference domain by

$$\int_{\hat{\Omega}} \left((\mathbf{DF}(\hat{\mathbf{x}}; \boldsymbol{\mu}))^{-\top} \widehat{\nabla} \mathbf{u} + \widehat{\nabla} \mathbf{u}^\top (\mathbf{DF}(\hat{\mathbf{x}}; \boldsymbol{\mu}))^{-1} \right) \\ : \mathbb{C} \left((\mathbf{DF}(\hat{\mathbf{x}}; \boldsymbol{\mu}))^{-\top} \widehat{\nabla} \mathbf{v} + \widehat{\nabla} \mathbf{v}^\top (\mathbf{DF}(\hat{\mathbf{x}}; \boldsymbol{\mu}))^{-1} \right) \cdot |\det(\mathbf{DF}(\hat{\mathbf{x}}; \boldsymbol{\mu}))| \, d\hat{\mathbf{x}}$$

and

$$\int_{\hat{\Omega}} \mathbf{u}^\top \mathbf{v} |\det(\mathbf{DF}(\hat{\mathbf{x}}; \boldsymbol{\mu}))| \, d\hat{\mathbf{x}}.$$

While the deformation gradient $\mathbf{DF}(\hat{\mathbf{x}}; \boldsymbol{\mu}) = \text{Id} + \mu_1 \mathbf{D}\boldsymbol{\varphi}_1(\hat{\mathbf{x}}) + \dots + \mu_m \mathbf{D}\boldsymbol{\varphi}_m(\hat{\mathbf{x}})$ is affinely parameter-dependent, its inverse $(\mathbf{DF}(\hat{\mathbf{x}}; \boldsymbol{\mu}))^{-1} \in \mathbb{R}^{d \times d}$ is not. This prevents the use of an efficient offline-online decomposition, see Section 3.2.2.1, so we need to compute a decomposable approximation as described in the following.

3.3.1 Application of the empirical interpolation method

The *empirical interpolation method* (EIM), see, e.g., [17, 96, 178], is a convenient tool to create an affine parameter-dependent approximation to a general bilinear form. The empirical interpolation creates an approximation of parameter-dependent scalar functions

$$g(\mathbf{x}; \boldsymbol{\mu}) \approx \sum_q \alpha_q(\boldsymbol{\mu}) g_q(\mathbf{x}).$$

As it is an approximation for scalar parts of the integrand of the bilinear form, the main challenge is to identify the scalar functions on which empirical interpolation shall be applied.

We note that for a simple linear transformation of the domain, an affine parameter dependence is automatically given, see also [150, 160], and the thickness parameter considered before. This can also be used for piecewise affine transformations on a substructuring of the domain, see, e.g., [103, Chapter 6.2], [189, Chapter 5.1] and [3, 239]. In contrast, here we consider general nonlinear transformations.

Remark 3.3.2. *For the Poisson equation and problems which include related terms, the bilinear form transforms to*

$$\int_{\hat{\Omega}} \nabla \mathbf{u}^\top \mathbf{DF}(\hat{\mathbf{x}}; \boldsymbol{\mu})^{-\top} \mathbf{DF}(\hat{\mathbf{x}}; \boldsymbol{\mu})^{-1} |\det(\mathbf{DF}(\hat{\mathbf{x}}; \boldsymbol{\mu}))| \nabla \mathbf{v} \, d\hat{\mathbf{x}},$$

and it remains to handle the interior product, which is a matrix in $\mathbb{R}^{d \times d}$.

Empirical interpolation for this term was applied in several works, e.g., [46, 165, 187, 193]. Due to the symmetric gradient in the case of elasticity, the transformation is more complex to approximate.

The straightforward application of empirical interpolation needs to be computed for each of the d^2 entries of $(\mathbf{DF}(\hat{\mathbf{x}}; \boldsymbol{\mu}))^{-1}$ independently. By the product with $\mathbb{C}(\mathbf{DF}(\hat{\mathbf{x}}; \boldsymbol{\mu}))^{-1}$, a large amount of affine terms appear. We can reduce the number of terms, for which an empirical interpolation is done, by using an explicit formula of the inverse, using the adjugate matrix:

$$A^{-1} = (\det A)^{-1} \text{adj } A,$$

where for $d = 3$ and $A = \begin{pmatrix} a & b & c \\ d & e & f \\ g & h & i \end{pmatrix}$,

$$\text{adj } A = \begin{pmatrix} ei - fh & ch - bi & bf - ce \\ fg - di & ai - cg & cd - af \\ dh - eg & bg - ah & ae - bd \end{pmatrix}.$$

The matrix part $\text{adj } \mathbf{DF}(\hat{\mathbf{x}}; \boldsymbol{\mu})$ is affinely parameter-dependent, with $(m + 1)^2$ terms, due to the quadratic terms in the matrix. The stiffness integral now reads

$$\int_{\hat{\Omega}} \text{sym}(\widehat{\mathbf{V}} \mathbf{u}^\top \text{adj } \mathbf{DF}(\hat{\mathbf{x}}; \boldsymbol{\mu})) : \mathbb{C} \text{sym}(\text{adj } \mathbf{DF}(\hat{\mathbf{x}}; \boldsymbol{\mu})^\top \widehat{\mathbf{V}} \mathbf{v}) |\det(\mathbf{DF}(\hat{\mathbf{x}}; \boldsymbol{\mu}))|^{-1} d\hat{\mathbf{x}},$$

and it remains to apply empirical interpolation to $|\det \mathbf{DF}(\hat{\mathbf{x}}; \boldsymbol{\mu})|^{-1}$.

Still, a large amount of affine terms appear, since the $(m + 1)^2$ terms of the adjugate of \mathbf{u} are multiplied by those of \mathbf{v} and the terms of the empirical interpolation. However, in the following tests we obtained a significant improvement, when using the adjugate matrix, compared to the naive application of empirical interpolation on $(\mathbf{DF}(\hat{\mathbf{x}}; \boldsymbol{\mu}))^{-1}$.

In both cases, the decomposition includes a significant number of terms. Since in complex vibroacoustical computations often the solver is the bottleneck, as it is quite sensitive to the number of degrees of freedom, the reduced basis method can still be applied reasonably. However, the error estimator becomes computationally inefficient, as its decomposition contains the product of all affine parts. To avoid the frequent use of the error estimator, we consider a POD-based basis construction. The error estimator without its decomposition can still be used as an indicator, to ensure, that the size of the current reduced space is sufficiently large for the desired accuracy.

3.3.2 Geometry variations of the violin bridge

We apply the approximation introduced above to geometry variations of the violin bridge, see Figure 3.3 for the multi-patch isogeometric discretization. The bridge of a violin is a very convenient example for geometry variations, as there exists a large variety of shapes that are used in practice. In addition to the previously considered three-dimensional model, we also consider a two-dimensional model. Four boundary modifications are defined manually and

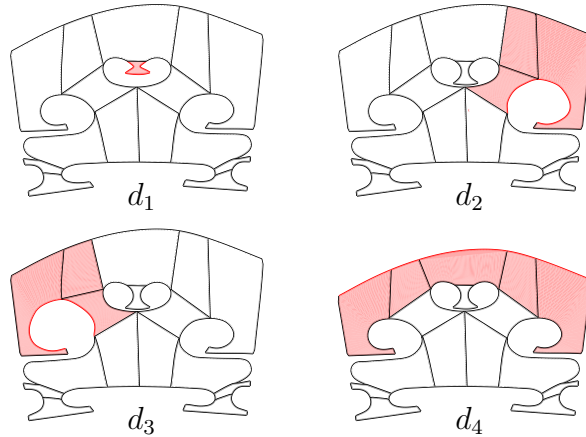


Figure 3.10: Four two-dimensional displacement modes.

then extended into the interior as described above. First, we compute the surrogate model based on the affine-decomposition using $\text{adj } \mathbf{DF}$ paired with EIM for the $(\det \mathbf{DF})^{-1}$ -term, on each patch individually. Then a POD is used to construct the reduced basis for the approximation of the first K eigenvalues.

We start with a two-dimensional model of the violin bridge and consider the four predefined deformation modes presented in Figure 3.10. Sample eigenmodes are shown in Figure 3.11 for the reference domain and a domain with maximal geometry change, $\Omega(\boldsymbol{\mu})$ with $\boldsymbol{\mu} = (1, 1, 1, 1)$. We see a large influence of the geometry parameter on the eigenvalues of interest. Using empirical interpolation with a stopping tolerance of 10^{-4} resulted in a total of 1155 parameter-independent parts of the stiffness matrix. Based on this decomposition, we perform a POD-based reduced basis model order reduction. For different numbers of eigenvalues, the convergence is shown in Figure 3.12, which is as promising as in the case of only a few affine pars. Again a large growth in the error for a given basis size is observed, when we increase K , the number of eigenvalues of interest.

For the three-dimensional setting, we extend the deformation modes in the

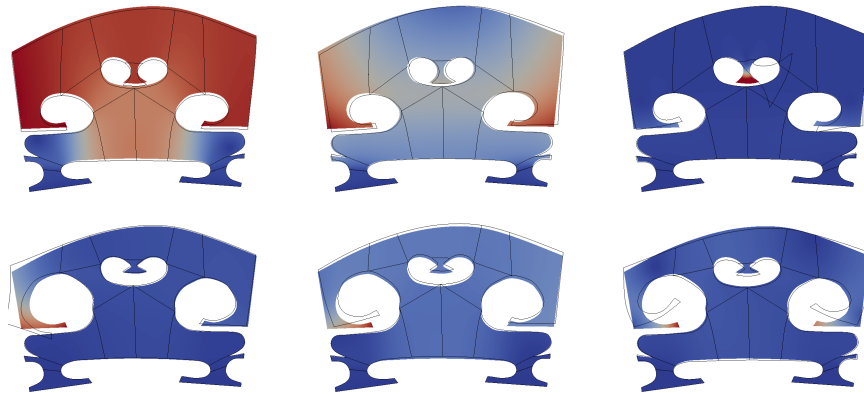


Figure 3.11: Comparison of two-dimensional eigenfunctions. From left to right: Second, third and sixth eigenvalue. Top: Undeformed. Bottom: Maximal deformation.

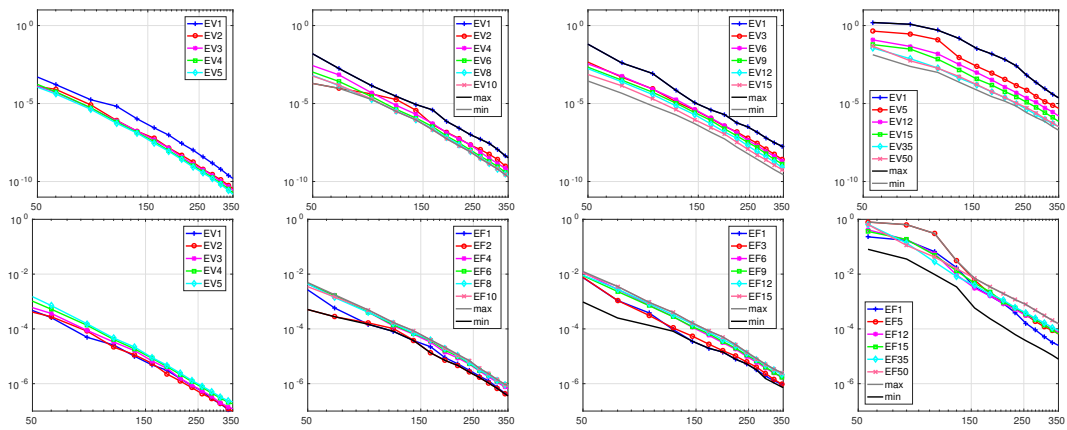


Figure 3.12: Model order reduction for the two-dimensional case. Top: Eigenvalue convergence. Bottom: Eigenfunction convergence. Left to right: $K = 5, 10, 15, 50$.

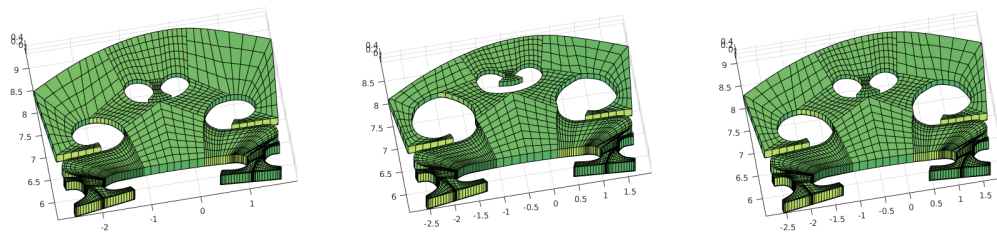


Figure 3.13: Some possible geometries. From left to right: Reference domain, maximal deformation, random deformation.

thickness direction, taking care of the non-constant thickness. See Figure 3.13 for an illustration of the geometry variations. Empirical interpolation leads to 10 010 affine matrices. This large amount is due to the curse of dimensions as the affine parts for different components multiply. In Figure 3.14 the convergence of a POD-based reduced basis method is shown. As in the two-dimensional setting, we observe a fast convergence of the eigenvalues and eigenfunctions even for such a challenging problem.

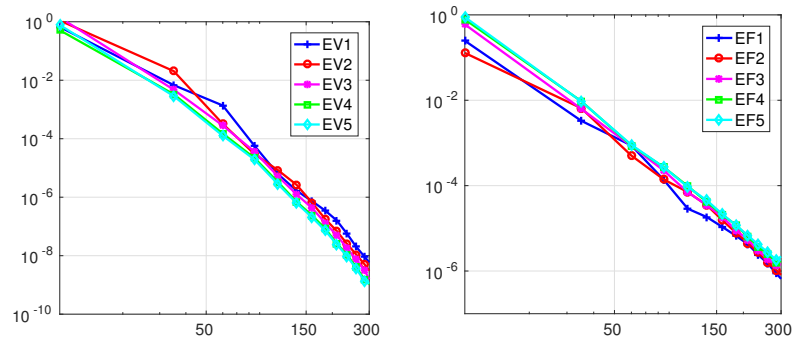


Figure 3.14: Model order reduction for the three-dimensional case with $K = 5$. Left: Eigenvalue convergence. Right: Eigenfunction convergence.

In summary, we have seen the possibility to apply reduced basis methods to geometry variations combined with the empirical interpolation method even for linear elasticity. The amount of affine matrices limits the successful use of this model reduction to situations where the geometry handling, integration or the eigenvalue solver are the bottleneck of the detailed system. The two-dimensional example was significantly more efficient than the three-dimensional problem as it is less affected by the curse of dimensionality. More sophisticated methods to generate a decomposable approximation of the stiffness and mass matrix, e.g., the multi-component empirical interpolation method introduced in [213, Chapter 4.3.2], could significantly improve the efficiency especially for three-dimensional problems.

4 A priori trace and flux estimates for Signorini-type problems

In this chapter, we consider the Poisson equation with unilateral Signorini boundary conditions and provide optimal order convergence rates in norms associated with the Signorini boundary Γ_S . More precisely, we consider a priori error estimates for the trace in the $H_{00}^{1/2}(\Gamma_S)$ norm and for the Lagrange multiplier, i.e., the flux, in the $H^{-1/2}(\Gamma_S)$ norm. As a corollary we show improved a priori estimates in the L^2 norm for the primal variable on Ω and for the dual variable on Γ_S . While convergence rates for traces can often be established using estimates in the domain, these rates are typically not optimal. The order of the finite element approximation of variational inequalities in the $L^2(\Omega)$ norm is firstly addressed in the early paper [163]. However, the theoretical results are limited to very special situations. A generalization can be found in [54, 205], but for a straightforward application to Signorini problems, the required dual regularity is lacking, so we do not follow these ideas. Recently introduced techniques allow optimal estimates on interfaces and boundaries for linear problems under moderately stronger regularity assumptions, see [5, 6, 157, 158, 222]. These techniques can also be used to compensate a lack of regularity in the dual problem, see [110]. A reformulation of the primal variational inequality on the boundary, as applied in [73, 200, 203], and a Strang lemma for variational inequalities allow us to use these techniques for the non-linear Signorini problem.

Results of this section have been published by the author in collaboration with O. Steinbach and B. Wohlmuth in the article “Trace and flux a priori error estimates in finite-element approximations of Signorini-type problems” in the year 2016, [204].

4.1 Optimal a priori estimates

In this section the problem setting and main result are stated. We state the discretization of the Signorini-type problem as a primal formulation. Two reformulations which play an important part in the analysis are briefly recalled: a saddle point problem and a variational formulation of the Schur complement.

4.1.1 Primal discretization and main result

We consider the Poisson equation with Signorini-type boundary conditions, see Section 1.2.3 for an introduction. We assume Ω to be polyhedral and convex and $\Gamma_N = \emptyset$. For simplicity of notation, we assume Γ_S to be one face of the boundary $\partial\Omega$. For $\hat{f} \in L^2(\Omega)$, $\hat{g} \in H^{1/2}(\Gamma_S)$, we consider:

$$\begin{aligned} -\Delta u &= \hat{f} && \text{in } \Omega, \\ u &= 0 && \text{on } \Gamma_D, \\ u &\leq \hat{g}, \quad \partial_{\mathbf{n}} u \leq 0, \quad (u - \hat{g}) \partial_{\mathbf{n}} u = 0 && \text{on } \Gamma_S. \end{aligned}$$

We assume that \hat{g} is positive in a neighborhood of $\partial\Gamma_S$ and that the actual contact set $\Gamma^{\text{act}} = \{\mathbf{x} \in \Gamma_S : u(\mathbf{x}) = \hat{g}(\mathbf{x})\}$ is a compact subset of Γ_S .

Remark 4.1.1. *As remarked in Section 1.2.3.2, the regularity of Signorini-type problems is typically restricted to be not more than $H^{5/2-\varepsilon}(\Omega)$. We are interested in the effects of the approximation caused by the Signorini boundary condition, so let us assume, that the regularity is not reduced any further, i.e., that $u \in H^{5/2-\varepsilon}(\Omega)$.*

4.1.1.1 Weak formulations

The non-linear Signorini boundary condition yields a constrained minimization problem, see, e.g., [94, 130]. We consider $V = H_D^1(\Omega)$ and its trace space restricted to Γ_S as $W = H_{00}^{1/2}(\Gamma_S)$. We define the convex set of admissible functions by $K = \{v \in V : v|_{\Gamma_S} \leq \hat{g}\}$ and consider the bilinear and linear forms $a(u, v) = \int_{\Omega} \nabla u^\top \nabla v \, d\mathbf{x}$ and $f(v) = \int_{\Omega} \hat{f} v \, d\mathbf{x}$.

The weak solution $u \in K$ then satisfies the variational inequality

$$a(u, v - u) \geq f(v - u), \quad v \in K. \tag{4.1}$$

For the discretization, we assume a family of shape-regular simplicial triangulations \mathcal{T}_h . We denote by N_{V_h} the number of vertices of the triangulation except the ones on $\bar{\Gamma}_D$ and by N_{M_h} the number of vertices on Γ_S . Note that, since the Signorini boundary is a face of the polyhedral domain, both boundary parts are exactly represented by the triangulation. We denote the discrete primal space using first order conforming finite elements as V_h , spanned by the nodal Lagrange basis φ_i , $i = 1, \dots, N_{V_h}$ and denote the discrete trace space restricted to Γ_S by W_h . For simplicity let us assume that \hat{g} is affine and strictly positive. The discretization of (4.1) then reads: Find $u_h \in K_h = \{v_h \in V_h : v_h|_{\Gamma_S} \leq \hat{g}\}$,

such that

$$a(u_h, v_h - u_h) \geq f(v_h - u_h), \quad v_h \in K_h. \quad (4.2)$$

In the more general case a suitable approximation of \hat{g} can be used in the definition of K_h . We note that since \hat{g} is affine one has $K_h \subset K$.

4.1.1.2 Main results

$H^1(\Omega)$ error estimates of order h for contact problems are given in [115] under some regularity assumption on the active set, as well as more recently in [72, 105] under weaker assumptions on the solution.

The main result of this chapter is summarized in the following theorem and proved in the following sections.

Theorem 4.1.2. *Let u be the solution of (4.1) and u_h be the solution of (4.2). Assuming $u \in H^{5/2-\varepsilon}(\Omega)$, $\varepsilon \in (0, 1/2]$ fixed, we get*

$$\|u - u_h\|_{H_{00}^{1/2}(\Gamma_S)} \leq ch^{3/2-\varepsilon} \|u\|_{H^{5/2-\varepsilon}(\Omega)}.$$

Note that the constant c depends on ε and tends to infinity if ε tends to zero.

Based on this trace estimate, we can easily improve the $L^2(\Omega)$ estimate, up to the order $h^{3/2-\varepsilon}$. Additionally we show optimal approximation results for the boundary flux $\partial_{\mathbf{n}}u|_{\Gamma_S}$ in the natural $H^{-1/2}(\Gamma_S)$ norm.

4.1.2 Equivalent reformulations

Three different but equivalent variational formulations play a crucial role in our analysis. Since \hat{g} is affine, the pointwise condition $u_h \leq \hat{g}$ can be reformulated in a variationally consistent way, using a biorthogonal dual basis. This choice yields the second variational formulation, a saddle point formulation, where the primal solution as well as the flux on the Signorini boundary are unknowns. The third formulation, a variational formulation for the Schur complement posed on Γ_S , is adequate to bound the primal trace error. However, the Schur complement of the discrete formulation differs from the Galerkin discretization of the continuous Schur complement.

4.1.2.1 Saddle point formulation

The second formulation, a saddle point problem, is widely used for Signorini-type as well as contact problems. It can be obtained from the theory of constrained optimization, see for example [74, 121]. Associated to the dual space

of W , $M = H^{-1/2}(\Gamma_S)$, is the convex cone $M^+ = \{\mu \in M: \langle v, \mu \rangle_{\Gamma_S} \geq 0, v \in W, v \geq 0\}$, where $\langle \cdot, \cdot \rangle_{\Gamma_S}$ denotes the duality pairing between $H_{00}^{1/2}(\Gamma_S)$ and $H^{-1/2}(\Gamma_S)$.

The saddle point problem reads: Find $(u, \lambda) \in V \times M^+$, such that

$$a(u, v) + \langle v, \lambda \rangle_{\Gamma_S} = f(v), \quad v \in V, \quad (4.3a)$$

$$\langle u, \mu - \lambda \rangle_{\Gamma_S} \leq \langle \hat{g}, \mu - \lambda \rangle_{\Gamma_S}, \quad \mu \in M^+. \quad (4.3b)$$

Let the vertices be enumerated such that the first N_{M_h} vertices lie on Γ_S . Associated to the primal Lagrange basis functions $\varphi_i, i = 1, \dots, N_{M_h}$, which do not vanish on Γ_S , are biorthogonal basis functions $\psi_i \in L^2(\Gamma_S), i = 1, \dots, N_{M_h}$, satisfying $\langle \varphi_j, \psi_i \rangle_{\Gamma_S} = \delta_{ij} \langle \varphi_j, 1 \rangle_{\Gamma_S}$. The standard choice are piecewise linear basis functions with the same support on Γ_S as the corresponding primal basis function. This uniquely determines the basis by an inversion of the local mass matrix, see for example [229]. The discrete dual space M_h is spanned by the biorthogonal basis functions $\psi_i \in L^2(\Gamma_S)$, and a uniform inf-sup stability for the discrete spaces V_h and M_h holds, see [228]. The convex cone M^+ is discretized as the positive span of the biorthogonal basis functions, i.e., $M_h^+ = \{\sum_{i=1}^{N_{M_h}} \alpha_i \psi_i, \alpha_i \geq 0\}$. A crosspoint modification is in practice not required due to our assumption that Γ^{act} is a compact subset of Γ_S .

The discretized saddle point formulation of (4.3) then reads: Find $(u_h, \lambda_h) \in V_h \times M_h^+$, such that

$$a(u_h, v_h) + \langle v_h, \lambda_h \rangle_{\Gamma_S} = f(v_h), \quad v_h \in V_h, \quad (4.4a)$$

$$\langle u_h, \mu_h - \lambda_h \rangle_{\Gamma_S} \leq \langle \hat{g}, \mu_h - \lambda_h \rangle_{\Gamma_S}, \quad \mu_h \in M_h^+. \quad (4.4b)$$

We point out, that $M_h \subset M$ but the discrete cone M_h^+ is not included in M^+ . The equivalence of the primal formulation (4.2) with a pointwise constraint and the weak constraint of the saddle point problem holds since \hat{g} is affine. In the more general case, one can define K_h as $\{v_h \in V_h: \langle v_h, \lambda_h \rangle_{\Gamma_S} \leq \langle \hat{g}, \lambda_h \rangle_{\Gamma_S}, \lambda_h \in M_h^+\}$. Then (4.2) and (4.4) are still equivalent.

4.1.2.2 Reformulation as a Schur complement system

Due to the fact, that the inequality constraint is solely located on the boundary, we can easily rewrite (4.3) and (4.4) as Schur complement systems. On the continuous level, we define the Steklov–Poincaré operator $S: W \rightarrow M$ by solving the Dirichlet problem

$$-\Delta w_z = 0 \text{ in } \Omega, \quad w_z = 0 \text{ on } \Gamma_D, \quad w_z = z \text{ on } \Gamma_S,$$

for any $z \in W$ and defining $Sz = \partial_{\mathbf{n}} w_z|_{\Gamma_S}$.

The continuous Newton potential $N\hat{f} = -\partial_{\mathbf{n}} \hat{w}_{\hat{f}}|_{\Gamma_S} \in M$ is defined based on the solution of the homogeneous Dirichlet problem $-\Delta \hat{w}_{\hat{f}} = \hat{f}$ in Ω and $\hat{w}_{\hat{f}} = 0$ on $\partial\Omega$. Based on these operators, we can formulate the Schur complement system which is a variational inequality on the Signorini boundary. The primal trace $u_S = u|_{\Gamma_S} \in K_S = \{v \in H_{00}^{1/2}(\Gamma_S) : v \leq \hat{g}\}$ solves

$$\langle v - u_S, Su_S \rangle_{\Gamma_S} \geq \langle v - u_S, N\hat{f} \rangle_{\Gamma_S}, \quad v \in K_S. \quad (4.5)$$

An equivalent characterization of the Steklov–Poincaré operator is possible as the Lagrange multiplier $\lambda_z = -Sz$ of a saddle point problem where $(w_z, \lambda_z) \in V \times M$ solves

$$a(w_z, v) + \langle v, \lambda_z \rangle_{\Gamma_S} = 0, \quad v \in V, \quad (4.6a)$$

$$\langle w_z, \mu \rangle_{\Gamma_S} = \langle z, \mu \rangle_{\Gamma_S}, \quad \mu \in M, \quad (4.6b)$$

which corresponds to weakly imposed Dirichlet conditions, see [16]. The continuous Newton potential can also be defined as the Lagrange multiplier of an analogue saddle point formulation with a non-trivial right hand side in (4.6a) but a trivial one in (4.6b). The Steklov–Poincaré operator and the Newton potential map Dirichlet data and volume data to Neumann data, respectively. They have several applications, for example in domain decomposition and boundary element methods, see [180, 201, 202, 214].

Using a mixed finite element approximation to the above Dirichlet problem (4.6), we define a mesh-dependent Steklov–Poincaré operator $S_h : W \rightarrow M_h$ by $S_h z = -\lambda_{z,h}$, where $(w_{z,h}, \lambda_{z,h}) \in V_h \times M_h$ solves

$$a(w_{z,h}, v_h) + \langle v_h, \lambda_{z,h} \rangle_{\Gamma_S} = 0, \quad v_h \in V_h, \quad (4.7a)$$

$$\langle w_{z,h}, \mu_h \rangle_{\Gamma_S} = \langle z, \mu_h \rangle_{\Gamma_S}, \quad \mu_h \in M_h. \quad (4.7b)$$

An analogue discretization yields a mesh-dependent Newton potential $N_h \hat{f}$. Denote by W_h the trace space of V_h . Up to scaling factors, the matrix formulation for $S_h|_{W_h}$ and $N_h \hat{f}$ coincide with the discrete Schur complement system of the matrix formulation of (4.2) by construction. The uniform continuity of S_h directly follows from the saddle point theory using the inf-sup stability of the discrete spaces, while the uniform W_h -ellipticity follows using basic properties of discrete harmonic functions, e.g., [214, Lemma 4.10]. Precisely, one has $\langle v_h, S_h v_h \rangle_{\Gamma_S} = a(w_{v,h}, w_{v,h})$, where $w_{v,h} \in V_h$ is the discrete harmonic extension of $v_h \in W_h$, hence $\langle v_h, S_h v_h \rangle_{\Gamma_S} = |w_{v,h}|_{H^1(\Omega)}^2 \geq c \|v_h\|_{H_{00}^{1/2}(\Gamma_S)}^2$.

The Schur complement system of (4.2) can be represented as an approxima-

tive discretization of (4.5). For $K_{S,h} = \{v_h \in W_h : v_h \leq g\}$ find $u_{S,h} \in K_{S,h}$, such that

$$\langle v_h - u_{S,h}, S_h u_{S,h} \rangle_{\Gamma_S} \geq \langle v_h - u_{S,h}, N_h \hat{f} \rangle_{\Gamma_S}, \quad v_h \in K_{S,h}. \quad (4.8)$$

The three weak formulations (4.1), (4.3) and (4.5) are equivalent as well as the three discrete variational problems (4.2), (4.4) and (4.8).

4.2 Proof of the a priori estimates

Since the Galerkin formulation of the continuous Schur complement differs from the discrete Schur complement, a Strang lemma is now applied, and the error is related to the difference of two Steklov–Poincaré operators. A rate for the primal error in the $H_{00}^{1/2}(\Gamma_S)$ norm is proven based on anisotropic norms and dual problems with local data. As a corollary improved rates for the $L^2(\Omega)$ norm are shown.

4.2.1 Application of a Strang lemma

While u solves the variational inequality (4.5) with the operators S and N , the discrete solution u_h solves the variational inequality (4.8) with the mesh-dependent operators S_h and N_h . In this subsection, we show that the $H_{00}^{1/2}(\Gamma_S)$ error can be bounded by two terms. The first term is the $H^{-1/2}(\Gamma_S)$ norm of the difference between $N\hat{f} - S(u|_{\Gamma_S}) = \lambda$ and $N_h\hat{f} - S_h(u|_{\Gamma_S}) = \tilde{\lambda}_h \in M_h$. Note that $\tilde{\lambda}_h$ is the discrete dual solution of the linear saddle point problems defining the Dirichlet–Neumann map, see Equation (4.7). Associated with $\tilde{\lambda}_h$ is $\tilde{u}_h = \hat{w}_{f,h} + w_{u|_{\Gamma_S},h}$ and $(\tilde{u}_h, \tilde{\lambda}_h) \in V_h \times M_h$ solves

$$\begin{aligned} a(\tilde{u}_h, v_h) + \langle v_h, \tilde{\lambda}_h \rangle_{\Gamma_S} &= f(v_h), \quad v_h \in V_h, \\ \langle \tilde{u}_h, \mu_h \rangle_{\Gamma_S} &= \langle u, \mu_h \rangle_{\Gamma_S}, \quad \mu_h \in M_h. \end{aligned}$$

The second term is the discretization error of the variational inequality on the boundary (4.5). Let $\bar{u}_h \in K_{S,h}$ be such that

$$\langle v_h - \bar{u}_h, S\bar{u}_h \rangle_{\Gamma_S} \geq \langle v_h - \bar{u}_h, N\hat{f} \rangle_{\Gamma_S}, \quad v_h \in K_{S,h}. \quad (4.9)$$

Lemma 4.2.1. *The trace error of the Signorini problem (4.1) can be bounded by*

$$\|u - u_h\|_{H_{00}^{1/2}(\Gamma_S)} \leq c \|\lambda - \tilde{\lambda}_h\|_{H^{-1/2}(\Gamma_S)} + c \|u - \bar{u}_h\|_{H_{00}^{1/2}(\Gamma_S)}.$$

Proof. The proof of this lemma follows the lines of [168, Theorem 3.2]. Since the proof is fundamental, we work it out. We start with the trivial triangle inequality

$$\|u - u_h\|_{H_{00}^{1/2}(\Gamma_S)} \leq \|u - \bar{u}_h\|_{H_{00}^{1/2}(\Gamma_S)} + \|\bar{u}_h - u_h\|_{H_{00}^{1/2}(\Gamma_S)}.$$

For the second term $\bar{u}_h - u_h$, we use the W_h -ellipticity of the mesh-dependent Steklov–Poincaré operator and apply the variational inequalities on the Signorini boundary (4.8) and (4.9):

$$\begin{aligned} c \|\bar{u}_h - u_h\|_{H_{00}^{1/2}(\Gamma_S)}^2 &\leq \langle \bar{u}_h - u_h, S_h(\bar{u}_h - u_h) \rangle_{\Gamma_S} \\ &\leq \langle \bar{u}_h - u_h, S_h \bar{u}_h \rangle_{\Gamma_S} + \langle \bar{u}_h - u_h, N\hat{f} - N_h\hat{f} \rangle_{\Gamma_S} - \langle \bar{u}_h - u_h, S\bar{u}_h \rangle_{\Gamma_S} \\ &= \langle \bar{u}_h - u_h, N\hat{f} - S\bar{u}_h - (N_h\hat{f} - S_h\bar{u}_h) \rangle_{\Gamma_S} \\ &\leq \|\bar{u}_h - u_h\|_{H_{00}^{1/2}(\Gamma_S)} \|N\hat{f} - S\bar{u}_h - (N_h\hat{f} - S_h\bar{u}_h)\|_{H^{-1/2}(\Gamma_S)}. \end{aligned}$$

Using the boundedness of the operators and once again the triangle inequality, we get

$$\begin{aligned} \|\bar{u}_h - u_h\|_{H_{00}^{1/2}(\Gamma_S)} &\leq c \|N\hat{f} - Su - (N_h\hat{f} - S_hu)\|_{H^{-1/2}(\Gamma_S)} \\ &\quad + c \|S(u - \bar{u}_h)\|_{H^{-1/2}(\Gamma_S)} + c \|S_h(u - \bar{u}_h)\|_{H^{-1/2}(\Gamma_S)} \\ &\leq c \|\lambda - \tilde{\lambda}_h\|_{H^{-1/2}(\Gamma_S)} + c \|u - \bar{u}_h\|_{H_{00}^{1/2}(\Gamma_S)}. \quad \square \end{aligned}$$

A bound of $u - \bar{u}_h$ can be shown using Falk’s lemma, see [79, Theorem 1], which is an analogue result to Céa’s lemma for variational inequalities. Since \hat{g} is affine, the discretization of the variational inequality is conforming in the sense, that $K_{S,h} \subset K_S$, and Falk’s lemma reads

$$\|u - \bar{u}_h\|_{H_{00}^{1/2}(\Gamma_S)} \leq c \inf_{v_h \in K_{S,h}} \left(\|u - v_h\|_{H_{00}^{1/2}(\Gamma_S)} + \langle \lambda, u - v_h \rangle_{\Gamma_S}^{1/2} \right). \quad (4.10)$$

Lemma 4.2.2. *Let $u \in K_S$ be the solution to the variational inequality on the boundary (4.5) and $\bar{u}_h \in K_{S,h}$ the Galerkin approximation, see Equation (4.9). Assuming $u \in H^{5/2-\varepsilon}(\Omega)$, we get*

$$\|u - \bar{u}_h\|_{H_{00}^{1/2}(\Gamma_S)} \leq ch^{3/2-\varepsilon} |u|_{H^{5/2-\varepsilon}(\Omega)}.$$

Proof. This type of estimate was already considered in the context of boundary element methods, in [200, Theorem 3.1] and [203, Section 3], where additional assumptions on the boundary of the active set were made. To keep this text self-contained, we present a proof, based on techniques for $H^1(\Omega)$ estimates.

In this proof only the Signorini boundary Γ_S is considered, so any notation refers to \mathbb{R}^{d-1} . We introduce the triangulation \mathcal{T}_h^S on the Signorini boundary which is induced by the triangulation of Ω . We note, that the induced triangulation on the Signorini boundary is also shape-regular and denote by h_{τ_h} the diameter of an element $\tau_h \in \mathcal{T}_h^S$.

We use recently introduced techniques from [72] based on non-standard L^1 and L^2 estimates. We use Falk's lemma (4.10) with $v_h = J_h u \in K_{S,h}$, where for $d = 2$, J_h is the piecewise linear nodal interpolation operator and for $d = 3$, J_h is the Chen–Nochetto operator, see [49]. It remains to bound

$$\langle \lambda, u - J_h u \rangle_{\Gamma_S} = \sum_{\tau_h \in \mathcal{T}_h^S} \int_{\tau_h} \lambda(u - J_h u) \, d\gamma.$$

One of the main ideas of this proof is to derive two estimates for each element, where dependent of the measure of the active area in a surrounding patch one of the two estimates is applied. Given any $\tau_h \in \mathcal{T}_h^S$, we set $\Delta_{\tau_h} = \tau_h$ for $d = 2$ and $\Delta_{\tau_h} \subset \Gamma_S$ as the patch surrounding τ_h for $d = 3$.

On the patch, we define the local active area $\Delta_{\tau_h}^{\text{act}} = \Delta_{\tau_h} \cap \Gamma^{\text{act}}$ and the local inactive area $\Delta_{\tau_h}^{\text{inact}} = \Delta_{\tau_h} \setminus \Delta_{\tau_h}^{\text{act}}$, see Figure 4.1.

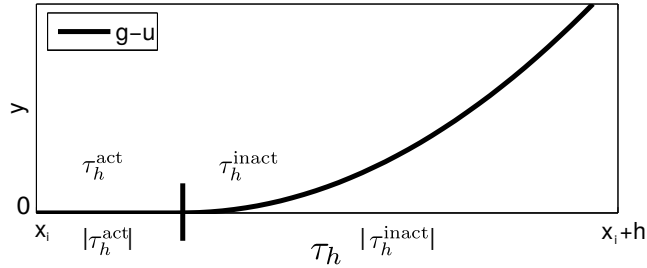


Figure 4.1: Active and inactive area within one element τ_h for $d = 2$, i.e., $\Delta_{\tau_h} = \tau_h$.

Note that by construction only the elements with $|\Delta_{\tau_h}^{\text{act}}| > 0$ and $|\Delta_{\tau_h}^{\text{inact}}| > 0$ are of interest, otherwise either λ or $u - J_h u$ is equal to zero. Recently developed non-standard estimates for u and λ , see, [72], yield

$$\begin{aligned} & \int_{\tau_h} \lambda(u - J_h u) \, d\gamma \\ & \leq c \min \left(\frac{|\Delta_{\tau_h}|^{1/2}}{|\Delta_{\tau_h}^{\text{inact}}|^{1/2}}, \frac{|\Delta_{\tau_h}|^{1/2}}{|\Delta_{\tau_h}^{\text{act}}|^{1/2}} \right) h_{\tau_h}^{3-2\varepsilon} \left(|\lambda|_{H^{1-\varepsilon}(\Delta_{\tau_h})}^2 + |u|_{H^{2-\varepsilon}(\Delta_{\tau_h})}^2 \right). \end{aligned}$$

Since $|\Delta_{\tau_h}^{\text{act}}| + |\Delta_{\tau_h}^{\text{inact}}| = |\Delta_{\tau_h}|$, one of the measures is greater than or equal to

$|\Delta_{\tau_h}|/2$. Summing over the elements and applying the trace inequality yields the desired estimate. \square

4.2.2 A priori estimate of the primal trace

In this section, an upper bound for $\|\lambda - \tilde{\lambda}_h\|_{H^{-1/2}(\Gamma_S)}$ is shown which concludes the primal trace estimate in Theorem 4.1.2. The Lagrange multiplier arises from a linear Dirichlet problem with a weak enforcement of the boundary values which is covered by the problem formulation in [158]. However, the required regularity of $B_{2,1}^{5/2}(\Omega)$ is not given in our case. Thus we have to generalize these results. We follow the lines of [158] but will not work with the Besov space $B_{2,1}^{5/2}(\Omega)$. Reducing the regularity from $B_{2,1}^{5/2}(\Omega)$ to $H^{5/2-\varepsilon}(\Omega)$ automatically results in a reduced convergence order, but we do not lose a log-term.

The first two subsections collect some technical tools for the proof which is carried out in Subsection 4.2.2.3. Firstly, for a Scott–Zhang operator, we show optimal approximation results in anisotropic norms. Secondly, for two dual problems, estimates in these norms are shown. As a corollary of the main result, we show improved rates in the $L^2(\Omega)$ norm.

4.2.2.1 Anisotropic norms and quasi-interpolation results

Estimating the dual solution on the boundary can be related to bounds of the primal solution in a neighborhood of $\partial\Omega$. We define strips in Ω around the boundary of width δ by $\mathfrak{S}(\delta) = \{\mathbf{x} \in \Omega : \text{dist}(\mathbf{x}, \partial\Omega) \leq \delta\}$. Using a dual Neumann problem with local volume data, we can relate the dual error to the primal error in a strip $\mathfrak{S}(ch)$. As a technical tool to derive local error estimates for the dual problems on these strips, we use anisotropic norms as in [157, 158, 222]. We simplify the original definition, which was based on a technical decomposition of the domain into ‘cylinders’. Instead, we use an intuitive decomposition into triangles or pyramids, based on the faces of the polygonal domain.

For a formal definition, we first decompose the domain Ω into a set of patches which are triangles if $d = 2$ and pyramids if $d = 3$. Each patch connects one face with the barycenter of Ω . Since Ω is convex the barycenter \mathbf{x}_c lies in the interior of Ω . Let an enumeration of the faces be given by γ_i , $i = 1, \dots, N_\gamma$, and consider one face γ_i . The patch Ω_i is the triangle and pyramid in 2D and 3D respectively, with γ_i as base side and \mathbf{x}_c as the top. Obviously $\bar{\Omega} = \cup_{i=1}^{N_\gamma} \bar{\Omega}_i$, see Figure 4.2. For each patch Ω_i , we define the anisotropic norm $L(\mathbf{p}, 2; \Omega_i)$ based on a decomposition of the patch into a $(d-1)$ -dimensional part parallel to the face γ_i and the one dimensional distance to the face. Given $i \in \{1, \dots, N_\gamma\}$, without any loss of generality, we assume that γ_i lies in the x_1, \dots, x_{d-1} -plane

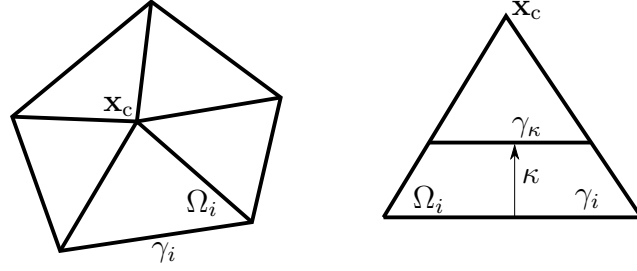


Figure 4.2: Left: Decomposition of a 2D domain into the patches. Right: One patch after a suitable rotation.

and Ω lies in the positive half space $\{(\mathbf{x}', \kappa), \mathbf{x}' \in \mathbb{R}^{d-1}, \kappa \geq 0\}$. We denote by $\gamma_\kappa = \{(\mathbf{x}', \kappa) \in \Omega_i, \mathbf{x}' \in \mathbb{R}^{d-1}\}$ for $\kappa \geq 0$, the part in Ω_i parallel to γ_i , having the distance κ to the plane of γ_i . We note that for $\mathbf{x} = (\mathbf{x}', \kappa) \in \Omega_i$ it holds $c\kappa \leq \text{dist}(\mathbf{x}, \partial\Omega) \leq \kappa$. We have $\gamma_\kappa = \emptyset$ for $\kappa < 0$ and $\kappa \geq D$, where D is the diameter of Ω . By the Fubini–Tonelli formula, the integral over Ω_i can be decomposed as

$$\int_{\Omega_i} v \, dx = \int_{\kappa=0}^D \int_{\gamma_\kappa} v \, d\mu \, d\kappa,$$

where $d\mu$ denotes the $(d-1)$ -dimensional Lebesgue measure. We define anisotropic norms $L(\mathbf{p}, 2; \Omega_i)$, $1 \leq \mathbf{p} \leq \infty$, by

$$\begin{aligned} \|v\|_{L(\mathbf{p}, 2; \Omega_i)}^{\mathbf{p}} &= \int_{\kappa=0}^D \left(\int_{\gamma_\kappa} v^2 \, d\mu \right)^{\mathbf{p}/2} d\kappa, \quad 1 \leq \mathbf{p} < \infty, \\ \|v\|_{L(\infty, 2; \Omega_i)} &= \text{ess sup}_{\kappa \in (0, D)} \left(\int_{\gamma_\kappa} v^2 \, d\mu \right)^{1/2}. \end{aligned}$$

Adding the components of each patch, we define anisotropic norms $L(\mathbf{p}, 2)$ on the entire domain Ω :

$$\begin{aligned} \|v\|_{L(\mathbf{p}, 2)}^{\mathbf{p}} &= \sum_{i=1}^{N_\gamma} \|v\|_{L(\mathbf{p}, 2; \Omega_i)}^{\mathbf{p}}, \quad 1 \leq \mathbf{p} < \infty, \\ \|v\|_{L(\infty, 2)} &= \max_{i=1, \dots, N_\gamma} \|v\|_{L(\infty, 2; \Omega_i)}. \end{aligned}$$

Note that the patches cover Ω without any overlap and the $L(2, 2)$ norm coincides with the $L^2(\Omega)$ norm.

The Hölder inequality $\int_\Omega fg \, dx \leq \|f\|_{L(\mathbf{p}, 2)} \|g\|_{L(\mathbf{q}, 2)}$ for $1/\mathbf{p} + 1/\mathbf{q} = 1$ follows from the one-dimensional Hölder inequality. Furthermore an interpolation result analogue to $L^{\mathbf{p}}$ spaces is valid, see, e.g., [207].

Lemma 4.2.3. *For $1 < \mathbf{p} < \infty$ and $1/\mathbf{p} + 1/\mathbf{q} = 1$, one has*

$$L(\mathbf{p}, 2) = (L(1, 2), L(\infty, 2))_{1/\mathbf{q}, \mathbf{p}}.$$

Proof. For convenience of the reader, we sketch the main steps. Consider any patch Ω_i , $i \in \{1, \dots, N_\gamma\}$. For any $1 \leq \mathbf{r} \leq \infty$ and $v \in L(\mathbf{r}, 2; \Omega_i)$, $I = (0, D)$, consider $f_v \in L^{\mathbf{r}}(I)$ which is defined for almost every $\kappa \in I$ by $f_v(\kappa) = \|v\|_{L^2(\gamma_\kappa)}$. One has $\|v\|_{L(\mathbf{r}, 2; \Omega_i)} = \|f_v\|_{L^{\mathbf{r}}(I)}$, and we can show the equality of the two K -functionals

$$\begin{aligned} K(t, v; L(1, 2; \Omega_i), L(\infty, 2; \Omega_i)) &= \inf_{v=v_0+v_1} (\|v_0\|_{L(1, 2; \Omega_i)} + t\|v_1\|_{L(\infty, 2; \Omega_i)}), \\ K(t, f_v; L^1(I), L^\infty(I)) &= \inf_{f_v=f_0+f_1} (\|f_0\|_{L^1(I)} + t\|f_1\|_{L^\infty(I)}), \end{aligned}$$

and use the standard $L^{\mathbf{p}}$ -interpolation $L^{\mathbf{p}}(I) = (L^1(I), L^\infty(I))_{1/\mathbf{q}, \mathbf{p}}$, see [207, Lemma 22.6].

On the one hand, any decomposition $f_v = f_0 + f_1$ directly implies a decomposition by $v_i(\mathbf{x}', \kappa) = v(\mathbf{x}', \kappa)f_i(\kappa)/f_v(\kappa)$ for $\mathbf{x}' \in \mathbb{R}^{d-1}$. The case $f_v(\kappa) = 0$ is trivial and can be excluded. One has $v = v_0 + v_1$ and $f_{v_i} = f_i$. As a consequence

$$K(t, v; L(1, 2; \Omega_i), L(\infty, 2; \Omega_i)) \leq K(t, f_v; L^1(I), L^\infty(I)).$$

On the other hand for any decomposition $v = v_0 + v_1$ one has

$$f_{v_0}(\kappa) + f_{v_1}(\kappa) = \|v_0\|_{L^2(\gamma_\kappa)} + \|v_1\|_{L^2(\gamma_\kappa)} \geq \|v_0 + v_1\|_{L^2(\gamma_\kappa)} = f_v(\kappa).$$

Hence, the decomposition of f_v by $f_v = f_0 + f_1$,

$$f_i(\kappa) = f_{v_i}(\kappa) \frac{f_v(\kappa)}{f_{v_0}(\kappa) + f_{v_1}(\kappa)} \leq f_{v_i}(\kappa), \quad i = 0, 1,$$

yields $\|f_0\|_{L^1(I)} \leq \|v_0\|_{L(1, 2)}$ as well as $\|f_1\|_{L^\infty(I)} \leq \|v_1\|_{L(\infty, 2)}$. This implies

$$K(t, v; L(1, 2; \Omega_i), L(\infty, 2; \Omega_i)) \geq K(t, f_v; L^1(I), L^\infty(I))$$

and concludes the equality of both K -functionals.

Since the patches cover Ω without any overlap, the interpolation property for $L(\mathbf{p}, 2)$ follows. \square

As a preliminary to our analysis, we state approximation results of a Scott–Zhang-type quasi-interpolation operator in the anisotropic norms. We consider $P_h: V \rightarrow V_h$ as in [196], based on the biorthogonal basis on Γ_S , preserving the

homogeneous Dirichlet data on Γ_D . The boundary values are preserved such that $P_h v|_{\Gamma_D} = 0$ and $\langle P_h v, \mu_h \rangle_{\Gamma_S} = \langle v, \mu_h \rangle_{\Gamma_S}$ for $\mu_h \in M_h$. On Γ_S , optimal order L^2 approximation properties

$$\|v - P_h v\|_{L^2(\Gamma_S)} \leq ch^{2-\varepsilon} |v|_{H^{2-\varepsilon}(\Gamma_S)} \quad (4.11)$$

for $v \in V \cap H^{5/2-\varepsilon}(\Omega)$ are given. An approximation result in the $L(\mathbf{q}, 2)$ norm is given by the following lemma.

Lemma 4.2.4. *For $v \in V \cap H^{5/2-\varepsilon}(\Omega)$, and $1/2 \geq \varepsilon > 0$, one has*

$$\|\nabla(v - P_h v)\|_{L(\mathbf{q}, 2)} \leq ch \|v\|_{H^{5/2-\varepsilon}(\Omega)}, \quad \text{with } \mathbf{q} = 1/\varepsilon.$$

Proof. Since the $L(2, 2)$ norm coincides with the $L^2(\Omega)$ norm, we have the standard approximation result

$$\|\nabla(v - P_h v)\|_{L(2, 2)} \leq ch |v|_{H^2(\Omega)}.$$

For $\mathbf{q} > 2$, we show the estimate by an interpolation argument, using the $L(2, 2)$ and the $L(\infty, 2)$ estimate. For the $L(\infty, 2)$ norm, we can easily adapt the proof in [158, Lemma 4.1] using local approximation results of the Scott–Zhang operator [196, Equation 4.3]. For any patch Ω_i , $i \in \{1, \dots, N_\gamma\}$ and $\kappa > 0$, we first define two strips around γ_κ . A strip of width 2δ in Ω is defined by $\mathfrak{S}_i(\delta, \kappa) = \{\mathbf{x} \in \Omega : \text{dist}(\mathbf{x}, \gamma_\kappa) < \delta\}$ and a discrete neighborhood can be constructed by the elements intersecting γ_κ : $\mathcal{I}_\kappa = \{\tau_h \in \mathcal{T}_h : \gamma_\kappa \cap \overline{\tau_h} \neq \emptyset\}$. Note, that we cannot expect $\mathfrak{S}_i(\delta, \kappa) \subset \Omega_i$, but this inclusion is not necessary for our analysis. Using these strips, local estimates of the Scott–Zhang operator yield

$$\begin{aligned} & \|\nabla(v - P_h v)\|_{L^2(\gamma_\kappa)}^2 \\ & \leq c \sum_{T \in \mathcal{I}_\kappa} \left(\frac{1}{h} \|\nabla(v - P_h v)\|_{L^2(T)}^2 + h \|\nabla^2(v - P_h v)\|_{L^2(T)}^2 \right) \\ & \leq ch |v|_{H^2(\mathfrak{S}_i(\bar{c}h, \kappa))}^2 \leq ch^2 \|v\|_{B_{2,1}^{5/2}(\Omega)}^2, \end{aligned}$$

where in the last step [145, Lemma 2.1] was used. Consequently, we have

$$\|\nabla(v - P_h v)\|_{L(\infty, 2)} \leq ch \|v\|_{B_{2,1}^{5/2}(\Omega)}.$$

To show this estimate for interpolation spaces, we can apply the interpolation property [207, Lemma 22.3]. By the reiteration theorem and Lemma 4.2.3, we have the interpolation representations $L(\mathbf{q}, 2) = (L(2, 2), L(\infty, 2))_{1-2\varepsilon, \mathbf{q}}$ as

well as $H^{5/2-\varepsilon}(\Omega) = (H^2(\Omega), B_{2,1}^{5/2}(\Omega))_{1-2\varepsilon,2} \subset (H^2(\Omega), B_{2,1}^{5/2}(\Omega))_{1-2\varepsilon,q}$. As a consequence the stated estimate is also valid in the interpolated spaces. \square

4.2.2.2 Dual problems

In this subsection, we follow the lines of [158, Section 5] and define a dual Dirichlet problem with locally supported data. For $v \in L^2(\Omega)$, $\text{supp } v \subset \overline{\mathfrak{S}(h)}$, we denote by $T^{\text{D}}v$ the solution operator of

$$-\Delta w = v \quad \text{in } \Omega, \quad w = 0 \quad \text{on } \partial\Omega, \quad (4.12)$$

i.e., $T^{\text{D}}v = w$.

In contrast to [158], we cannot assume $B_{2,1}^{5/2}(\Omega)$ regularity for the solution of (4.1), but only $H^{5/2-\varepsilon}(\Omega)$ regularity. Naive interpolation of the final estimate does not yield optimal results but an additional log-term. For optimal results, we need the stronger estimate given in the following lemmas. In the next lemma, we state a regularity estimate in a weighted Sobolev space using the local support of the data of the dual problem. Based on this estimate, we then state an approximation result for the Galerkin approximation of the dual solution in an anisotropic norm.

Lemma 4.2.5. *For $v \in L^2(\Omega)$, $\text{supp } v \subset \overline{\mathfrak{S}(h)}$ and $w = T^{\text{D}}v$ there exists $0 < \tilde{c} < \infty$ independent of v and h , such that*

$$\|\delta_{\Gamma}^{1/2-\varepsilon/2} \nabla^2 w\|_{L^2(\Omega \setminus \mathfrak{S}(\tilde{c}h))} \leq ch^{1/2-\varepsilon/2} \|v\|_{L^2(\Omega)},$$

where δ_{Γ} is the distance function to $\partial\Omega$.

Proof. We follow the idea of [158, Lemma 5.4], but instead of several local translations of w , we consider a global scaling of the coordinate system. To exploit the local data of the dual problem, we choose a sufficiently large scaling factor such that the transformation of w is harmonic in a neighborhood of Ω . This allows us to apply interior regularity results for the transformation of w , see [91, Theorem 8.8]:

$$\|\nabla^2 z\|_{L^2(B_1)} \leq c \|z\|_{H^1(B_{1+\rho})}, \quad (4.13)$$

for $-\Delta z = 0$ on $B_{1+\rho}$, a ball of radius $1 + \rho$ for a fixed $\rho > 0$.

Without loss of generality, assume that the barycenter of Ω is the origin of the coordinate system and we denote $l = \min_{\mathbf{x} \in \partial\Omega} |\mathbf{x}| > 0$. For sufficiently small h , we define a neighborhood of Ω by a scaling $\tilde{\Omega} = \{(1+4C_1h)\mathbf{x} : \mathbf{x} \in \Omega\}$. Since we estimate w only on $\Omega \setminus \mathfrak{S}(\tilde{c}h)$, where \tilde{c} is selected later, we can choose the scaling factor appropriately. The constant C_1 is sufficiently large, but fixed

and independent of h , such that for $\mathbf{x} \in \mathfrak{S}(h)$ one has $(1 + 2C_1h)\mathbf{x} \notin \Omega$. We scale w to a function on this neighborhood by $\tilde{w}: \tilde{\Omega} \rightarrow \mathbb{R}$, $\tilde{w}(\mathbf{x}) = w(\mathbf{x}/(1 + 4C_1h))$.

Note that the introduced scaling preserves harmonic functions, more precisely for $\mathbf{x} \in \Omega$ and $h < 3/4l - 1/(4C_1)$, we have $(1 + C_1h)/(1 + 4C_1h)\mathbf{x} \in \Omega \setminus \mathfrak{S}(h)$, and thus

$$\Delta \tilde{w} = 0 \text{ at } (1 + C_1h)\mathbf{x}, \quad \mathbf{x} \in \Omega.$$

Since the scaling factor is uniformly bounded, it also preserves Sobolev norms, i.e.,

$$c \|\tilde{w}\|_{H^\sigma(\tilde{\Omega})} \leq \|w\|_{H^\sigma(\Omega)} \leq C \|\tilde{w}\|_{H^\sigma(\tilde{\Omega})}, \quad \sigma \in \{0, 3/2\}.$$

To apply the transformation \tilde{w} , we choose \tilde{c} sufficiently large such that the transformation of $\Omega \setminus \mathfrak{S}(\tilde{c}h)$ is a subset of $\Omega \setminus \mathfrak{S}(h)$ and thus

$$\|\delta_\Gamma^{1/2-\varepsilon/2} \nabla^2 w\|_{L^2(\Omega \setminus \mathfrak{S}(\tilde{c}h))} \leq c \|(\delta_\Gamma + h)^{1/2-\varepsilon/2} \nabla^2 \tilde{w}\|_{L^2(\Omega \setminus \mathfrak{S}(h))}, \quad \text{for } \mathbf{x} \in \Omega.$$

Interior regularity (4.13) yields $\|\nabla^2 \tilde{w}\|_{L^2(B_r)} \leq cr^{-1/2+\varepsilon/2} \|\tilde{w}\|_{H^{3/2+\varepsilon/2}(B_{r(1+\rho)})}$ for a fixed $\rho > 0$ and any concentric balls of radius r and $r(1 + \rho)$, such that $B_{r(1+\rho)} \subset \Omega$. A covering of $\Omega \setminus \mathfrak{S}(h)$ using balls of center \mathbf{x}_i and radii $r_i \sim h + \delta_\Gamma(\mathbf{x}_i)$ shows

$$\|(\delta_\Gamma + h)^{1/2-\varepsilon/2} \nabla^2 \tilde{w}\|_{L^2(\Omega \setminus \mathfrak{S}(h))} \leq c \|\tilde{w}\|_{H^{3/2+\varepsilon/2}(\Omega)}.$$

Details on the Besicovitch covering theorem can be found in [78, Section 1.5.2] and [156, Chapter 5].

An analogue computation as in [158, Lemma 5.4], where the case $\varepsilon = 0$ was considered, concludes the proof. We bound the K -functional of the fractional Sobolev space $(H^1(\Omega), H^2(\Omega))_{1/2+\varepsilon/2, 2} = H^{3/2+\varepsilon/2}(\Omega)$ by

$$\begin{aligned} \|\tilde{w}\|_{H^{3/2+\varepsilon/2}(\Omega)}^2 &= \int_{t=0}^h \left(t^{-1/2-\varepsilon/2} K(t, \tilde{w})\right)^2 t^{-1} dt + \int_{t=h}^1 \left(t^{-1/2-\varepsilon/2} K(t, \tilde{w})\right)^2 t^{-1} dt \\ &\leq \int_{t=0}^h \left(t^{-1/2-\varepsilon/2} K(t, \tilde{w})\right)^2 t^{-1} dt + \int_{t=h}^1 t^{-1-\varepsilon} dt \sup_{t>0} \left(t^{-1/2} K(t, \tilde{w})\right)^2. \end{aligned} \quad (4.14)$$

Again applying the interior regularity (4.13), we get the estimate $\|\tilde{w}\|_{H^2(\Omega)} \leq ch^{-1/2} \|w\|_{H^{3/2}(\Omega)}$ which yields $K(t, \tilde{w}) \leq ct \|\tilde{w}\|_{H^2(\Omega)} \leq cth^{-1/2} \|w\|_{H^{3/2}(\Omega)}$. Substituting this upper bound in the first integral of (4.14) and observing that it holds $\sup_{t>0} \left(t^{-1/2} K(t, \tilde{w})\right) \leq \|w\|_{B_{2,\infty}^{3/2}(\Omega)}$, yields

$$\|\tilde{w}\|_{H^{3/2+\varepsilon/2}(\Omega)} \leq ch^{-\varepsilon/2} \|w\|_{B_{2,\infty}^{3/2}(\Omega)}.$$

Finally [158, Lemma 5.2] states $\|w\|_{B_{2,\infty}^{3/2}(\Omega)} \leq ch^{1/2}\|v\|_{L^2(\Omega)}$ which concludes the proof. \square

Remark 4.2.6. *A closer look reveals that the upper bound depends on ε . More precisely if ε tends to zero it tends to infinity. The first term on the right of (4.14) is robust in ε , but the constant in the second term can only be bounded by $\varepsilon^{-1/2}$ and in the limit case $\varepsilon = 0$ a log-term in h appears.*

Using local error estimates and the weighted regularity result proven above, we show an approximation result for the Galerkin approximation of the dual problem in anisotropic norms.

Lemma 4.2.7. *Given $v \in L^2(\Omega)$ with $\text{supp } v \subset \overline{\mathfrak{S}(h)}$, consider $w = T^D v$ and the Galerkin approximation $w_h \in V_h \cap H_0^1(\Omega)$. For $1 < \mathbf{p} = (1 - \varepsilon)^{-1} \leq 2$, one has following approximation property:*

$$\|\nabla(w - w_h)\|_{L(\mathbf{p},2)} \leq ch^{3/2-\varepsilon}\|v\|_{L^2(\Omega)}.$$

Proof. We show the estimate on each patch Ω_i , $i \in \{1, \dots, N_\gamma\}$. In the definition of the norm, we decompose the integral in κ from 0 to D into two parts and find

$$\begin{aligned} & \|\nabla(w - w_h)\|_{L(\mathbf{p},2;\Omega_i)}^{\mathbf{p}} \\ &= \int_{\kappa=0}^{\tilde{c}_1 h} \|\nabla(w - w_h)\|_{L^2(\gamma_\kappa)}^{\mathbf{p}} \, d\kappa + \int_{\kappa=\tilde{c}_1 h}^D \|\nabla(w - w_h)\|_{L^2(\gamma_\kappa)}^{\mathbf{p}} \, d\kappa, \end{aligned}$$

where \tilde{c}_1 has to be adapted to the constant \tilde{c} resulting from the previous lemma.

The first term is an integral over a strip of width $\mathcal{O}(h)$. The Hölder inequality with the exponents $2/\mathbf{p}$, $2/(2 - \mathbf{p})$ and the Fubini–Tonelli formula obviously yield for $\mathbf{p} = (1 - \varepsilon)^{-1}$

$$\begin{aligned} & \int_{\kappa=0}^{\tilde{c}_1 h} \|\nabla(w - w_h)\|_{L^2(\gamma_\kappa)}^{\mathbf{p}} \, d\kappa \leq ch^{(2-\mathbf{p})/2} \left(\int_{\kappa=0}^{\tilde{c}_1 h} \|\nabla(w - w_h)\|_{L^2(\gamma_\kappa)}^2 \, d\kappa \right)^{\mathbf{p}/2} \\ & \leq ch^{\mathbf{p}(1/2-\varepsilon)} \|\nabla(w - w_h)\|_{L^2(\mathfrak{S}(\tilde{c}_1 h))}^{\mathbf{p}}. \end{aligned}$$

Since Ω is convex, we have $\|\nabla(w - w_h)\|_{L^2(\mathfrak{S}(\tilde{c}_1 h))} \leq \|\nabla(w - w_h)\|_{L^2(\Omega)} \leq ch\|v\|_{L^2(\Omega)}$, which gives

$$\int_{\kappa=0}^{\tilde{c}_1 h} \|\nabla(w - w_h)\|_{L^2(\gamma_\kappa)}^{\mathbf{p}} \, d\kappa \leq ch^{\mathbf{p}(3/2-\varepsilon)}\|v\|_{L^2(\Omega)}^{\mathbf{p}}.$$

The second integral is estimated using a local approximation property and the regularity result given in Lemma 4.2.5. First, we insert $\kappa^{1/2}\kappa^{-1/2}$, note

$\kappa \leq c \delta_\Gamma$ and use the Hölder inequality with the same exponents as before:

$$\begin{aligned} & \int_{\kappa=\tilde{c}_1 h}^D \kappa^{-1/2} \kappa^{1/2} \|\nabla(w - w_h)\|_{L^2(\gamma_\kappa)}^p \, d\kappa \\ & \leq \left(\int_{\kappa=\tilde{c}_1 h}^D \kappa^{-1/(2-p)} \, d\kappa \right)^{(2-p)/2} \left(\int_{\kappa=\tilde{c}_1 h}^D \kappa^{1/p} \|\nabla(w - w_h)\|_{L^2(\gamma_\kappa)}^2 \, d\kappa \right)^{p/2} \\ & \leq ch^{-p\varepsilon/2} \|\delta_\Gamma^{1/2-\varepsilon/2} \nabla(w - w_h)\|_{L^2(\Omega \setminus \mathfrak{S}(\tilde{c}_1 h))}^p. \end{aligned}$$

Again, we note that the value of the constant does not stay bounded for $\varepsilon \rightarrow 0$.

Based on the discussion in [158, Section 5.1.2], we derive the bound

$$\begin{aligned} & \|\delta_\Gamma^{1/2-\varepsilon/2} \nabla(w - w_h)\|_{L^2(\Omega \setminus \mathfrak{S}(\tilde{c}_1 h))} \tag{4.15} \\ & \leq c \|\delta_\Gamma^{1/2-\varepsilon/2} \nabla(w - I_h w)\|_{L^2(\Omega \setminus \mathfrak{S}(\tilde{c}_2 h))} + c \|\delta_\Gamma^{-1/2-\varepsilon/2} (w - w_h)\|_{L^2(\Omega \setminus \mathfrak{S}(\tilde{c}_2 h))} \end{aligned}$$

for an arbitrary but fixed \tilde{c}_2 , if \tilde{c}_1 is chosen sufficiently large. I_h denotes the standard nodal interpolation operator. This estimate is based on local approximation properties found in [220, 221] and a Besicovitch covering argument.

To estimate the first term, we exploit the regularity result which was derived in Lemma 4.2.5. Based on \tilde{c} , which is given from the previous lemma, we can choose \tilde{c}_2 and \tilde{c}_1 sufficiently large, such that

$$\begin{aligned} \|\delta_\Gamma^{1/2-\varepsilon/2} \nabla(w - I_h w)\|_{L^2(\Omega \setminus \mathfrak{S}(\tilde{c}_2 h))} & \leq ch \|\delta_\Gamma^{1/2-\varepsilon/2} \nabla^2 w\|_{L^2(\Omega \setminus \mathfrak{S}(\tilde{c} h))} \\ & \leq ch^{3/2-\varepsilon/2} \|v\|_{L^2(\Omega)}. \end{aligned}$$

Using the convexity of Ω , the second term of (4.15) can be bounded easily by

$$\begin{aligned} \|\delta_\Gamma^{-1/2-\varepsilon/2} (w - w_h)\|_{L^2(\Omega \setminus \mathfrak{S}(\tilde{c}_2 h))} & \leq ch^{-1/2-\varepsilon/2} \|w - w_h\|_{L^2(\Omega)} \\ & \leq ch^{3/2-\varepsilon/2} \|v\|_{L^2(\Omega)}. \quad \square \end{aligned}$$

The previously shown bounds in anisotropic norms are sufficient to show primal estimates in a neighborhood of the boundary. For a final bound of the Lagrange multiplier, we also need to consider a dual problem with Neumann data, as defined in [158, Section 5.2]. Given $v \in L^2(\Omega)$, $\text{supp } v \subset \overline{\mathfrak{S}(h)}$, define w_v^N such that

$$-\Delta w_v^N = v - \frac{1}{|\Omega|} \int_\Omega v \, d\mathbf{x} \quad \text{in } \Omega, \quad \partial_{\mathbf{n}} w_v^N = 0 \quad \text{on } \partial\Omega, \quad \int_\Omega w_v^N \, d\mathbf{x} = 0. \tag{4.16}$$

Denote by V_h^{-1} the space of discrete functions without any restriction of

the boundary values. Using the same arguments as before, we can adapt the proof of [158, Lemma 5.7] and show the following statement based on the dual Neumann problem.

Corollary 4.2.8. *Let $u \in V \cap H^{5/2-\varepsilon}(\Omega)$ and $u_h^N \in V_h^{-1}$ satisfy the orthogonality condition $a(u - u_h^N, v_h) = 0$ for $v_h \in V_h^{-1}$ and $\int_{\mathfrak{S}(h)} u - u_h^N \, d\mathbf{x} = 0$, then*

$$\begin{aligned} \|u - u_h^N\|_{L^2(\mathfrak{S}(h))} &\leq ch^{5/2-\varepsilon} \|u\|_{H^{5/2-\varepsilon}(\Omega)}, \\ \left| u - u_h^N \right|_{H^{1/2}(\partial\Omega)} &\leq ch^{3/2-\varepsilon} \|u\|_{H^{5/2-\varepsilon}(\Omega)}. \end{aligned}$$

4.2.2.3 Error bound for the Dirichlet–Neumann map

With the results of the previous subsection, we can estimate the $H^{-1/2}(\Gamma_S)$ error of the Dirichlet–Neumann map $N\hat{f} - S(u|_{\Gamma_S})$ and the mesh-dependent Dirichlet–Neumann map $N_h\hat{f} - S_h(u|_{\Gamma_S})$, see Section 4.1.2.2, in two steps. This bound is the last step to show the primal estimate in Theorem 4.1.2. Firstly, we relate the error of the dual variable to the error of the primal variable in a small strip around $\partial\Omega$ using the dual Neumann problem (4.16). Secondly, the error in the strip is estimated using the dual Dirichlet problem (4.12) and the approximation results derived in the anisotropic norms.

Theorem 4.2.9. *Assuming the solution u of the Signorini problem (4.1) to be in $H^{5/2-\varepsilon}(\Omega)$, $\varepsilon \in (0, 1/2]$ fixed, then one has*

$$\|\lambda - \tilde{\lambda}_h\|_{H^{-1/2}(\Gamma_S)} \leq ch^{3/2-\varepsilon} \|u\|_{H^{5/2-\varepsilon}(\Omega)}.$$

Proof. The proof is divided into two steps. Firstly, we bound the dual error by the primal error in a small neighborhood of the boundary. Secondly, we bound the primal error in a small strip using the anisotropic estimates stated in Lemma 4.2.4 and 4.2.7.

To be more precise, the first step is to show the upper bound

$$\|\lambda - \tilde{\lambda}_h\|_{H^{-1/2}(\Gamma_S)} \leq ch^{3/2-\varepsilon} \|u\|_{H^{5/2-\varepsilon}(\Omega)} + c \frac{1}{h} \|u - \tilde{u}_h\|_{L^2(\mathfrak{S}(h))}. \quad (4.17)$$

We use the saddle point formulation to represent the dual error by discrete harmonic functions on the domain. Using the stability of the harmonic extension and an inverse trace inequality, we can relate the dual error to the primal error in the strip $S(h)$.

We start using the uniform inf-sup stability in the $H^{-1/2}(\Gamma_S)$ norm to get

$$\begin{aligned} \|\lambda - \tilde{\lambda}_h\|_{H^{-1/2}(\Gamma_S)} &\leq c \inf_{\mu_h \in M_h} \|\lambda - \mu_h\|_{H^{-1/2}(\Gamma_S)} + c \sup_{z_h \in W_h} \frac{\langle z_h, \lambda - \tilde{\lambda}_h \rangle_{\Gamma_S}}{\|z_h\|_{H_{00}^{1/2}(\Gamma_S)}} \\ &\leq ch^{3/2-\varepsilon} \|\lambda\|_{H^{1-\varepsilon}(\Gamma_S)} + c \sup_{z_h \in W_h} \frac{a(\tilde{u}_h - u, \mathcal{E}_h z_h)}{\|z_h\|_{H_{00}^{1/2}(\Gamma_S)}}, \end{aligned}$$

where $\mathcal{E}_h z_h \in V_h$ is the discrete harmonic extension of $z_h^\Gamma \in H^{1/2}(\partial\Omega)$ which is the trivial extension to $\partial\Omega$ of $z_h \in W_h \subset H_{00}^{1/2}(\Gamma_S)$.

We replace u by a discrete function $u_h^N \in V_h^{-1}$ satisfying the requirements of Corollary 4.2.8. We also use the fact that $\mathcal{E}_h z_h$ and $\tilde{u}_h - u_h^N$ are discrete harmonic to see

$$\sup_{z_h \in W_h} \frac{a(\tilde{u}_h - u, \mathcal{E}_h z_h)}{\|z_h\|_{H_{00}^{1/2}(\Gamma_S)}} = \sup_{z_h \in W_h} \frac{a(\tilde{u}_h - u_h^N, \mathcal{E}_h z_h)}{\|z_h\|_{H_{00}^{1/2}(\Gamma_S)}} \leq c \left| \tilde{u}_h - u_h^N \right|_{H^{1/2}(\partial\Omega)}.$$

Using an inverse inequality, we get

$$\begin{aligned} \left| \tilde{u}_h - u_h^N \right|_{H^{1/2}(\partial\Omega)} &\leq c \frac{1}{h} \|\tilde{u}_h - u_h^N\|_{L^2(\mathfrak{S}(h))} \\ &\leq c \frac{1}{h} \|u - u_h^N\|_{L^2(\mathfrak{S}(h))} + c \frac{1}{h} \|u - \tilde{u}_h\|_{L^2(\mathfrak{S}(h))}. \end{aligned}$$

Now Corollary 4.2.8 results in (4.17).

To bound $\|u - \tilde{u}_h\|_{L^2(\mathfrak{S}(h))}$, we employ different Galerkin orthogonalities to get a suitable representation of the error in the whole domain based on the solution of the dual problem. Applying Green's formula, we obtain the representation of the local error $e_h = u - \tilde{u}_h$:

$$\begin{aligned} \|e_h\|_{L^2(\mathfrak{S}(h))} &= \sup_{\|v\|_{L^2(\mathfrak{S}(h))}=1} (e_h, v)_{L^2(\Omega)} = \sup_{\|v\|_{L^2(\mathfrak{S}(h))}=1} \left(e_h, -\Delta(T^D v) \right)_{L^2(\Omega)} \\ &= \sup_{\|v\|_{L^2(\mathfrak{S}(h))}=1} a(T^D v, e_h) - \left\langle e_h, \partial_n(T^D v) \right\rangle_{\Gamma_S}, \end{aligned}$$

where $T^D v \in H_0^1(\Omega)$ is the solution to the dual problem (4.12).

Let us introduce the conforming finite element approximation of $w = T^D v$ as $w_h \in V_h \cap H_0^1(\Omega)$, and denote $\lambda_w = -\partial_n w|_{\Gamma_S}$. We recall the following orthogonality results: Using the Galerkin orthogonality in the domain for the variational inequality (4.2), one has $a(w_h, e_h) = 0$, since $w_h = 0$ on $\partial\Omega$. We recall, that the definition of the Scott–Zhang operator P_h , see Section 4.2.2.1, guarantees $\langle u - P_h u, \mu_h \rangle_{\Gamma_S} = 0$ as well as $\langle P_h u - \tilde{u}_h, \mu_h \rangle_{\Gamma_S} = 0$ for $\mu_h \in M_h$.

We can then conclude that

$$a(w - w_h, P_h u - \tilde{u}_h) + \langle P_h u - \tilde{u}_h, \lambda_w \rangle_{\Gamma_S} = 0.$$

For $1/\mathbf{p} + 1/\mathbf{q} = 1$, we find using the terms discussed above

$$\begin{aligned} a(w, e_h) + \langle e_h, \lambda_w \rangle_{\Gamma_S} &= a(w - w_h, u - P_h u) + \inf_{\mu_h \in M_h} \langle u - P_h u, \lambda_w - \mu_h \rangle_{\Gamma_S} \\ &\leq \|\nabla(w - w_h)\|_{L(\mathbf{p},2)} \|\nabla(u - P_h u)\|_{L(\mathbf{q},2)} \\ &\quad + \|u - P_h u\|_{L^2(\Gamma_S)} \inf_{\mu_h \in M_h} \|\lambda_w - \mu_h\|_{L^2(\Gamma_S)}. \end{aligned}$$

The convexity of Ω guarantees $\lambda_w \in H^{1/2}(\Gamma_S)$ with $\|\lambda_w\|_{H^{1/2}(\Gamma_S)} \leq c \|v\|_{L^2(\Omega)}$. Setting $\mathbf{q} = \varepsilon^{-1}$, $\mathbf{p} = (1 - \varepsilon)^{-1}$, the best approximation of the dual space, Equation (4.11) and Lemmas 4.2.4 and 4.2.7 yield the result. \square

Summarizing the results of Lemmas 4.2.1, 4.2.2 and Theorem 4.2.9 shows the a priori result for the primal variable of Theorem 4.1.2.

4.2.2.4 An improved result on the $L^2(\Omega)$ error

Based on [163] a convergence order $h^{3/2}$ in the $L^2(\Omega)$ norm was stated in [54]. However the required $H^2(\Omega)$ regularity of the dual problem is very strong, since the dual problem is a variational inequality with mixed boundary conditions. Based on the improved trace estimate, we can show almost the same order without involving a dual inequality problem.

Corollary 4.2.10. *Let u be the solution of (4.1) and u_h be the solution of (4.2). Assuming $u \in H^{5/2-\varepsilon}(\Omega)$, $\varepsilon \in (0, 1/2]$ fixed, we get*

$$\|u - u_h\|_{L^2(\Omega)} \leq ch^{3/2-\varepsilon} \|u\|_{H^{5/2-\varepsilon}(\Omega)}.$$

Proof. The proof is based on an Aubin–Nitsche-type argument using a linear dual problem with homogeneous Dirichlet conditions. Due to the non-linear Signorini condition, an additional error term on Γ_S needs to be bounded.

Let $w \in H_0^1(\Omega)$ solve $-\Delta w = u - u_h$ in Ω . Since Ω is convex, one has $\|w\|_{H^2(\Omega)} \leq c \|u - u_h\|_{L^2(\Omega)}$ and $\|\partial_{\mathbf{n}} w\|_{L^2(\Gamma_S)} \leq \|w\|_{H^2(\Omega)}$. Applying Green's formula yields

$$\|u - u_h\|_{L^2(\Omega)}^2 = \int_{\Omega} \nabla w^\top \nabla(u - u_h) \, d\mathbf{x} - \langle u - u_h, \partial_{\mathbf{n}} w \rangle_{\Gamma_S}.$$

The first term can be bounded as it is standard in Aubin–Nitsche arguments, due to the homogeneous Dirichlet values of w . For the second term, we use

the trace estimate provided in Theorem 4.1.2:

$$\begin{aligned} \langle u - u_h, \partial_{\mathbf{n}} w \rangle_{\Gamma_S} &\leq \|u - u_h\|_{L^2(\Gamma_S)} \|\partial_{\mathbf{n}} w\|_{L^2(\Gamma_S)} \\ &\leq ch^{3/2-\varepsilon} \|u\|_{H^{5/2-\varepsilon}(\Omega)} \|w\|_{H^2(\Omega)}. \end{aligned} \quad \square$$

Remark 4.2.11. *We note that in the proof of the $L^2(\Omega)$ norm we use the trivial bound $\|u - u_h\|_{L^2(\Gamma_S)} \leq \|u - u_h\|_{H^{1/2}(\Gamma_S)}$. Thus an extra $h^{1/2}$ would be gained, if a higher order $L^2(\Gamma_S)$ bound was available.*

4.3 Lagrange multiplier estimates

The $H^{-1/2}(\Gamma_S)$ norm for the Lagrange multiplier of the Signorini problem arising in the saddle point formulation (4.3) can be estimated using similar arguments as those used in Theorem 4.2.9. Due to the given primal estimate of Theorem 4.1.2, no estimate on a strip is needed here. By standard techniques, the $L^2(\Gamma_S)$ norm can also be estimated.

Theorem 4.3.1. *Let (u, λ) be the exact solution of the saddle point formulation (4.3). If the regularity requirement $u \in H^{5/2-\varepsilon}(\Omega)$, $\varepsilon \in (0, 1/2]$ fixed, holds, then*

$$\begin{aligned} \|\lambda - \lambda_h\|_{H^{-1/2}(\Gamma_S)} &\leq ch^{3/2-\varepsilon} \|u\|_{H^{5/2-\varepsilon}(\Omega)}, \\ \|\lambda - \lambda_h\|_{L^2(\Gamma_S)} &\leq ch^{1-\varepsilon} \|u\|_{H^{5/2-\varepsilon}(\Omega)}. \end{aligned}$$

Proof. The first line of the saddle point problem (4.3a) and its Galerkin discretization (4.4a) yield $a(u - u_h, v_h) + \langle v_h, \lambda - \lambda_h \rangle_{\Gamma_S} = 0$ for $v_h \in V_h$. Similar arguments as in the proof of Theorem 4.2.9 give

$$\begin{aligned} \|\lambda - \lambda_h\|_{H^{-1/2}(\Gamma_S)} &\leq ch^{3/2-\varepsilon} \|\lambda\|_{H^{1-\varepsilon}(\Gamma_S)} + c \sup_{z_h \in W_h} \frac{a(u_h - u, \mathcal{E}_h z_h)}{\|z_h\|_{H_{00}^{1/2}(\Gamma_S)}} \\ &\leq ch^{3/2-\varepsilon} \|\lambda\|_{H^{1-\varepsilon}(\Gamma_S)} + c \left| u_h - u_h^N \right|_{H^{1/2}(\partial\Omega)}, \end{aligned}$$

where we exploit the fact that $a(u, \mathcal{E}_h z_h) = a(u_h^N, \mathcal{E}_h z_h)$ and a stability estimate for discrete harmonic functions, see [214, Lemma 4.10]. It is important to note, that $u_h^N \in V_h^{-1}$, which is defined as in the proof of Theorem 4.2.9, only depends on u , not on u_h or \tilde{u}_h . Nevertheless $u_h - u_h^N$ is discrete harmonic due to the Galerkin approximation of the saddle point problem. Using Corollary 4.2.8

and the primal estimate of Theorem 4.1.2, we conclude

$$\begin{aligned} |u_h - u_h^N|_{H^{1/2}(\partial\Omega)} &\leq |u - u_h|_{H_0^{1/2}(\Gamma_S)} + |u - u_h^N|_{H^{1/2}(\partial\Omega)} \\ &\leq ch^{3/2-\varepsilon} \|u\|_{H^{5/2-\varepsilon}(\Omega)}. \end{aligned}$$

The remaining error estimate in the $L^2(\Gamma_S)$ norm follows by an inverse inequality and the best approximation properties:

$$\begin{aligned} \|\lambda - \lambda_h\|_{L^2(\Gamma_S)} &\leq \inf_{\mu_h \in M_h} \left(\|\lambda - \mu_h\|_{L^2(\Gamma_S)} + \|\mu_h - \lambda_h\|_{L^2(\Gamma_S)} \right) \\ &\leq c \inf_{\mu_h \in M_h} \left(\|\lambda - \mu_h\|_{L^2(\Gamma_S)} + \frac{1}{\sqrt{h}} \|\mu_h - \lambda\|_{H^{-1/2}(\Gamma_S)} \right) \\ &\quad + \frac{c}{\sqrt{h}} \|\lambda - \lambda_h\|_{H^{-1/2}(\Gamma_S)}. \quad \square \end{aligned}$$

4.4 Numerical results

We choose an example with an analytically known solution on the domain $\Omega = (0, 1.4 + 0.27/e) \times (0, 0.5)$, where $\Gamma_S = (0, 1.4 + 0.27/e) \times \{0\}$. The choice of the domain is done in order to have an easy representation of the solution with an asymmetry over the Signorini boundary. We choose the volumetric and Dirichlet boundary data as well as the initial gap $\hat{g}(x) = 1$ according to the exact solution which is constructed as follows.

In polar coordinates, the singular component (see also Section 1.2.3.2) is given by $u_{\text{sing}}(r, \theta) = r^{3/2} \sin(3/2 \theta)$ which we also denote $u_{\text{sing}}(x, y)$ in Cartesian coordinates. As this singular component has a one-sided active area, we need to modify the function to ensure the condition that the active set Γ^{act} is a compact subset of the Signorini boundary Γ_S . The singular function is translated such that the transmission point between the active and inactive part is at $x_l = 0.2 + 0.3/\pi \approx 0.295$. A spline of polynomial order four is used as a cut-off function u_{cut} . Adding a weighted reflection of this function, we get a function with a compact contact area. The second transmission point is set to $x_r = 1.2 - 0.3/\pi \approx 1.105$. For some scalar weight $a > 0$ (in the examples $a = 0.7$), the solution is given for $\mathbf{x} = (x, y)^\top$ by

$$u(\mathbf{x}) = \left(u_{\text{sing}}(x - x_l, y) u_{\text{cut}}(x) + a u_{\text{sing}}(x_r - x, y) u_{\text{cut}}(1.4 - x) \right) (1 - y^2) + 1.$$

For the right hand side $\hat{f} = -\Delta u$, the Dirichlet data $\hat{u} = u|_{\Gamma_D}$ and $\hat{g}(x) = 1$, the solution solves the Signorini problem (4.1). The actual contact area is given by $\Gamma^{\text{act}} = [0.2 + 0.3/\pi, 1.2 - 0.3/\pi]$. This choice of the contact area was made to ensure that no vertex of the mesh coincides with its boundary.

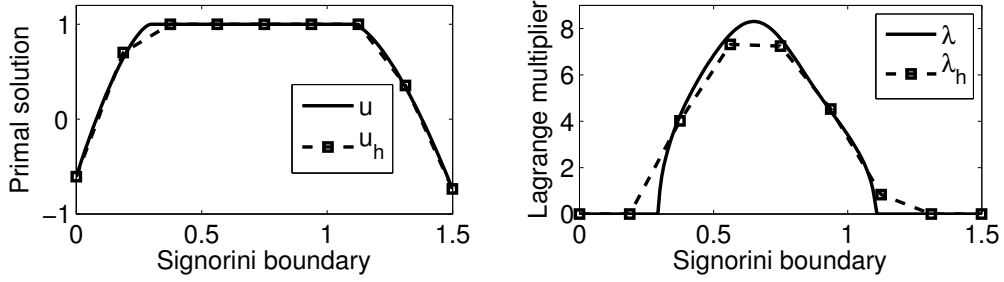


Figure 4.3: Exact solution and finite element approximation on level 2. Values for the primal solution (left) and the dual solution (right).

The domain yields an asymmetry of the contact area. The desired regularity $u \in H^{5/2-\varepsilon}(\Omega)$ is given by construction. We start from a coarse, quadrilateral, initial mesh of 4×2 elements and refine uniformly.

The exact solution on the Signorini boundary as well as a coarse finite element approximation are displayed in Figure 4.3. In Figure 4.4, the error distribution restricted to Γ_S on a fine finite element grid is shown. Since the discrete Lagrange multiplier is based on a biorthogonal basis and hence is discontinuous, a post-processing is applied for the visualization and the error computation. Instead of $\lambda_h = \sum_{i=1}^{N_{M_h}} \lambda_i \psi_i \in M_h$, we represent the Lagrange multiplier as

$$\hat{\lambda}_h = \sum_{i=1}^{N_{M_h}} \lambda_i \varphi_i \in W_h.$$

As it was shown in [114, Section 3.3], the order of convergence of $\hat{\lambda}_h$ is the same as for λ_h . Although the proof was shown for rates up to the order h , it can be easily extended to our situation.

The error distribution reflects the singularities of the solution at $\partial\Gamma^{\text{act}}$. We observe two peaks of large errors at the boundary of the active set caused by

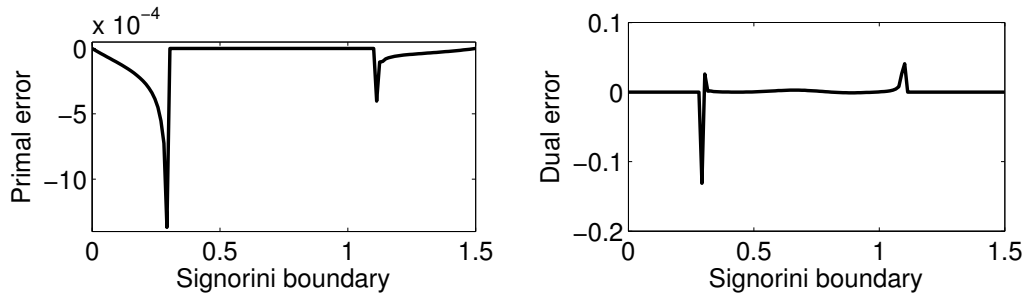


Figure 4.4: Discretization error displayed at the Signorini boundary. Error of the primal variable (left) and of the dual variable (right) at level $k = 6$.

Table 4.1: Relative errors of the primal and dual solution at different mesh levels k and an averaged numerical convergence order.

k	$\ \lambda - \lambda_h\ _{L^2(\Gamma_S)}$		$\ u - u_h\ _{L^2(\Gamma_S)}$		$\ u - u_h\ _{L^2(\Omega)}$	
1	3.2629e-01	—	2.1724e-01	—	1.0050e-01	—
2	1.2955e-01	1.33	4.2717e-02	2.35	2.5761e-02	1.96
3	4.4331e-02	1.44	7.0192e-03	2.48	6.2041e-03	2.01
4	1.8560e-02	1.38	2.3468e-03	2.18	1.5550e-03	2.00
5	1.5159e-02	1.11	9.3812e-04	1.96	4.0559e-04	1.99
6	5.8243e-03	1.16	1.8083e-04	2.05	9.8738e-05	2.00
7	2.7746e-03	1.15	4.0096e-05	2.07	2.4336e-05	2.00
8	1.9410e-03	1.06	1.7967e-05	1.94	6.4165e-06	1.99
9	9.8497e-04	1.05	4.6480e-06	1.94	1.5986e-06	1.99
10	4.0873e-04	1.07	9.7558e-07	1.97	3.8972e-07	2.00
11	1.7042e-04	1.09	1.9775e-07	2.01	9.5737e-08	2.00

the reduced regularity at these points. The error in the interior of the domain is of a similar order, hence the overall error is not dominated by the error on the boundary.

In Table 4.1, the computed L^2 norms of the error as well as the estimated rate of convergence are depicted for each level k . Errors in fractional Sobolev norms are given in Figure 4.5. The $L^2(\Gamma_S)$, $L^2(\Omega)$ and $H^1(\Omega)$ norms were computed by an adaptive integration to guarantee reliable results for the non-smooth solution. The dual norm $H^{-1}(\Gamma_S)$, was estimated as the norm of the dual space to a fine finite element space. To be more precise, the post-processed Lagrange multiplier on each level $k = 1, \dots, 11$ was prolonged to level 15. On this level, we replace λ by the piecewise linear interpolation and compute $\widehat{\lambda}_{h_k} - \mathcal{I}_{15}\lambda \in W_{h_{15}}$. Note that we have $\widehat{\lambda}_{h_k} \in W_{h_k} \subset W_{h_{15}}$ due to the post-processing as described above. The $H^{-1}(\Gamma_S)$ norm is approximated by the dual norm of $W_{h_{15}}$, i.e.,

$$\|\lambda - \lambda_{h_k}\|_{H^{-1}(\Gamma_S)} \approx \sup_{w_{h_{15}} \in W_{h_{15}}} \frac{\int_{\Gamma_S} (\widehat{\lambda}_{h_k} - \mathcal{I}_{15}\lambda) w_{h_{15}} \, dx}{\|w_{h_{15}}\|_{H^1(\Gamma_S)}}.$$

The fractional order Sobolev spaces $H_{00}^{1/2}(\Gamma_S)$ and $H^{-1/2}(\Gamma_S)$ were bounded using their interpolation property, i.e.,

$$\|v\|_{H_{00}^{1/2}(\Gamma_S)} \leq \|v\|_{H^1(\Gamma_S)}^{1/2} \|v\|_{L^2(\Gamma_S)}^{1/2}, \quad \|v\|_{H^{-1/2}(\Gamma_S)} \leq \|v\|_{H^{-1}(\Gamma_S)}^{1/2} \|v\|_{L^2(\Gamma_S)}^{1/2}.$$

The averaged convergence rates α_k as given in Table 4.1, were computed in

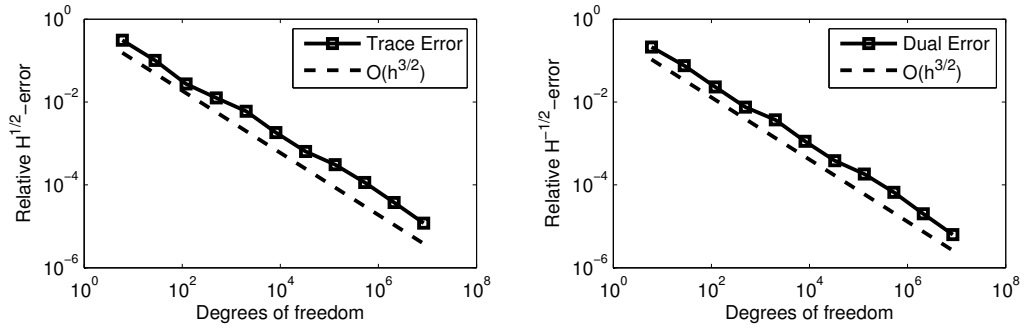


Figure 4.5: Estimated convergence rates in fractional Sobolev spaces. Left: $H_{00}^{1/2}(\Gamma_S)$ norm for the primal solution. Right: $H^{-1/2}(\Gamma_S)$ norm for the dual solution.

comparison to the first solution, by the formula

$$\left(\frac{\text{err}_1}{\text{err}_k}\right) = \left(\frac{1}{2}\right)^{\alpha_k(k-1)}.$$

We observe optimal order convergence rates in the L^2 norms, which is as expected from our theory for the Lagrange multiplier, whereas for the $L^2(\Omega)$ and the $L^2(\Gamma_S)$ norm, we obtain better rates, than given by the theory. A closer look reveals, that the convergence rates from level to level for the values on Γ_S vary more strongly. This is related to the fact, that the discrete resolution of

Table 4.2: Distance of the transmission points x_l and x_r to the discrete transmission points $x_{l,h}$ and $x_{r,h}$ on level k , compared to the mesh size h .

k	$ x_l - x_{l,h} $	$ x_l - x_{l,h} /h$	$ x_r - x_{r,h} $	$ x_r - x_{r,h} /h$
1	$7.9339e-02$	0.21	$1.9989e-02$	0.05
2	$7.9339e-02$	0.42	$1.9989e-02$	0.11
3	$1.4369e-02$	0.15	$1.9989e-02$	0.21
4	$1.4369e-02$	0.31	$2.6865e-02$	0.57
5	$9.0579e-03$	0.39	$3.4384e-03$	0.15
6	$2.6556e-03$	0.23	$3.4384e-03$	0.29
7	$3.2012e-03$	0.55	$3.4384e-03$	0.59
8	$2.7280e-04$	0.09	$5.1006e-04$	0.17
9	$2.7280e-04$	0.19	$5.1006e-04$	0.35
10	$2.7280e-04$	0.37	$2.2203e-04$	0.30
11	$9.3246e-05$	0.25	$1.4402e-04$	0.39

the active set is restricted to the vertices of the finite element mesh. Depending on the quality of the approximation of the active set, the rates for values on

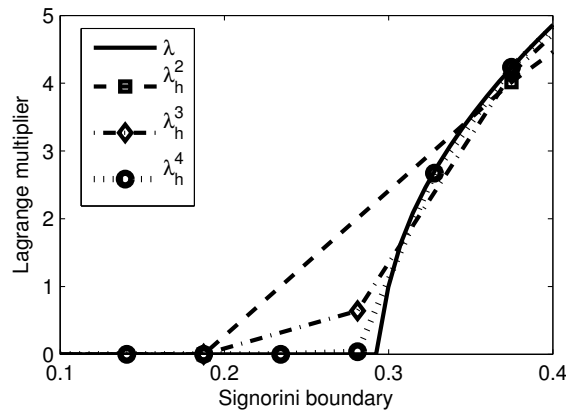


Figure 4.6: Zoom of dual solution and approximations at levels 2 to 4 around the left transmission point.

Γ_S can be larger or smaller than expected. In Figure 4.5, we see that the averaging described above is a reasonable estimate for the convergence rate.

We are also interested in a good resolution of the actual contact set, so we take a closer look at the solution near the boundary of the active set. The discrete active set is taken as the coincidence set of the primal solution, i.e., $\Gamma_h^{\text{act}} = \{\mathbf{x} \in \Gamma_S: u_h(\mathbf{x}) = 1\}$. In Table 4.2, the distance between the transmission points and the discrete transmission points is shown and compared to the mesh size. We note, that the distance is always smaller than the mesh size. Since no vertex matches with a transmission point, this is the best we can expect. Figure 4.6 shows the dual solution and some finite element approximations on the Signorini boundary.

5 Discontinuous and weakly conforming methods

In addition to the patch-wise conforming approximations considered so far, we now study approximations which are discontinuous on the element level. These more relaxed schemes can improve the approximation, especially in locking situations. Due to the weak coupling, spurious stresses do not appear as strong as with conforming methods, which improves the robustness in locking situations.

In general, element-wise discontinuous methods significantly increase the number of degrees of freedom on a fixed grid as well as the density of the stiffness matrix in comparison to standard conforming methods. To tackle this problem, we present two hybrid methods, where the degrees of freedom are locally condensed out and the final equation system is of a reduces size and more efficient. This hybridization can be performed efficiently in parallel.

At first, a flexible hybrid non-conforming method is introduced and investigated from a theoretical as well as numerical point of view. Local and global inf-sup stability are discussed and optimal a priori estimates are given based on the theory of non-conforming methods. The numerical examples include volume locking and contact problems, where optimal rates are observed. Then, after an introduction of several discontinuous Galerkin methods, the presented methods are compared in a numerical study. The study includes several important challenging situations, such as anisotropic geometries and meshes, material jumps and nearly incompressible elasticity. As a comparison also conforming standard and isogeometric finite elements are included.

Parts of the results shown in this chapter have been published by the author in collaboration with H. R. Bayat, J. Krämer, S. Reese, C. Wieners, B. Wohlmuth and S. Wulfinghoff in the article “Numerical evaluation of discontinuous and nonconforming finite element methods in solid mechanics”, which was submitted for publication in the year 2017, [19], in the conference proceeding “A hybrid weakly nonconforming discretization for linear elasticity”, in 2016 [135] and parts are also included in an article in preparation “A robust weakly conforming hybrid discontinuous Galerkin method for linear elasticity” planned to be submitted in 2017 [136].

5.1 Hybridizable weakly conforming method

We introduce a novel hybrid discontinuous Galerkin method for elliptic problems with a discontinuous ansatz space in the elements and individually chosen constraints on the faces. This *weakly conforming method* (WCM) can be stated in a primal-dual formulation with the primal element-wise degrees of freedom and the dual Lagrange multiplier of the coupling conditions. In the assembly the interior degrees of freedom are locally eliminated. We provide local criteria for the well-posedness and stability of this elimination process, and we numerically illustrate an adaptive choice of the coupling constraints.

The proposed method is a generalization of well-known non-conforming methods like Crouzeix-Raviart elements, see [59, 84], and Rannacher-Turek elements [182]. See [80] for applications to linear elasticity. We also refer to [51, 52, 198] and the references therein for further hybridization approaches applied to scalar equations and the Stokes equation.

We first investigate well-posedness and convergence of the non-conforming method and remark on the efficient hybridization later. Numerical results, including the new adaptive features and a contact discretization, are shown based on an implementation in the parallel finite element software M++ [154, 223].

5.1.1 Problem formulation

We consider piecewise discontinuous functions on the triangulation \mathcal{T}_h and introduce a coupling on the faces $F \in \mathcal{F}_h$ of the skeleton Γ . On each element $\tau_h \in \mathcal{T}_h$, we define a finite-dimensional local approximation space $\mathbf{V}_h(\tau_h) \subset (H^1(\tau_h))^d$ and the global broken space \mathbf{V}_h as

$$\mathbf{V}_h = \{\mathbf{v}_h \in (L^2(\Omega))^d: \mathbf{v}_h|_{\tau_h} \in \mathbf{V}_h(\tau_h), \quad \tau_h \in \mathcal{T}_h\}.$$

On \mathbf{V}_h , the bilinear form needs to be defined mesh-dependent as

$$a_h(\mathbf{u}_h, \mathbf{v}_h) = \sum_{\tau_h \in \mathcal{T}_h} \int_{\tau_h} \boldsymbol{\sigma}(\mathbf{u}_h) : \boldsymbol{\varepsilon}(\mathbf{v}_h) \, d\mathbf{x},$$

while the right hand side $f(\mathbf{v}_h) = \int_{\Omega} \widehat{\mathbf{f}}^\top \mathbf{v}_h \, d\mathbf{x}$ can be stated as before.

Since a_h is not elliptic on the broken space \mathbf{V}_h , we add a weak coupling across the faces of the triangulation. The set of Dirichlet faces $F \in \mathcal{F}_h$, $F \subset \Gamma_D$ is denoted by \mathcal{F}_h^D , while the set of interior faces $F \in \mathcal{F}_h$, $F \not\subset \partial\Omega$ is denoted by $\mathcal{F}_h^{\text{int}}$. For an interior face $F \in \mathcal{F}_h^{\text{int}}$, we denote one of the two neighboring elements as $\tau_{h,+}$, the other as $\tau_{h,-}$. Analogously for a (possibly broken) function

\mathbf{v} the trace on F from element $\tau_{h,+}$ is denoted by \mathbf{v}_+ , while the trace from element $\tau_{h,-}$ is denoted by \mathbf{v}_- . We note that the choice is only needed for notational reasons and does not influence the solution. By incorporating the boundary values $\hat{\mathbf{u}}, \hat{\mathbf{t}}$ into the jump terms we can easily account for a weak fulfillment of the boundary conditions. For each face $F \in \mathcal{F}_h$ we denote the displacement jump

$$[\mathbf{v}]_{(\hat{\mathbf{u}})} = \begin{cases} \mathbf{v}_+ - \mathbf{v}_-, & \text{for } F \not\subset \partial\Omega \\ \mathbf{v} - \hat{\mathbf{u}}, & \text{for } F \subset \Gamma_D \\ \mathbf{0}, & \text{for } F \subset \Gamma_N. \end{cases} \quad (5.1)$$

with $[\cdot] = [\cdot]_{(\mathbf{0})}$, as well as the averaged normal stress

$$\{\boldsymbol{\sigma}(\mathbf{v})\mathbf{n}\}_{(\hat{\mathbf{t}})} = \begin{cases} (\boldsymbol{\sigma}(\mathbf{v}_+)\mathbf{n}_+ + \boldsymbol{\sigma}(\mathbf{v}_-)\mathbf{n}_-)/2 & \text{for } F \not\subset \partial\Omega \\ \boldsymbol{\sigma}(\mathbf{v})\mathbf{n}, & \text{for } F \subset \Gamma_D \\ \boldsymbol{\sigma}(\mathbf{v})\mathbf{n} - \hat{\mathbf{t}}, & \text{for } F \subset \Gamma_N, \end{cases} \quad (5.2)$$

with $\{\cdot\} = \{\cdot\}_{(\mathbf{0})}$.

Choosing appropriate local coupling spaces $\mathbf{W}_p(F), \mathbf{W}_d(F) \subset (L^2(F))^d$, we can define the affine weakly conforming approximation space

$$\mathbf{X}_h(\hat{\mathbf{u}}, \hat{\mathbf{t}}) = \left\{ \mathbf{v}_h \in \mathbf{V}_h : \int_F [\mathbf{v}_h]_{(\hat{\mathbf{u}})}^\top \boldsymbol{\mu}_F \, d\gamma = 0, \quad \boldsymbol{\mu}_F \in \mathbf{W}_p(F), \right. \\ \left. \int_F \{\boldsymbol{\sigma}(\mathbf{v}_h)\mathbf{n}\}_{(\hat{\mathbf{t}})}^\top \boldsymbol{\eta}_F \, d\gamma = 0, \quad \boldsymbol{\eta}_F \in \mathbf{W}_d(F), \quad F \in \mathcal{F}_h \right\}. \quad (5.3)$$

The test space is the corresponding linear space $\mathbf{X}_h = \mathbf{X}_h(\mathbf{0}, \mathbf{0})$.

The weakly conforming method is then defined abstractly as $\mathbf{u}_h \in \mathbf{X}_h(\hat{\mathbf{u}}, \hat{\mathbf{t}})$:

$$a_h(\mathbf{u}_h, \mathbf{v}_h) = f(\mathbf{v}_h), \quad \mathbf{v}_h \in \mathbf{X}_h. \quad (5.4)$$

We consider component-wise polynomial spaces for the displacement and the coupling as follows: For given element degrees $p_{\tau_h}^1, \dots, p_{\tau_h}^d \geq 1$, we set

$$\mathbf{V}_h(\tau_h) = \mathbb{P}_{p_{\tau_h}^1} \times \dots \times \mathbb{P}_{p_{\tau_h}^d}.$$

Although not explicitly noted, in the case of quadrilaterals or hexahedral elements the corresponding tensorial spaces \mathbb{Q}_p , see Section 1.1.2.2, are considered for the element-wise space. Defining the primal coupling space $\mathbf{W}_p(F)$, special care must be taken to eliminate local rotations. For lowest-order couplings (i.e., for some $p_F^i = 0$), the polynomial space $\mathbb{P}_{p_F^1} \times \dots \times \mathbb{P}_{p_F^d}$ must be enhanced

by some linear functions $\mathbf{W}_{\text{RM}}(F) \subset (\mathbb{P}_1)^d$, which are discussed later. For local degrees $p_F^1, \dots, p_F^d \geq 0$, we define

$$\mathbf{W}_p(F) = \mathbb{P}_{p_F^1} \times \dots \times \mathbb{P}_{p_F^d} + \mathbf{W}_{\text{RM}}(F).$$

We note that for $p_F^1, \dots, p_F^d \geq 1$ it holds $\mathbf{W}_p(F) = \mathbb{P}_{p_F^1} \times \dots \times \mathbb{P}_{p_F^d}$.

The dual coupling space is defined similarly by polynomials of the degrees $q_F^1, \dots, q_F^d \geq -1$:

$$\mathbf{W}_d(F) = \mathbb{P}_{q_F^1} \times \dots \times \mathbb{P}_{q_F^d},$$

where we consider $\mathbb{P}_{-1} = \{0\}$. We note that inhomogeneous Neumann boundary conditions are solely implemented using the dual coupling space. Hence for $F \subset \Gamma_N$, we assume $q_F^i \geq 0$, $i = 1, \dots, d$, while for $F \subset \Gamma_D$, we assume $q_F^i = -1$.

Now, let us comment on the application of the weakly conforming method to contact problems. The weakly coupled discontinuous space allows an easy and local implementation of contact conditions. We consider piecewise constant Lagrange multipliers, which yields the energy minimization on the convex set

$$\mathbf{K}_h = \left\{ \mathbf{v}_h \in \mathbf{X}_h(\hat{\mathbf{u}}, \hat{\mathbf{t}}) : \int_F \mathbf{v}_h^\top \mathbf{n} \, d\gamma \leq \int_F \hat{g} \, d\gamma, \quad F \in \mathcal{F}_h, F \subset \Gamma_C \right\},$$

or the equivalent variational inequality $\mathbf{u}_h \in \mathbf{K}_h$, such that

$$a_h(\mathbf{u}_h, \mathbf{v}_h - \mathbf{u}_h) \geq f(\mathbf{v}_h - \mathbf{u}_h), \quad \mathbf{v}_h \in \mathbf{K}_h.$$

Also locally linear test functions for the contact would be possible, but due to the reduced regulation of contact problems, this would not improve the primal convergence rates. Hence, due to its simplicity, we only consider a lowest order contact discretization. The solution of the variational inequality is based on an active set strategy as described in Section 5.1.3.1.

5.1.2 A priori analysis

We analyze the weakly conforming method in the abstract framework of non-conforming methods. At first, the ellipticity of the method is studied and the conditions on the coupling for a uniform ellipticity are derived. Based on the uniform ellipticity, optimal order estimates are given for a primal coupling. At the end of this section, the problem is reformulated as an inf-sup stable saddle-point problem, which is the basis for the hybridization, where the element-wise degrees of freedom are eliminated.

5.1.2.1 Ellipticity: local rigid body modes

A main requirement for the well-posedness of non-conforming methods is a uniform ellipticity. For the Poisson problem it is sufficient to consider $p_F \geq 0$, see [38]. An example are non-conforming Crouzeix-Raviart elements with $p_{\tau_h} = 1$ and $p_F = 0$, see, e.g., [76]. For the same coupling degree applied to linear elasticity a mesh-dependent ellipticity constant is observed on regular two-dimensional grids, see [132, 133, 134], which yields a reduced convergence rate. On tetrahedral and unstructured triangular grids even singular matrices are possible. Only for $p_{\tau_h}^i \geq 1$ a uniform ellipticity is given, see [39, 132]. A closer insight in the difficulty is given by considering the *rigid body modes* (RM) of linear elasticity. There we will also note, that the condition $p_{\tau_h}^i \geq 1$ can be weakened by considering a more complicated condition.

The non-zero displacements without any contribution to the internal energy are called rigid body modes. More precisely $\mathbf{u}^{\text{RM}} \in (H^1(\Omega))^d$, such that

$$\int_{\Omega} \boldsymbol{\sigma}(\mathbf{u}^{\text{RM}}) : \boldsymbol{\varepsilon}(\mathbf{u}^{\text{RM}}) \, d\mathbf{x} = 0.$$

Since $\boldsymbol{\sigma}(\mathbf{u}) = \mathbb{C}\boldsymbol{\varepsilon}(\mathbf{u})$ with \mathbb{C} positive definite, it must hold $\boldsymbol{\varepsilon}(\mathbf{u}^{\text{RM}}) = \mathbf{0}$. The kernel of $\boldsymbol{\varepsilon}$ is easily computed and spanned by the six vectors

$$\begin{aligned} \mathbf{u}^{\text{RM},1}(x, y, z) &= \begin{pmatrix} 1 \\ 0 \\ 0 \end{pmatrix}, \quad \mathbf{u}^{\text{RM},2}(x, y, z) = \begin{pmatrix} 0 \\ 1 \\ 0 \end{pmatrix}, \quad \mathbf{u}^{\text{RM},3}(x, y, z) = \begin{pmatrix} 0 \\ 0 \\ 1 \end{pmatrix}, \\ \mathbf{u}^{\text{RM},4}(x, y, z) &= \begin{pmatrix} -y \\ x \\ 0 \end{pmatrix}, \quad \mathbf{u}^{\text{RM},5}(x, y, z) = \begin{pmatrix} -z \\ 0 \\ x \end{pmatrix}, \quad \mathbf{u}^{\text{RM},6}(x, y, z) = \begin{pmatrix} 0 \\ -z \\ y \end{pmatrix}, \end{aligned}$$

for $d = 3$ and the three vectors

$$\mathbf{u}^{\text{RM},1}(x, y) = \begin{pmatrix} 1 \\ 0 \end{pmatrix}, \quad \mathbf{u}^{\text{RM},2}(x, y) = \begin{pmatrix} 0 \\ 1 \end{pmatrix}, \quad \mathbf{u}^{\text{RM},3}(x, y) = \begin{pmatrix} -y \\ x \end{pmatrix},$$

for $d = 2$. The first d modes are simple translations, while the remaining modes are linearized rotations. These rotations with no energy contribution are the main difference to the singular mode of the scalar Poisson problem, which is not more than the constant function $u(\mathbf{x}) = 1$.

While in the conforming setting, the rigid body modes are usually eliminated by the boundary conditions, they play a crucial role for non-conforming methods. Due to the missing continuity, the broken space \mathbf{V}_h contains these modes locally on each element. On each element six (resp. three for $d = 2$)

local rigid body modes exist, yielding a total of $6|\mathcal{T}_h|$ singular modes, where $|\mathcal{T}_h|$ denotes the number of elements. To obtain a uniform ellipticity requirement, the minimal continuity requirement in \mathbf{X}_h is the elimination of these local rigid body modes.

A coupling of the mean value (i.e., $p_{\tau_h}^i = 0$) is insufficient to eliminate local rotations, which can appear in a variety of forms, mostly in checkerboard patterns, see Figure 5.1. The pattern on uniform rectangular grids (left in Figure 5.1) does not comply with any continuous Dirichlet boundary conditions, so it cannot appear globally. However, it appears weighted, with the largest magnitude in the interior of the domain, which is sufficient to show an h -dependent ellipticity constant, see [133]. Considering triangular grids, singular patches can appear in points where four triangles share one vertex, see Figure 5.1 (middle). On tetrahedral meshes even during regular refinement singular modes appear, see Figure 5.1 (right).

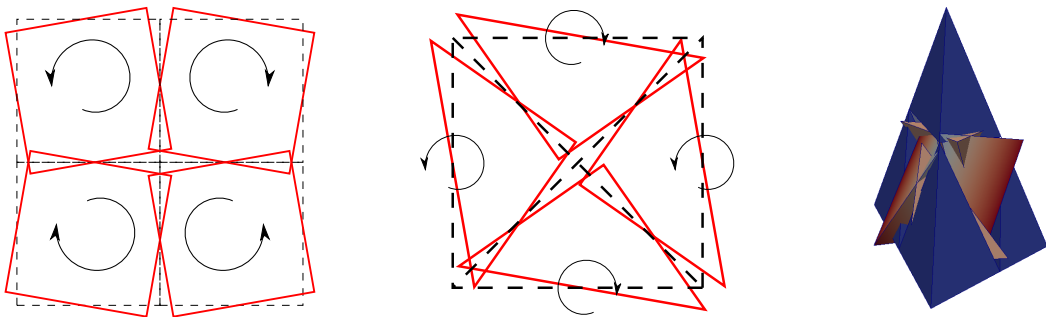


Figure 5.1: Local rotational modes. Left: Checkerboard mode on a uniform rectangular grid. Middle: Singular mode on a patch of four triangles. Right: Singular modes appearing during regular refinements of a tetrahedron.

These few simple examples show the importance to eliminate the local rigid modes properly. Since the number of coupling conditions correspond to the degrees of freedom in the hybrid setting, we aim to reduce the number of necessary coupling conditions. As shown in [39], $p_{\tau_h}^i = 1$ yields a uniform ellipticity, but this results in nine degrees of freedom on each face for $d = 3$. Only six degrees of freedom need to be eliminated, so we expect that six coupling conditions are sufficient. These conditions can be found by considering the trace of the rigid modes.

We note that the dual coupling $\mathbf{W}_d(F)$ does not influence the local rigid modes at all, as they satisfy $\boldsymbol{\sigma}(\mathbf{u}^{\text{RM}}) = \mathbf{0}$ by construction.

Let an element $\tau_h \in \mathcal{T}_h$ and a face F be given. For simplicity, we assume the face to be a subset of the xy -plane with $\mathbf{n} = (0, 0, 1)^\top$. In practice, we can introduce a local coordinate system. Then the local rotational modes on F are

given as

$$\begin{aligned}\mathbf{u}^{\text{RM},4}(x, y, 0) &= \begin{pmatrix} -y \\ x \\ 0 \end{pmatrix} = x \mathbf{e}_y - y \mathbf{e}_x, \\ \mathbf{u}^{\text{RM},5}(x, y, 0) &= \begin{pmatrix} 0 \\ 0 \\ x \end{pmatrix} = x \mathbf{n}, \quad \mathbf{u}^{\text{RM},6}(x, y, 0) = \begin{pmatrix} 0 \\ 0 \\ y \end{pmatrix} = y \mathbf{n}.\end{aligned}$$

These are the modes to eliminate and we define

$$\mathbf{W}_{\text{RM}}(F) = \mathbf{n} \mathbb{P}_1 + \text{span}\{x \mathbf{e}_y - y \mathbf{e}_x\}$$

for $d = 3$, while for $d = 2$ we consider

$$\mathbf{W}_{\text{RM}}(F) = \mathbf{n} \mathbb{P}_1.$$

In the lowest order case $p_F^i = 0$, $i = 1, \dots, d$, the dimension of the primal coupling space $\mathbf{W}_p(F)$ is 3 for $d = 2$ and 6 for $d = 3$, which corresponds to the number of local rotational modes.

Based on the coupling modes, ellipticity of the presented method can be shown. The proof is closely related to [39], where the more restrictive case $\mathbf{W}_p(F) = (\mathbb{P}_1)^d$ is considered. Looking at the proof one notes that it is sufficient to eliminate the local rigid body modes using the coupling, which means that it includes the case $\mathbf{W}_p(F) = (\mathbb{P}_0)^d + \mathbf{W}_{\text{RM}}(F)$, see also [152].

Assume that for all $F \in \mathcal{F}_h$, it holds $(\mathbb{P}_0)^d + \mathbf{W}_{\text{RM}}(F) \subset \mathbf{W}_p(F)$ and note that we consider the case $|\Gamma_D| > 0$, then [39, Inequality (1.15)] yields a positive constant c , such that

$$\|\boldsymbol{\varepsilon}(\mathbf{v}_h)\|_{L^2(\Omega)} \geq c \|\mathbf{v}_h\|_{H^1(\mathcal{T}_h)}, \quad \mathbf{v}_h \in \mathbf{X}_h. \quad (5.5)$$

5.1.2.2 Optimal order error estimates for non-conforming methods

Based on the stated ellipticity, a simple a priori estimate for h -refinement can be given. Let us consider a purely primal coupling with minimal degree p' , i.e., $q_F^i = 0$, $p_F^i \geq p'$, $\Gamma_N = \emptyset$, and a minimal element degree p : $p_{\tau_h}^i \geq p$. For simplicity of notation $\hat{\mathbf{u}} = \mathbf{0}$.

Theorem 5.1.1. *Let $\mathbf{W}_{\text{RM}}(F) \subset \mathbf{W}_p(F)$ for $F \in \mathcal{F}_h$. For $\mathbf{u} \in (H^{s+1}(\Omega))^d$ the weak solution of linear elasticity (1.4) with $1 \leq s \leq \min(p, p' + 1)$ and $\mathbf{u}_h \in \mathbf{X}_h$ the weakly conforming discretization (5.4), it holds*

$$\|\mathbf{u} - \mathbf{u}_h\|_{H^1(\mathcal{T}_h)} \leq ch^s |\mathbf{u}|_{H^{s+1}(\Omega)}.$$

Under the additional assumption of dual regularity, also the L^2 error is of an optimal order:

$$\|\mathbf{u} - \mathbf{u}_h\|_{L^2(\Omega)} \leq ch^{s+1} |\mathbf{u}|_{H^{s+1}(\Omega)}.$$

Proof. The proof is based on standard techniques, see, e.g., [76, Chapter 3.2.3], which are easily adapted to the higher order and the equation of elasticity. For the sake of completeness, we present the main steps.

While the uniform discrete ellipticity is given by (5.5), continuity with respect to the $H^1(\mathcal{T}_h)$ norm follows by the same arguments as the continuous problem.

It remains to bound the consistency error, based on the second Lemma of Strang, see Section 1.1.2.3. The conforming finite element space is a subspace of \mathbf{X}_h , so the best approximation property follows trivially. The consistency term remains:

$$\sup_{\mathbf{w}_h \in \mathbf{X}_h} \frac{a_h(\mathbf{u}, \mathbf{w}_h) - f(\mathbf{w}_h)}{\|\mathbf{w}_h\|_{H^1(\mathcal{T}_h)}}.$$

Let $\mathbf{w}_h \in \mathbf{X}_h$. Since $\widehat{\mathbf{f}} = -\operatorname{div} \boldsymbol{\sigma}(\mathbf{u})$, integration by parts yields

$$\sum_{\tau_h \in \mathcal{T}_h} \int_{\tau_h} \boldsymbol{\sigma}(\mathbf{u}) : \boldsymbol{\varepsilon}(\mathbf{w}_h) - \widehat{\mathbf{f}}^\top \mathbf{w}_h \, d\mathbf{x} = \sum_{F \in \mathcal{F}_h} \int_F (\boldsymbol{\sigma}(\mathbf{u}) \mathbf{n}_+)^\top [\mathbf{w}_h] \, d\gamma.$$

On each face $F \in \mathcal{F}_h$, we define π_F , the (multi-valued) L^2 projection onto the polynomials of degree s from each of the neighboring elements individually. We note that $[\pi_F \mathbf{w}_h] = 0$ by construction of \mathbf{X}_h , hence

$$\begin{aligned} \sum_{F \in \mathcal{F}_h} \int_F (\boldsymbol{\sigma}(\mathbf{u}) \mathbf{n}_+)^\top [\mathbf{w}_h] \, d\gamma &= \sum_{F \in \mathcal{F}_h} \int_F (\boldsymbol{\sigma}(\mathbf{u}) \mathbf{n}_+)^\top [\mathbf{w}_h - \pi_F \mathbf{w}_h] \, d\gamma \\ &= \sum_{F \in \mathcal{F}_h} \int_F (\boldsymbol{\sigma}(\mathbf{u}) \mathbf{n}_+ - \pi_F(\boldsymbol{\sigma}(\mathbf{u}) \mathbf{n}_+))^\top [\mathbf{w}_h - \pi_F \mathbf{w}_h] \, d\gamma \\ &\leq \sum_{\tau_h \in \mathcal{T}_h} \sum_{F \in \mathcal{F}_h(\tau_h)} \|\boldsymbol{\sigma}(\mathbf{u}) \mathbf{n}_+ - \pi_F(\boldsymbol{\sigma}(\mathbf{u}) \mathbf{n}_+)\|_{0,F} \|\mathbf{w}_h - \pi_F \mathbf{w}_h\|_{0,F}, \end{aligned}$$

using the orthogonality of the L^2 projection. $\mathcal{F}_h(\tau_h)$ denotes the faces of τ_h and the traces on $\mathcal{F}_h(\tau_h)$ are the ones from τ_h . Now standard norm equivalences on the reference element, see [36], yield the expected approximation order as

$$\|\boldsymbol{\sigma}(\mathbf{u}) \mathbf{n}_+ - \pi_F(\boldsymbol{\sigma}(\mathbf{u}) \mathbf{n}_+)\|_{0,F} \leq ch^{s-1/2} |\mathbf{u}|_{H^{s+1}(\tau_h)}$$

and

$$\|\mathbf{w}_h - \pi_F \mathbf{w}_h\|_{0,F} \leq ch^{1/2} |\mathbf{w}|_{H^1(\tau_h)},$$

which in combination shows the $H^1(\mathcal{T}_h)$ estimate.

The L^2 estimate can be shown by a non-conforming variant of the Aubin–Nitsche trick, see [34, Chapter 3] for details. The starting point is the abstract formulation given in [34, Chapter 3, Lemma 1.4]:

$$\begin{aligned} \|\mathbf{u} - \mathbf{u}_h\|_{L^2(\Omega)} \leq & \sup_{\mathbf{g} \in (L^2(\Omega))^d} \|\mathbf{g}\|_{L^2(\Omega)}^{-1} \left\{ c \|\mathbf{u} - \mathbf{u}_h\|_{H^1(\mathcal{T}_h)} \|\mathbf{w}_{\mathbf{g}} - \mathbf{w}_{\mathbf{g},h}\|_{H^1(\mathcal{T}_h)} \right. \\ & + |a_h(\mathbf{u} - \mathbf{u}_h, \mathbf{w}_{\mathbf{g}}) - (\mathbf{u} - \mathbf{u}_h, \mathbf{g})_0| \\ & \left. + |a_h(\mathbf{u}, \mathbf{w}_{\mathbf{g}} - \mathbf{w}_{\mathbf{g},h}) - f(\mathbf{w}_{\mathbf{g}} - \mathbf{w}_{\mathbf{g},h})| \right\}, \end{aligned}$$

where $\mathbf{w}_{\mathbf{g}} \in (H_D^1(\Omega))^d$ solves the standard dual problem

$$a(\mathbf{v}, \mathbf{w}_{\mathbf{g}}) = (\mathbf{g}, \mathbf{v})_0, \quad \mathbf{v} \in (H_D^1(\Omega))^d,$$

and $\mathbf{w}_{\mathbf{g},h} \in \mathbf{X}_h$ is a non-conforming approximation:

$$a_h(\mathbf{v}_h, \mathbf{w}_{\mathbf{g},h}) = (\mathbf{g}, \mathbf{v}_h)_0, \quad \mathbf{v}_h \in \mathbf{X}_h.$$

The first term is the standard term appearing with the conforming Aubin–Nitsche method. The second and third terms are similar to the consistency term, treated above, the first one formulated for the dual problem, the second one for the primal problem. Proceeding as above yields

$$|a_h(\mathbf{u} - \mathbf{u}_h, \mathbf{w}_{\mathbf{g}}) - (\mathbf{u} - \mathbf{u}_h, \mathbf{g})_0| \leq ch |\mathbf{w}_{\mathbf{g}}|_{H^2(\Omega)} |\mathbf{u} - \mathbf{u}_h|_{H^1(\mathcal{T}_h)},$$

and

$$|a_h(\mathbf{u}, \mathbf{w}_{\mathbf{g}} - \mathbf{w}_{\mathbf{g},h}) - f(\mathbf{w}_{\mathbf{g}} - \mathbf{w}_{\mathbf{g},h})| \leq ch^s |\mathbf{u}|_{H^{s+1}(\Omega)} |\mathbf{w}_{\mathbf{g}} - \mathbf{w}_{\mathbf{g},h}|_{H^1(\mathcal{T}_h)},$$

and the H^1 estimate above completes the proof. \square

5.1.2.3 Saddle point framework

Here we present an alternative formulation to the previous purely primal formulation. The primal-dual saddle point problem is of particular importance, as it is the basis for the hybridization considered in Section 5.1.3.1. We show the well-posedness of the saddle-point formulation, based on a local criterion. For convenience of notation, we consider a purely primal coupling, $q_F^i = 0$, $F \in \mathcal{F}_h$ and $\Gamma_N = \emptyset$, and note that the introduction of a dual coupling can be considered the same way.

The previous results did not pose any upper bound on the degree of the coupling space. This is due to the fact that in case of an over-constrain, the space \mathbf{X}_h turns out as the conforming finite element space and we get the

results of a conforming method. While this works in theory, the space \mathbf{X}_h is not available for a practical implementation. Instead, the broken space \mathbf{V}_h and face degrees of freedom can be used. In the case of an over-constrain, the face degrees of freedom will not be uniquely defined.

The functional analysis framework for the coupling spaces is considered element-wise using the $H^{1/2}(\partial\tau_h) - H^{-1/2}(\partial\tau_h)$ coupling, which can be considered globally defining

$$H^{1/2}(\partial\mathcal{T}_h) = \prod_{\tau_h \in \mathcal{T}_h} H^{1/2}(\partial\tau_h), \quad H^{-1/2}(\partial\mathcal{T}_h) = \prod_{\tau_h \in \mathcal{T}_h} H^{-1/2}(\partial\tau_h).$$

Grouping the face-wise coupling spaces element-wise and noting that it holds $\partial\tau_h = \cup_{F \in \mathcal{F}_h(\tau_h)} \bar{F}$ yields local coupling spaces as a subspace of $(H^{-1/2}(\partial\tau_h))^d$:

$$\widehat{\mathbf{W}}_h(\partial\tau_h) = \left\{ \boldsymbol{\mu}_h \in (L^2(\partial\tau_h))^d : \boldsymbol{\mu}_h|_F \in \mathbf{W}_p(F), F \in \mathcal{F}_h(\tau_h) \right\},$$

which can be collected globally to

$$\widehat{\mathbf{W}}_h(\partial\mathcal{T}_h) = \prod_{\tau_h \in \mathcal{T}_h} \widehat{\mathbf{W}}_h(\partial\tau_h) \subset (H^{-1/2}(\partial\mathcal{T}_h))^d.$$

Note that the spaces are multi-valued on each interior face, with one value from each neighboring element. We denote the value on the neighbor $\tau_{h,+}$ by $\boldsymbol{\mu}_{h,+}$ and the value on the other neighbor $\tau_{h,-}$ by $\boldsymbol{\mu}_{h,-}$. Since $\widehat{\mathbf{W}}_h(\partial\tau_h) \subset (L^2(\partial\tau_h))^d$, we can also consider the coupled subset

$$\mathbf{W}_h(\partial\mathcal{T}_h) = \{ \boldsymbol{\mu}_h \in \widehat{\mathbf{W}}_h(\partial\mathcal{T}_h) : \boldsymbol{\mu}_{h,+}|_F + \boldsymbol{\mu}_{h,-}|_F = 0, \quad F \in \mathcal{F}_h^{\text{int}} \}.$$

Using the representation of the global coupling within $(H^{-1/2}(\partial\mathcal{T}_h))^d$ allows us to reformulate the weakly conforming space (5.3) as

$$\mathbf{X}_h(\hat{\mathbf{u}}, \mathbf{0}) = \left\{ \mathbf{v}_h \in \mathbf{V}_h : \sum_{\tau_h \in \mathcal{T}_h} \langle \mathbf{v}_h, \boldsymbol{\mu}_h \rangle_{\partial\tau_h} = \sum_{F \in \mathcal{F}_h^{\text{D}}} \langle \hat{\mathbf{u}}, \boldsymbol{\mu}_h \rangle_F, \quad \boldsymbol{\mu}_h \in \mathbf{W}_h(\partial\mathcal{T}_h) \right\}.$$

We can analyze the method in a saddle point framework as the solution \mathbf{u}_h of the weakly conforming methods (5.4) is the primal solution of the saddle point problem $(\mathbf{u}_h, \boldsymbol{\lambda}_h) \in \mathbf{V}_h \times \mathbf{W}_h(\partial\mathcal{T}_h)$, such that

$$\begin{aligned} a_h(\mathbf{u}_h, \mathbf{v}_h) + \sum_{\tau_h \in \mathcal{T}_h} \langle \mathbf{v}_h, \boldsymbol{\lambda}_h \rangle_{\partial\tau_h} &= f(\mathbf{v}_h), \quad \mathbf{v}_h \in \mathbf{V}_h, \\ \sum_{\tau_h \in \mathcal{T}_h} \langle \mathbf{u}_h, \boldsymbol{\mu}_h \rangle_{\partial\tau_h} &= \sum_{F \in \mathcal{F}_h^{\text{D}}} \langle \hat{\mathbf{u}}, \boldsymbol{\mu}_h \rangle_F, \quad \boldsymbol{\mu}_h \in \mathbf{W}_h(\partial\mathcal{T}_h). \end{aligned}$$

From the theory of saddle point problems (see Section 1.1.2.4) we know that the key points are the kernel ellipticity as well as the inf-sup stability. We have treated the kernel ellipticity (i.e., the ellipticity on \mathbf{X}_h) in the previous section, so let us comment on the inf-sup stability. We assume the following uniform local inf-sup condition:

Assumption 5.1.2. *There exists a positive constant c , such that for all elements $\tau_h \in \mathcal{T}_h$ a local inf-sup condition holds:*

For $\boldsymbol{\mu}_{\tau_h} \in \mathbf{W}_h(\partial\tau_h)$ it holds

$$\sup_{\mathbf{v}_{\tau_h} \in \mathbf{V}_h(\tau_h)} \frac{\langle \mathbf{v}_{\tau_h}, \boldsymbol{\mu}_{\tau_h} \rangle_{\partial\tau_h}}{\|\mathbf{v}_{\tau_h}\|_{H^1(\tau_h)}} \geq c \|\boldsymbol{\mu}_{\tau_h}\|_{H^{-1/2}(\partial\tau_h)}.$$

Since $\mathbf{V}_h(\tau_h)$ and $\mathbf{W}_h(\partial\tau_h)$ are polynomial spaces their dimension is uniformly bounded if we set an upper degree bound on the spaces. In this case, under the assumption of shape-regular elements, the inf-sup condition reduces to a purely algebraic condition. It holds if the coupling matrix $\langle \mathbf{v}_{\tau_h}, \boldsymbol{\mu}_{\tau_h} \rangle_{\partial\tau_h}$ has full rank $\dim \mathbf{W}_h(\partial\tau_h)$. A detailed discussion of inf-sup stable pairings is given in a section below.

Based on the uniform local inf-sup stability on all elements stated in Assumption 5.1.2, a global inf-sup stability follows in the product space norms $(H^1(\mathcal{T}_h), H^{-1/2}(\partial\mathcal{T}_h))$. For any $\boldsymbol{\mu}_h \in \mathbf{W}(\partial\mathcal{T}_h)$,

$$\sup_{\mathbf{v}_h \in \mathbf{V}_h} \frac{\sum_{\tau_h \in \mathcal{T}_h} \langle \mathbf{v}_h, \boldsymbol{\mu}_h \rangle_{\partial\tau_h}}{\|\mathbf{v}_h\|_{H^1(\mathcal{T}_h)}} \geq c \|\boldsymbol{\mu}_h\|_{H^{-1/2}(\partial\mathcal{T}_h)}.$$

The local Fortin operators can be combined to a stable global one and be applied to a continuous supremizer based on the local duality.

The global inf-sup estimate shows that the global saddle point problem is well posed when local criteria are met. Although we do not solve the saddle point problem directly, it is the basis for the hybridization presented in the following.

5.1.3 Hybridization and practical formulations

While the saddle point problem is mathematically well-posed, it poses additional difficulties for the practical implementation. The use of element-based and face-based degrees of freedom significantly enlarges the linear equation system and the indefinite saddle point structure poses extra difficulties to the linear solver, see Section 1.1.2.4.

5.1.3.1 Local condensation of element-wise degrees of freedom

For practical implementations a hybridization to the face degrees of freedom as introduced in [224] can be performed. The additional work is purely element-wise and can be done in parallel.

A key point of the hybridization is the multi-valued Lagrange multiplier space $\widehat{\mathbf{W}}_h(\partial\mathcal{T}_h)$. Exemplarily, we present the hybridization for a pure primal coupling with $\Gamma_D = \partial\Omega$ and note that the dual coupling is treated in the same way. We introduce a third variable $\mathbf{u}_{\Gamma,h}$ which implements the condition $\boldsymbol{\mu}_{h,+} = -\boldsymbol{\mu}_{h,-}$.

For $F \in \mathcal{F}_h$ the new variable $\mathbf{u}_{\Gamma,h}$ is in the algebraic dual space of the coupling space $(\mathbf{W}_p(F))^*$. Then obviously

$$\mathbf{W}_h(\partial\mathcal{T}_h) = \left\{ \boldsymbol{\mu}_h \in \widehat{\mathbf{W}}(\partial\mathcal{T}_h) : \sum_{F \in \mathcal{F}_h} \langle \{\boldsymbol{\mu}_h\}, \mathbf{v}_{\Gamma,h} \rangle_F = 0, \mathbf{v}_{\Gamma,h} \in \prod_{F \in \mathcal{F}_h^{\text{int}}} (\mathbf{W}_p(F))^* \right\},$$

where we formally set $\langle \cdot, \mathbf{v}_{\Gamma,h} \rangle_F = 0$ for boundary faces $F \in \mathcal{F}_h^D$. Hence, we can reformulate the non-conforming method (5.4) as a nested saddle point problem: $(\mathbf{u}_h, \boldsymbol{\lambda}_h, \mathbf{u}_{\Gamma,h}) \in \mathbf{V}_h \times \widehat{\mathbf{W}}_h(\partial\mathcal{T}_h) \times \prod_{F \in \mathcal{F}_h^{\text{int}}} (\mathbf{W}_p(F))^*$, such that

$$a_h(\mathbf{u}_h, \mathbf{v}_h) + \sum_{\tau_h \in \mathcal{T}_h} \langle \mathbf{v}_h, \boldsymbol{\lambda}_h \rangle_{\partial\tau_h} = f(\mathbf{v}_h), \quad \mathbf{v}_h \in \mathbf{V}_h, \quad (5.6a)$$

$$\sum_{\tau_h \in \mathcal{T}_h} \langle \mathbf{u}_h - \mathbf{u}_{\Gamma,h}, \boldsymbol{\mu}_h \rangle_{\partial\tau_h} = \sum_{F \in \mathcal{F}_h^D} \langle \widehat{\mathbf{u}}, \boldsymbol{\mu}_h \rangle_F, \quad \boldsymbol{\mu}_h \in \widehat{\mathbf{W}}_h(\partial\mathcal{T}_h), \quad (5.6b)$$

$$- \sum_{\tau_h \in \mathcal{T}_h} \langle \mathbf{v}_{\Gamma,h}, \boldsymbol{\mu}_h \rangle_{\partial\tau_h} = 0, \quad \mathbf{v}_{\Gamma,h} \in \prod_{F \in \mathcal{F}_h^{\text{int}}} (\mathbf{W}_p(F))^*. \quad (5.6c)$$

For a practical implementation $\mathbf{u}_{\Gamma,h}$ can be chosen in an affine space, where $\langle \mathbf{u}_{\Gamma,h}, \boldsymbol{\mu}_h \rangle_F = \langle \widehat{\mathbf{u}}, \boldsymbol{\mu}_h \rangle_F$ on Dirichlet faces $F \in \mathcal{F}_h^D$. This way the boundary conditions are a natural part of the hybridized system and fit well into existing finite element codes. For the sake of simplicity, we do not perform this step in the following.

Algebraically the nested saddle point problem (5.6) reads

$$\begin{pmatrix} A_h & B_h^\top & 0 \\ B_h & 0 & C_h^\top \\ 0 & C_h & 0 \end{pmatrix} \begin{pmatrix} u_h \\ \lambda_h \\ u_{\Gamma,h} \end{pmatrix} = \begin{pmatrix} f_h \\ g_h \\ 0 \end{pmatrix},$$

where we can form the Schur-complement for the outer saddle point problem as follows. The first two lines can be uniquely solved for (u_h, λ_h) in dependence

on $u_{\Gamma,h}$:

$$\begin{pmatrix} u_h \\ \lambda_h \end{pmatrix} = \begin{pmatrix} A_h & B_h^\top \\ B_h & 0 \end{pmatrix}^{-1} \left(\begin{pmatrix} f_h \\ g_h \end{pmatrix} - \begin{pmatrix} 0 \\ C_h^\top \end{pmatrix} u_{\Gamma,h} \right),$$

which we can insert into the last line, $C_h \lambda_h = 0$, to get

$$C_h \begin{pmatrix} 0 & \text{Id} \end{pmatrix} \begin{pmatrix} A_h & B_h^\top \\ B_h & 0 \end{pmatrix}^{-1} \begin{pmatrix} 0 \\ \text{Id} \end{pmatrix} C_h^\top u_{\Gamma,h} = C_h \begin{pmatrix} 0 & \text{Id} \end{pmatrix} \begin{pmatrix} A_h & B_h^\top \\ B_h & 0 \end{pmatrix}^{-1} \begin{pmatrix} f_h \\ g_h \end{pmatrix}.$$

The resulting equation system is symmetric and positive definite, with the stability estimates of [224, Lemma 4]. See also [225] for an analogue substructuring of first-order systems.

Due to the broken setting in \mathbf{V}_h and $\widehat{\mathbf{W}}_h(\partial\mathcal{T}_h)$, the inversion of the saddle point matrix

$$\begin{pmatrix} A_h & B_h^\top \\ B_h & 0 \end{pmatrix}$$

can be done by purely element-wise computations and is thus well suited for an efficient parallelization.

The algebraic equation $C_h \lambda_h = 0$ corresponds to the equilibrium of the Lagrange multipliers: $\lambda_{h,+} = -\lambda_{h,-}$, which allows an interpretation of the reduced system based on a discrete Steklov–Poincaré operator. Due to the unique solvability of the element-wise problem, the Lagrange multiplier locally only depends on the trace data, i.e., on $\tau_h \in \mathcal{T}_h$, $\lambda_h = \lambda_h(u_{\Gamma,h})$ with both λ_h and $u_{\Gamma,h}$ only evaluated on the element τ_h . See Figure 5.2 for an illustration

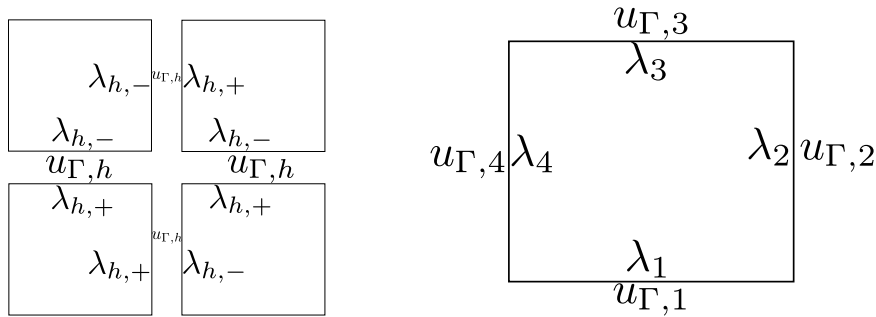


Figure 5.2: Sketch of the local variables considered during the hybridization. Left: Illustration of the multi-valued Lagrange multiplier. Communication only necessary for $u_{\Gamma,h}$, not for values of λ_h on different elements. Right: Local element-wise components.

of the variables. The dependence of the Lagrange multiplier can be regarded as a discrete Steklov–Poincaré operator, mapping Dirichlet data to Neumann

data. The final, hybridized equation then solves

$$\lambda_{h,+}(u_{\Gamma,h}) = -\lambda_{h,-}(u_{\Gamma,h}).$$

In the case of non-linear elasticity, the interior equation becomes non-linear. Then nested iterations need to be solved, an outer one for the non-linear Schur-complement system and an inner one solving the local equation systems. Both iterations could be performed by a Newton iteration.

With contact conditions, the inequality constraint is evaluated purely locally as an active set strategy. In each iteration step, the local evaluation of the Schur complement is at first performed using homogeneous Neumann conditions. Then the discrete contact condition is evaluated and the Schur complement is evaluated using either homogeneous Neumann conditions (inactive) or recomputed using inhomogeneous Dirichlet conditions (active).

5.1.3.2 Choice of the local degrees of freedom

In this section, we discuss some possible element pairings. Even with the assembly being efficiently performed in parallel, a higher degree yield a larger computational effort, so we try to keep the degree as low as possible. First, we discuss possible element pairings for a pure displacement coupling in 2D and then discuss a general adaptive choice of the displacement and stress coupling degrees of freedom.

Suitable element pairings The most convenient pairings would be with the primal degree p and the dual degree $p - 1$, like the standard Crouzeix-Raviart elements in the linear case. On rectangular elements the element space must be chosen modified, yielding Rannacher-Turek elements [182]. As discussed in Section 5.1.2.1 these low order elements do not yield a uniform ellipticity constant and can show a reduced convergence. While Crouzeix-Raviart elements on triangles can be generalized for odd degrees, e.g., [80], for $p = 2$ the local inf-sup condition is lacking, see [84].

In general, the inf-sup constant can be improved in two ways. Enlarging the primal space (element-wise degree), or lowering the dual space (coupling degree). For the P2-P1 pairing in 2D, we show that both ways are possible. Here P2-P1 denotes the global choice of $p_{\tau_h}^i = 2$ and $p_F^i = 1$ and is noted as such independent of the element geometry.

The quadratic ansatz is inf-sup stable with respect to the normal coupling $(\mathbb{P}_0)^2 + \mathbf{n}\mathbb{P}_1$ for $d = 2$ (PN), which was discussed in Section 5.1.2.1. See Figure 5.3 (left) for an illustration of the pairing. The downside is that the normal coupling PN yields on the faces only the approximation order of \mathbb{P}_0 ,

introducing a gap between the primal and dual approximation order.

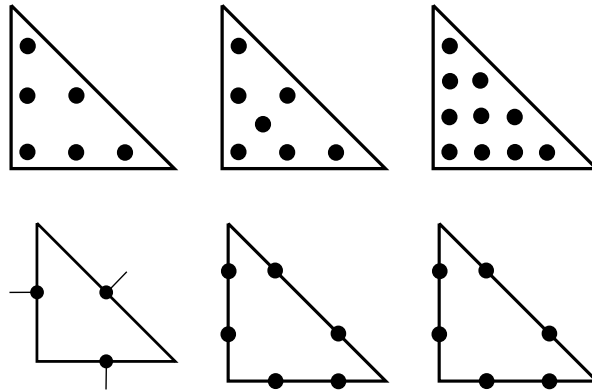


Figure 5.3: Suitable couplings, primal (top) and dual (bottom) degrees of freedom. From left to right: P2-PN, P2[⊕]-P1, P3-P1.

Adding just one function to each component of the primal space yields the inf-sup stability with respect to the P1 coupling. We denote the extended primal space by P2[⊕], see Figure 5.3. The extra function is

$$u^{\oplus}(x, y) = (x^2 - 1)(2x + 3y - 3) - (y^2 - 1)(2y + 3x - 3),$$

defined on the reference triangle $\{(x, y) : x, y \geq 0, x + y \leq 1\}$, and

$$u^{\oplus}(x, y) = x^3y - y^3x,$$

defined on the reference square $(-1, 1)^2$, see Figure 5.4. They are chosen to have a positive first moment with the average zero on each face, where a consistent orientation of the faces is used. This pairing is the only pairing, which does not introduce a gap between the primal and dual approximation order. On the downside, the presented set of functions only works for $d = 2$ and a quadratic primal space. For further situations these functions need to be computed individually.

A superset of P2[⊕] which is more convenient to implement is the P3-P1 pairing, also shown in the comparison of Figure 5.3.

For more general couplings an adaptive strategy can be used. Whenever a lack of the local inf-sup stability is noticed during the element-wise computation, the primal degree is enlarged locally.

Adaptive choice of the spaces A main feature of the weakly conforming method is its flexibility in the element-based and face-based degrees of freedom.

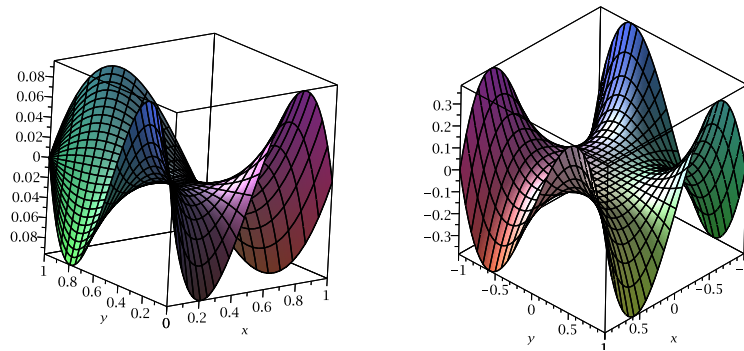


Figure 5.4: Additional primal basis function for the $P2^\oplus$ - $P1$ pairing. Left: On a triangle. Right: On a quadrilateral.

We propose an adaptive refinement strategy to identify the degrees of freedom which reduce the error most efficiently. Unlike the previous cases, we do not require to use full polynomial spaces. Instead, we consider the hierarchical orthonormal polynomial basis as the potential face moments of the coupling space. This means $\mathbb{P}_{\hat{p}} = \text{span}\{p_1^{\text{orth}}, \dots, p_{\dim \mathbb{P}_{\hat{p}}}^{\text{orth}}\}$, with $\int_F p_i^{\text{orth}} p_j^{\text{orth}} d\gamma = \delta_{ij}$ for a maximal polynomial degree \hat{p} . For $d = 2$, we choose a rescaling of the Lagrange polynomials, which can be computed recursively [179, Chapter 4.4.1], otherwise we can perform an orthogonalization from a monomial basis. For each component of the vectorial spaces $\mathbf{W}_p(F)$, $\mathbf{W}_d(F)$, the basis functions can be chosen individually.

In every adaptivity loop, we compute the primal and dual consistency errors $[\mathbf{u}_h]$ and $\{\boldsymbol{\sigma}(\mathbf{u}_h)\mathbf{n}\}$ on every face, tested with the face moments and correctly weighted with respect to the mesh size. More precisely, we compute

$$\eta_{i,\delta}^{F,p} = h^{1/2} \int_F [u_\delta] p_i^{\text{orth}} d\gamma \quad \text{and} \quad \eta_{i,\delta}^{F,d} = h^{-1/2} \int_F \{\boldsymbol{\sigma}(\mathbf{u}) \mathbf{n}^\top \mathbf{e}_\delta\} p_i^{\text{orth}} d\gamma,$$

with $\mathbf{e}_1, \dots, \mathbf{e}_d$ the natural basis of \mathbb{R}^d . We note that the sum of the square of the error components for each moment yields the face terms of the residual error estimate:

$$h \|[\mathbf{u}_h]\|_{L^2(F)}^2 = \sum_{i,\delta} (\eta_{i,\delta}^{F,p})^2 \quad \text{and} \quad h^{-1} \|\{\boldsymbol{\sigma}(\mathbf{u}_h)\mathbf{n}\}\|_{L^2(F)}^2 = \sum_{i,\delta} (\eta_{i,\delta}^{F,d})^2,$$

since $\mathbf{u} \in (\mathbb{P}_{\hat{p}})^d$. The volume residual $f + \Delta u$ could additionally be used to control the element degree or an adaptive h -refinement, which we do not consider here.

For a given threshold parameter, we select the face moments with the largest

error contribution $\eta_{i,\delta}^{F,p}/\eta_{i,\delta}^{F,d}$ according to a Dörfler marking strategy [68] and include it in the corresponding primal/dual coupling space. We note that the moments to be coupled are chosen independently for the d components, to account for possible anisotropic structures. Then, the local element degree is adjusted according to the number of local face degrees of freedom.

5.2 Numerical evaluation of the non-conforming method

As the first numerical tests of this chapter, we evaluate the weakly conforming method in various situations. The method is implemented in the the parallel finite element software M++ [154, 223]. The examples include well-known benchmark problems with a known solution, a new benchmark setting for contact problems and two- as well as three-dimensional nearly incompressible materials.

5.2.1 Uniform and adaptive refinements

In the first section, we evaluate the weakly conforming method on two examples with an analytically known exact solution. In the first example, we confirm the theoretical convergence rates, while we illustrate the adaptive choice of the degrees of freedom in the second example.

5.2.1.1 Verification of the convergence results with uniform h -refinement

To study the behavior during uniform h -refinement and to validate the convergence results given in Theorem 5.1.1, we consider a smooth example with a known solution. As such, we reconsider the example of a plate with a hole introduced in Section 1.2.1.2 with $\mu_{\text{Lamé}}, \lambda_{\text{Lamé}} = 1$. We note that for higher order methods, an exact geometry approximation becomes crucial to obtain optimal convergence orders, see [50, 145]. Here for simplicity, we use a low-order geometry approximation, but we apply the value of the exact solution to the inexact Dirichlet boundary. This way, we obtain the optimal rates of the methods without the technical difficulties of the geometry approximation.

The initial mesh consists of four elements and a uniform mesh refinement is considered. The low-order geometry approximation is realized by shifting the new vertices with respect to a predefined geometry mapping. On each level, we compare the element pairings P1-P0, P2-PN, P3-P1 and P4-P2.

The absolute error in the L^2 norm and the estimated order of convergence is given in Table 5.1 and in Table 5.2 the error in the energy norm is given. With one exception, we observe the expected convergence rates of Theorem 5.1.1. For the P2-PN pairing, the dual approximation order is zero, which theoretically implies convergence of order two in the L^2 norm by Theorem 5.1.1. The improved observed convergence order of 2.5 could be due to the higher dual approximation order in the normal direction, while the lowest order only affects the tangential part of the solution. This observation is similar to observations with the isogeometric mortar methods in Section 2.2.2.1, where the primal error converges faster than expected. Here it seems to be limited to the case P2-PN as the effect cannot be seen with the P3-P1 and P4-P2 pairings. In all shown cases, the L^2 error is of an order h smaller than the energy error.

We note that the unstable P1-P0 pairing shows optimal convergence rates, besides the probably h -dependent ellipticity. However, the L^2 error on the initial grid is about eight times larger than for P2-PN. We note that optimal convergence does not always hold and examples exist with a reduced convergence rate. With an analogue triangular mesh for this example, the stiffness matrix using P1-P0 is even singular and no discrete solution exists. We refer to the discussion of Section 5.1.2.1 with the singular mode shown in Figure 5.1.

Table 5.1: $L^2(\Omega)$ error with an estimated rate of convergence for different non-conforming pairings.

k	P1-P0		P2-PN		P3-P1		P4-P2	
0	2.231e+01	-	3.024e+00	-	1.012e+00	-	2.420e-01	-
1	6.501e+00	1.78	1.234e+00	1.29	2.482e-01	2.03	3.048e-02	2.99
2	1.726e+00	1.91	2.689e-01	2.20	4.083e-02	2.60	2.670e-03	3.51
3	4.411e-01	1.97	4.677e-02	2.52	6.040e-03	2.76	1.977e-04	3.76
4	1.111e-01	1.99	7.790e-03	2.59	8.721e-04	2.79	1.325e-05	3.90
5	2.787e-02	2.00	1.330e-03	2.55	1.217e-04	2.84	8.559e-07	3.95
6	6.980e-03	2.00	2.326e-04	2.52	1.632e-05	2.90	5.447e-08	3.97
7	1.750e-03	2.00	4.111e-05	2.50	2.124e-06	2.94	3.466e-09	3.97

5.2.1.2 Adaptive choice of the degrees of freedom on an L-shape

The adaptive strategy described in Section 5.1.3.2 is evaluated for a Dirichlet test problem on the L-shaped domain $\Omega = (-1, 1)^2 \setminus [0, 1] \times [-1, 0]$ with a strong stress singularity at the re-entrant corner [192]. To avoid the symmetry of the solution, we consider a small rotation of the singularity, which remains

Table 5.2: Energy error $(\int_{\Omega} \boldsymbol{\varepsilon}(\mathbf{u} - \mathbf{u}_h) : \boldsymbol{\sigma}(\mathbf{u} - \mathbf{u}_h) \, d\mathbf{x})^{1/2}$ with estimated rate of convergence for different non-conforming pairings.

k	P1-P0		P2-PN		P3-P1		P4-P2	
0	2.721e+00	-	8.224e-01	-	4.287e-01	-	1.466e-01	-
1	1.426e+00	0.93	4.287e-01	0.94	1.661e-01	1.37	3.432e-02	2.09
2	7.370e-01	0.95	1.756e-01	1.29	5.434e-02	1.61	6.580e-03	2.38
3	3.734e-01	0.98	6.229e-02	1.49	1.602e-02	1.76	1.000e-03	2.72
4	1.875e-01	0.99	2.071e-02	1.59	4.490e-03	1.84	1.338e-04	2.90
5	9.383e-02	1.00	6.860e-03	1.59	1.210e-03	1.89	1.713e-05	2.97
6	4.693e-02	1.00	2.320e-03	1.56	3.170e-04	1.93	2.166e-06	2.98
7	2.346e-02	1.00	7.976e-04	1.54	8.127e-05	1.96	2.725e-07	2.99

of the same order, i.e.,

$$\mathbf{u} \begin{pmatrix} r \cos(\theta + \pi/6) \\ r \sin(\theta + \pi/6) \end{pmatrix} = \begin{pmatrix} \cos(\theta)u_r(r, \theta) - \sin(\theta)u_\theta(r, \theta) \\ \sin(\theta)u_r(r, \theta) + \cos(\theta)u_\theta(r, \theta) \end{pmatrix}.$$

The displacement in radial and angular direction, respectively u_r and u_θ , is given by

$$u_r(r, \theta) = \frac{r^\alpha}{2\mu} \left(-(\alpha + 1) \cos((\alpha + 1)\theta) + (C_2 - \alpha - 1)C_1 \cos((\alpha - 1)\theta) \right),$$

$$u_\theta(r, \theta) = \frac{r^\alpha}{2\mu} \left((\alpha + 1) \sin((\alpha + 1)\theta) + (C_2 + \alpha - 1)C_1 \sin((\alpha - 1)\theta) \right),$$

with $C_1 = -\cos((\alpha + 1)\omega) / \cos((\alpha - 1)\omega)$, $C_2 = 2(\lambda + 2\mu) / (\lambda + \mu)$, $\omega = 3\pi/4$, and $\alpha \approx 0.54448373678$ the positive solution of $\alpha \sin(2\omega) + \sin(2\omega\alpha) = 0$, see Figure 5.5. The stress singularity at the re-entrant corner is partly resolved using a sequence of graded meshes [7], where the element size decreases with the distance to the singularity.

On every mesh we study the convergence by adaptively increasing the face degrees of freedom: On every level, we start with $p_F^i = 0$, no dual coupling, i.e., $q_F^i = -1$, and $p_{\tau_h}^i = 2$. Then a certain number of adaptive loops are performed: In the fully adaptive case 5 adaptive loops are performed, while with the stepwise loop on mesh level $2 + k$, we perform k adaptive loops. The error values on the different meshes and after a different number of loops are compared with respect to the number of degrees of freedom N_h , see Figure 5.6. We note a significant drop in the error during the adaptivity loops, showing a good performance with respect to the necessary degrees of freedom. Comparing the results for $\nu = 0.3$ and $\nu = 0.499$, we note the absence of volumetric

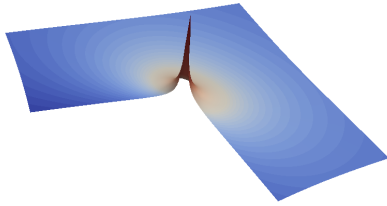


Figure 5.5: Stress distribution $|\sigma|$ on the L-shaped domain.

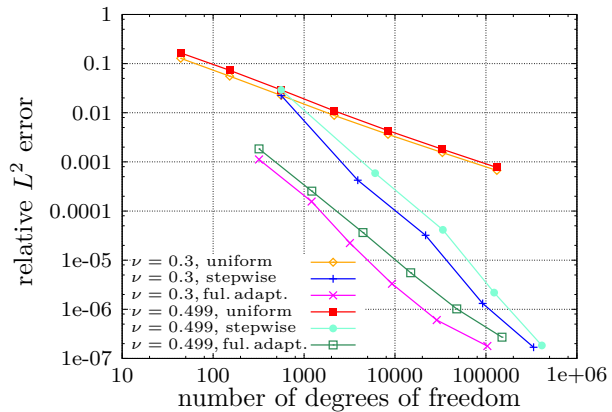


Figure 5.6: Convergence of the relative $L^2(\Omega)$ error with uniform h -refinement and an adaptive choice of the face degrees of freedom.

locking, due to the high-order and the non-conformity of the method, which we later reconsider in some more detail.

5.2.2 Application to contact problems

The hybridization allows an easy approximation of one-body contact problems, see Section 5.1.3.1. Here we test the contact discretization on a mathematical benchmark problem with a manufactured solution of the typical regularity of contact problems. With this example we may compute errors and convergence rates. We first present a general manufactured solution to a linearized, frictionless contact problem, which is based on the scalar Signorini problem and later show the numerical results.

The singular component of Signorini's problem

$$u_{\text{sing}}(r, \theta) = -r^{3/2} \sin(3/2 \theta)$$

was already the basis for the solution in Section 4.4. We show that it can also be used as a benchmark problem for elastic contact with $\hat{g} = 0$. We choose a shift $\beta \in (0, 1)$ and consider $\Omega = (-\beta, 1-\beta) \times (0, 1)$ with $\Gamma_C = (-\beta, 1-\beta) \times \{0\}$ and $\Gamma_D = \partial\Omega \setminus \Gamma_C$ and set

$$\mathbf{u}(r, \theta) = \begin{pmatrix} u_x(r, \theta) \\ u_y(r, \theta) \end{pmatrix} = \alpha \begin{pmatrix} -r^{3/2} \cos(3/2 \theta) \\ -r^{3/2} \sin(3/2 \theta) \end{pmatrix},$$

with a positive scaling $\alpha > 0$. A straightforward computation shows that the

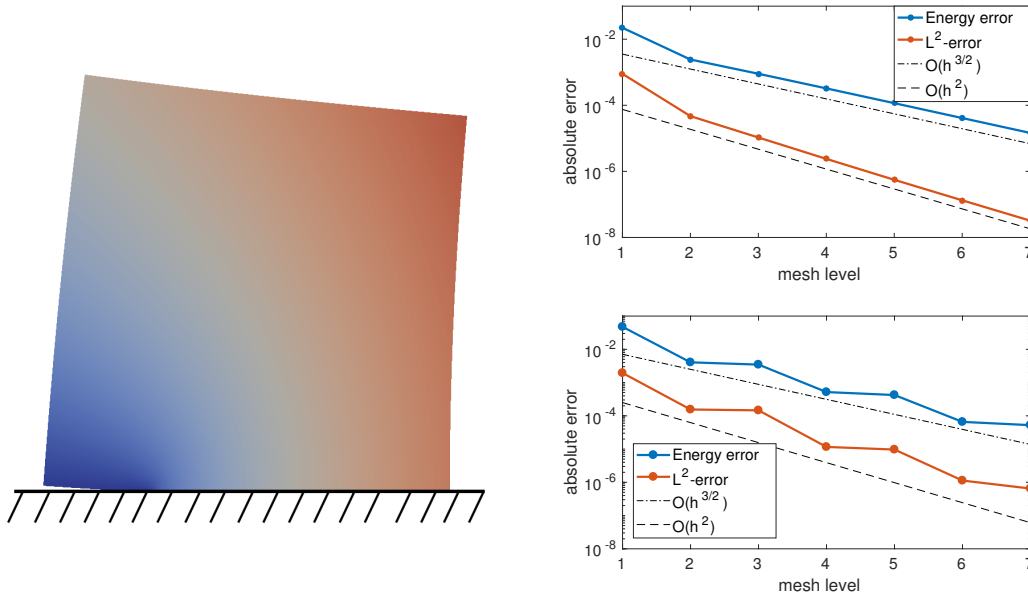


Figure 5.7: Left: Deformed geometry solving the manufactured contact solution for $\beta = 1/4$. Right: Convergence for $\beta = 1/4$ (top) and $\beta = 5/12$ (bottom). L^2 error $\|u - u_h\|_{L^2(\Omega)}$ and energy error $\|\boldsymbol{\sigma}(u) - \boldsymbol{\sigma}(u_h)\|_{L^2(\Omega)}$ with the estimated order of convergence.

constructed displacement \mathbf{u} solves the contact problem for

$$\hat{\mathbf{f}} = \begin{pmatrix} (\lambda_{\text{Lamé}} + \mu_{\text{Lamé}})\partial_{xy}u_y + (\lambda_{\text{Lamé}} + \mu_{\text{Lamé}})\partial_{xx}u_x \\ (\lambda_{\text{Lamé}} + \mu_{\text{Lamé}})\partial_{xy}u_x + (\lambda_{\text{Lamé}} + \mu_{\text{Lamé}})\partial_{yy}u_y \end{pmatrix},$$

and $\hat{\mathbf{u}} = \mathbf{u}|_{\Gamma_D}$. The contact force can be computed as

$$\boldsymbol{\sigma}(\mathbf{u}) \mathbf{n}^\top \mathbf{n} = 2\alpha(\lambda_{\text{Lamé}} + \mu_{\text{Lamé}})\partial_y u_y,$$

which satisfies the stated conditions for unilateral frictionless contact. The point $\mathbf{x}_t = (0, 0)^\top$ is the transition point, between active contact given as $(0, 1 - \beta) \times \{0\}$ and a positive distance to the rigid body at $(-\beta, 0) \times \{0\}$.

The non-constant body force makes it an untypical example for solid mechanics, but from a mathematical viewpoint it serves as a good example since we know the exact solution and we have the typical reduced regularity of contact problems, see [161, 192]

See Figure 5.7 (left) for a plot of the solution for $\lambda_{\text{Lamé}} = \mu_{\text{Lamé}} = 1$ and $\alpha = 1/10$. On the square $(-\beta, 1 - \beta) \times (0, 1)$, we start with one element and perform uniform refinements, but we consider two different choices for β . For $\beta = 1/4$ the active contact area can (starting with level 2) be exactly represented by the mesh since the transition point \mathbf{x}_t is a vertex of the mesh. This is in general

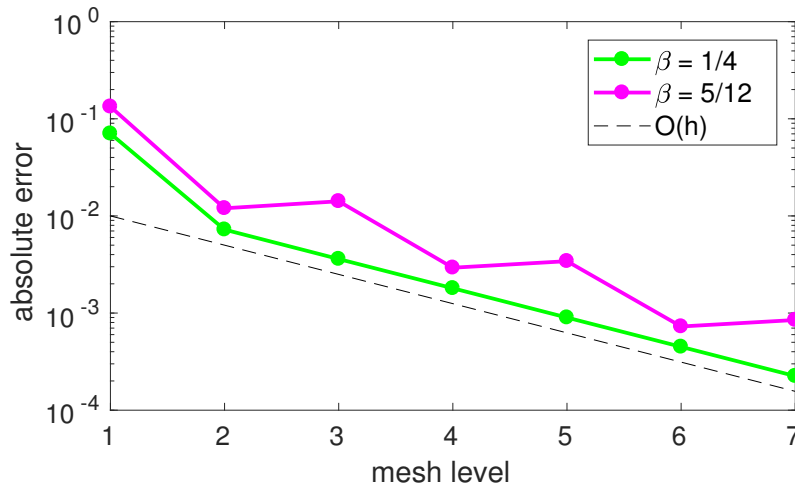


Figure 5.8: Convergence of the $L^2(\Gamma_S)$ error of the Lagrange multiplier for $\beta = 1/4$ and $\beta = 5/12$ with the estimated order of convergence.

a too simple situation, so we also consider $\beta = 5/12$, where the mesh will at no point represent the active contact area. The convergence for $p_{\tau_h}^i = 3$ and $p_F^i = 1$ with a \mathbb{P}_0 contact discretisation is shown in Figure 5.7 (right). We note convergence of the expected order, corresponding to the reduced regularity of $(H^{5/2-\varepsilon}(\Omega))^2$. The H^1 convergence order of $h^{3/2}$ corresponds to the regularity of the problem, while the L^2 convergence order is the same as for solving a Dirichlet-Neumann problem with an a priori given coincidence set, see [110].

While the estimated order is the same, the convergence behavior is different for $\beta = 1/4$ and $\beta = 5/12$. For $\beta = 1/4$, as soon as the transition point \mathbf{x}_t is a vertex of the mesh, the error reduction is uniform. In contrast for $\beta = 5/12$, in some refinement steps, the error reduction is small, while it is large in others. In the average, the same rate as for $\beta = 1/4$ is observed. This is due to the variable approximation of the transition point on different mesh levels. See also the finite element results shown in Section 4.4, where the approximation of the transmission point was investigated in detail.

As we have proven optimal convergence rates for the Lagrange multiplier of a finite element discretization in Section 4.3, let us also take a look at the Lagrange multiplier. In Figure 5.8 the convergence of the dual L^2 -error is shown. We again note a non-uniform error reduction for the case $\beta = 5/12$, but optimal $\mathcal{O}(h)$ convergence rates in both cases. Note, that we use a low order Lagrange multiplier and thus cannot expect a higher rate. In conclusion, we have numerically validated the convergence results of the standard finite element case also for the weakly conforming method.

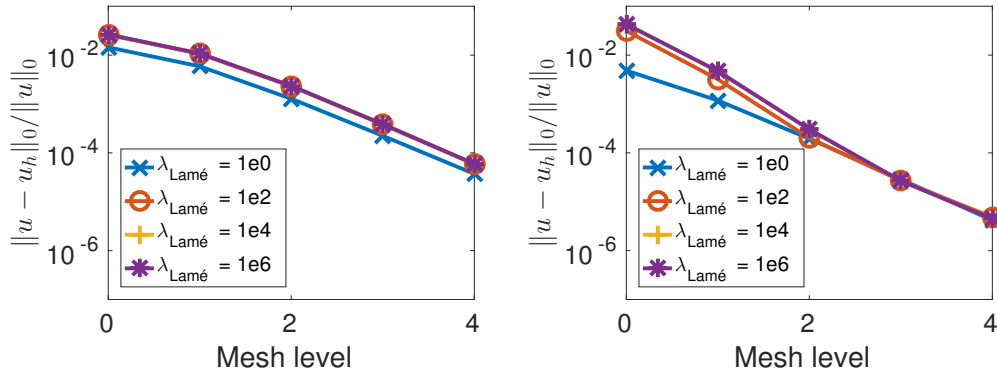


Figure 5.9: Convergence of the relative L^2 error for different values of $\lambda_{\text{Lamé}}$. Left: P2-PN pairing. Right: P3-P1 pairing.

5.2.3 Performance for nearly-incompressible elasticity

We investigate the behavior of WCM for nearly-incompressible materials based on two examples. At first, we investigate the convergence for different values of the Lamé parameter $\lambda_{\text{Lamé}}$ and then show a three-dimensional example, that highlights the importance of locking-free discretizations.

5.2.3.1 Nearly incompressible plate with hole

We investigate locking of WCM in comparison to the conforming methods, which were considered in the introduction of this thesis, see Section 1.2.1.2. To get comparable results, we consider the same problem setting of a plate with a hole.

The relative L^2 error for different values of $\lambda_{\text{Lamé}}$ are shown in Figure 5.9. We compare the case of $p_F^i = 1$ to the case of a normal coupling. We see no deterioration of the method for larger values of the Lamé parameter $\lambda_{\text{Lamé}}$. This is in accordance with [80], where optimal-order error estimates of non-conforming methods were shown, which are uniform with respect to $\lambda_{\text{Lamé}}$.

Comparing these results with the finite element results, which were presented in Section 1.2.1.2, we note that already for the lowest-order P2-PN method, the error is smaller than for conforming bilinear elements with reduced integration. With the P3-P1 method, we see a robust and increased order of convergence. Only on the first two meshes, the difference between the error for $\lambda_{\text{Lamé}} = 1$ and $\lambda_{\text{Lamé}} \geq 100$ is significantly larger. As a result, for $\lambda_{\text{Lamé}} \geq 100$ on the initial mesh the error of P2-PN is slightly smaller than with the higher order P3-P1 method. This effect already vanishes during the first mesh refinement. In particular for $\lambda_{\text{Lamé}} \geq 100$ the error does not increase with $\lambda_{\text{Lamé}}$.

5.2.3.2 Cook's membrane

As the second example, we consider a three-dimensional variant of Cook's membrane, which is a frequently used benchmark problem for locking effects. We use the classical cantilever geometry in the xz -plane with a thickness of 1 in the y -direction, see Figure 5.10.

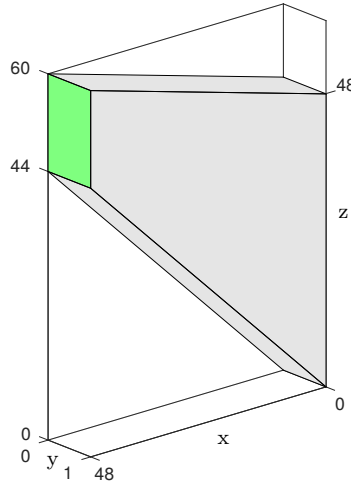


Figure 5.10: Setting of the three-dimensional version of Cook's membrane. A constant traction is applied to the green surface.

We apply the traction $\hat{\mathbf{t}} = \frac{1}{2}(0, 10^{-3}, 1)^\top$ MPa to the tip-surface $\{48\} \times (0, 1) \times (44, 60)$ (dimensions given in mm), homogeneous Dirichlet boundaries in the plane where $x = 0$ and homogeneous Neumann conditions of the remaining surfaces, see Figure 5.11 for a plot of the solution. To capture the stress-singularities of the solution a locally refined initial mesh is used, where extra elements were inserted close to the corners. We consider a nearly incompressible material of $E = 240.565$ MPa, $\nu = 0.4999$. In addition to the volume locking also aspects of shear-locking are relevant in this setting.

We compare the weakly conforming method with $p_{\tau_h} = 3$ and $p_F = 1$ to conforming Q1 and Q2 methods. For the convergence, the displacement of the tip $\mathbf{A} = (48, 0, 60)^\top$ in the y -direction is observed in Figure 5.12. While the conforming results show severe locking effects, the weakly conforming solution shows a good quality already on the first mesh. For three-dimensional problems this is of a great importance as computing power is limited and the number of degrees of freedom, as well as the memory consumption, grows drastically during mesh-refinement. Hence, on complex three-dimensional problems, it is only feasible to work on coarse grids and it is important to have a good solution quality also on coarse grids.

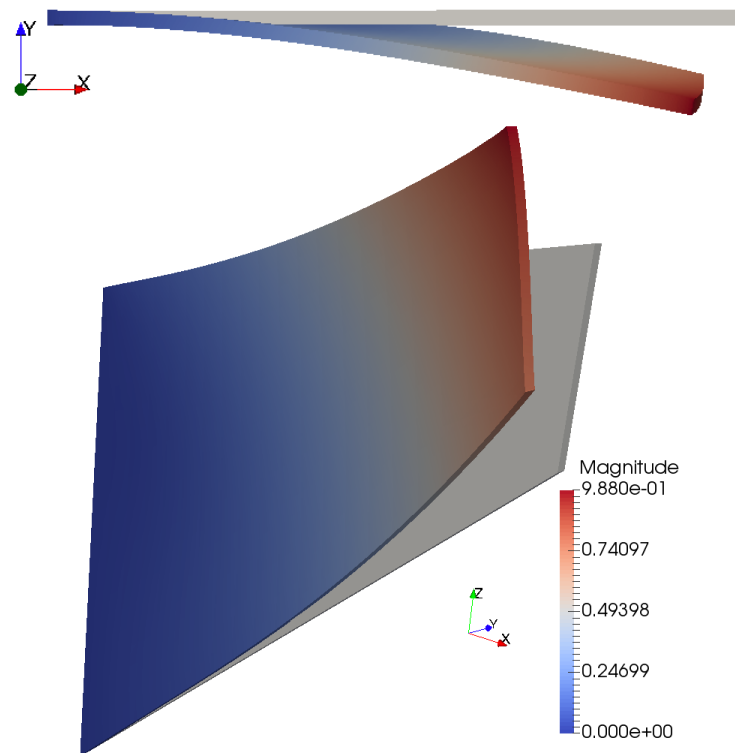


Figure 5.11: Magnified representation of the deformed geometry with the initial geometry from two viewpoints.

5.3 Review of interior penalty discontinuous Galerkin methods

In this section, we shortly recapitulate interior penalty discontinuous Galerkin (DG) methods for non-linear solid mechanics. In contrast to the previously considered weakly conforming method, with DG methods the solution space is not constrained, but the strong force equilibrium is directly applied to broken function spaces, see [18]. Applying integration by parts, we obtain a non-symmetric and singular variational setting, which can be stabilized by an additional non-symmetric term or by penalty, see [11, 12]. The symmetric version is applied to linear models in solid mechanics in [65, 97, 100, 146, 226]. Further formulations are applied to plasticity in [2, 147], for finite elasticity in [124, 211] and for failure in [159]. The use of discontinuous Petrov-Galerkin (DPG) methods for linear elasticity is studied in [37, 86, 126]. Hybrid methods for linear models are considered in [199], and divergence-free hybrid methods

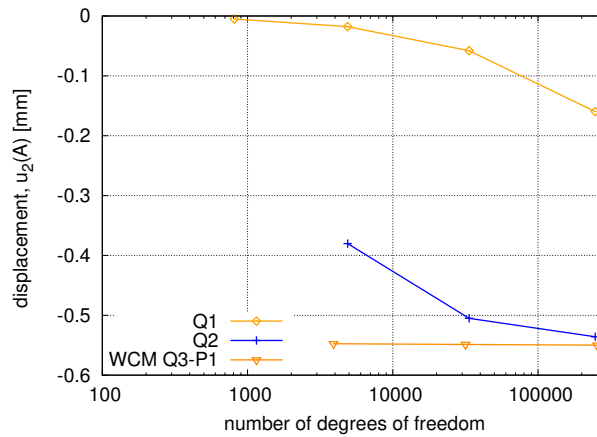


Figure 5.12: Convergence plot of tip-displacement for Cook's membrane.

are analyzed in [143]. An extensive overview on existing DG methods is given in [64, 184].

At first, purely primal methods are shown and then a hybrid DG method as introduced in [235] is presented. We directly introduce the methods for the case of non-linear elasticity, but, for simplicity of the presentation, we only consider the two-dimensional case on quadrilateral elements with homogeneous Dirichlet data $\hat{\mathbf{u}} = \mathbf{0}$. For an $H(\text{div})$ -conforming stress and a discontinuous test function \mathbf{v}_h , the 1st Piola–Kirchhoff stress tensor $\mathbf{P} = \mathbf{P}(\text{Id} + \text{Grad } \mathbf{u})$ satisfies

$$\sum_{\tau_h \in \mathcal{T}_h} \int_{\tau_h} \mathbf{P} : \text{Grad } \mathbf{v}_h \, d\mathbf{x} = \int_{\Gamma} \{\mathbf{P}\} \mathbf{N}_+^\top [\mathbf{v}_h] \, d\gamma + \int_{\Gamma_N} \hat{\mathbf{t}}^\top \mathbf{v}_h \, d\gamma, \quad (5.7)$$

where $\Gamma = \bigcup_{F \in \mathcal{F}_h} \bar{F}$ denotes the skeleton of the triangulation and the averaged stress

$$\{\mathbf{P}\} = \begin{cases} (\mathbf{P}_+ + \mathbf{P}_-)/2 & \text{for } F \not\subset \partial\Omega \\ \mathbf{P}, & \text{for } F \subset \partial\Omega, \end{cases}$$

is defined analogously to the average of the normal stress (5.2). We remark that $[\mathbf{v}_h] = \mathbf{0}$ on Γ_N by definition of the jump (5.1). Based on this identity, we present different variants of the DG method.

5.3.1 The discontinuous Galerkin method

As with the weakly conforming method, for DG methods we choose local polynomial ansatz spaces $\mathbf{V}_h(\tau_h)$, and define the broken (discontinuous) ansatz and

test space

$$\mathbf{V}_h^{\text{DG}} = \left\{ \mathbf{u}_h \in \left(L^2(\Omega) \right)^2 : \mathbf{u}_h|_{\tau_h} \in \mathbf{V}_h(\tau_h) \right\}. \quad (5.8)$$

Then, based on the weak force equilibrium (5.7), we define the consistent non-linear DG form

$$\begin{aligned} a_h^{\text{DG}}(\mathbf{u}, \mathbf{v}) &= \sum_{\tau_h \in \mathcal{T}_h} \int_{\tau_h} \mathbf{P}(\text{Id} + \text{Grad } \mathbf{u}) : \text{Grad } \mathbf{v} \, d\mathbf{x} \\ &\quad - \int_{\Gamma} \{ \mathbf{P}(\text{Id} + \text{Grad } \mathbf{u}) \} \mathbf{N}_+^\top[\mathbf{v}] \, d\gamma, \end{aligned}$$

which is linear in the second argument, and for the exact solution \mathbf{u} we have

$$a_h^{\text{DG}}(\mathbf{u}, \mathbf{v}_h) = f(\mathbf{v}_h), \quad \mathbf{v}_h \in \mathbf{V}_h^{\text{DG}}.$$

Since the linearization of the DG form is not positive definite for discontinuous ansatz functions, a stabilization is needed. Now, we discuss several possibilities (noted by an index $*$) to achieve stability by choosing an additional possibly non-linear form $s_h^*(\cdot, \cdot)$, linear in the second argument, so that in the case of small deformations

$$a_h^{\text{DG}}(\mathbf{u}_h, \mathbf{u}_h) + s_h^*(\mathbf{u}_h, \mathbf{u}_h) > 0, \quad \mathbf{u}_h \in \mathbf{V}_h^{\text{DG}}, \mathbf{u}_h \neq \mathbf{0}.$$

Then, for sufficiently small $\hat{\mathbf{t}}$, there exists a unique solution $\mathbf{u}_h \in \mathbf{V}_h^{\text{DG}}$, satisfying

$$a_h^{\text{DG}}(\mathbf{u}_h, \mathbf{v}_h) + s_h^*(\mathbf{u}_h, \mathbf{v}_h) = f(\mathbf{v}_h), \quad \mathbf{v}_h \in \mathbf{V}_h^{\text{DG}}. \quad (5.9)$$

In order to preserve asymptotic consistency, $s_h^*(\mathbf{u}, \mathbf{v}_h) \rightarrow 0$ for $h \rightarrow 0$ is required for the solution \mathbf{u} of the continuous problem and for discontinuous test functions \mathbf{v}_h . In general for DG methods even full consistency $s_h^*(\mathbf{u}, \mathbf{v}_h) = 0$ is achieved.

The convergence properties and the robustness of DG methods depend on the choice of the ansatz space and the stabilization. The most popular stabilization is the Nitsche-type penalty, which yields the incomplete interior penalty method (IIPDG)

$$s_h^{\text{IIPDG}}(\mathbf{u}_h, \mathbf{v}_h) = \int_{\Gamma} \frac{\theta}{h} [\mathbf{u}_h]^\top [\mathbf{v}_h] \, d\gamma, \quad (5.10)$$

introduced in [167] with the mesh-independent parameter $\theta > 0$. Note that in general this parameter depends on the polynomial degree of the local ansatz spaces $\mathbf{V}_h(\tau_h)$. While this choice preserves the asymptotic order of the ap-

proximation as well as the condition number, good numerical results have also been observed with alternative h -scalings of the penalty parameter. Hence for some examples we allow θ to be h -dependent.

The symmetric interior penalty method (SIPDG) is obtained by minimizing the energy (see also Section 1.2.4), extended with consistency and stabilization terms, i.e.,

$$\begin{aligned} \mathbf{u}_h^{\text{SIPDG}} = \arg \min_{\mathbf{u}_h \in \mathbf{V}_h^{\text{DG}}} & \left(\sum_{\tau_h \in \mathcal{T}_h} \int_{\tau_h} \psi(\text{Id} + \text{Grad } \mathbf{u}_h) \, d\mathbf{x} \right. \\ & \left. - \int_{\Gamma} \{\mathbf{P}(\text{Id} + \text{Grad } \mathbf{u}_h)\} \mathbf{N}_+^\top[\mathbf{u}_h] \, d\boldsymbol{\gamma} - f(\mathbf{u}_h) + \frac{1}{2} s_h^{\text{IPDG}}(\mathbf{u}_h, \mathbf{u}_h) \right). \end{aligned}$$

In the variational form this additionally yields the adjoint consistency term

$$s_h^{\text{SIPDG}}(\mathbf{u}_h, \mathbf{v}_h) = s_h^{\text{IPDG}}(\mathbf{u}_h, \mathbf{v}_h) - s_h^{\text{adj}}(\mathbf{u}_h, \mathbf{v}_h), \quad (5.11)$$

where

$$s_h^{\text{adj}}(\mathbf{u}_h, \mathbf{v}_h) = \int_{\Gamma} [\mathbf{u}_h]^\top \{\partial_F \mathbf{P}(\text{Id} + \text{Grad } \mathbf{u}_h) \text{Grad } \mathbf{v}_h\} \mathbf{N}_+ \, d\boldsymbol{\gamma}.$$

In the case of linear elasticity, the system matrix is symmetric and in this case one obtains optimal $L^2(\Omega)$ convergence, see [11].

The case of s_h^{adj} without any Nitsche-type stabilization is considered in [18], where we observe robustness and obtain a non-symmetric linearization in (5.9). To analyze robustness for linear materials in the nearly incompressible case, penalty terms adapted to the large value of $\lambda_{\text{Lamé}}$ are considered in [97, 100].

In case of bilinear ansatz spaces $\mathbf{V}_h(\tau_h)$, a reduced integration on the element faces together with a simple Nitsche-type penalty was introduced in [20], which shows improved convergence in case of locking. We consider the bilinear form

$$\begin{aligned} a_h^{\text{RIDG}}(\mathbf{u}_h, \mathbf{v}_h) = & \sum_{\tau_h \in \mathcal{T}_h} \int_{\tau_h} \mathbf{P}(\text{Id} + \text{Grad } \mathbf{u}_h) : \text{Grad } \mathbf{v}_h \, d\mathbf{x} \\ & - \int_{\Gamma}^{\text{RI}} \{\mathbf{P}(\text{Id} + \text{Grad } \mathbf{u}_h)\} \mathbf{N}_+^\top[\mathbf{v}_h] + \int_{\Gamma}^{\text{RI}} \frac{\theta}{h} [\mathbf{u}_h]^\top [\mathbf{v}_h], \end{aligned} \quad (5.12)$$

where \int^{RI} denotes the mid-point rule approximating the integral on every element face.

While robustness and even a full convergence analysis is provided for many different DG variants in the linear setting, it remains important to reduce the computational cost. For all these methods the system matrix has the same structure with entries connecting all degrees of freedom of neighboring ele-

ments. Hybrid methods aim to reduce the numerical expense while preserving the robustness properties as we have already observed for the weakly conforming method.

Remark 5.3.1. *Optimal L^2 norm error estimates can be shown for sufficiently regular linear problems under the assumption of adjoint consistency, which follows from the symmetry of the methods, see, e.g., [64, Chapter 4.2.4]. While this works for SIPDG, for the further methods examples exist with a sub-optimal L^2 norm, see [184, Chapter 2.8].*

Also L^∞ norm error estimates are, to the best of our knowledge, currently only available for the symmetric interior penalty method, see [48].

5.3.2 A low-order hybrid discontinuous Galerkin method with conforming traces

Here we shortly recapitulate the hybrid DG method as proposed in [235]. For the hybrid DG method we use a second discrete space

$$\mathbf{V}_{\Gamma,h} \subset \left\{ \mathbf{u}_{\Gamma,h} \in (C^0(\Gamma))^2 : \mathbf{u}_{\Gamma,h} = \mathbf{0} \text{ on } \Gamma_D \right\},$$

for the approximation of the displacement vector on the skeleton and use traces of conforming bilinear ansatz functions, i.e., face-wise linear skeleton functions in $\mathbf{V}_{\Gamma,h}$. In the interior of the elements, we use the discontinuous space \mathbf{V}_h^{DG} with linear ansatz functions $\mathbf{V}_h(\tau_h)$, see (5.8). For a given linear skeleton function $\mathbf{u}_{\Gamma,h} \in \mathbf{V}_{\Gamma,h}$, we consider the linear volume approximation $\mathbf{u}_h = \Pi_h^{\text{lin}} \mathbf{u}_{\Gamma,h} \in \mathbf{V}_h^{\text{DG}}$, defined in every quadrilateral element by the linear projection

$$\int_{\partial\tau_h}^h \Pi_h^{\text{lin}} \mathbf{u}_{\Gamma,h}^\top \mathbf{v}_h = \int_{\partial\tau_h}^h \mathbf{u}_{\Gamma,h}^\top \delta \mathbf{u}_h, \quad \mathbf{v}_h \in \mathbf{V}_h(\tau_h),$$

where the boundary integral on $\partial\tau_h$ is approximated by a trapezoidal quadrature rule

$$\int_{\partial\tau_h}^h f = \sum_{j=1}^4 w_j f(\mathbf{X}_{\tau_h,j})$$

using the element corners $\mathbf{X}_{\tau_h,1}, \mathbf{X}_{\tau_h,2}, \mathbf{X}_{\tau_h,3}, \mathbf{X}_{\tau_h,4}$ and weights $w_j > 0$. Since the strain approximation $\mathbf{F}_h = \text{Id} + \text{Grad } \mathbf{u}_h$ is constant in τ_h , we obtain $\text{Div } \mathbf{P}(\mathbf{F}_h) = \mathbf{0}$ and

$$\int_{\tau_h} \mathbf{P}(\mathbf{F}_h) : \text{Grad}(\mathbf{v}_h) \, d\mathbf{x} = \int_{\partial\tau_h} \mathbf{P}(\mathbf{F}_h) \mathbf{N}^\top \mathbf{v}_h \, d\gamma \approx \int_{\partial\tau_h}^h \mathbf{P}(\mathbf{F}_h) \mathbf{N}^\top \mathbf{v}_h.$$

This defines the non-symmetric hybrid form

$$a_h^{\text{HDG}}(\mathbf{u}_{\Gamma,h}, \mathbf{v}_{\Gamma,h}) = \sum_{\tau_h \in \mathcal{T}_h} \int_{\partial\tau_h}^h \mathbf{P}(\text{Id} + \text{Grad} \Pi_h^{\text{lin}} \mathbf{u}_{\Gamma,h}) \mathbf{N}^\top \mathbf{v}_{\Gamma,h}.$$

Adapting the standard Nitsche-type penalty term (5.10) to the hybridization yields

$$s_h^{\text{HDG}}(\mathbf{u}_{\Gamma,h}, \mathbf{v}_{\Gamma,h}) = \sum_{\tau_h \in \mathcal{T}_h} \frac{\theta}{h} \int_{\partial\tau_h}^h \left(\Pi_h^{\text{lin}} \mathbf{u}_{\Gamma,h} - \mathbf{u}_{\Gamma,h}^{\text{lin}} \right)^\top \mathbf{v}_{\Gamma,h}.$$

Then, the hybrid solution $\mathbf{u}_{\Gamma,h} \in \mathbf{V}_{\Gamma,h}$ is computed by

$$a_h^{\text{HDG}}(\mathbf{u}_{\Gamma,h}, \mathbf{v}_{\Gamma,h}) + s_h^{\text{HDG}}(\mathbf{u}_{\Gamma,h}, \mathbf{v}_{\Gamma,h}) = \int_{\Gamma_N} \widehat{\mathbf{t}}^\top \mathbf{v}_{\Gamma,h} \, d\gamma, \quad \mathbf{v}_{\Gamma,h} \in \mathbf{V}_{\Gamma,h}.$$

The system matrix is non-symmetric with the sparsity pattern of conforming bilinear elements and all computations can be performed on element level which makes it convenient to include it in standard finite element codes.

We note that the hybrid DG method is based on the incomplete interior penalty method, hence straightforward L^2 estimates based on an Aubin–Nitsche argument cannot be expected, see Remark 5.3.1.

5.4 Comparison of the non-conforming and discontinuous methods

In the following study, we compare the introduced non-conforming and discontinuous methods, to see their advantages and disadvantages. First, we compare the two hybrid methods theoretically and point out common and individual properties. In the following numerical study, we apply the presented methods to challenging problems of linear and non-linear elasticity. Also a comparison with conforming isogeometric and standard finite elements is given.

5.4.1 Comparison of the hybrid approaches

We shortly discuss the similarities and differences of the presented hybrid discontinuous Galerkin method and the hybrid weakly conforming Galerkin method, see Table 5.3 for an overview. While both methods include a parallelizable hybridization, which reduces to degrees of freedom on the skeleton, the consequences are different. The main differences are based on the different skeleton space, which is a low order continuous space for the hybrid DG method, while it is a discontinuous one of arbitrary degree for the weakly con-

forming method. The sparsity structure of the hybrid DG method is the same as for conforming bilinear elements, having two degrees of freedom per node and a 9-point stencil structure on uniform grids. The structure for the weakly conforming method is different, as the degrees of freedom are located at the faces which results in a 7-point stencil structure on uniform grids. In order to be stable, at least three degrees of freedom are required on each face, i.e., on each point of the stencil structure.

The local element-wise spaces are linear for the hybrid DG methods, while they are of higher order for the weakly conforming space. The hybrid DG method achieves stability by a penalty term, while for the weakly conforming space the face degrees of freedom directly pose weak constraints on the discontinuous solution space so that no penalty term is required.

Table 5.3: Comparison of the hybrid DG and the hybrid weakly conforming methods

	HDG (Sec. 5.3.2)	Hybrid WCM (Sec. 5.1)
skeleton space	continuous	(face-wise) discontinuous
location & nr. of dofs	2 per node	at least 3 per face
stencil size	18 ($2 \cdot 9$)	min. 21 ($3 \cdot 7$)
local space	linear	higher-order ($p \geq 2$)
stability by	penalty term	weak conformity

5.4.2 Numerical comparison of non-conforming and discontinuous formulations

In this section, we consider two benchmark configurations. The first test demonstrates the robustness of discontinuous discretizations for a thin beam with respect to anisotropy. As the second test, we consider a loading test for a ring with soft and hard material layer.

We use only basic geometries, so that these test cases can be realized in different codes and with various methods. An overview of the abbreviations and the used software is given in Table 5.4. We use the parallel finite element framework M++ introduced in [223] for most of the methods. The presented results for RIDG and HDG are based on the values presented in [19], which were realized as an additional module in the finite element software FEAP [208].

5.4.2.1 A long thin elastic beam

The presented methods are first tested with respect to an anisotropic geometry as well as anisotropic elements. A thin beam is fixed on the left side and

Table 5.4: Overview of the considered methods, their abbreviation and the software used.

Abbreviation	Discretization technique	Software
Q1	conforming bilinear (Section 1.1.2.2)	M++
Q2	conforming serendipity (Section 1.1.2.2)	M++
SIPDG(Q1)	symmetric interior penalty DG method (5.11) with bilinear ansatz	M++
SIPDG(Q2)	symmetric interior penalty DG method (5.11) with serendipity ansatz	M++
WCM(1)	weakly conforming method (5.4), P3-P1 pairing	M++
WCM(2)	weakly conforming method (5.4), P4-P2 pairing	M++
IGA(p)	isogeometric discretization (Section 2.1), degree p	Matlab
RIDG	reduced integration method (5.12)	FEAP
HDG	hybrid DG method (Section 5.3.2)	FEAP

loaded vertically on the right side. We observe the convergence by considering the vertical displacement $u_2(\mathbf{A})$ in the test point \mathbf{A} . In Figure 5.13, the geometry setup, boundary conditions and the point \mathbf{A} are shown.

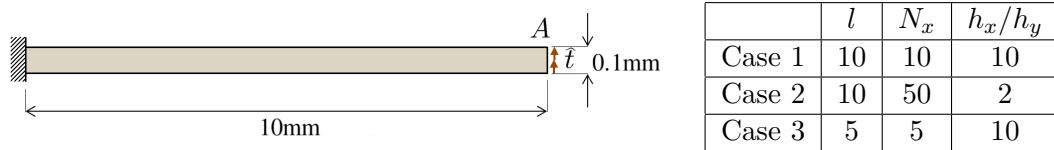


Figure 5.13: Configurations of the beam example. Geometry shown for case 1 and 2 ($l = 10$ mm). In case 3 we use $l = 5$ mm.

We keep the height of the beam kept constant, whereas we choose the length once as 10 mm and once as 5 mm. Also the element aspect ratio for the long beam is changed. Once, we consider anisotropic elements with a high aspect ratio of $h_x/h_y = 10$ and once more regular ones with $h_x/h_y = 2$. For the short beam, we only consider the anisotropic element shape, i.e., $h_x/h_y = 10$. The initial mesh in all cases is chosen to consist of one element in the vertical direction and N_x elements in the horizontal direction. Then a uniform mesh refinement is considered. In the linear case, the traction force \hat{t} is set to 0.001 MPa and then increased for the non-linear deformation. The beam consists of an isotropic elastic material with Young's modulus $E = 16.8$ GPa and Poisson's ratio $\nu = 0.4$, chosen as a linear material law for the first tests and later as a Neo-Hooke material.

We compute the three cases of the beam with the linear material law and

with the methods summarized in Table 5.4. For SIPDG(Q1) and SIPDG(Q2) we choose $\theta = \mu$, for RIDG $\theta = 100Eh/l$ and for HDG we choose $\theta = 2Ea/(3(a+b)(1-\nu^2))$, where a is the element height and b is the element length. All quadratic schemes proved to be locking free. The conforming finite elements and the standard DG method show severe locking in the bilinear case.

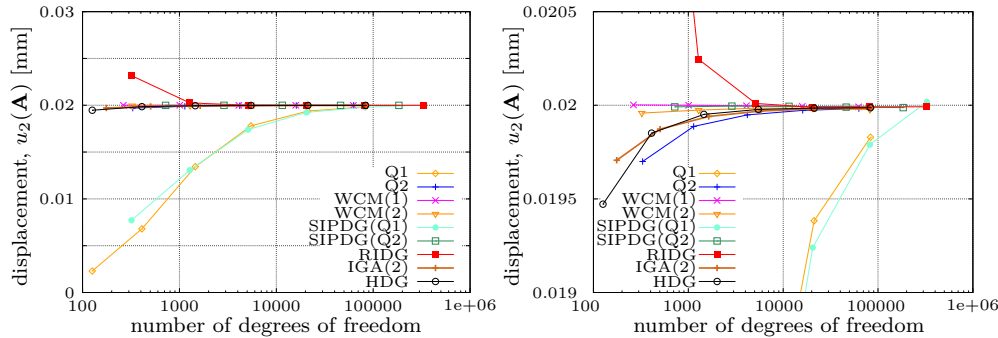


Figure 5.14: Left: Vertical displacement of the point **A** for the beam in case 1 with respect to total degrees of freedom. Right: Zoom of the same setting.

Convergence in the anisotropic case 1 The results for case 1, where the elements and the beam geometry are the most anisotropic, is shown in Figure 5.14. Severe shear locking, see [24, Chapter 8], can be found with Q1 and SIPDG(Q1), where a fine mesh is necessary for viable results. The equally bad approximation per degree of freedom of SIPDG(Q1) compared with Q1 is due to the higher amount of global degrees of freedom. This cancels the smaller error of the DG scheme. In contrast, the linear methods RIDG and HDG are close to the exact solution already with only a fraction of degrees of freedom. Both methods apply techniques to prevent shear locking. RIDG makes use of a reduced integration scheme on the boundary, which relaxes the continuity constraints for the discrete solution and prevents spurious shear stresses from appearing during the bending of the beam. The HDG method reduces spurious shear stresses by a twofold approach. In addition to a reduced integration, the local, discontinuous ansatz space is made smaller, reducing the bilinear ansatz, which introduces the main spurious stresses in conforming methods. Also the lowest order weakly conforming method WCM(1) shows no sign of shear locking, which is achieved by increasing the computational effort inside each element. The hybridization reduces the problem to the skeleton, where piecewise linear degrees of freedom are considered.

Figure 5.14 (right) gives a closer look on the higher order methods. In contrast to the observations of the linear case, the biquadratic SIPDG shows an improvement compared to the conforming biquadratic elements. On the same mesh, the quadratic isogeometric elements show a similar error as the conforming biquadratic elements, but with less degrees of freedom. Both WCM variants are about as close to the exact solution as SIPDG(Q2).

We note a monotone convergence behavior for all considered methods in Figure 5.14. While for the conforming methods, the vertical tip displacement is an increasing function over the degrees of freedom, for the discontinuous methods it may also be decreasing.

Since the complexity of the methods is not only influenced by the number of degrees of freedom, we comment on the memory efficiency. Not only does this influence the memory consumption, but also the computational cost of a linear solver. In terms of the sparsity, isogeometric methods are a special case, as the basis functions are neither nodal nor element-wise. In general each basis function is coupled with $2p$ basis functions in each direction, which are $(2p)^2$ on a two-dimensional tensor product structure. With conforming finite element methods each degree of freedom is coupled with the degrees of freedom on the elements adjacent to the associated node. On regular grids this results in four elements for each vertex. The situation is different for standard DG methods of the same polynomial degree, where the stencil size on regular grids is significantly larger. The consistency term includes face integrals of the normal stress, resulting in a coupling of all degrees of freedom on neighboring elements, i.e., five elements. Not only do more elements interfere, but there are also more degrees of freedom located on each element, due to the discontinuous ansatz. Hybrid methods show a different behavior than the standard DG methods. A detailed discussion of the stencil size can be found in Section 5.4.1. We point out that the HDG has the same sparsity structure as Q1, which allows for the direct use of standard routines tailored to conforming Q1. With the hybrid WCM method degrees of freedom are located on the faces, hence only two neighboring elements interfere. However, stability requires at least three degrees of freedom per face, resulting in a larger stencil than the HDG method, but still a smaller one than for standard DG methods.

Comparison to a more regular beam geometry and element shape Here we study the influence of the anisotropy of the beam geometry and of the element shape on the quality of the considered methods. We restrict ourselves to low-order methods for the sake of clearer comparison. In case 2 the beam geometry is kept as in case 1, but we consider more regular elements. As a consequence, we need more elements in the length direction of the beam, which

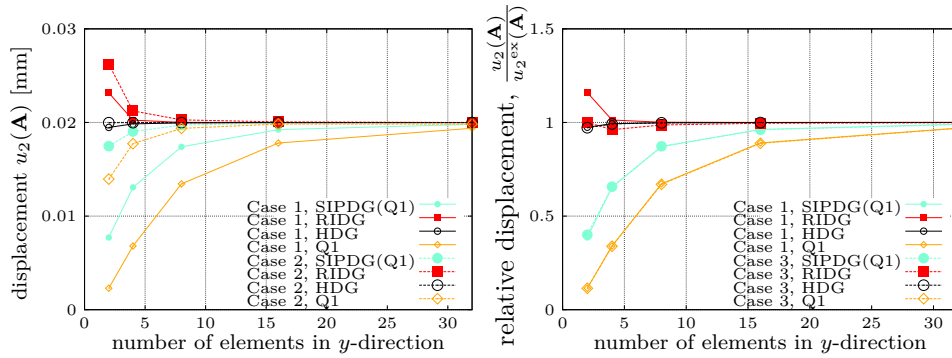


Figure 5.15: Comparison of the vertical displacement of the point \mathbf{A} for the beam in cases 1 and 2 (left) and cases 1 and 3 (right).

influence the number of degrees of freedom. In the left of Figure 5.15, we compare the tip displacement with respect to the number of elements in the height direction, but we keep in mind the different total number of elements. The methods which showed locking-effects, Q1 and SIPDG(Q1), clearly improve due to the additional number of elements. On the other hand, RIDG does not improve and HDG improved only little by introducing more elements in the length direction. Both methods show the good quality of the finer mesh in case 2 already on the coarse meshes of case 1. This shows their efficiency in terms of error per degrees of freedom for anisotropic geometries.

For the last comparison in case 3, we keep the same anisotropic element geometry as in case 1 but the beam geometry is more regular with only half its length. Since a change of the beam geometry influences the exact displacement, we consider a relative displacement for the comparison. We could equivalently adapt the applied force, since we compute the equations of linear elasticity. The results are shown in the right of Figure 5.15, where we see hardly any differences between the two cases. Only the approximation of RIDG changes on the first meshes, but remains on a similar level of approximation.

In conclusion, these comparisons show that the negative effects of shear locking are mainly influenced by the anisotropic element shape and not the anisotropic beam geometry.

The remaining methods which are not included in the comparisons of Figure 5.15 show relative errors less than 2% already on the initial mesh and keep this good approximation also in the other cases.

Non-linear beam Now, let us consider a non-linear adaptation of the beam setting. We consider case 1, increase the applied load and consider the non-

linear Neo-Hooke material law as given in Section 1.2.4. To be in accordance with the setting of [235], we replace the applied surface traction by a vertical point-force of 0.1 N, applied to the upper right corner **A**. The deformed beam as well as the stress distribution of σ_{11} is shown in Figure 5.16 (right). The convergence comparison of conforming finite element and isogeometric approaches as well as the HDG method is shown in Figure 5.16 (left). We note that the HDG values are the ones presented in [235, Section 4.3] with $\theta = 2Eh^2/(3l^2(1-\nu^2))$. While severe locking can be observed for Q1, the HDG methods greatly improves the approximation. With the conforming methods a clear benefit of a higher order can be seen, although locking effects are still present, which can be seen in the comparison with the solution of HDG. The smaller error per degree of freedom for higher order methods comes at the cost of a higher effort for the integration and a more complex sparsity structure of the stiffness matrix.

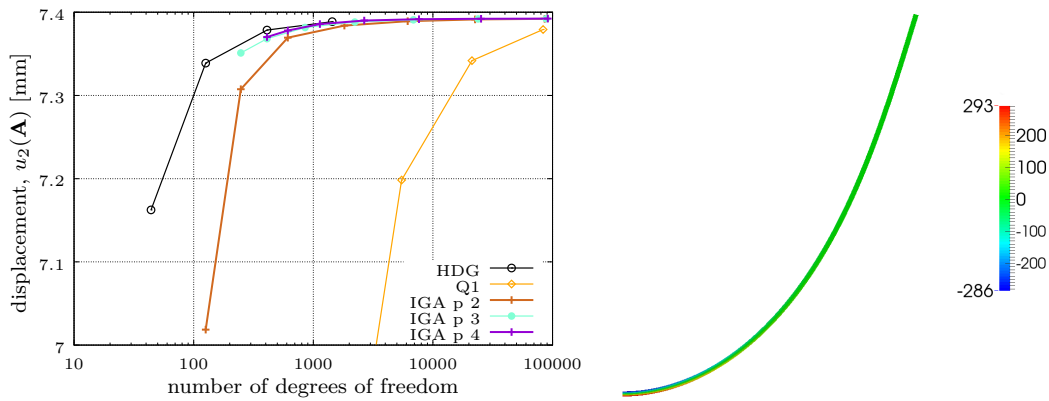


Figure 5.16: Left: Vertical displacement of the point **A** for the non-linear beam with respect to the global degrees of freedom Right: Deformation of the non-linear beam and the stress distribution σ_{11} .

5.4.2.2 Bimaterial annulus under symmetric pressure

The final numerical example is a bimaterial annulus with large deformations that is motivated by an example in [86]. The ring is given by the outer radius $R_o = 1.1$ and the inner radius $R_i = 0.5$ with the origin as the center. All dimensions are given in mm. The interface of the two materials is given at the radius $R_{if} = 1$. We apply a symmetric traction from the top and the bottom, so we can restrict ourselves to one quarter of the ring shown in Figure 5.17. On the part of the outer boundary, where $X < 1.1 \cos(0.3\pi)$, a vertical traction $\mathbf{PN} = \hat{\mathbf{t}}$ is applied. On the remaining part of the outer boundary and on

the inner boundary, homogeneous Neumann boundary conditions are applied. Symmetry boundary conditions $\mathbf{P}\mathbf{N}^\top\mathbf{N} = 0$ and $\mathbf{u}^\top\mathbf{N} = 0$ are applied for $X = 0$ and for $Y = 0$.

The bimaterial ring consists of two Neo-Hooke materials, see (1.9). The outer part of the ring $|\mathbf{X}| > 1$ is made of a steel with $E_S = 200$ GPa, $\nu_S = 0.285$, while the remaining ring is made of a rubber-like material with $E_R = 0.01$ GPa, $\nu_R = 0.499$. The surface traction is given as $\hat{t}_2 = 30$ MPa (thickness 1 mm).

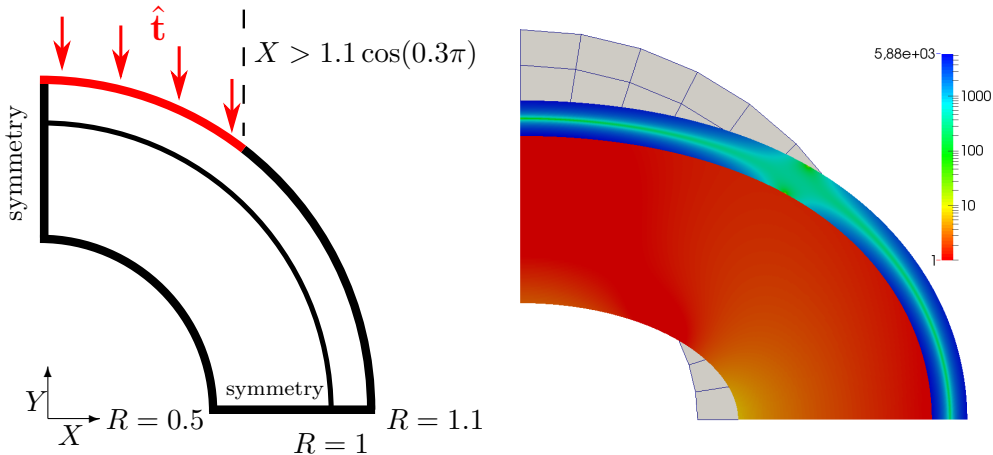


Figure 5.17: Bimaterial annulus: Sketch of the computational domain, exploiting the symmetric structure (left) and undeformed and deformed domain including stress distribution (right).

The curved geometry is approximated linearly. More precisely, the nodes of a uniformly refined mesh are mapped onto the quarter annulus by a predefined mapping. While for linear DG methods this is optimal, for higher order methods a better geometry approximation improves the approximation for sufficiently regular solutions, see [145]. Anyways, we cannot expect full regularity of the solution, since the example includes discontinuous Neumann data.

We consider the vertical displacement on the top of the inter-material layer, i.e., $u_2(\mathbf{A})$ with $\mathbf{A} = (0, 1)$. The penalty parameter for SIPDG(Q2) is chosen as $\theta = 1000\mu$ and for HDG as $\theta = \mu/2$. The plot of the displacement is shown in Figure 5.18 (left), where convergence for all considered methods can be seen. The bilinear conforming approximation shows a significantly larger error due to volume locking effects in the nearly incompressible rubber and shear locking in the outer ring. A closer look at the estimated error in Figure 5.18 (right) shows that, in terms of error per degree of freedom, the approximation

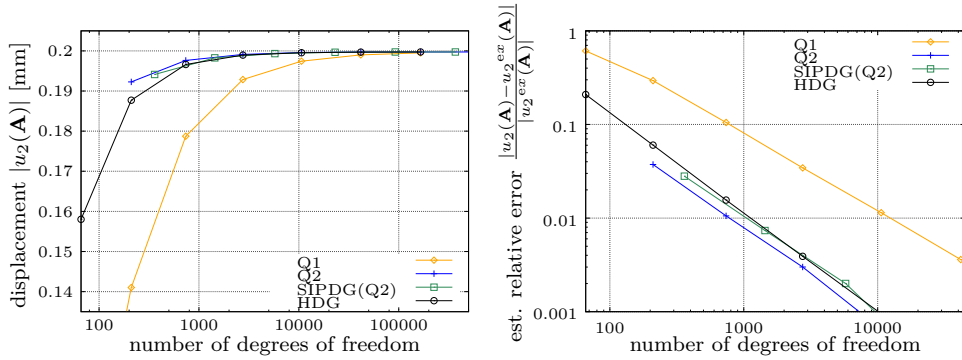


Figure 5.18: Left: Vertical displacement of the solution at the point \mathbf{A} for linear approximations HDG and conforming Q1, and quadratic approximations SIPDG(Q2) and conforming Q2. Right: Estimated relative error for the bimaterial annulus with respect to an extrapolated value for a reference solution on a fine mesh.

of the linear HDG method is on the same level as the quadratic methods SIPDG(Q2) and Q2. The improvement in comparison to Q1 can be explained by the reduced locking of the HDG method, while the low regularity induced by the discontinuous Neumann data restricts the convergence order for higher order discretizations.

For large non-linear problems, an efficient parallelization of the assembly process is of special importance. In every iteration step a reassembly of the non-linear parts is necessary for any method. This includes the computational cost of the hybridization, however this is done by a purely element-wise operation and can straightforwardly be done in parallel. We note that the Nitsche-type penalty term (5.10) does not need to be reassembled during the non-linear iteration. The adjoint consistency term (5.11) includes the linearization of the non-linear stress and needs to be recomputed in each iteration step. Using an incomplete DG method the term is avoided, as it is for the hybrid DG.

Conclusion and outlook

In this thesis, the application of several hybrid methods to solid mechanics has been presented. We have discussed situations where the use of hybrid methods is beneficial, including non-linear examples of eigenvalue problems, contact problems and large deformations. Theoretical results for several hybrid methods show optimal bounds in different norms of interest. The practical use of a hybrid isogeometric finite element method has been illustrated by the vibroacoustical analysis of a violin bridge.

Isogeometric mortar methods have been introduced to gain more flexibility of the tensor product spline approximation. The resulting primal-dual saddle point problem can be simplified by the use of biorthogonal basis functions. However, a special construction with an extended support is necessary to retain optimal convergence rates. We have highlighted the importance of an exact evaluation of the surface integrals by a numerical study on the effect of the variational crime. A more robust formulation reduces the integration effort as it does not require the costly construction of a merged mesh, but still we have presented a few situations, where the method shows sub-optimal results.

When solving eigenvalue problems, smooth splines show a better approximation of the whole spectrum in comparison to classical finite elements. We have confirmed the good approximation of a large part of the spectrum also for isogeometric mortar methods and we have then presented a vibroacoustical application. The bridge of a violin has been discretized as a three-dimensional model with 16 isogeometric patches. The efficiency of the parameter- and geometry-dependent computation has been improved by a model reduction using the reduced basis method, accompanied by the empirical interpolation method. The application of empirical interpolation to complex geometry variations is challenging as it results in a large affine decomposition, while a simple thickness variation that was considered, does not pose any additional problems.

Mortar methods in domain decomposition are closely related to discretizations of contact constraints. As a mathematical model, we have considered Signorini-type problems and we have proven optimal order convergence for a standard finite element approximation in the $H_{00}^{1/2}(\Gamma_S)$ norm. Based on this estimate, optimal order error bounds for the Lagrange multiplier in the $H^{-1/2}(\Gamma_S)$ norm and for the primal error in the $L^2(\Omega)$ norm have been derived. The analysis is based on a variational formulation of the continuous and the

discrete Schur complement system which are variational inequalities posed on the boundary. The difficulties arising from the non-linearity are handled by a Strang lemma and modern duality techniques with local estimates for the resulting linear problem.

Finally, the application of interior penalty discontinuous Galerkin method and of a weakly conforming method to solid mechanics has been investigated. For a hybrid weakly conforming method, we have discussed the choice of face-wise and element-wise degrees of freedom. An adaptive choice of the face-wise degrees of freedom has been successfully tested numerically. The application to contact problems shows optimal rates using a local active set strategy. After a review of interior penalty discontinuous Galerkin methods, the methods have been compared numerically with each other and conforming classical and isogeometric finite elements. Also the complexity of the assembly and the memory efficiency have been addressed. Improved locking behavior can be seen for the novel non-conforming method and for two modern discontinuous Galerkin methods.

Many of the results presented in this thesis open up interesting topics of future research. Let us briefly comment on three of them.

The novel construction of isogeometric biorthogonal basis with optimal approximation order shows good results for mortar methods on two-dimensional domains. An extension to three-dimensional problems by a tensor product construction has been sketched. There, the mortar coupling needs to be posed in the parametric space of the slave domain, instead of the geometric space. The change of the coupling integral should be studied numerically. Besides the presented application to mortar methods, also the application to robust multi-field formulations in solid mechanics, as in [139], could be of interest.

The vibroacoustical example proved the potential of isogeometric mortar methods, although it did not yet include studies of practical interest for violin builders. The next steps could include the calibration of the geometry and material data based on real data, where the presented model reduction techniques help to reduce the computational effort. Techniques of uncertainty quantification might be useful to take account of the material uncertainty of wood. Then shape-optimization techniques can be applied to improve the acoustics of a violin. A refined model could be obtained by including the body of the violin to the geometry.

The results of the weakly conforming method are promising, but some research remains to understand its full potential. For example, the efficiency of the presented adaptive algorithm could be improved by a multi-level strategy, where a part of the coupling degrees are determined on a coarser mesh. Also applications to two-body contact problems, heterogeneous materials and the inclusion of modern element technologies are interesting open questions.

Figures

1.1	Inner forces of a body. Along the imaginary plane cut the traction is $\mathbf{t} = \boldsymbol{\sigma}(\mathbf{u})\mathbf{n}$	20
1.2	Tonti diagram for the equations of linear elasticity.	22
1.3	Setting of the quarter plate with a hole. Left: Geometry and boundary conditions, with a sample grid on mesh level 1. Right: Undeformed mesh on level 4 with the deformed geometry (amplified). . .	27
1.4	Relative $L^2(\Omega)$ error for \mathbb{Q}_1 (left), \mathbb{Q}_1 with reduced integration (middle) and \mathbb{Q}_2 (right).	28
1.5	Illustration of the orthotropic structure of wood.	29
1.6	Illustration of non-admissible parameter values in a lower-dimensional sub-manifold of the set of all material parameter	29
2.1	Geometrical conforming case (left) and slave conforming case (right).	38
2.2	Checkerboard mode for $d = 2$ and $p = 6$	43
2.3	h -dependency of the L^2 inf-sup constant for dimension $d = 2$ and $d = 3$. Left: $p = 2$. Right: $p = 10$	44
2.4	Boundary modification of a spline of degree 3 for $d = 2$, left modification.	49
2.5	Different parametrizations of the infinite plate with a hole. From left to right: 2, 3 and 4 subdomains.	50
2.6	Left: Broken V primal error curves. Right: L^2 dual error curves. Respectively from the top to the bottom, for the 2, 3 and 4 patch parametrizations, for several pairings.	51
2.7	Non-conforming mesh with a non-matching interface.	52
2.8	Several L^2 error curves. Top left: Primal error for stable pairings of primal degree $p = 4$. Top right: Primal error for stable pairings of primal degree $p = 3$. Bottom left: Direct comparison of the primal error for pairings P4-P2 and P3-P1. Bottom right: Dual error for stable pairings of primal degree $p = 3$ and $p = 4$	53
2.9	Discrete Lagrange multiplier.	54
2.10	Setting and symmetry of the compressed bimaterial block.	55
2.11	Isogeometric initial grid of the left half of the block with four patches and four interfaces marked in red.	55
2.12	Compressed bimaterial block with stress distribution $ \boldsymbol{\sigma} $	57
2.13	Vertical displacement at the control point \mathbf{A} and the estimated relative error $ u_2(\mathbf{A}) - u_2^{\text{ex}}(\mathbf{A}) / u_2^{\text{ex}}(\mathbf{A}) $ with $u_2^{\text{ex}}(\mathbf{A}) \approx -1.82878$. . .	57

2.14	A quadratic basis function and its corresponding (rescaled) biorthogonal basis function with the same support.	58
2.15	Construction of the broken space W_h^{-1} from the primal space W_h for $p = 2$	59
2.16	Local basis contribution based on the B-spline \hat{B}_i^p for $p = 2$	61
2.17	Orthogonal basis function with same support (left) and basis functions orthogonal to all N_i (right) for $p = 2$	61
2.18	A quadratic basis function and its corresponding (rescaled) biorthogonal basis function with a local support and optimal approximation properties.	63
2.19	Initial meshes. Left: Square with mesh size ratio $\approx 1 : 1$ (c) and $2 : 3$ (a,b). Right: Annulus with mesh size ratio $\approx 1 : 1$ (c) and $2 : 3$ (a,b).	63
2.20	Stress magnitude of the elasticity equation on the annulus.	64
2.21	H^1 error for the square geometry. From left to right: $p = 2, 3, 4$. Top: Poisson equation. Bottom: Elasticity equation.	65
2.22	H^1 error for the annulus geometry. From left to right: $p = 2, 3, 4$. Top: Poisson equation. Bottom: Elasticity equation.	66
2.23	Left: Primal solution on Ω . Right: Lagrange multiplier along the interface.	68
2.24	Different meshes with one uniform mesh refinement (i.e., level 1). From the left to the right: M1 to M3.	69
2.25	L^2 primal (top) and dual (bottom) error curves for the case M3. Equal order pairings with $p = 1, 3, 5$ (from left to right) for the slave integration approach and a different number of additional quadrature points.	70
2.26	L^2 primal error curves for the cases M1 (left) and M2 (right). Pairing P3-P3 for the slave integration approach and a different number of additional quadrature points.	71
2.27	L^2 primal (left) and dual (right) error at refinement level number 6 as a function of the number of additional quadrature points for the case M3. Pairing P3-P3 for the slave integration approach.	71
2.28	L^2 primal (left) and dual (right) error curves for the case M3. Equal order pairing $p = 1$ for the non-symmetric approach and a different number of additional quadrature points.	72
2.29	L^2 primal error curves for the case M3. Different order pairings for the non-symmetric approach and a different number of additional quadrature points. Top left: P2-P0. Top right: P3-P1. Bottom left: P4-P2. Bottom right: P4-P0.	73
2.30	Meshes at refinement level 1 (left) and the slave domain (right) illustrating the curved interface.	74
2.31	L^2 primal error curves for the pairing P4-P4, for the three-dimensional example with the slave integration approach (left) and the non-symmetric approach (right).	74

2.32	L^2 primal error curves for the three-dimensional example with the pairings P3-P1 (left) and P4-P2 (right), for the non-symmetric approach and a different number of additional quadrature points. . . .	75
2.33	Comparison of the eigenvalue approximation of standard FEM and IGA with a smooth and a discontinuous ansatz on a one-dimensional domain with $p = 3$. Left: Whole spectrum. Right: Zoom onto the first (top) and last (bottom) eigenvalues.	77
2.34	Comparison of the eigenvalue approximation of standard FEM and IGA with a smooth and a discontinuous ansatz on a unit square with $p = 3$. Left: Whole spectrum with dashed lines at $n = \dim X_h - \dim M_h$ and $n = \dim X_h$. Right: Non-conforming initial mesh on the unit square.	78
2.35	Comparison of some eigenvalues and eigenfunctions of the beam with holes with the ones of a standard beam.	79
2.36	Geometry of the beam with three holes and its decomposition into 12 patches.	80
2.37	The first 100 eigenvalues on the initial mesh and after up to three refinement steps.	81
3.1	Example of a violin bridge.	84
3.2	Decomposition of the three-dimensional geometry into 16 patches Ω_k and 16 interfaces γ_l	85
3.3	Non-matching isogeometric mesh of the violin bridge.	85
3.4	Decomposition of the bimaterial bridge into 18 patches, coupled at 20 interfaces. Ebony inlay marked in gray.	86
3.5	Comparison of some eigenvalues and eigenfunctions with and without inlay. Top: No inlay. Bottom: Bimaterial bridge.	87
3.6	Influence of the thickness of the bridge on several eigenfunctions.	95
3.7	Convergence of the relative error of the eigenvalues (top) and eigenfunctions (bottom). Parameter range \mathcal{P}_1 with a fixed thickness $\mu_{10} = 1$ (left), with varying thickness $\mu_{10} \in [1/2, 2]$ (middle) and parameter range \mathcal{P}_2 with varying thickness $\mu_{10} \in [1/2, 2]$ (right).	96
3.8	Convergence of the relative (left), absolute (middle) error of the eigenvalues and eigenfunctions (right). Parameter range \mathcal{P}_1 with varying thickness $\mu_{10} \in [1/2, 2]$, simultaneous approximating 15 eigenpairs.	96
3.9	Sampling of the first and 15th eigenvalue within the parameter set \mathcal{P}_1 with varying thickness $\mu_{10} \in [1/2, 2]$ as used in the test set. Extremal values: $\min \lambda_1 = 0.29$, $\max \lambda_1 = 4.24$, $\min \lambda_{15} = 100.19$, $\max \lambda_{15} = 593.65$	97
3.10	Four two-dimensional displacement modes.	100
3.11	Comparison of two-dimensional eigenfunctions. From left to right: Second, third and sixth eigenvalue. Top: Undeformed. Bottom: Maximal deformation.	101

3.12	Model order reduction for the two-dimensional case. Top: Eigenvalue convergence. Bottom: Eigenfunction convergence. Left to right: $K = 5, 10, 15, 50$	101
3.13	Some possible geometries. From left to right: Reference domain, maximal deformation, random deformation.	101
3.14	Model order reduction for the three-dimensional case with $K = 5$. Left: Eigenvalue convergence. Right: Eigenfunction convergence.	102
4.1	Active and inactive area within one element τ_h for $d = 2$	110
4.2	Left: Decomposition of a 2D domain into the patches. Right: One patch after a suitable rotation.	112
4.3	Exact solution and finite element approximation on level 2. Values for the primal solution (left) and the dual solution (right).	124
4.4	Discretization error displayed at the Signorini boundary. Error of the primal variable (left) and of the dual variable (right) at level $k = 6$	124
4.5	Estimated convergence rates in fractional Sobolev spaces.	126
4.6	Zoom of dual solution and approximations at levels 2 to 4 around the left transmission point.	127
5.1	Local rotational modes. Left: Checkerboard mode on a uniform rectangular grid. Middle: Singular mode on a patch of four triangles. Right: Singular modes appearing during regular refinements of a tetrahedron.	134
5.2	Sketch of the local variables considered during the hybridization. Left: Illustration of the multi-valued Lagrange multiplier. Communication only necessary for $u_{\Gamma,h}$, not for values of λ_h on different elements. Right: Local element-wise components.	141
5.3	Suitable couplings, primal (top) and dual (bottom) degrees of freedom. From left to right: P2-PN, P2 ⁺ -P1, P3-P1.	143
5.4	Additional primal basis function for the P2 ⁺ -P1 pairing. Left: On a triangle. Right: On a quadrilateral.	144
5.5	Stress distribution $ \boldsymbol{\sigma} $ on the L-shaped domain.	148
5.6	Convergence of the relative $L^2(\Omega)$ error with uniform h -refinement and an adaptive choice of the face degrees of freedom.	148
5.7	Left: Deformed geometry for $\beta = 1/4$ solving the manufactured contact solution. Right: Convergence for $\beta = 1/4$ (top) and $\beta = 5/12$ (bottom).	149
5.8	Convergence of the $L^2(\Gamma_S)$ error of the Lagrange multiplier for $\beta = 1/4$ and $\beta = 5/12$ with the estimated order of convergence.	150
5.9	Convergence of the relative L^2 error for different values of $\lambda_{\text{Lamé}}$. Left: P2-PN pairing. Right: P3-P1 pairing.	151
5.10	Setting of the three-dimensional version of Cook's membrane. A constant traction is applied to the green surface.	152

5.11	Magnified representation of the deformed geometry with the initial geometry from two viewpoints.	153
5.12	Convergence plot of tip-displacement for Cook's membrane.	154
5.13	Configurations of the beam example. Geometry shown for case 1 and 2 ($l = 10$ mm). In case 3 we use $l = 5$ mm.	160
5.14	Left: Vertical displacement of the point A for the beam in case 1 with respect to total degrees of freedom. Right: Zoom of the same setting.	161
5.15	Comparison of the vertical displacement of the point A for the beam in cases 1 and 2 (left) and cases 1 and 3 (right).	163
5.16	Left: Vertical displacement of the point A for the non-linear beam with respect to the global degrees of freedom Right: Deformation of the non-linear beam and the stress distribution σ_{11}	164
5.17	Bimaterial annulus: Sketch of the computational domain, exploiting the symmetric structure (left) and undeformed and deformed domain including stress distribution (right).	165
5.18	Left: Vertical displacement of the solution at the point A for linear approximations HDG and conforming Q1, and quadratic approximations SIPDG(Q2) and conforming Q2. Right: Estimated relative error for the bimaterial annulus with respect to an extrapolated value for a reference solution on a fine mesh.	166

Tables

2.1	Vertical displacement evaluated on the first four grid levels and the estimated relative error.	57
2.2	Last estimated order of convergence of the primal and dual L^2 errors for the cases M1 and M2. Pairing P5-P5 for the slave integration approach and a different number of additional quadrature points. .	70
2.3	Number of degrees of freedom for the beam with holes on different mesh levels	80
3.1	Reference parameter and considered parameter ranges.	93
3.2	The 10 smallest eigenvalues for different thickness parameters, with the other parameters fixed to the reference value.	94
4.1	Relative errors of the primal and dual solution at different mesh levels k and an averaged numerical convergence order.	125
4.2	Distance of the transmission points x_l and x_r to the discrete transmission points $x_{l,h}$ and $x_{r,h}$ on level k , compared to the mesh size h . .	126
5.1	$L^2(\Omega)$ error with an estimated rate of convergence for different non-conforming pairings.	146
5.2	Energy error $(\int_{\Omega} \boldsymbol{\varepsilon}(\mathbf{u} - \mathbf{u}_h) : \boldsymbol{\sigma}(\mathbf{u} - \mathbf{u}_h) \, d\mathbf{x})^{1/2}$ with estimated rate of convergence for different non-conforming pairings.	147
5.3	Comparison of the hybrid DG and the hybrid weakly conforming methods	159
5.4	Overview of the considered methods, their abbreviation and the software used.	160

Bibliography

- [1] Y. Achdou and O. Pironneau. *Computational Methods for Option Pricing*. Society for Industrial and Applied Mathematics, 2005.
- [2] J. Albery and C. Carstensen. Discontinuous Galerkin time discretization in elastoplasticity: motivation, numerical algorithms, and applications. *Comput. Methods Appl. Mech. Engrg.*, 191(43):4949–4968, 2002.
- [3] A. Ammar, A. Huerta, F. Chinesta, E. Cueto, and A. Leygue. Parametric solutions involving geometry: A step towards efficient shape optimization. *Comput. Methods Appl. Mech. Engrg.*, 268:178–193, 2014.
- [4] P. Antolin, A. Buffa, and M. Fabre. A priori error for unilateral contact problems with Lagrange multipliers and IsoGeometric Analysis. <https://arxiv.org/abs/1701.03150>, 2017.
- [5] T. Apel, J. Pfefferer, and A. Rösch. Finite element error estimates for Neumann boundary control problems on graded meshes. *Comput. Optim. Appl.*, 52:3–28, 2012.
- [6] T. Apel, J. Pfefferer, and A. Rösch. Finite element error estimates on the boundary with application to optimal control. *Math. Comp.*, 84:33–70, 2015.
- [7] T. Apel, A.-M. Sändig, and J. R. Whiteman. Graded mesh refinement and error estimates for finite element solutions of elliptic boundary value problems in non-smooth domains. *Math. Methods Appl. Sci.*, 19(1):63–85, 1996.
- [8] A. Apostolatos, R. Schmidt, R. Wüchner, and K.-U. Bletzinger. A Nitsche-type formulation and comparison of the most common domain decomposition methods in isogeometric analysis. *Internat. J. Numer. Methods Engrg.*, 97:473–504, 2014.
- [9] D. N. Arnold. Discretization by finite elements of a model parameter dependent problem. *Numer. Math.*, 37(3):405–421, 1981.

- [10] D. N. Arnold and G. Awanou. The serendipity family of finite elements. *Found. Comput. Math.*, 11(3):337–344, 2011.
- [11] D. N. Arnold, F. Brezzi, B. Cockburn, and D. Marini. Discontinuous Galerkin methods for elliptic problems. In B. Cockburn, G. E. Karniadakis, and C.-W. Shu, editors, *Discontinuous Galerkin Methods: Theory, Computation and Applications*, pages 89–101. Springer, Berlin, 2000.
- [12] D. N. Arnold, F. Brezzi, B. Cockburn, and D. Marini. Unified analysis of discontinuous Galerkin methods for elliptic problems. *SIAM J. Numer. Anal.*, 39(5):1749–1779, 2002.
- [13] F. Auricchio, L. Beirão da Veiga, T. J. R. Hughes, A. Reali, and G. Sangalli. Isogeometric collocation methods. *Math. Models Methods Appl. Sci.*, 20:2075–2107, 2010.
- [14] I. Babuška and T. Strouboulis. *The Finite Element Method and its Reliability*. Numerical mathematics and scientific computation. Clarendon Press, 2001.
- [15] I. Babuška and M. Suri. Locking effects in the finite element approximation of elasticity problems. *Numer. Math.*, 62(1):439–463, 1992.
- [16] I. Babuška. The finite element method with Lagrangian multipliers. *Numer. Math.*, 20(3):179–192, 1973.
- [17] M. Barrault, Y. Maday, N. C. Nguyen, and A. T. Patera. An ‘empirical interpolation’ method: application to efficient reduced-basis discretization of partial differential equations. *C. R. Acad. Sci. Paris. Ser. I*, 339:667–672, 2004.
- [18] C. E. Baumann and J. T. Oden. A discontinuous *hp* finite element method for convection-diffusion problems. *Comput. Methods Appl. Mech. Engrg.*, 175(3):311–341, 1999.
- [19] H. R. Bayat, J. Krämer, L. Wunderlich, S. Wulfinghoff, S. Reese, B. Wohlmuth, and C. Wieners. Numerical evaluation of discontinuous and nonconforming finite element methods in solid mechanics. *Submitted to Comput. Mech.*, 2017.
- [20] H. R. Bayat, S. Wulfinghoff, S. Reese, and F. Cavaliere. The discontinuous Galerkin method with reduced integration scheme for the boundary terms in almost incompressible linear elasticity. *PAMM. Proc. Appl. Math. Mech.*, 16(1):189–190, 2016.

-
- [21] Y. Bazilevs, L. Beirão da Veiga, J. A. Cottrell, T. J. R. Hughes, and G. Sangalli. Isogeometric analysis: Approximation, stability and error estimates for h -refined meshes. *Math. Models Methods Appl. Sci.*, 16(7):1031–1090, 2006.
- [22] L. Beirão da Veiga, A. Buffa, G. Sangalli, and R. Vázquez. Mathematical analysis of variational isogeometric methods. *Acta Numer.*, 23:157–287, 2014.
- [23] L. Beirão da Veiga, D. Cho, and G. Sangalli. Anisotropic NURBS approximation in isogeometric analysis. *Comput. Methods Appl. Mech. Engrg.*, 209–212:1–11, 2012.
- [24] T. Belytschko, W. K. Liu, B. Moran, and K. Elkhodary. *Nonlinear Finite Elements for Continua and Structures*. Wiley, 2014.
- [25] F. Ben Belgacem. The mortar finite element method with Lagrange multipliers. *Numer. Math.*, 84:173–197, 1999.
- [26] F. Ben Belgacem, P. Hild, and P. Laborde. Extension of the mortar finite element method to a variational inequality modeling unilateral contact. *Math. Models Methods Appl. Sci.*, 9:287–303, 1999.
- [27] F. Ben Belgacem and Y. Maday. The mortar finite element method for three dimensional finite elements. *ESAIM Math. Model. Numer. Anal.*, 31(2):289–302, 1997.
- [28] F. Ben Belgacem and Y. Renard. Hybrid finite element methods for the Signorini problem. *Math. Comp.*, 72:1117–1145, 2003.
- [29] M. Benzi, G. H. Golub, and J. Liesen. Numerical solution of saddle point problems. *Acta Numer.*, 14:1–137, 2005.
- [30] C. Bernardi, Y. Maday, and A. T. Patera. Domain decomposition by the mortar element method. In H. Kaper and M. Garbey, editors, *Asymptotic and Numerical Methods for Partial Differential Equations with Critical Parameters*, volume 384 of *NATO ASI Series*, pages 269–286. Springer, 1993.
- [31] C. Bernardi, Y. Maday, and A. T. Patera. A new nonconforming approach to domain decomposition: the mortar element method. In H. Brezis and J. Lions, editors, *Nonlinear partial differential equations and their applications.*, volume XI, pages 13–51. Collège de France, 1994.

- [32] D. Boffi, F. Brezzi, and M. Fortin. *Mixed Finite Element Methods and Applications*. Springer, Berlin, 2013.
- [33] R. Bouclier, J.-C. Passieux, and M. Salaün. Development of a new, more regular, mortar method for the coupling of NURBS subdomains within a NURBS patch: Application to a non-intrusive local enrichment of NURBS patches. *Comput. Methods Appl. Mech. Engrg.*, 316:123–150, 2017.
- [34] D. Braess. *Finite elements. Theory, fast solvers, and applications in solid mechanics*. Cambridge University Press, Cambridge, third edition, 2007.
- [35] D. Braess, W. Dahmen, and C. Wieners. A multigrid algorithm for the mortar finite element method. *SIAM J. Numer. Anal.*, 37:48–69, 1999.
- [36] J. H. Bramble and S. R. Hilbert. Estimation of linear functionals on Sobolev spaces with application to Fourier transforms and spline interpolation. *SIAM J. Numer. Anal.*, 7(1), 1970.
- [37] J. Bramwell, L. Demkowicz, J. Gopalakrishnan, and W. Qiu. A locking-free *hp* DPG method for linear elasticity with symmetric stresses. *Numer. Math.*, 122(4):671–707, 2012.
- [38] S. C. Brenner. Poincaré–Friedrichs inequalities for piecewise H^1 functions. *SIAM J. Numer. Anal.*, 41(1):306–324, 2003.
- [39] S. C. Brenner. Korn’s inequalities for piecewise H^1 vector fields. *Math. Comp.*, 73(247):1067–1087, 2004.
- [40] S. C. Brenner and L. R. Scott. *The Mathematical Theory of Finite Element Methods*. Texts in Applied Mathematics 15. Springer, New York, 2008.
- [41] E. Brivadis. *Isogeometric mortar methods with applications in contact mechanics*. PhD thesis, Scuola Universitaria Superiore IUSS Pavia, October 2016.
- [42] E. Brivadis, A. Buffa, B. Wohlmuth, and L. Wunderlich. The influence of quadrature errors on isogeometric mortar methods. In B. Jüttler and B. Simeon, editors, *Isogeometric Analysis and Applications 2014*, pages 33–50. Springer International Publishing, Cham, 2015.
- [43] E. Brivadis, A. Buffa, B. Wohlmuth, and L. Wunderlich. Isogeometric mortar methods. *Comput. Methods Appl. Mech. Engrg.*, 284:292–319, 2015.

-
- [44] V. Bucur. *Handbook of Materials for String Musical Instruments*. Springer, 2016.
- [45] A. Buffa, R. Vázquez, G. Sangalli, and L. Beirão da Veiga. Approximation estimates for isogeometric spaces in multipatch geometries. *Numer. Methods Partial Differential Equations*, 31(2), 2015.
- [46] C. Canuto, T. Tonn, and K. Urban. A posteriori error analysis of the reduced basis method for nonaffine parametrized nonlinear PDEs. *SIAM J. Numer. Anal.*, 47(3):2001–2022, 2009.
- [47] L. Cazabeau, C. Lacour, and Y. Maday. Numerical quadratures and mortar methods. In *Computational Science for the 21st Century*, pages 119–128. John Wiley and Sons, 1997.
- [48] Z. Chen and H. Chen. Pointwise error estimates of discontinuous Galerkin methods with penalty for second-order elliptic problems. *SIAM J. Numer. Anal.*, 42(3):1146–1166, 2004.
- [49] Z. Chen and R. Nochetto. Residual type a posteriori error estimates for elliptic obstacle problems. *Numer. Math.*, 84(4):527–548, 2000.
- [50] P. G. Ciarlet. *The Finite Element Method for Elliptic Problems*. Classics in Applied Mathematics. Society for Industrial and Applied Mathematics, 2002.
- [51] B. Cockburn and J. Gopalakrishnan. New hybridization techniques. *GAMM-Mitt.*, 28(2):154–182, 2005.
- [52] B. Cockburn, J. Gopalakrishnan, and R. Lazarov. Unified hybridization of discontinuous Galerkin, mixed, and continuous Galerkin methods for second order elliptic problems. *SIAM J. Numer. Anal.*, 47(2):1319–1365, 2009.
- [53] A. Collin, G. Sangalli, and T. Takacs. Analysis-suitable G^1 multi-patch parametrizations for C^1 isogeometric spaces. *Comput. Aided Geom. Design*, 47:93–113, 2016.
- [54] P. Coorevits, P. Hild, K. Lhalouani, and T. Sassi. Mixed finite element methods for unilateral problems: Convergence analysis and numerical studies. *Math. Comp.*, 71:1–25, 2001.

- [55] L. Coox, F. Greco, O. Atak, D. Vandepitte, and W. Desmet. A robust patch coupling method for NURBS-based isogeometric analysis of non-conforming multipatch surfaces. *Comput. Methods Appl. Mech. Engrg.*, 316:235–260, 2017.
- [56] J. A. Cottrell, T. J. R. Hughes, and Y. Bazilevs. *Isogeometric Analysis. Towards Integration of CAD and FEA*. Wiley, Chichester, 2009.
- [57] J. A. Cottrell, A. Reali, Y. Bazilevs, and T. J. R. Hughes. Isogeometric analysis of structural vibrations. *Comput. Methods Appl. Mech. Engrg.*, 195(41–43):5257–5296, 2006.
- [58] R. Courant, H. Robbins, and I. Stewart. *What is Mathematics?: An Elementary Approach to Ideas and Methods*. Oxford Paperbacks. Oxford University Press, 1996.
- [59] M. Crouzeix and P.-A. Raviart. Conforming and nonconforming finite element methods for solving the stationary Stokes equations I. *R.A.I.R.O.*, 7(R3):33–75, 1973.
- [60] C. de Falco, A. Reali, and R. Vázquez. GeoPDEs: A research tool for isogeometric analysis of PDEs. *Adv. Eng. Softw.*, 42(12):1020–1034, 2011.
- [61] L. De Lorenzis, I. Temizer, P. Wriggers, and G. Zavarise. A large deformation frictional contact formulation using NURBS-based isogeometric analysis. *Internat. J. Numer. Methods Engrg.*, 87:1278–1300, 2011.
- [62] L. De Lorenzis, P. Wriggers, and T. J. R. Hughes. Isogeometric contact: a review. *GAMM-Mitt.*, 37(1):85–123, 2014.
- [63] L. De Lorenzis, P. Wriggers, and G. Zavarise. A mortar formulation for 3D large deformation contact using NURBS-based isogeometric analysis and the augmented Lagrangian method. *Comput. Methods Appl. Mech. Engrg.*, 49:1–20, 2012.
- [64] D. A. Di Pietro and A. Ern. *Mathematical Aspects of Discontinuous Galerkin Methods*. Springer, 2012.
- [65] D. A. Di Pietro and S. Nicaise. A locking-free discontinuous Galerkin method for linear elasticity in locally nearly incompressible heterogeneous media. *Appl. Numer. Math.*, 63:105–116, 2013.

- [66] M. Dittmann, M. Franke, I. Temizer, and C. Hesch. Isogeometric analysis and thermomechanical mortar contact problems. *Comput. Methods Appl. Mech. Engrg.*, 274:192–212, 2014.
- [67] J. Donea and A. Huerta. *Finite Element Methods for Flow Problems*. Wiley, 2003.
- [68] W. Dörfler. A convergent adaptive algorithm for Poisson’s equation. *SIAM J. Numer. Anal.*, 33(3):1106–1124, 1996.
- [69] W. Dornisch, J. Stöckler, and R. Müller. Dual and approximate dual basis functions for B-splines and NURBS – comparison and application for an efficient coupling of patches with the isogeometric mortar method. *Comput. Methods Appl. Mech. Engrg.*, 316:449–496, 2017.
- [70] W. Dornisch, G. Vitucci, and S. Klinkel. The weak substitution method – an application of the mortar method for patch coupling in NURBS-based isogeometric analysis. *Internat. J. Numer. Methods Engrg.*, 103(3):205–234, 2015.
- [71] M. Drohmann, B. Haasdonk, S. Kaulmann, and M. Ohlberger. A software framework for reduced basis methods using DUNE-RB and RBmatlab. *Advances in DUNE*, pages 77–88, 2012.
- [72] G. Drouot and P. Hild. Optimal convergence for discrete variational inequalities modelling Signorini contact in 2D and 3D without additional assumptions on the unknown contact set. *SIAM J. Numer. Anal.*, 53:1488–1507, 2015.
- [73] C. Eck, O. Steinbach, and W. Wendland. A symmetric boundary element method for contact problems with friction. *Math. Comput. Simulation*, 50:43–61, 1999.
- [74] I. Ekeland and R. Temam. *Convex Analysis and Variational Problems*. Classics in Applied Mathematics. Society for Industrial and Applied Mathematics, Philadelphia, 1999.
- [75] H. C. Elman and Q. Liao. Reduced basis collocation methods for partial differential equations with random coefficients. *SIAM/ASA J. Uncertain. Quantif.*, 1(1):192–217, 2013.
- [76] A. Ern and J.-L. Guermond. *Theory and Practice of Finite Elements*. Springer, 2004.

- [77] J. A. Evans, Y. Bazilevs, I. Babuška, and T. J. R. Hughes. n -widths, sup–infs, and optimality ratios for the k -version of the isogeometric finite element method. *Comput. Methods Appl. Mech. Engrg.*, 198(21–26):1726–1741, 2009.
- [78] L. C. Evans and R. F. Gariepy. *Measure Theory and Fine Properties of Functions*. Studies in Advanced Mathematics. CRC Press, Boca Raton, 1992.
- [79] R. S. Falk. Error estimates for the approximation of a class of variational inequalities. *Math. Comp.*, 28(128):963–971, 1974.
- [80] R. S. Falk. Nonconforming finite element methods for the equations of linear elasticity. *Math. Comp.*, 57(196):529–550, 1991.
- [81] K. A. Fischer and P. Wriggers. Frictional 2D contact formulations for finite deformations based on the mortar method. *Comput. Mech.*, 36:226–244, 2005.
- [82] N. H. Fletcher and T. D. Rossing. *The Physics of Musical Instruments*. Springer, New York, 2nd edition, 1998.
- [83] Forest Products Laboratory. *Wood Handbook - Wood as an Engineering Material*. The Laboratory, 2010.
- [84] M. Fortin and M. Soulie. A non-conforming piecewise quadratic finite element on triangles. *Internat. J. Numer. Methods Engrg.*, 19(4):505–520, 1983.
- [85] J. Frischkorn and S. Reese. Solid-beam finite element analysis of Nitinol stents. *Comput. Methods Appl. Mech. Engrg.*, 291:42–63, 2015.
- [86] F. Fuentes, B. Keith, L. Demkowicz, and P. Le Tallec. Coupled variational formulations of linear elasticity and the DPG methodology. *ICES Report*, 16-21, 2016.
- [87] I. Fumagalli, A. Manzoni, N. Parolini, and M. Verani. Reduced basis approximation and a posteriori error estimates for parametrized elliptic eigenvalue problems. *ESAIM Math. Model. Numer. Anal.*, 50(6):1857–1885, 2016.
- [88] D. Fußeder, B. Simeon, and A.-V. Vuong. Fundamental aspects of shape optimization in the context of isogeometric analysis. *Comput. Methods Appl. Mech. Engrg.*, 286:313–331, 2015.

-
- [89] D. Gallistl, P. Huber, and D. Peterseim. On the stability of the Rayleigh–Ritz method for eigenvalues. *Numer. Math.*, 2017.
- [90] A.-L. Gerner and K. Veroy. Certified reduced basis methods for parametrized saddle point problems. *SIAM J. Sci. Comput.*, 34(5):A2812–A2836, 2012.
- [91] D. Gilbarg and N. S. Trudinger. *Elliptic Partial Differential Equations of Second Order*. Classics in Mathematics. Springer, Berlin, 2001.
- [92] S. Glas and K. Urban. On non-coercive variational inequalities. *SIAM J. Numer. Anal.*, 52:2250–2271, 2014.
- [93] S. Glas and K. Urban. Numerical investigations of an error bound for reduced basis approximations of noncoercive variational inequalities. *IFAC-PapersOnLine*, 48(1):721–726, 2015.
- [94] R. Glowinski. *Numerical Methods for Nonlinear Variational Problems*. Springer, New York, 1984.
- [95] H. Gomez and L. De Lorenzis. The variational collocation method. *Comput. Methods Appl. Mech. Engrg.*, 309:152–181, 2016.
- [96] M. A. Grepl, Y. Maday, N. C. Nguyen, and A. T. Patera. Efficient reduced-basis treatment of nonaffine and nonlinear partial differential equations. *ESAIM Math. Model. Numer. Anal.*, 41(3):575–605, 2007.
- [97] B. J. Grieshaber, A. T. McBride, and B. D. Reddy. Uniformly convergent interior penalty methods using multilinear approximations for problems in elasticity. *SIAM J. Numer. Anal.*, 53(5):2255–2278, 2015.
- [98] P. Grisvard. *Elliptic Problems in Nonsmooth Domains*. Society for Industrial and Applied Mathematics, Philadelphia, 2011.
- [99] B. Haasdonk, J. Salomon, and B. Wohlmuth. A reduced basis method for parametrized variational inequalities. *SIAM J. Numer. Anal.*, 50:2656–2676, 2012.
- [100] P. Hansbo and M. G. Larson. Discontinuous Galerkin methods for incompressible and nearly incompressible elasticity by Nitsche’s method. *Comput. Methods Appl. Mech. Engrg.*, 191(17):1895–1908, 2002.
- [101] H. Hertz. Über die Berührung fester elastischer Körper. *J. Reine Angew. Math.*, 92:156–171, 1882.

- [102] C. Hesch and P. Betsch. Isogeometric analysis and domain decomposition methods. *Comput. Methods Appl. Mech. Engrg.*, 213–216:104–112, 2012.
- [103] K. S. Hesthaven, G. Rozza, and B. Stamm. *Certified Reduced Basis Methods for Parametrized Partial Differential Equations*. SpringerBriefs in Mathematics. Springer, 2016.
- [104] P. Hild. Numerical implementation of two nonconforming finite element methods for unilateral contact. *Comput. Methods Appl. Mech. Engrg.*, 184:99–123, 2000.
- [105] P. Hild and Y. Renard. An improved a priori error analysis for finite element approximations of Signorini’s problem. *SIAM J. Numer. Anal.*, 50(5):2400–2419, 2012.
- [106] C. Hofer, U. Langer, and I. Touloupoulos. Discontinuous Galerkin isogeometric analysis of elliptic diffusion problems on segmentations with gaps. *SIAM J. Sci. Comput.*, 38(6):A3430–A3460, 2016.
- [107] C. Hofer and I. Touloupoulos. Discontinuous Galerkin isogeometric analysis of elliptic problems on segmentations with non-matching interfaces. *Comput. Math. Appl.*, 72(7):1811–1827, 2016.
- [108] K. Höllig. *Finite Element Methods with B-Splines*. Frontiers in Applied Mathematics. Society for Industrial and Applied Mathematics, 2003.
- [109] T. Horger. *Complexity Reduction for Finite Element Methods with Applications to Eigenvalue Problems*. PhD thesis, Technische Universität München, July 2016.
- [110] T. Horger, J. M. Melenk, and B. Wohlmuth. On optimal L^2 and surface flux convergence in FEM. *Comput. Vis. Sci.*, 16:231–246, 2013.
- [111] T. Horger, A. Reali, B. Wohlmuth, and L. Wunderlich. Improved approximation of eigenvalues in isogeometric methods for multi-patch geometries and Neumann boundaries. <https://arxiv.org/abs/1701.06353>, 2017.
- [112] T. Horger, B. Wohlmuth, and T. Dickopf. Simultaneous reduced basis approximation of parameterized elliptic eigenvalue problems. *ESAIM: Mathematical Modelling and Numerical Analysis*, 51(2):443–465, 2017.
- [113] T. Horger, B. Wohlmuth, and L. Wunderlich. Reduced basis isogeometric mortar approximations for eigenvalue problems in vibroacoustics. In

- P. Benner, M. Ohlberger, A. Patera, G. Rozza, and K. Urban, editors, *Model Reduction of Parametrized Systems*, pages 91–106. Springer, 2017.
- [114] S. Hübner. *Discretization techniques and efficient algorithms for contact problems*. PhD thesis, Universität Stuttgart, 2008.
- [115] S. Hübner and B. Wohlmuth. An optimal a priori error estimate for non-linear multibody contact problems. *SIAM J. Numer. Anal.*, 43(1):156–173, 2005.
- [116] T. J. R. Hughes. *The Finite Element Method: Linear Static and Dynamic Finite Element Analysis*. Dover Publications, 2000.
- [117] T. J. R. Hughes, J. A. Cottrell, and Y. Bazilevs. Isogeometric analysis: CAD, finite elements, NURBS, exact geometry and mesh refinement. *Comput. Methods Appl. Mech. Engrg.*, 194:4135–4195, 2005.
- [118] T. J. R. Hughes, J. A. Evans, and A. Reali. Finite element and NURBS approximations of eigenvalue, boundary-value, and initial-value problems. *Comput. Methods Appl. Mech. Engrg.*, 272:290–320, 2014.
- [119] T. J. R. Hughes, A. Reali, and G. Sangalli. Duality and unified analysis of discrete approximations in structural dynamics and wave propagation: Comparison of p -method finite elements with k -method NURBS. *Comput. Methods Appl. Mech. Engrg.*, 197(49–50):4104–4124, 2008.
- [120] L. Iapichino, A. Quarteroni, G. Rozza, and S. Volkwein. Reduced basis method for the Stokes equations in decomposable domains using greedy optimization. *ECMI 2014*, pages 1–7, 2014.
- [121] K. Ito and K. Kunisch. *Lagrange Multiplier Approach to Variational Problems and Applications*. Society for Industrial and Applied Mathematics, Philadelphia, 2008.
- [122] B. Jakobsen and F. Rosendahl. The Sleipner platform accident. *Struct. Eng. Int.*, 3:190–193, 1994.
- [123] E. V. Jansson. Violin frequency response – bridge mobility and bridge feet distance. *Appl. Acoust.*, 65(12):1197–1205, 2004.
- [124] H. Kabaria, A. J. Lew, and B. Cockburn. A hybridizable discontinuous Galerkin formulation for non-linear elasticity. *Comput. Methods Appl. Mech. Engrg.*, 283:303–329, 2015.

- [125] M. Kaltenbacher. *Numerical Simulation of Mechatronic Sensors and Actuators. Finite Elements for Computational Multiphysics*. Springer, 2015.
- [126] B. Keith, F. Fuentes, and L. Demkowicz. The DPG methodology applied to different variational formulations of linear elasticity. *Comput. Methods Appl. Mech. Engrg.*, 309:579–609, 2016.
- [127] J. Kiendl, Y. Bazilevs, M.-C. Hsu, R. Wüchner, and K.-U. Bletzinger. The bending strip method for isogeometric analysis of Kirchhoff-Love shell structures comprised of multiple patches. *Comput. Methods Appl. Mech. Engrg.*, 199(37–40):2403–2416, 2010.
- [128] J. Kiendl, K.-U. Bletzinger, J. Linhard, and R. Wüchner. Isogeometric shell analysis with Kirchhoff-Love elements. *Comput. Methods Appl. Mech. Engrg.*, 198(49–52):3902–3914, 2009.
- [129] J.-Y. Kim and S.-K. Youn. Isogeometric contact analysis using mortar method. *Internat. J. Numer. Methods Engrg.*, 89(12):1559–1581, 2012.
- [130] D. Kinderlehrer and G. Stampacchia. *An Introduction to Variational Inequalities and Their Applications*. Society for Industrial and Applied Mathematics, Philadelphia, 2000.
- [131] S. K. Kleiss, C. Pechstein, B. Jüttler, and S. Tomar. IETI - Isogeometric Tearing and Interconnecting. *Comput. Methods Appl. Mech. Engrg.*, 247-248:201–215, 2012.
- [132] P. Knobloch. On Korn’s inequality for nonconforming finite elements. *Technische Mechanik*, 20(3):205–214, 2000.
- [133] P. Knobloch. Influence of mesh-dependent Korn’s inequality on the convergence of nonconforming finite element schemes. *Proceedings of Czech–Japanese Seminar in Applied Mathematics 2004*, pages 85–95, 2004.
- [134] P. Knobloch and L. Tobiska. On Korn’s first inequality for quadrilateral nonconforming finite elements of first order approximation properties. *Int. J. Numer. Anal. Model.*, 2(4):439–458, 2005.
- [135] J. Krämer, C. Wieners, B. Wohlmuth, and L. Wunderlich. A hybrid weakly nonconforming discretization for linear elasticity. *PAMM. Proc. Appl. Math. Mech.*, 16(1):849–850, 2016.

-
- [136] J. Krämer, C. Wieners, B. Wohlmuth, and L. Wunderlich. A robust weakly conforming hybrid discontinuous Galerkin method for linear elasticity. *In preparation*, 2017.
- [137] R. Krause and B. Wohlmuth. Nonconforming domain decomposition techniques for linear elasticity. *East-West J. Numer. Math.*, 8(3):177–206, 2000.
- [138] B. Lamichhane. *Higher Order Mortar Finite Elements with Dual Lagrange Multiplier Spaces and Applications*. PhD thesis, Universität Stuttgart, 2006.
- [139] B. Lamichhane, A. T. McBride, and B. D. Reddy. A finite element method for a three-field formulation of linear elasticity based on biorthogonal systems. *Comput. Methods Appl. Mech. Engrg.*, 258:109–117, 2013.
- [140] B. Lamichhane and B. Wohlmuth. Biorthogonal bases with local support and approximation properties. *Math. Comp.*, 76:233–249, 2007.
- [141] U. Langer and S. E. Moore. Discontinuous Galerkin isogeometric analysis of elliptic PDEs on surfaces. In T. Dickopf, M. J. Gander, L. Halpern, R. Krause, and L. F. Pavarino, editors, *Domain Decomposition Methods in Science and Engineering XXII*, pages 319–326. Springer, Cham, 2016.
- [142] T. A. Laursen. *Computational Contact and Impact Mechanics; Fundamentals of Modeling Interfacial Phenomena in Nonlinear Finite Element Analysis*. Springer, Berlin, 2002.
- [143] C. Lehrenfeld and J. Schöberl. High order exactly divergence-free hybrid discontinuous Galerkin methods for unsteady incompressible flows. *Comput. Methods Appl. Mech. Engrg.*, 307:339–361, 2016.
- [144] K. Lhalouani and T. Sassi. Nonconforming mixed variational formulation and domain decomposition for unilateral problems. *East-West J. Numer. Math.*, 7:23–30, 1999.
- [145] J. Li, J. M. Melenk, B. Wohlmuth, and J. Zou. Optimal a priori estimates for higher order finite elements for elliptic interface problems. *Appl. Numer. Math.*, 60:19–37, 2010.
- [146] R. Liu, M. F. Wheeler, and C. Dawson. A three-dimensional nodal-based implementation of a family of discontinuous Galerkin methods for elasticity problems. *Computers & Structures*, 87(3–4):141–150, 2009.

- [147] R. Liu, M. F. Wheeler, and I. Yotov. On the spatial formulation of discontinuous Galerkin methods for finite elastoplasticity. *Comput. Methods Appl. Mech. Engrg.*, 253:219–236, 2013.
- [148] A. Lovgren, Y. Maday, and E. Ronquist. A reduced basis element method for the steady Stokes problem. *ESAIM Math. Model. Numer. Anal.*, 40:529–552, 2006.
- [149] L. Machiels, Y. Maday, I. B. Oliveira, A. T. Patera, and D. V. Rovas. Output bounds for reduced-basis approximations of symmetric positive definite eigenvalue problems. *C. R. Acad. Sci., Paris, Sér. I*, 331(2):153–158, 2000.
- [150] L. Machiels, Y. Maday, A. T. Patera, and D. V. Rovas. A blackbox reduced-basis output bound method for shape optimization. In *Domain Decomposition Methods in Sciences and Engineering*, pages 429–436, 2000. 12th International Conference on Domain Decomposition Methods, Chiba, Japan.
- [151] Y. Maday, F. Rapetti, and B. Wohlmuth. The influence of quadrature formulas in 2D and 3D mortar element methods. In *Recent developments in domain decomposition methods. Some papers of the workshop on domain decomposition, ETH Zürich, Switzerland, June 7–8. 2001*, pages 203–221. Springer, 2002.
- [152] K.-A. Mardal and R. Winther. An observation on Korn’s inequality for nonconforming finite element methods. *Math. Comp.*, 75(253):1–6, 2005.
- [153] I. Martini, B. Haasdonk, and G. Rozza. Certified reduced basis approximation for the coupling of viscous and inviscid parametrized flow models. *J. Sci. Comput.*, pages 1–23, 2017.
- [154] D. Maurer and C. Wieners. A parallel block LU decomposition method for distributed finite element matrices. *Parallel Comput.*, 37:742–758, 2011.
- [155] T. W. McDevitt and T. A. Laursen. A mortar-finite element formulation for frictional contact problems. *Internat. J. Numer. Methods Engrg.*, 48:1525–1547, 2000.
- [156] J. M. Melenk. *hp-Finite Element Methods for Singular Perturbations*. Lecture Notes in Mathematics 1796. Springer, Berlin, 2002.

-
- [157] J. M. Melenk, H. Rezaïjafari, and B. Wohlmuth. Quasi-optimal a priori estimates for fluxes in mixed finite element methods and an application to the Stokes–Darcy coupling. *IMA J. Numer. Anal.*, 34(1):1–27, 2014.
- [158] J. M. Melenk and B. Wohlmuth. Quasi-optimal approximation of surface based Lagrange multipliers in finite element methods. *SIAM J. Numer. Anal.*, 50(4):2064–2087, 2012.
- [159] J. Mergheim, E. Kuhl, and P. Steinmann. A hybrid discontinuous Galerkin/interface method for the computational modelling of failure. *Comm. Numer. Methods Engrg.*, 20(7):511–519, 2004.
- [160] R. Milani, A. Quarteroni, and G. Rozza. Reduced basis method for linear elasticity problems with many parameters. *Comput. Methods Appl. Mech. Engrg.*, 197(51-52):4812–4829, 2008.
- [161] M. Moussaoui and K. Khodja. Régularité des solutions d’un problème mêlé Dirichlet–Signorini dans un domaine polygonal plan. *Commun. Part. Diff. Eq.*, 17:805–826, 1992.
- [162] N. I. Muskhelishvili. *Some Basic Problems of the Mathematical Theory of Elasticity*. Springer, 1977. Translated from the Russian.
- [163] F. Natterer. Optimale L_2 -Konvergenz finiter Elemente bei Variationsungleichungen. *Bonner Math. Schriften*, 89:1–12, 1976.
- [164] F. Negri, A. Manzoni, and G. Rozza. Reduced basis approximation of parametrized optimal flow control problems for the Stokes equations. *Comput. Math. Appl.*, 69(4):319–336, 2015.
- [165] N. C. Nguyen. A posteriori error estimation and basis adaptivity for reduced-basis approximation of nonaffine-parametrized linear elliptic partial differential equations. *J. Comput. Phys.*, 227(2):983–1006, 2007.
- [166] V. P. Nguyen, P. Kerfriden, M. Brino, S. Bordas, and E. Bonisoli. Nitsche’s method for two and three dimensional NURBS patch coupling. *Comput. Mech.*, 53(6):1163–1182, 2014.
- [167] J. Nitsche. Über ein Variationsprinzip zur Lösung von Dirichlet-Problemen bei Verwendung von Teilräumen, die keinen Randbedingungen unterworfen sind. In *Abhandlungen aus dem mathematischen Seminar der Universität Hamburg*, volume 36, pages 9–15. Springer, 1971.

- [168] G. Of, T. X. Phan, and O. Steinbach. An energy space finite element approach for elliptic Dirichlet boundary control problems. *Numer. Math.*, 129:723–748, 2015.
- [169] P. Oswald and B. Wohlmuth. On polynomial reproduction of dual FE bases. In N. Debit, M. Garbey, R. Hoppe, D. Keyes, Y. Kuznetsov, and J. Périaux, editors, *Domain Decomposition Methods in Science and Engineering*, pages 85–96. CIMNE, 2002. 13th International Conference on Domain Decomposition Methods, Lyon, France.
- [170] G. S. H. Pau. Reduced basis method for simulation of nanodevices. *Phys. Rev. B*, 78:155425, Oct 2008.
- [171] B. Peherstorfer, K. Willcox, and M. Gunzburger. Survey of multifidelity methods in uncertainty propagation, inference, and optimization. Technical Report 16-1, Aerospace Computational Design Laboratory, Massachusetts Institute of Technology, 2016.
- [172] L. Piegl and W. Tiller. *The NURBS Book*. Springer, 1997.
- [173] A. Popp. *Mortar Methods for Computational Contact Mechanics and General Interface Problems*. PhD thesis, Technische Universität München, 2012.
- [174] A. Popp and W. A. Wall. Dual mortar methods for computational contact mechanics - overview and recent developments. *GAMM-Mitt.*, 37(1):66–84, 2014.
- [175] M. A. Puso. A 3D mortar method for solid mechanics. *Internat. J. Numer. Methods Engrg.*, 59:315–336, 2004.
- [176] M. A. Puso and T. A. Laursen. A mortar segment-to-segment contact method for large deformation solid mechanics. *Comput. Methods Appl. Mech. Engrg.*, 193:601–629, 2004.
- [177] A. Quarteroni. *Numerical Models for Differential Problems*, volume 8 of *MS&A*. Springer, Milan, 2nd edition, 2014.
- [178] A. Quarteroni, A. Manzoni, and F. Negri. *Reduced Basis Methods for Partial Differential Equations. An Introduction*. Springer, 2016.
- [179] A. Quarteroni and A. Valli. *Numerical Approximation of Partial Differential Equations*. Springer Series in Computational Mathematics. Springer-Verlag, Berlin, New York, 1994.

-
- [180] A. Quarteroni and A. Valli. *Domain Decomposition Methods for Partial Differential Equations*. Numerical Mathematics and Scientific Computing. Oxford University Press, Oxford, 1999.
- [181] O. Rand and V. Rovenski. *Analytical Methods in Anisotropic Elasticity: with Symbolic Computational Tools*. Birkhäuser, 2007.
- [182] R. Rannacher and S. Turek. Simple nonconforming quadrilateral Stokes element. *Numer. Methods Partial Differential Equations*, 8(2):97–111, 1992.
- [183] T. Ranz. *Ein feuchte- und temperaturabhängiger anisotroper Werkstoff: Holz*. Beiträge zur Materialtheorie. Universität der Bundeswehr München, 2007.
- [184] B. Rivière. *Discontinuous Galerkin Methods for Solving Elliptic and Parabolic Equations*. Society for Industrial and Applied Mathematics, 2008.
- [185] O. E. Rodgers and T. R. Masino. The effect of wood removal on bridge frequencies. *Catgut Acoust Soc. J.*, 1(6), 1990.
- [186] T. D. Rossing, editor. *The Science of String Instruments*. Springer, 2010.
- [187] G. Rozza. Reduced basis methods for Stokes equations in domains with non-affine parameter dependence. *Comput. Vis. Sci.*, 12(1):23–35, 2009.
- [188] G. Rozza, D. B. P. Huynh, and A. Manzoni. Reduced basis approximation and a posteriori error estimation for Stokes flows in parametrized geometries: roles of the inf-sup stability constants. *Numer. Math.*, 125(1):115–152, 2013.
- [189] G. Rozza, D. B. P. Huynh, and A. T. Patera. Reduced basis approximation and a posteriori error estimation for affinely parametrized elliptic coercive partial differential equations. Application to transport and continuum mechanics. *Arch. Comput. Methods Eng.*, 15(3):229–275, 2008.
- [190] G. Rozza and K. Veroy. On the stability of the reduced basis method for Stokes equations in parametrized domains. *Comput. Methods Appl. Mech. Engrg.*, 196:1244–1260, 2007.
- [191] M. Ruess, D. Schillinger, A. Özcan, and E. Rank. Weak coupling for isogeometric analysis of non-matching and trimmed multi-patch geometries. *Comput. Methods Appl. Mech. Engrg.*, 269:46–71, 2014.

- [192] A. Rössle. Corner singularities and regularity of weak solutions for the two-dimensional Lamé equations on domains with angular corners. *J. Elasticity*, 60:57–75, 2000.
- [193] F. Salmoiraghi, F. Ballarin, L. Heltai, and G. Rozza. Isogeometric analysis-based reduced order modelling for incompressible linear viscous flows in parametrized shapes. *Adv. Model. Simul. Eng. Sci.*, 3:21, 2016.
- [194] F. Scarpini and M. A. Vivaldi. Error estimates for the approximation of some unilateral problems. *R.A.I.R.O. Anal. Numér.*, 11(2):197–208, 1977.
- [195] L. Schumaker. *Spline Functions: Basic Theory*. Cambridge University Press, Cambridge, third edition, 2007.
- [196] L. R. Scott and S. Zhang. Finite element interpolation of nonsmooth functions satisfying boundary conditions. *Math. Comp.*, 54(190):483–493, 1990.
- [197] A. Seitz, P. Farah, J. Kremheller, B. Wohlmuth, W. A. Wall, and A. Popp. Isogeometric dual mortar methods for computational contact mechanics. *Comput. Methods Appl. Mech. Engrg.*, 301:259–280, 2016.
- [198] R. Sevilla and A. Huerta. *Tutorial on Hybridizable Discontinuous Galerkin (HDG) for Second-Order Elliptic Problems*, pages 105–129. Springer, Cham, 2016.
- [199] S. Soon, B. Cockburn, and H. K. Stolarski. A hybridizable discontinuous Galerkin method for linear elasticity. *Internat. J. Numer. Methods Engrg.*, 80(8):1058–1092, 2009.
- [200] W. Spann. On the boundary element method for the Signorini problem of the Laplacian. *Numer. Math.*, 65:337–356, 1993.
- [201] O. Steinbach. *Stability Estimates for Hybrid Coupled Domain Decomposition Methods*. Lecture Notes in Mathematics 1809. Springer, Berlin, 2003.
- [202] O. Steinbach. *Numerical Approximation Methods for Elliptic Boundary Value Problems. Finite and Boundary Elements*. Springer, New York, 2008.
- [203] O. Steinbach. Boundary element methods for variational inequalities. *Numer. Math.*, 126:173–197, 2014.

-
- [204] O. Steinbach, B. Wohlmuth, and L. Wunderlich. Trace and flux a priori error estimates in finite-element approximations of Signorini-type problems. *IMA J. Numer. Anal.*, 36(3):1072–1095, 2016.
- [205] F.-T. Suttmeier. *Numerical Solution of Variational Inequalities by Adaptive Finite Elements*. Vieweg + Teubner, Wiesbaden, 2008.
- [206] B. Szabó and I. Babuška. *Introduction to Finite Element Analysis: Formulation, Verification and Validation*. Wiley, 2011.
- [207] L. Tartar. *An Introduction to Sobolev Spaces and Interpolation Spaces*. Lecture Notes of the Unione Matematica Italiana 3. Springer, Berlin, 2007.
- [208] R. L. Taylor. FEAP—a finite element analysis program. *Version 7.5 Theory Manual*, 2003.
- [209] I. Temizer, M. M. Abdalla, and Z. Gürdal. An interior point method for isogeometric contact. *Comput. Methods Appl. Mech. Engrg.*, 276:589–611, 2014.
- [210] I. Temizer, P. Wriggers, and T. J. R. Hughes. Three-dimensional mortar-based frictional contact treatment in isogeometric analysis with NURBS. *Comput. Methods Appl. Mech. Engrg.*, 209–212:115–128, 2012.
- [211] A. Ten Eyck and A. Lew. Discontinuous Galerkin methods for non-linear elasticity. *Internat. J. Numer. Methods Engrg.*, 67(9):1204–1243, 2006.
- [212] S. Timoshenko and J. Goodier. *Theory of Elasticity*. Mc Graw-Hill, New York, 1951.
- [213] T. Tonn. *Reduced-basis method (RBM) for non-affine elliptic parametrized PDEs*. PhD thesis, Universität Ulm, September 2012.
- [214] A. Toselli and O. Widlund. *Domain Decomposition Methods – Algorithms and Theory*. Springer Series in Computational Mathematics 34. Springer, Berlin, 2005.
- [215] S. Triebenbacher, M. Kaltenbacher, B. Wohlmuth, and B. Flemisch. Applications of the mortar finite element method in vibroacoustics and flow induced noise computations. *Acta Acust. united Ac.*, 96(3):536–553, 2010.

- [216] M. Tur, F. J. Fuenmayor, and P. Wriggers. A mortar-based frictional contact formulation for large deformations using Lagrange multipliers. *Comput. Methods Appl. Mech. Engrg.*, 198:2860–2873, 2009.
- [217] M. J. Turner, R. W. Clough, H. C. Martin, and L. J. Topp. Stiffness and deflection analysis of complex structures. *J. Aeronaut. Sci.*, 23(9):805–823, 1956.
- [218] S. Vallaghé, D. B. P. Huynh, D. J. Knezevic, L. Nguyen, and A. T. Patera. Component-based reduced basis for parametrized symmetric eigenproblems. *Adv. Model. Simul. Eng. Sci.*, 2, 2015.
- [219] R. Vázquez. A new design for the implementation of isogeometric analysis in Octave and Matlab: GeoPDEs 3.0. *Comput. Math. Appl.*, 72:523–554, 2016.
- [220] L. Wahlbin. Local behavior in finite element methods. In P. G. Ciarlet and J. L. Lions, editors, *Finite Element Methods (Part 1)*, volume 2 of *Handbook of Numerical Analysis*, pages 353–522. North-Holland, Amsterdam, 1991.
- [221] L. Wahlbin. *Superconvergence in Galerkin Finite Element Methods*. Lecture Notes in Mathematics 1605. Springer, Berlin, 1995.
- [222] C. Waluga and B. Wohlmuth. Quasi-optimal a priori interface error bounds and a posteriori estimates for the interior penalty method. *SIAM J. Numer. Anal.*, 52(6):3259–3279, 2013.
- [223] C. Wieners. A geometric data structure for parallel finite elements and the application to multigrid methods with block smoothing. *Comput. Vis. Sci.*, 13:161–175, 2010.
- [224] C. Wieners. The skeleton reduction for finite element substructuring methods. In B. Karasözen, M. Manguoğlu, M. Tezer-Sezgin, S. Göktepe, and Ö. Uğur, editors, *Numerical Mathematics and Advanced Applications ENUMATH 2015*, pages 133–141. Springer International Publishing, Cham, 2016.
- [225] C. Wieners and B. Wohlmuth. Robust operator estimates and the application to substructuring methods for first-order systems. *ESAIM Math. Model. Numer. Anal.*, 48:1473–1494, 2014.
- [226] T. Wihler. Locking-free adaptive discontinuous Galerkin FEM for linear elasticity problems. *Math. Comp.*, 75(255):1087–1102, 2006.

-
- [227] C. Wilking and M. Bischoff. Alternative integration algorithms for three-dimensional mortar contact. *Comput. Mech.*, 59(2):203–218, 2017.
- [228] B. Wohlmuth. A mortar finite element method using dual spaces for the Lagrange multiplier. *SIAM J. Numer. Anal.*, 38:989–1012, 2000.
- [229] B. Wohlmuth. *Discretization Methods and Iterative Solvers Based on Domain Decomposition*. Lecture Notes in Computational Science and Engineering 17. Springer, Berlin, 2001.
- [230] B. Wohlmuth. Variationally consistent discretization schemes and numerical algorithms for contact problems. *Acta Numer.*, 20:569–734, 2011.
- [231] B. Wohlmuth, A. Popp, M. W. Gee, and W. A. Wall. An abstract framework for a priori estimates for contact problems in 3D with quadratic finite elements. *Comput. Mech.*, 49:735–747, 2012.
- [232] J. Woodhouse. On the “bridge hill” of the violin. *Acta Acust. united Ac.*, 91(1):155–165, 2005.
- [233] P. Wriggers. *Nichtlineare Finite-Element-Methoden*. Springer, 2001.
- [234] P. Wriggers. *Computational Contact Mechanics*. Springer, Berlin, 2006.
- [235] S. Wulfinghoff, H. R. Bayat, A. Alipour, and S. Reese. A low-order locking-free hybrid discontinuous Galerkin element formulation for large deformations. *Comput. Methods Appl. Mech. Engrg.*, 323:353–372, 2017.
- [236] L. Wunderlich. Modern Discretization Techniques for Partial Differential Equations. Master’s thesis, Technische Universität München, Germany, 2014.
- [237] L. Wunderlich. Contact and mesh-tying using mortar methods. In S. C. Brenner, C. Carstensen, L. Demkowicz, and P. Wriggers, editors, *Computational Engineering*, volume 43, pages 2578–2580. Mathematisches Forschungsinstitut Oberwolfach, 2015.
- [238] C.-Z. Zhang, G.-M. Zhang, B.-Y. Ye, and L.-D. Liang. Violin bridge mobility analysis under in-plane excitation. *Sensors*, 13(11):15290–15306, 2013.
- [239] S. Zlotnik, P. Díez, D. Modesto, and A. Huerta. Proper generalized decomposition of a geometrically parametrized heat problem with geophysical applications. *Internat. J. Numer. Methods Engrg.*, 103(10):737–758, 2015.